SEISMIC EXPLORATION FOR METALLIC MINERAL DEPOSITS

KEBABONYE LALETSANG

SEISMIC EXPLORATION FOR METALLIC MINERAL DEPOSITS

By Kebabonye Laletsang, BSc., MSc.

A thesis submitted to the School of Graduate Studies in partial fulfilment of the requirements for the degree of Doctor of Philosophy

Department of Earth Sciences

Memorial University of Newfoundland

1 August 2001

St. John's, Newfoundland

Abstract

This thesis examines the effects of geometry on the seismic response of mineral deposits. Massive mineral deposits have comparable velocities to silicate rocks but are denser. Hence they are characterized by higher acoustic impedances which should cause strong seismic anomalies. However, mineral deposits cause only weak diffractions in seismic data because of their small sizes and complex geometries. Conventional data processing may fail to detect mineral deposits because it attenuates the diffractions.

P-wave reflection coefficients for a density-driven acoustic impedance contrast are large near normal incidence. The SV-wave has a stronger reflection coefficient with a reversed phase compared with the P-wave coefficient beyond normal incidence. Hence, large source to receiver offsets cannot record strong P-wave responses if the acoustic impedance contrast is density-driven. This finding is important in that, while deep targets are sought, source to receiver offsets must be small to record a strong P-wave response.

3D seismic data for an egg-shaped model show a seismic response comprising concentric, circular diffraction patterns in time slices. For a cylinder-shaped model with a rugged surface, the data show that the relief and dip impact strongly on the seismic response. Time slices through these data show circular but discontinuous diffraction patterns. 3D data for a disk-shaped model equal in size to the Fresnel zone, show that its surface structure cannot be mapped, but it can still be detected in time slices from the circular diffraction patterns. Using 2D numerical models, this thesis demonstrates that small, dipping targets produce diffraction seismic responses with amplitudes displaced down-dip, with phase

reversals at large angles of incidence for different source locations.

The modelling results are tested on 2D field data recorded on the Duck Pond deposit (NF), which dips 35-40° SW and comprises segments with different dips. In this case, little diffraction energy resides in the plane of the seismic section and clearly 3D data are required to obtain a better seismic response.

It is concluded that massive mineral deposits can be directly detected or imaged with reflection seismic if the appropriate parameters are used, namely, 3D seismic surveys with small source to receiver offsets and processing tailored to preserve the weak diffractions.

Acknowledgements

Financial support for this work was provided through a research grant awarded to me by the University of Botswana, and supplemented by my supervisor and co-supervisors, Drs. J.A. Wright, C.A. Hurich, and W.J. Scott, through their research grants. Further financial assistance was provided by the Memorial University Imaging Consortium (MUSIC). The field data used in this thesis were provided by Noranda Inc.. The staff of Thundermin Resources Inc. introduced me to the geology of the Tally Pond prospect, and provided the drill hole survey data. I am sincerely grateful to the above-mentioned for the financial and logistical support they provided.

I would like to express my sincere gratitude and thanks to my fellow students and faculty, who provided an amiable and enabling learning environment, and the departmental technical staff, especially Messrs A. Kocurko, P. Barnes, R. Patzold, D. Smith, and Dr. S. Deemer, who patiently guided me through the technical and logistical aspects of the experiments and data analysis. Great appreciation is due to my supervisor and co-supervisors, Drs. J.A. Wright, C.A. Hurich, and W.J. Scott, who have patiently guided me through the manuscript, and provided constant encouragement and direction.

Finally, I would like to express sincere gratitude and appreciation to my wife, Sannah, and our children, Bonolo and Bakang, for allowing me time to compile this thesis, and the patience they have showed during the process.

Table of Contents

List of Tables

List of Figures

List of Abbreviations

2D	two dimensional
3D	three dimensional
CMP	common mid-point
Cu-Zn	copper-zinc
F-K	frequency-spatial (K) domain
Ni-Cu-Co	nickel-copper-cobalt
NMO	normal moveout
S/N	signal to noise
TWT	two-way time
Zn-Pb-Cu	zinc-lead-copper
MVT	Mississippi Valley Type
VMS	Volcanogenic Massive Sulphide
SEDEX	Sedimentary Exhalative

CHAPTER 1

1.0 INTRODUCTION

1.1 Objectives and Purpose

This thesis discusses the potential applicability of reflection seismic methods for detecting and imaging mineral deposits at depths ≥600 m and the processing of seismic data acquired for that purpose. It focusses on the use of surface reflection seismic methods to explore for metallic mineral deposits, but the discussion includes pyrite and pyrrhotite which are not mined for metals but for sulphur. Emphasis is placed on massive deposits because they are viable targets for reflection seismic methods. Issues pertinent to the detection and imaging of mineral deposits with reflection seismic are explored with 3D analogue and 2D numerical modelling, and tested on 2D field data. The scope of this work is restricted to P-wave exploration, but S-waves are discussed with regard to some relevant theoretical issues.

The purpose of this work is to investigate the constraints that the geometry of mineral deposits imposes on their seismic response using seismic modelling. The geometric attributes of mineral deposits investigated include the effects of surface relief, dip, depth, and size, on the seismic response. Results from 3D and 2D seismic models are compared by extracting 2D profiles from the former, and subjecting them to a similar processing sequence as the 2D field data. The data are processed using post-stack and prestack depth imaging techniques for comparison.

1.2 The Problem

Mineral exploration evolved from the location of surface mineral indications (gossans) to discoveries at shallow depths with the use of geophysical methods. Many shallow deposits discovered in this manner are now nearing exhaustion, and predictably, the search for new discoveries is currently focused at greater depths. The conventional geophysical techniques are now mostly inadequate to locate mineral deposits at these greater depths because of limited depth penetration, and more effective techniques are required. One geophysical technique potentially suitable for this purpose is the reflection seismic method, which has been proven in the oil and gas industry. It is seldom used in base mineral exploration partly because the seismic signature of these deposits is poorly understood and also because of cost constraints.

Currently magnetotelluric (MT) and audio-magnetotelluric (AMT) techniques are used to map conductive targets at depths of up to ~1500 m (Stevens, 1998; Balch et al., 1998). However, conventional geophysical techniques do not have sufficient resolution to detect mineral deposits at depths ≥600 m (Macnae, 1988; Pretorius et al., 1989). Pemberton (1989) reviewed the discoveries of massive sulphide deposits, and conceded that none of those discovered with conventional geophysics occurred at depths exceeding 122 m. Conventional geophysical methods are used down-hole to extend the detection range downward and sideways. This application is, however, costly because it requires drill holes or tunnels, but does not effectively screen the prospect area sufficiently to enable timely strategic decisions to be made. Nevertheless, mineral exploration at depths of 1-3 km is

feasible if performed near existing mines where infrastructure and improved mining and recovery techniques exist.

Mining companies face a depletion of their existing mineral reserves unless new deposits are discovered. The incentive to explore is the increasing market demand for mineral products, new techniques used to process low grade deposits, and to extend the lifespan of existing mines and the service industries. Conventional geophysical exploration is generally limited to depths $\leq$600 m, and since it is exhaustive at the time of initial discovery, fertile ground is likely to exist at greater depths than those previously explored. Furthermore, it is becoming rarer to discover mineral deposits at shallow depths in non-frontier areas because previous exploration would have discovered them (Mutyorauta, 1987). The need to explore deeper than before for mineral deposits requires the use of geophysical techniques with better depth penetration and resolution than conventional geophysical methods.

Conventional geophysical exploration uses electromagnetic, electrical, and potential field techniques to identify drill targets because they are perceived to be more cost effective compared with reflection seismic methods, and they also have a proven track record. Most metallic mineral deposits are electrically conductive and of high density, so that they produce electromagnetic, electrical, and gravity anomalies. They also often produce strong magnetic responses because some, such as massive sulphides and iron ores, contain the common magnetic minerals, magnetite and pyrrhotite. Sphalerite-rich mineral deposits are an exception in that they are non-conductive, non-magnetic, and produce only subtle gravity

anomalies at depths ≥600 m because they are typically small. However, they possess high acoustic impedances (>20 kg/s/m^2) and should make viable reflection seismic targets. Similarly, many oxide mineral deposits have high density and should also make good reflection seismic targets if they are of a sufficient size.

The mining industry is investigating the adaptation of the reflection seismic method to mineral exploration because of its potential to directly detect or image mineral deposits at depths greater than those possible with conventional geophysics. In contrast to the latter, reflection seismic methods do not suffer greatly from a loss of resolution with increasing depth. Reflection seismic methods can detect and image targets at depths of hundreds of metres to kilometres with comparable resolution. The oil and gas industry uses reflection seismic to map structural and stratigraphic traps for petroleum. The gold mining industry of South Africa uses reflection seismic to map auriferous conglomerates (Pretorius et al., 1989; Pretorius et al., 2000; Diering, 2000). High resolution reflection seismic surveys conducted for mineral exploration at conventional depths are described in Cooksley (1992). Lastly, reflection seismic were used to map kimberlite structures in Venezuela (Hearst, 1998).

The mining industry is considering the use of reflection seismic methods for the direct detection and imaging of metallic mineral deposits.[1] This application has been

---

[1]A distinction is made between seismic detection and imaging. Detection applies where the target is smaller than the seismic resolution limit, and yet it still produces sufficient seismic signal to be detectable above the noise in a seismogram.

demonstrated in at least two instances, but it is used only occasionally because of high costs and also the seismic and electrical noise prevalent at operating mine sites. Reflection seismic was first used in a mine to directly detect a siderite lode in Germany (Schmidt, 1959). Recently, underground reflection seismic was used to directly detect chromite deposits at Shurugwi, Zimbabwe (Mutyorauta, 1987). The underground environment differs from the surface in that it lacks the low velocity layer and hence allows the propagation of frequencies in the range of 200-600 Hz because of the high quality factor (Q) in crystalline rocks. These surveys are high resolution, but, since the spread lengths are constrained by the extent of the mine galleries, they are restricted to small detection distances. As stated earlier, the cost is of less concern if exploration is performed in or near operating mines where both infrastructure and modern recovery technologies are at hand.

For exploration at depths ≥600 m, reflection seismic can be used to map structure, detect, or even image the mineral deposits if they are of a sufficient size. Although initial exploration costs are high compared with the conventional methods, reflection seismic leads to less ambiguous interpretation because it uses propagating rather than diffusive wavefields. Propagating wavefields are focused on a narrow area, while diffusive wavefields such as those used in electromagnetic techniques sample a large volume of rock and hence record an averaged quantity (Boerner et al., 1990; White et al., 2000). As such, reflection seismic methods can reduce the overall exploration costs by enabling better optimization of drill targets. Reflection seismic gives an almost continuous lateral coverage and may thus improve subsurface mapping with lateral detail (Singh, 1983). This aspect is clearly

demonstrated in Pretorius et al. (1989) with regard to structural and stratigraphic mapping.

Direct detection and imaging of mineral deposits with reflection seismic has advantages over structural and stratigraphic mapping. In this case, mineral deposits can be detected when hosted by similar footwall and hangingwall rocks such as in duplex thrust stacks, e.g. at the former Buchans Mine (NF) (Wright et al., 1994). Sphalerite-rich mineral deposits at depths ≥600 m produce only small and diffuse gravity anomalies and do not respond to electrical methods because they are non-conductive (Hallof, 1992; Heiland, 1968). Reflection seismic may be able to detect sphalerite-rich mineral deposits at depths ≥600 m, based on their high acoustic impedance contrast. Furthermore, sack-form masses of chromite deposits with no structural or stratigraphic relationship to the host rock occur in alpine type mafic igneous complexes (Thayer, 1963; Stanton, 1972).[2] The factors that control the direct detection and imaging of mineral deposits with reflection seismic are reviewed in Chapter 2.

1.3 Seismic Mapping

Although reflection seismic methods map structure and stratigraphy successfully in sedimentary rocks, they have so far shown limited success in the exploration for base

---

[2] Sack-form masses are irregular and often substantial chromite mineral deposits which exhibit no obvious relationship to the fabric of the host rock.

mineral deposits in crystalline rocks. Sedimentary rocks have variable seismic velocities and densities controlled by porosity and to a lesser extent by the lithology (Sheriff and Geldart, 1995). They typically produce coherent reflection events since the formations are laterally extensive and separated by abrupt acoustic impedance boundaries. Crystalline rocks, on the other hand, contain negligible porosity and have high but similar seismic velocities of ~6000 m/s, which are controlled mainly by the lithology and increase only slightly with increasing depth (Sheriff and Geldart, 1995).

High resolution seismic data recorded for mineral exploration in crystalline rocks have been processed and interpreted by several workers (e.g. Dahle et al., 1985; Boerner et al., 1990; Adam et al., 1992; Milkereit et al., 1992; Spencer et al., 1993; Wright et al., 1994; Adam et al., 1996; Milkereit et al., 1996a & b; Adam et al., 1998; Perron and Calvert, 1998; Milkereit et al., 2000). It has emerged from these works that reflection seismic data acquired in crystalline rocks differ from those recorded in sedimentary rocks in many respects. The crystalline terrain consists of a low velocity weathered layer or overburden lying on high velocity basement. The interface between overburden and basement generates refracted vertically polarized shear waves (SV) which override the P-wave reflections and degrade the quality of the CMP stack if not sufficiently suppressed in processing (Adam et al., 1998). Furthermore, the crystalline geology contains small inhomogeneities which cause scattering of high frequencies.

Because of the problems mentioned above, conventional seismic data processing does not image mineral deposits adequately. One reason for this is that it is optimized to

preferentially enhance specular reflections and attenuate other seismic events, particularly diffractions. However, the seismic response caused by small mineral deposits may consist entirely of diffractions and out-of-plane events (in 2D surveys) with no specular reflections. Consequently, the critical issue in imaging mineral deposits is to preserve the diffracted wavefield in data acquisition and processing, so that it remains recognizable in the processed data. Attempts to achieve the best detection and imaging of mineral deposits with reflection seismic against the background of the enumerated problems are discussed in later chapters.

1.4 Thesis Outline

The remainder of this thesis is arranged in six chapters to address the issues indicated above. Chapters 2 and 3 examine the theory that governs the detection and imaging of mineral deposits with reflection seismic methods. In Chapter 2, I show that the seismic response of metallic mineral deposits is strong at narrow angles of incidence (0-20°) for P-waves, and that the angular extent of the strong seismic response is controlled by the Poisson's ratio of the deposit (for specular reflections). Within this aperture, the converted-mode SV-wave response is weak and should allow potentially successful P-wave imaging. This finding is significant in that, although it is expected that the high acoustic impedance contrast of mineral deposits should give rise to large reflection coefficients, no study has yet shown the optimal angles of incidence for these targets. I show further that, the foregoing notwithstanding, mineral deposits do not cause strong seismic anomalies in field data

because of their typically small size and complicated geometries.

Chapter 3 describes the physical properties of common metallic mineral deposits. I use examples of 2D synthetic models to show the expected seismic response of typical mineral deposits. These seismograms are strictly a 2D seismic response because the numerical models do not account for out-of-plane events which are normally present in field data. Nevertheless, the models qualitatively indicate the seismic response to be expected from similar deposits in field data.

Chapters 4 and 5 examine the effects of geometry on the seismic response through the use of analogue and numerical models. Through these models, I show that the geometry, especially surface relief, has a great impact on the seismic expression of mineral deposits. Furthermore, these models show that 2D seismic surveys might detect, but not adequately image typical mineral deposits.

The material developed in Chapters 2 through 5 is used in Chapter 6 to build an interpretation for the 2D field data. The latter confirms that the geometry of a mineral deposit is critical in determining whether it can be detected or imaged with reflection seismic. Chapter 7 presents the conclusions drawn from the issues examined in Chapters 2 through 6.

The approach used in this thesis differs from that commonly used in mineral exploration whereby one begins with field data and attempts to determine the nature of the seismic target. Aside from the background theory discussed in Chapter 2, the ideas and examples discussed in this thesis are my original contribution to the subject matter.

CHAPTER 2

2.0 REFLECTION SEISMIC METHODS

2.1 Overview

In this chapter, I review the physical properties that make mineral deposits potential targets to detect and image with reflection seismic methods, with the objective to identify the factors that control their seismic signature. The theoretical basis for expecting reflection seismic methods to directly detect or image mineral deposits is presented using velocity-density graphs of mineral deposits and their common host rocks for both P and S-waves.

Amplitude variation with increasing angles of incidence is examined using solutions of the Zoeppritz equations for geological scenarios representing realistic host rock-mineral deposit interfaces. The solutions to the Zoeppritz equations are applied to some examples of Canadian mineral deposits for which quantitative physical rock property information is available. Qualitative conclusions are drawn from these Zoeppritz solutions regarding the expected seismic response of typical mineral deposits. Even though the plane wave solutions of the Zoeppritz equations are strictly valid for specular reflections produced at plane interfaces, they nevertheless give a useful insight into the problem at hand. Plane interfaces represent the ideal end-member case compared with non-planar interfaces which invariably produce diffraction seismic responses.

I show why the reflection seismic method, unlike the conventional potential field and electrical methods, is able to maintain imaging resolution with increasing depth. Finally, I

review reflection seismic resolution and the conventional seismic data processing methods with the aim to identify the suitable processing parameters for mineral exploration.

2.2 Basis for Detection

Seismic methods are sensitive to acoustic impedance changes (for P-waves), which is the product of velocity and density. A graph of seismic velocity against density for ore and silicate minerals shows that they have similar seismic velocities and that all the ore minerals have higher densities than the silicate minerals (Figure 2.2-1). Hence, the ore minerals tend to have higher acoustic impedances than the silicate rocks because of the high density. In fact, mineral deposits have slownesses (inverse of seismic velocity) proportional between those of ore and silicate minerals based on the time average equation for velocity (Salisbury et al., 1996). Petrological considerations imply that the same may be true for oxide ore minerals such as those of chromium and iron. Mineral deposits are potential targets for reflection seismic methods because of the high acoustic impedances. However, mineral deposits are typically small compared with the wavelengths used in reflection seismic surveys, have complex geometries, and are often mantled by alteration haloes. As a result, they do not produce strong and unambiguous seismic expressions, despite the high acoustic impedances, but rather subtle and complex diffraction patterns in seismic records.

Figure 2.2-1 shows a velocity-density graph for ore minerals, mineral deposits, and their host rocks for P-waves. The data are plotted for a 200 MPa confining pressure, at which

the rocks show nearly intrinsic seismic velocities (Christensen, 1982; Salisbury et al.,1996; Harvey, 1997). Contours of equal acoustic impedance (Z) are overlain on the graph to allow a quick calculation the change in the impedance contrast at the interface between two different rocks or minerals. The normal incidence reflection coefficient, r_c, is calculated from:

$$r_c = \frac{Z_2 - Z_1}{Z_2 + Z_1} \qquad (1)$$

where Z_1 and Z_2 are acoustic impedances of the rock type on either side of the interface.

For example, pentlandite and pyrrhotite occur in mafic rocks ($Z \approx 18.75 \times 10^6$ kg/s/m^2) together and sometimes separately, and have similar acoustic impedances of ~21 x 10^6 kg/s/m^2. This scenario should produce a reflection coefficient of ~0.06. The reflection coefficient at the interface between mafic and felsic rocks is also ~0.06 ($Z = 16.5 \times 10^6$ and ~18.75×10^6 kg/s/m^2), and reflections are commonly observed on mafic/felsic rock interfaces. However, since mineral deposits are diluted with gangue, and the amplitude distribution in field data is affected by the geometric effects of dip and size, these deposits will produce a weak seismic response when hosted by mafic rocks. Moreover, mafic rocks usually contain magnetite, which reduces their acoustic impedance contrast against the mineral deposits.

Galena and sphalerite occur together in MVT deposits, hosted by metamorphosed

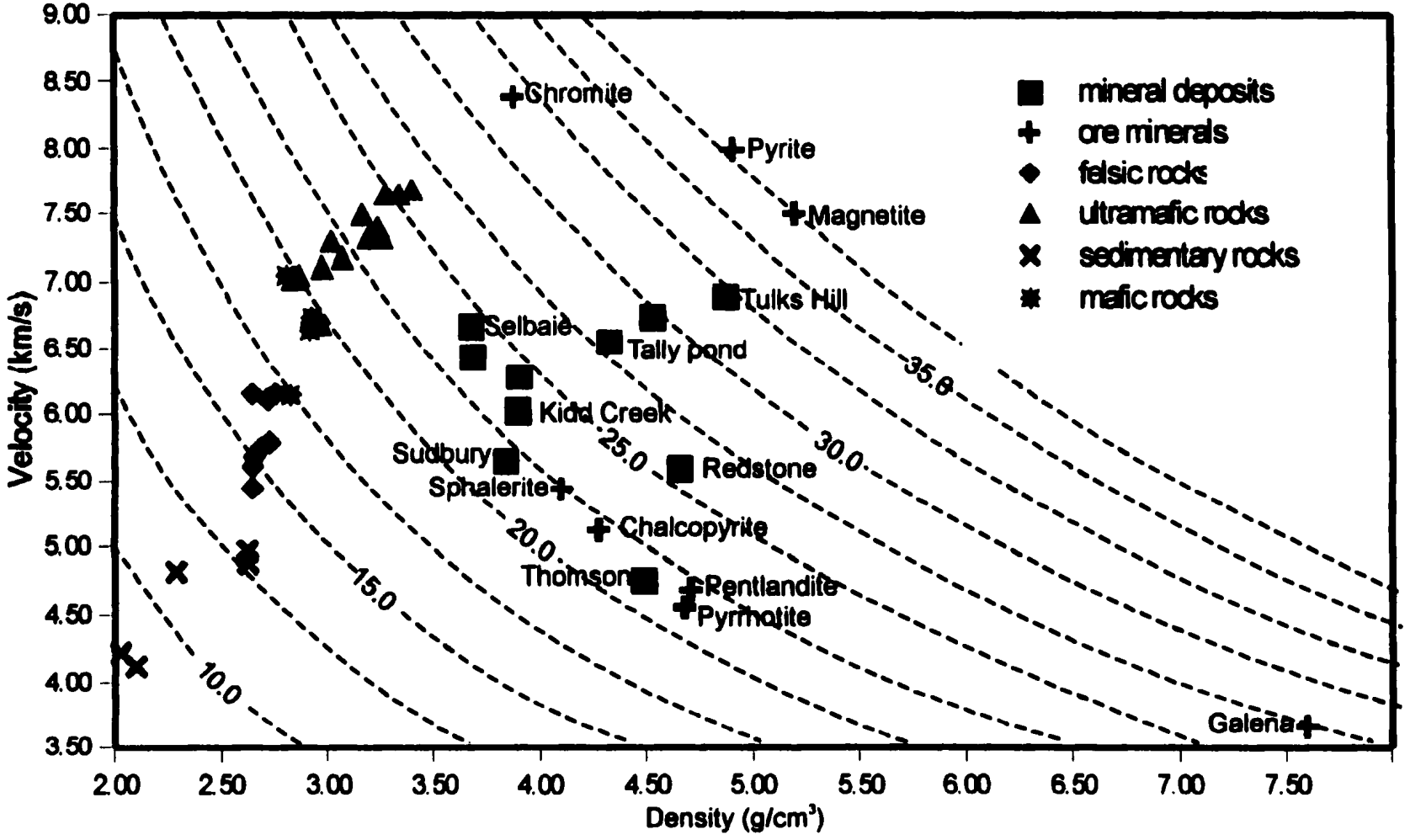

Figure 2.2-1: P-wave velocity-density graph showing the acoustic properties of mineral deposits and their host rocks. The contours are acoustic impedance in kg/s/m^2 x 10^6. Data were measured at 200 MPa and obtained from Harvey (1997), Christensen (1982), Birch (1960a & b), and Salisbury et al. (1996) (After Salisbury et al., 1996).

sediments.[3] It can be seen in Figure 2.2-1 that lead-zinc deposits ($Z \approx 22.5 \times 10^6$ kg/s/m^2) hosted by carbonate rocks ($Z \approx 12.5 \times 10^6$ kg/s/m^2) should produce a reflection coefficient of ~0.29, which is 4.8 times that produced by an interface between mafic and felsic rocks. This reflection coefficient should increase with higher grades of lead in MVT deposits since galena has a higher acoustic impedance ($Z \approx 27.5 \times 10^6$ kg/s/m^2) than sphalerite and the meta-sedimentary rocks. This fact makes a strong case for using reflection seismic methods to detect and/or image MVT deposits, given that they are difficult to detect with other geophysical methods. Cu-Zn mineral deposits hosted by felsic rocks should produce a reflection coefficient of ~0.13, but only half this value (~0.06) if hosted by mafic rocks. In either case, Cu-Zn deposits should be detectable with reflection seismic methods, provided the S/N ratio in the mafic rocks is acceptable.

Pyrite occurs with other massive sulphides and also separately in felsic and mafic rocks. In felsic rocks massive pyrite should produce a reflection coefficient of ~0.4, and a lower but nonetheless strong reflection coefficient of ~0.27 in mafic rocks. In both cases, pyrite-rich deposits should produce strong seismic anomalies. Low grade pyrite deposits should produce reflection coefficients of moderate strength in proportion to the pyrite content. However, pyrite typically occurs in the alteration zone and gradually increases in concentration towards the deposit centre.

---

[3] MVT refers to Mississippi Valley Type deposits. These are lead-zinc deposits hosted by metamorphosed carbonates and sandstones.

Chromite occurs in ultramafic rocks, which are often altered by serpentinization, a process which lowers their acoustic impedance. The acoustic properties of the ultramafic rocks plotted in Figure 2.2-1 are for fresh peridotites and hence depict minimum acoustic impedance contrasts against chromite. The reflection coefficient produced by chromite deposits in this figure is ~0.09, which is moderately strong and should be substantially higher in serpentinite. The magnitude of this reflection coefficient implies that if the S/N ratio is good, and geometric effects are minimal, chromite deposits should be detectable with reflection seismic methods. Indeed, podiform chromite deposits have been successfully detected with reflection seismic surveys in serpentinite at Shurugwi (Zimbabwe) by Mutyorauta (1987).

Figure 2.2-2 shows a shear wave velocity-density graph for the mineral deposits and host rocks. The normal incidence reflection coefficient for S-waves is calculated using eq. (1), but with the P-wave velocity substituted by the S-wave velocity. For shear waves, chalcopyrite and sphalerite have S-wave impedances similar to mafic and felsic rocks. However, these ore minerals often occur with pyrite, whose effect is to increase the S-wave impedance of the deposits. It can be seen in Figure 2.2-2 that the Cu-Zn and Zn-Pb-Cu deposits such as Tally Pond (NF), Tulks Hill (NF), Redstone (Timmins mining camp, ON), and Selbaie (Que), have high S-wave impedances largely because of the high pyrite content. The Tally Pond and Selbaie deposits have S-wave impedances of ~15 x 10^6 kg/s/m^2 and produce S-wave reflection coefficients of ~0.09 in mafic rocks, and ~0.2 in felsic rocks. For the S-wave reflectivity, a reflection coefficient at a mafic-felsic rock contact is ~0.09, so that

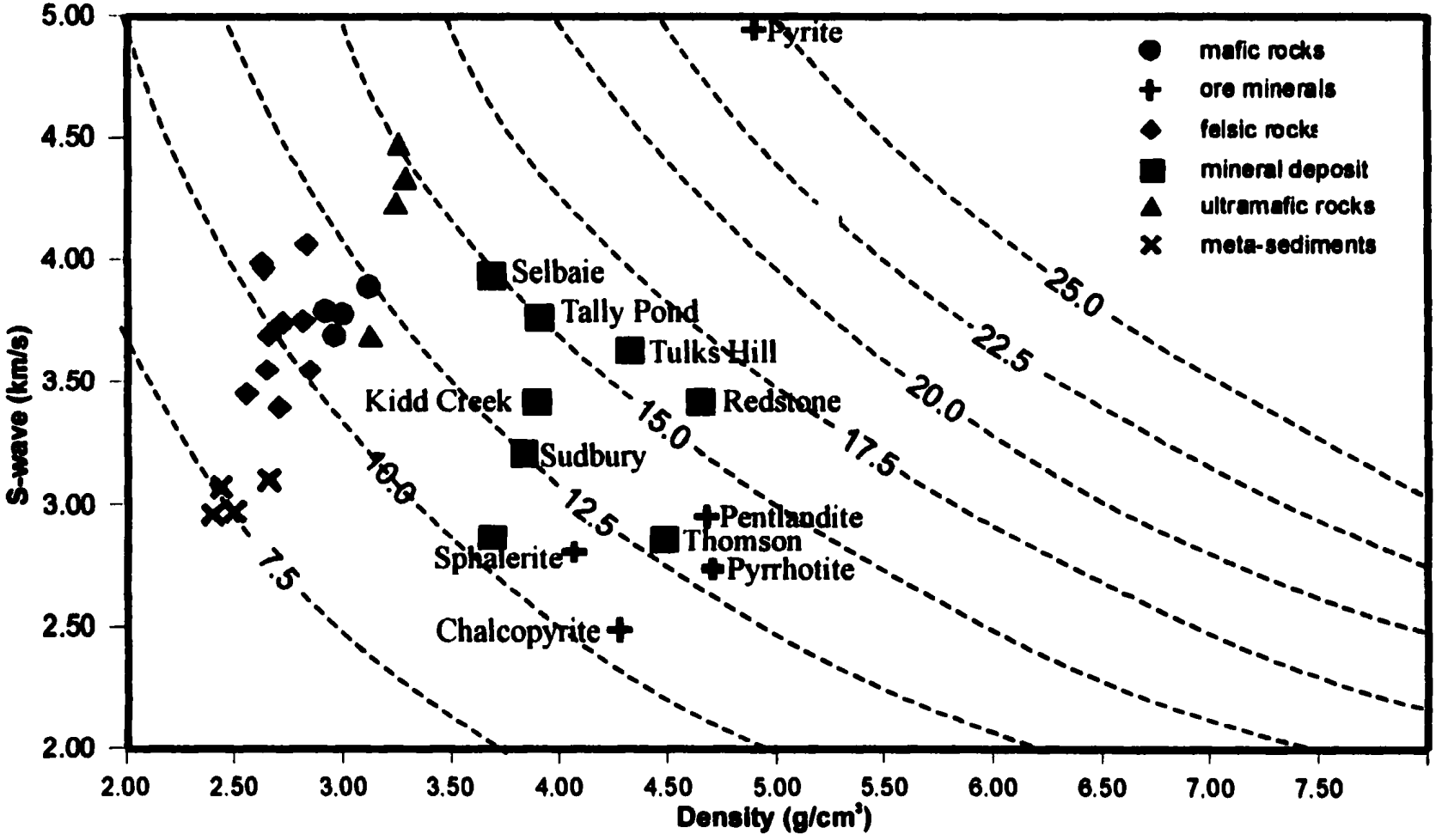

Figure 2.2-2: Shear wave velocity-density graph showing the properties of mineral deposits and their host rocks. The contours are S-wave impedance in kg/s/m^2 x 10^6. Data are plotted for a 200 MPa confining pressure. Data from Harvey (1997). (After Salisbury et al., 1996).

Cu-Zn and Zn-Pb-Cu deposits produce weak seismic responses compared with those produced by interfaces between mafic and felsic host rocks.

Ni-Cu deposits, composed largely of pentlandite and pyrrhotite, have only a slightly higher S-wave impedance than mafic rocks of ~13.5 x 10^6 kg/s/m^2. Taking due account of noise and geometric effects on the seismic response, these deposits should produce weak S-wave reflection coefficients when hosted by mafic rocks. The presence of pyrite, such as in the Redstone (ON) deposit, raises the S-wave impedance significantly, and makes the deposit detectable. In felsic rocks, Ni-Cu deposits produce an S-wave reflection coefficient of ~0.09, which is the same as the reflection coefficients produced by interfaces between the host rocks.

Overall, it can be seen that the S-wave reflection coefficients generated by mineral deposits with a low pyrite content are small. The amplitude of the reflection coefficients increases with increasing pyrite content and are large for massive pyrite. It is apparent from the foregoing discussion that the detection criteria are more stringent for S-wave reflection seismic surveys since the reflection coefficients are small for non-pyritic deposits.

The implication of the graph in Figure 2.2-1 is that mineral deposits should produce strong P-wave reflection coefficients against crystalline rocks if the S/N ratio is good. It can be deduced further that the main problem in detecting and imaging mineral deposits with reflection seismic methods (for P-waves) must reside with physical properties of mineral deposits which may contribute to a weak signal other than the acoustic impedance. However, the discussion of Figure 2.2-1 is restricted to normal incidence (0-20°) reflection coefficient

behaviour and does not show the seismic response to be expected in the case of incidence angles exceeding 20°. I explore this issue further in §2.3 through the use of Zoeppritz equations to examine the reflection coefficients at all angles of incidence for plane interfaces. The effects of geometry on the magnitude of the reflection coefficients are examined with physical and numerical models in Chapters 4 and 5.

2.3 Amplitude Analysis

The goal of reviewing the amplitude-incidence angle relations is to determine the effect of a density-driven acoustic impedance on the reflection coefficients. It is important to understand the properties of a density-driven acoustic impedance since it is the main detection criterion for Pb-Zn deposits hosted by carbonate rocks where there is no electrical conductivity contrast to enable discovery with electrical methods. Gravity exploration methods fail in this case because of limited depth resolution. The analysis presented herein represents an end-member scenario involving plane interfaces and reflected rather than diffracted waves. Nevertheless, it is a necessary starting point that should provide insight into the behaviour of diffractions with increasing angles of incidence as well. This analysis will also determine if long source to receiver offsets are necessary in reflection seismic surveys designed for mineral exploration.

Seismic anomalies related to the variation of P and S-wave amplitude with source to receiver offset (AVO) are used in the oil and gas industry as a direct indicator of gas

accumulations (Ostrander, 1984). The basis for AVO analysis is the Zoeppritz and Knott's equations which describe plane wave reflection and transmission coefficients across a seismic interface (Ostrander, 1984).[4] Solutions of the Zoeppritz equations for selected mineral deposit - host rock interfaces are plotted in Figures 2.3-3 through 2.3-7 and used to determine the reflection coefficients of P and converted-mode vertically polarized shear waves (SV) for angles of incidence from 0° to 90°. Converted-mode SV-waves are usually present in field data with long source to receiver offsets.

For a plane wave obliquely incident on a seismic interface, Snell's law (Figure 2.3-1 and eq. (2)) governs the angles of reflection and transmission for the wave types involved. Snell's law states that:

$$p = \frac{\sin\theta_1}{\alpha_1} = \frac{\sin\theta_2}{\alpha_2} = \frac{\sin\delta_1}{\beta_1} = \frac{\sin\delta_2}{\beta_2} \qquad (2)$$

where p is the ray parameter, θ and δ are the angles of emergence for the P-waves (A in Figure 2.3-1) and the converted-mode SV-waves (B in Figure 2.3-1) respectively. ρ, α, and β are the density, P-wave, and SV-wave velocities, and the subscripts 1 and 2 refer to the incident and transmission media, respectively.

A P-wave incident on a plane interface gives rise to reflected and transmitted

---

[4] These equations were derived by Knott in terms of energy potentials, and Zoeppritz in terms of amplitude displacements (Sheriff and Geldart, 1995). The treatment in this work is restricted to the Zoeppritz approach.

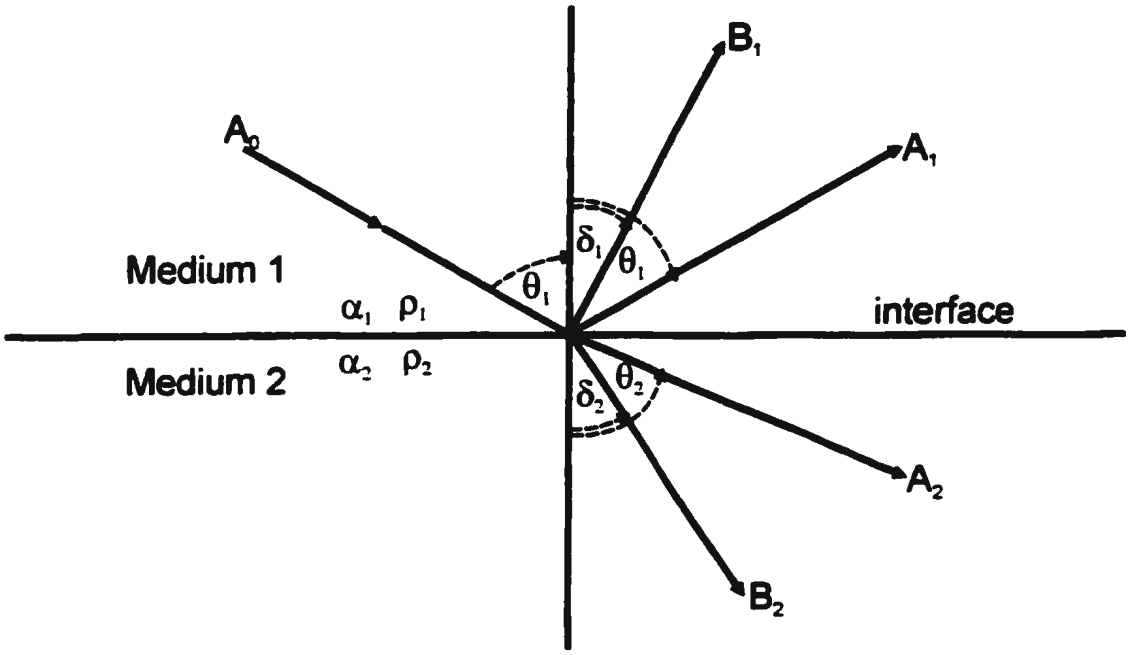

Figure 2.3-1: Definition diagram for the partitioning of seismic energy at a plane interface.

P-waves, as well as reflected and transmitted converted-mode SV-waves. The amplitudes of the waves produced at these interfaces are described by Zoeppritz equations for any plane geologic interface. Four boundary conditions must exist across the interface to allow a derivation of the Zoeppritz equations; namely the continuity of (i) normal stresses, (ii) tangential stresses, (iii) normal displacements, and (iv) tangential displacements (Grant and West, 1965; Sheriff and Geldart, 1995). One way to determine the amplitude-angle of incidence relationships for the rock interfaces is to cast the Zoeppritz equations in matrix form (eq. (3)) and solve the system of equations by substitution in a spreadsheet using the Cramer's determinant method. The equations are normalized with the amplitude of the

incident wave to reduce the number of variables from five to four, so that the solutions are amplitude ratios. In matrix form, the Zoeppritz equations are (Fowler, 1990):

$$\begin{bmatrix} \cos\theta_1 & -\sin\delta_1 & \cos\theta_2 & -\sin\delta_2 \\ \sin\theta_1 & \cos\delta_1 & -\sin\theta_2 & -\cos\delta_2 \\ Z_1\cos 2\delta_1 & -W_1\sin 2\delta_1 & -Z_2\cos 2\delta_2 & W_2\sin 2\delta_2 \\ \gamma_1 W_1\sin 2\theta_1 & W_1\cos 2\delta_1 & \gamma_2 W_2\sin 2\theta_2 & W_2\cos 2\delta_2 \end{bmatrix} \begin{bmatrix} A_1 \\ B_1 \\ A_2 \\ B_2 \end{bmatrix} = \begin{bmatrix} \cos\theta_1 \\ -\sin\theta_1 \\ -Z_1\cos 2\delta_1 \\ \gamma_1 W_1\sin 2\theta_1 \end{bmatrix} \quad (3)$$

where the seismic impedances Z and W, and the shear to P-wave velocity ratio, γ, are,

$$Z_1 = \rho_1\alpha_1, \quad Z_2 = \rho_2\alpha_2, \quad W_1 = \rho_1\beta_1, \quad W_2 = \rho_2\beta_2, \quad \gamma_1 = \frac{\beta_1}{\alpha_1}, \quad \gamma_2 = \frac{\beta_2}{\alpha_2}$$

and the incident and transmission angles θ and δ are as defined in eq. (2). The determinant expansion of eq. (3) is included in Appendix A.

Zoeppritz equations do not show the effect of density, P, or S-wave velocity on the reflection coefficient curves explicitly, and it is not clear which part of the responds to each elastic parameter or a combination thereof. In mineral exploration, we want to see the effect of density on the reflection coefficient curves explicitly because, as indicated in §2.2, it is the main factor which controls the seismic impedance of mineral deposits.

Shuey (1985) simplified and recast the Zoeppritz equations in terms of the P-wave velocity, density, and the Poisson's ratio (by factoring out the shear wave term) to show the contribution of each combination of these elastic parameters to the curves of reflection coefficients at different angles of incidence explicitly. The Shuey (1985) approximation to

the Zoeppritz equations is:

$$Rp(\theta) = R_0 + \left[A_0 R_0 + \frac{\Delta\sigma}{(1-\sigma)^2} \right] \sin^2\theta + \frac{1}{2}\frac{\Delta v_p}{v_p}\left(\tan^2\theta - \sin^2\theta\right) \qquad (4)$$

where $R_0 = \frac{1}{2}\left(\frac{\Delta v_p}{v_p} + \frac{\Delta\rho}{\rho} \right)$ is the reflection coefficient at normal incidence,

$$A_0 = \left(\frac{\Delta v_p / v_p}{\Delta v_p / v_p + \Delta\rho / \rho} \right) - 2\left(1 + \left(\frac{\Delta v_p / v_p}{\Delta v_p / v_p + \Delta\rho / \rho} \right) \right) \frac{1-2\sigma}{1-\sigma},$$

where the reflection angle θ is the average of the incident and transmitted angles for the P-wave, σ is the average Poisson's ratio in the incident and the transmission media, and v_p is the P-wave velocity. The assumptions made in this derivation are that the change in elastic properties is small compared with unity (i.e., $\Delta v_p/v_p$, $\Delta v_s/v_s$, and $\Delta\rho/\rho$, but $\Delta\sigma/\sigma$ needs not be small), and that both θ_1 and θ_2 are real and less than 90°. These restrictions, however, do not affect the results of the present study because all the calculations are done using the full Zoeppritz equations with no approximation. Shuey (1985) has shown from this re-arrangement of the Zoeppritz equations (eq. (4)) that the effect of density variation on the P-wave reflection coefficients is strong in the normal incidence region (0°-20°), the Poisson's ratio in the middle to wide angles of incidence (20°-60°), and P- wave velocity at wide angles of incidence (>60°). The effect of Poisson's ratio on plane wave reflection coefficients is discussed by Koefoed (1955; 1962). The importance of Poisson's ratio in mineral exploration is captured in its relationship to density, and is illustrated with the graph in Figure 2.3-2.

Figure 2.3-2 is a graph of the Poisson's ratio plotted against density for crystalline rocks, ore minerals, and massive sulphide deposits. This graph shows that chalcopyrite and sphalerite have high Poisson's ratios of 0.35 and 0.32 respectively, while pyrite has a low Poisson's ratio of 0.19. Pentlandite and pyrrhotite have intermediate values of Poisson's ratio (0.20 and 0.22 respectively). Mineral deposits have Poisson's ratios intermediate between the ore minerals and the crystalline rocks. The graph shows that the behaviour of Poisson's ratio in mineral deposits is similar, but not identical to, that established for other elastic parameters by Salisbury et al. (1996): that of a simple relationship between the density and seismic velocity of ore and silicate minerals. Based on this observation, it can be deduced that mineral deposits such as those at Tally Pond (NF), which comprise largely galena, sphalerite, and chalcopyrite, have a tendency toward lower Poisson's ratios because of dilution with pyrite and the felsic rocks. The observations in this graph show that the Poisson's ratio is an important elastic parameter which affects reflection coefficients produced by mineral deposit - host rock interfaces.

Figures 2.3-3 and 2.3-4 show graphs of reflection coefficients (amplitude ratios) for P and SV-waves calculated from the Zoeppritz equations for angles of incidence from 0° to 90°. In these graphs, the P-wave velocity ratio between the incident (mineral deposit) and transmission media (host rock) is 0.85, and both media have a Poisson's ratio of 0.26. The velocity ratio of 0.85 represents a host rock velocity of 6640 m/s and a mineral deposit velocity of 5660 m/s. With these parameters, the simulated interface represents a crystalline rock - mineral deposit scenario where the velocity contrast is moderate, and the rocks on

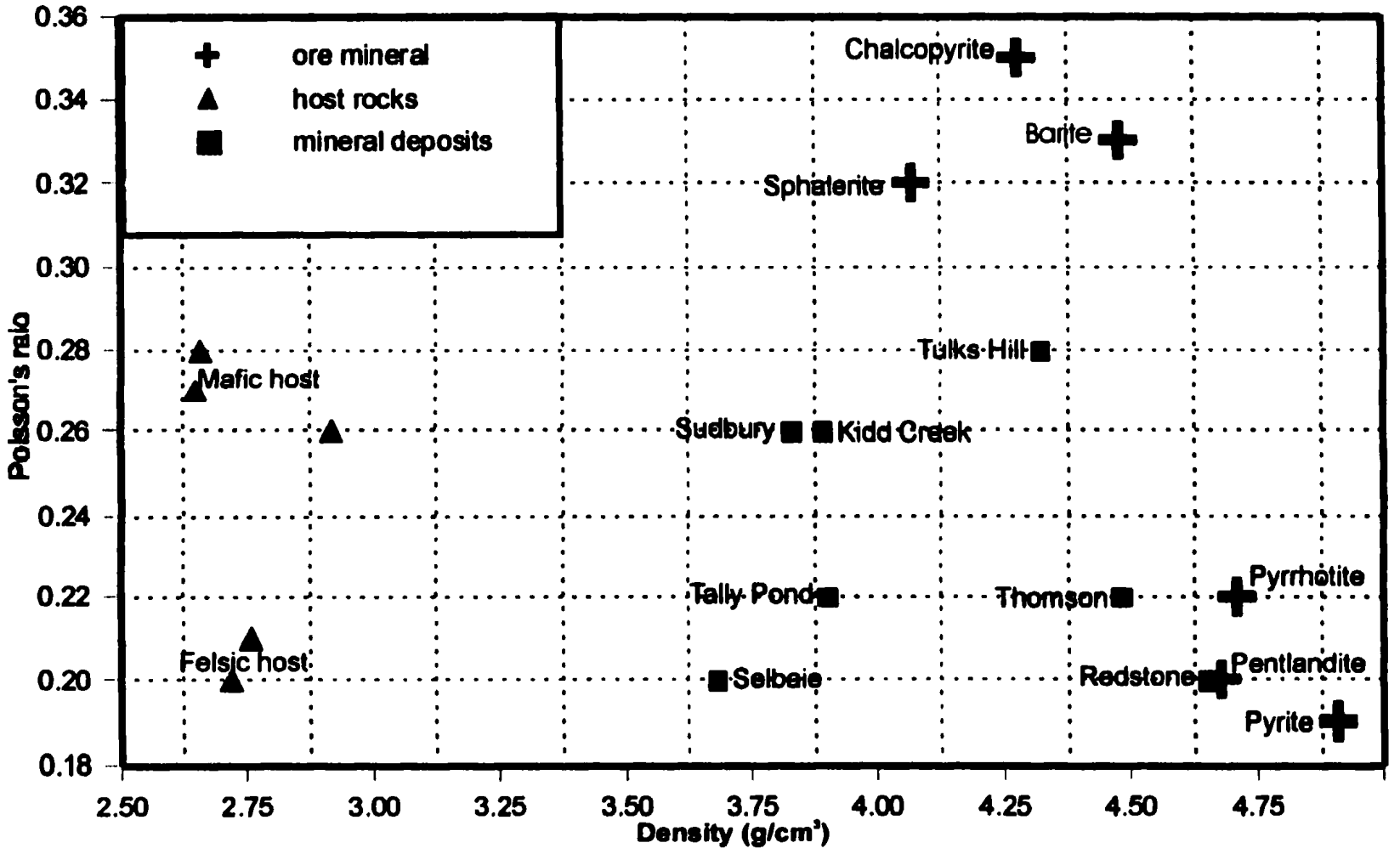

Figure 2.3-2: Poisson's ratio versus density for massive sulphide deposits, their host rocks, and pure ore minerals. The mineral deposits are separated from their host rocks on the basis of Poisson's ratio. (Vp and Vs data from Harvey, 1997).

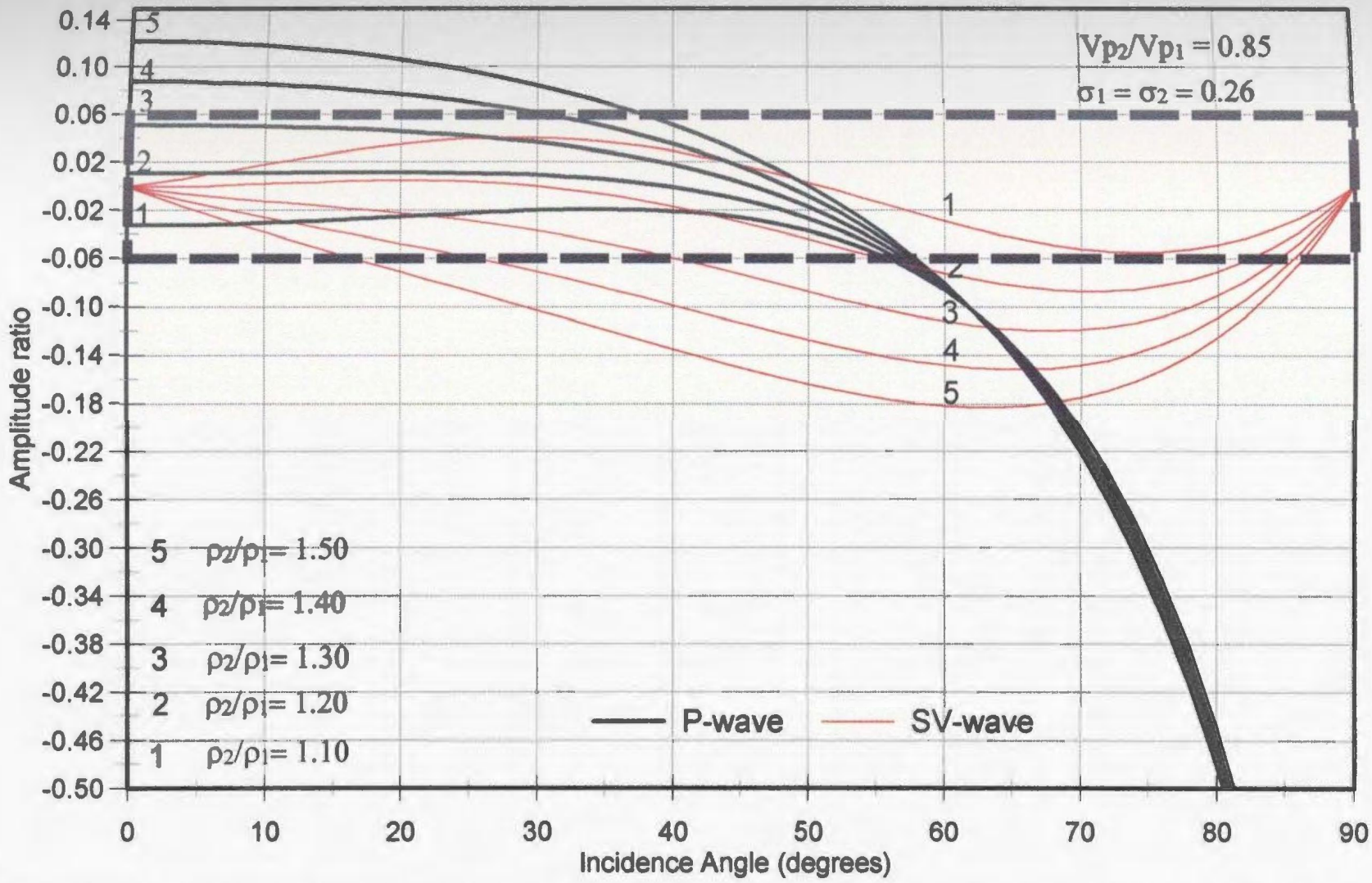

Figure 2.3-3: Reflection coefficients for an interface with the same Poisson's ratio on both sides, similar to some of the Sudbury deposits. The host rock is mafic with a density of 2.92 g/cm^3. The broken line shows the area where the P-wave reflection coefficient is less than ±0.06, which is expected from a mafic/felsic rock contact.

both sides of the interface have similar elastic parameters other than density. The physical attribute that seismically distinguishes mineral deposits from silicate rocks is their high acoustic impedance which is driven by density. The starting model in these graphs is a host rock with a density of 2.92 g/cm^3, similar to the rocks hosting the deposits in the Sudbury mining camp (see Figure 2.2-1). In the graphs discussed here, the density of the mineral deposit was initially set to 1.10 times that of the host rock (i.e. at 3.21 g/cm^3). As such it represents a low grade mineral deposit hosted by mafic rocks. The density of the mineral deposit was perturbed by up to 1.5 times that of the host rock in increments of 0.10 g/cm^3, while the other elastic parameters were fixed at the values shown in the figures. The elastic parameters were kept within the limits of those of the realistic mineral deposit properties presented in Chapter 3.

Figure 2.3-3 shows that the P-wave reflection coefficients decrease in amplitude with increasing angle of incidence. It is worth noting in Figure 2.3-3 that for curve numbers 1-3, which correspond to a density range of 3.21-3.80 g/cm^3, the interface produces a reflection coefficient less than ±0.06 for all angles of incidence where the curves are separate (0-55°). In this case, the reflection coefficients are less than those produced by mafic/felsic rock interfaces. This suggests that mineral deposits would be undetectable if they are low grade and their seismic velocities are similar to those of the host rocks, such as those of pyrrhotite-rich deposits hosted by crystalline rocks. It should be noted, however, that the gradient of the reflection coefficient curves is not controlled by the density, but by the Poisson's ratio. Curves 4 and 5 show that for a density contrast >1.30, the mineral deposits produce strong

reflection coefficients exceeding those caused by the host rocks for angles of incidence of 0-30°. This shows that mineral deposits with a density contrast >1.30 against the host rocks can be detected with reflection seismic, unless other physical properties besides the acoustic impedance may impose a greater effect.

The SV-wave reflection coefficients (Figure 2.3-3) show a strong amplitude response for a large density contrast, which becomes weaker as the density contrast diminishes. For the scenario depicted in this graph, it is apparent that the reflected SV-wave has stronger reflection coefficients than those of the P-wave at wide angles of incidence (30°-75°), but with reversed polarity. The reflection coefficients of the SV-wave decline beyond this point, while those of the P-waves increase in absolute amplitude. The implication of this scenario is that long source to receiver offsets corresponding to incidence angles of 30°-75° cannot record strong P-wave reflection amplitudes, but are good to record converted-mode SV-waves if the acoustic impedance is largely density-driven. Furthermore, these curves show clearly that a density-driven acoustic impedance responds differently to increasing angles of incidence from a velocity-driven acoustic impedance.

Figures 2.3-4 and 2.3-5 show reflection coefficient curves with different values of the Poisson's ratio in the host rock and the mineral deposit. This scenario mimics deposits such as those at Redstone and Sudbury, which have similar seismic velocities to the host rocks but different densities and Poisson's ratio. The P-wave curves (Figure 2.3-4) show that the reflection coefficients are decreasing less rapidly in amplitude with increasing angle of incidence for the greater Poisson's ratio (0.28) and more rapidly for the smaller Poisson's

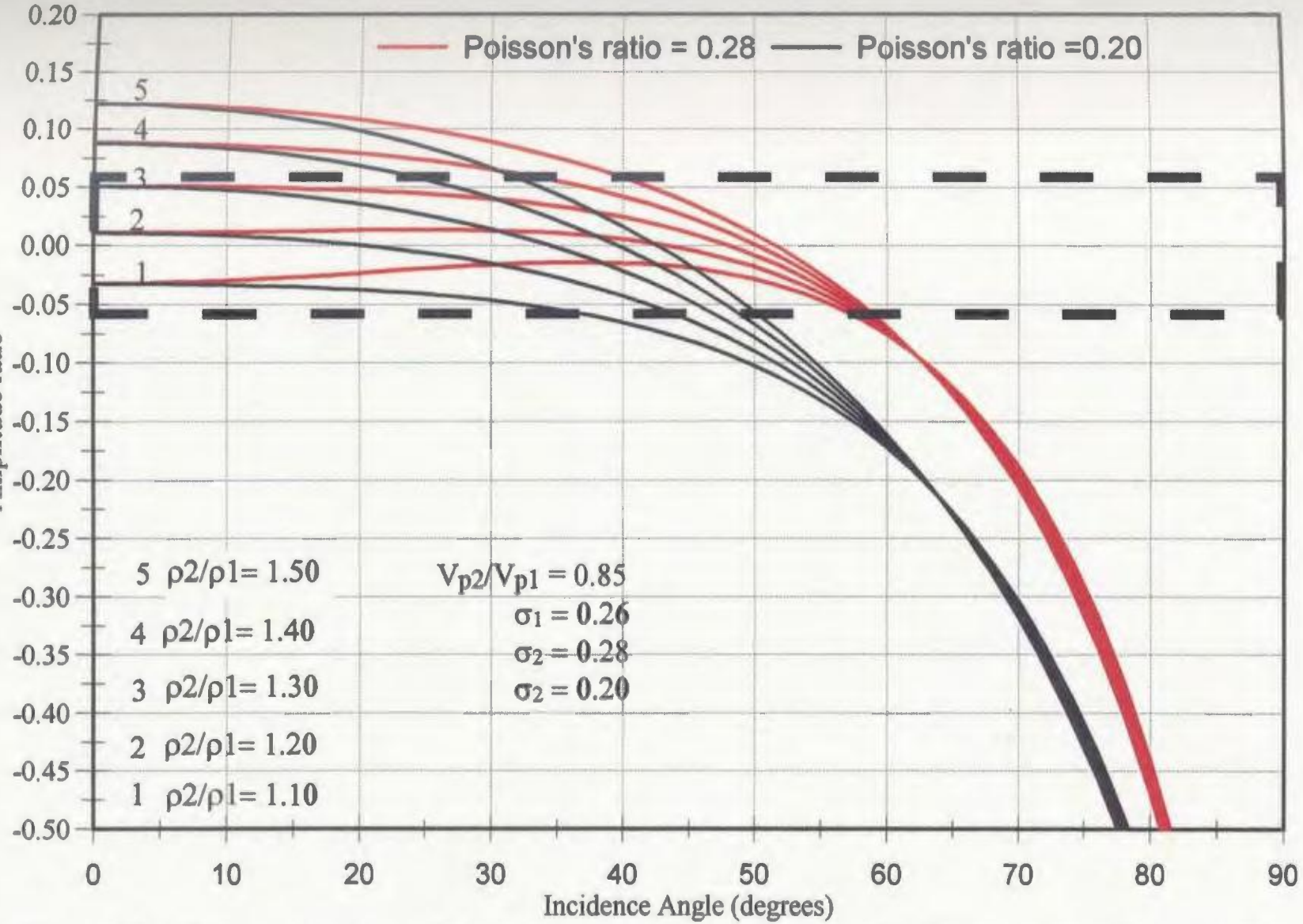

Figure 2.3-4: P-wave reflection coefficients for a crystalline rock scenario with different values of Poisson's ratio in the transmission medium (deposit). The broken line shows the area in which the reflection coefficient is less than ±0.06, the value expected at a mafic/felsic rock interface.

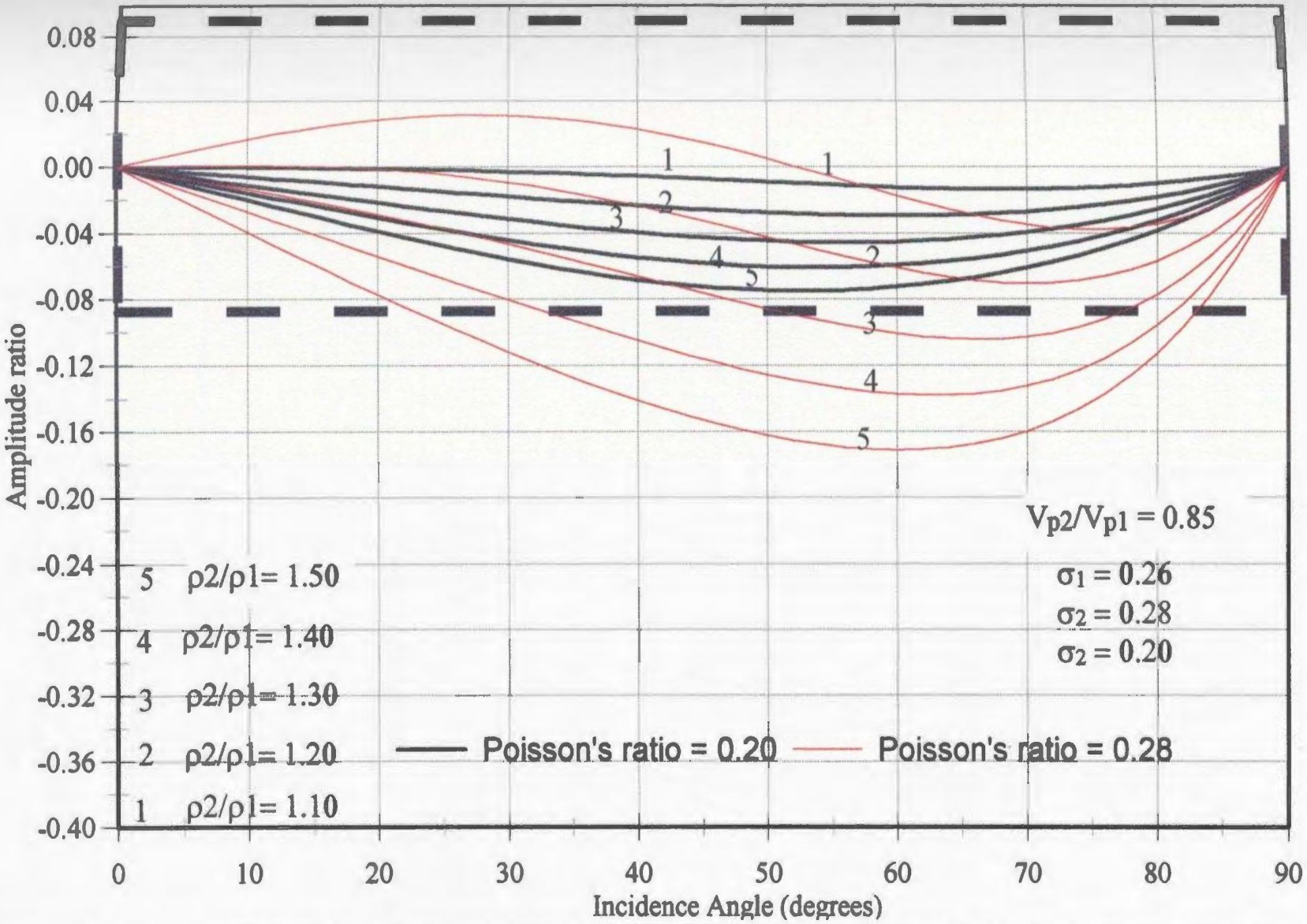

Figure 2.3-5: SV-wave reflection coefficients for different values of Poisson's ratio in the second medium (deposit). The broken line demarcates the region in which the reflection coefficient is less than that produced at the deposit-host rock interface. The reflection coefficients exceed ±0.09 only for the higher Poisson's ratio and at large angles of incidence.

ratio (0.20).

The SV-wave reflection coefficients show maxima at intermediate angles of incidence (30°-50°) for the lower Poisson's ratio (0.20), where their absolute amplitude remains less than that of the P-wave at normal incidence but with a reversed phase. For the higher Poisson's ratio (0.28), the SV-wave reflection coefficients at wide angles of 60°-75° exceed those of the P-wave at normal incidence. It is apparent from Figure 2.3-5 that the Poisson's ratio affects the SV-wave reflection coefficients similarly to the P-wave reflection coefficients in that the amplitudes increase with increasing Poisson's ratio at large angles of incidence.

Figure 2.3-6 shows P and SV-wave reflection coefficient curves for an interface with the same P-wave velocity on both sides, so that the impedance contrast is wholly density-driven. For this graph, a felsic host rock - mineral deposit interface is simulated. The host rock is a meta-sediment with a density of 2.65 g/cm^3. The initial mineral deposit density was set to 1.10 times that of the host rock (i.e., 2.92 g/cm^3) and then incremented at 0.10 g/cm^3 up to 1.5 times that of the host rock (i.e., 3.98 g/cm^3). The scenario depicted here is important because some mineral deposits (especially MVT) are hosted by footwall and hangingwall rocks with the same velocity, so that the seismic impedance contrast is wholly controlled by the density.

The P-wave reflection coefficient curves in Figure 2.3-6 decrease in amplitude in the normal incidence region (0-20°) in a similar way to those shown in Figures 2.3-3 and 2.3-5. The P-wave reflection coefficients in this case are strong in the normal incidence region

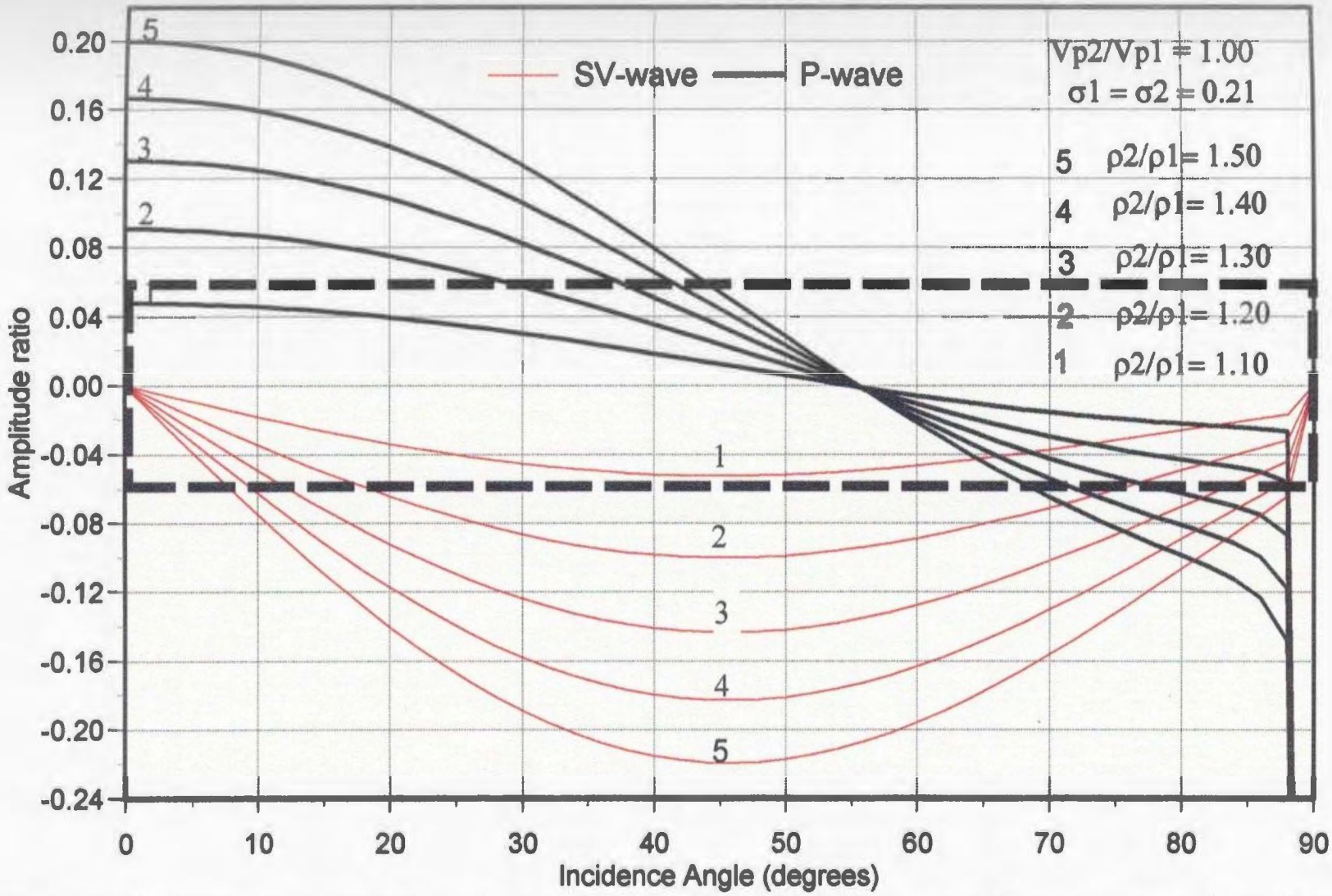

Figure 2.3-6: Reflection coefficient curves for a rock interface with the same seismic velocity on both sides. In this case the seismic impedance is wholly density-driven. Note that the reflection coefficients are large compared with those for a hybrid impedance. The rectangle encloses the region where the P-wave reflection coefficients are less than ±0.06.

even for the low density contrasts of 1.20 and 1.30, unlike in the preceding cases for a hybrid impedance driven partially by density and velocity. This strongly suggests that MVT deposits, represented by this scenario, should be excellent reflection seismic targets. It is clearly apparent in this figure that strong SV-wave amplitudes are produced at intermediate to wide angles of incidence (20-80°), where the P-wave reflection coefficients are weak.

The preceding discussion shows the effects of density and the Poisson's ratio on the reflection coefficients with increasing angle of incidence by varying these parameters independently for the simulated interfaces. The following graphs show reflection coefficient curves for specific mineral deposits to elucidate further the effect of density and Poisson's ratio on the reflection coefficients with increasing angle of incidence. Figure 2.3-7 shows reflection coefficient curves for the Sudbury, Kidd Creek, and Redstone mineral deposits. The Sudbury and Redstone mineral deposits have similar seismic velocities (Figures 2.2-1 and 2.2-2), but different densities and Poisson's ratio (Figure 2.3-2). The Kidd Creek deposit has a similar density and Poisson's ratio to the Sudbury but different seismic velocities from both the Sudbury and Redstone.

Figure 2.3-7 shows that the P and SV-wave reflection coefficient curves for the Kidd Creek and Sudbury deposits are nearly parallel and differ only in the initial magnitude because of the density difference. The reflection coefficient curve for the Redstone deposit has stronger P-wave normal incidence reflection coefficients because it is denser than those of the Sudbury and Kidd Creek. The P-wave reflection coefficient curve for the Redstone deposit declines more rapidly with increasing angle of incidence than those for the latter two

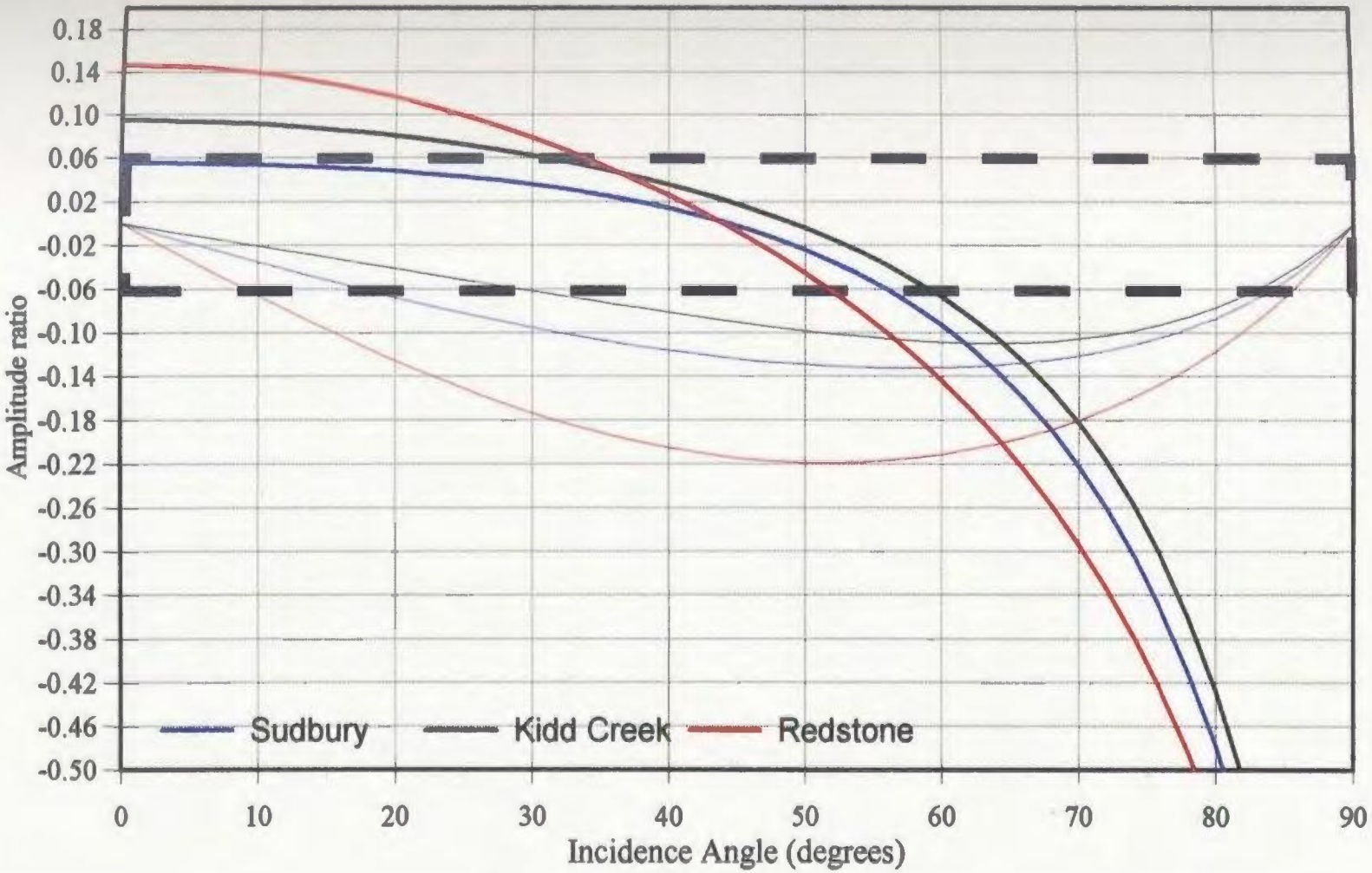

Figure 2.3-7: P-wave (thick) and SV-wave (thin) reflection coefficients for the Sudbury, Kidd Creek, and Redstone deposits. The first two differ in seismic velocity and density but have the same Poisson's ratio, hence the reflection coefficient curves are nearly parallel. Redstone has a different Poisson's ratio and therefore its reflection coefficient curve has a different rate of decline from the first two. The broken line shows the area where the reflection coefficient is less than ±0.06.

mineral deposits because the Redstone deposit has a lower Poisson's ratio (see Figure 2.3-2). These observations imply that since the effect of density on the amplitude of the reflection coefficients is substantial only in the normal incidence region, high grade mineral deposits cannot show a strong seismic response at intermediate to wide angles of incidence, except if they should also have a high Poisson's ratio. The Redstone deposit has a lower Poisson's ratio and hence shows lower P-wave reflection coefficients than the less dense Sudbury and Kidd Creek deposits at intermediate to wide angles of incidence, despite its high density. The SV-wave curves show high amplitudes and reversed phase at intermediate to wide angles of incidence. The SV-wave response differs from that of the P-waves in that the reflection coefficient for the Redstone deposit exceeds those of the other two at all angles of incidence.

The preceding discussion suggests that strong P-wave reflection coefficients should be produced in the normal incidence acquisition aperture by mineral deposit/host rock interfaces. Long source to receiver offsets are not desirable if the impedance is density-driven since the P-wave reflection coefficients decline rapidly with increasing angle of incidence. At intermediate to wide angles of incidence, the amplitude of the reflection coefficients is controlled by the Poisson's ratio, and density has little effect. In practice, long seismic lines with small source to receiver offsets should be recorded if the target is dipping to sample signal which is displaced down-dip. The observations made in this section are re-visited in Chapter 4.

2.4 Seismic Resolution

The resolving power of the reflection seismic method is dependant upon the wavelength, λ, which is governed by:

$$\lambda = \frac{v}{f} \tag{5}$$

where v is the seismic velocity of the rock, and f is the predominant frequency. Broader bandwidths lead to better resolution, and the goal in conventional reflection seismic surveys is to record the widest possible bandwidth. However, resolution is often limited by the bandwidth of the recorded seismic signal, which is usually ~2 octaves because of limited depth penetration of high frequencies. The wavelength in eq. (5) increases with increasing depth in reflection seismic surveys for two reasons: (i) the porosity of sedimentary rocks typically decreases with increasing depth due to compaction, thereby causing the velocity to increase, and (ii) the frequency decreases with increasing depth because high frequencies are attenuated more in the shallow less competent regions (Brown, 1991). Both of these factors are less severe in crystalline rocks because they contain negligible porosity and they also have a low seismic attenuation (Wright et al., 1994). This allows reflection seismic methods to maintain resolution better with increasing depth in crystalline than sedimentary rocks, and still better than the competing methods in both cases. Since velocity is fixed by the geology ($v_p \approx 6000$ m/s for crystalline rocks), only frequency is controlled in a reflection seismic survey. The wavelength recorded in conventional surface reflection seismic surveys

with a dominant frequency of 60 Hz is ~100 m. However, underground reflection seismic surveys can record dominant frequencies of up to ~300 Hz.

Seismic resolution is described in terms of vertical and horizontal components. Vertical resolution is ¼ of the dominant wavelength (λ) of the seismic signal (Brown, 1991; Sheriff and Geldart, 1995). It can be improved in data processing with spiking deconvolution which compresses the wavelet, thereby broadening the bandwidth. When reflection seismic targets are ~¼λ thick, constructive interference occurs between wavelet responses from the top and bottom interfaces of the target horizon and this causes the amplitude to increase anomalously, a phenomenon called amplitude tuning (Brown, 1991). The reflection amplitude in this case decreases proportionally as the bed thickness decreases below ~¼λ. Amplitude side lobe tuning may be useful in seismic exploration for mineral deposits because they are thin compared with the wavelengths used in reflection seismic surveys.

Lateral resolution equals the radius of the first Fresnel zone (eq. (6)) before migration (Brown, 1991; Sheriff and Geldart, 1995). It is increased in data processing by focusing the first Fresnel zone with migration to about one wavelength, but the degree of success depends on the S/N ratio (Brown, 1991; Goulty, 1997). Better focusing of the Fresnel zone energy, and hence better resolution, is achieved with 3D migration since in 2D seismic data the Fresnel zone is contracted only in the vertical plane below the seismic line.

The concept of Fresnel zones is central to the understanding of the lateral resolution of reflection seismic sections. It is an area from which seismic energy recorded by a detector

does not differ by more than half a cycle, such that there is constructive interference (Yilmaz, 1987; Sheriff and Geldart, 1995; Liner, 1999). Consider the geometry in Figure 2.4-1, the normal raypath length between the reflector and the coincident source and receiver (S/R to O) is Z_0. For a raypath length of $Z_0 + \frac{1}{4}\lambda$, the spherical wavefront intersects the reflector at the points A and A`. The waves arriving between these limits interfere constructively, and contribute energy to the reflection amplitude (Yilmaz, 1987).

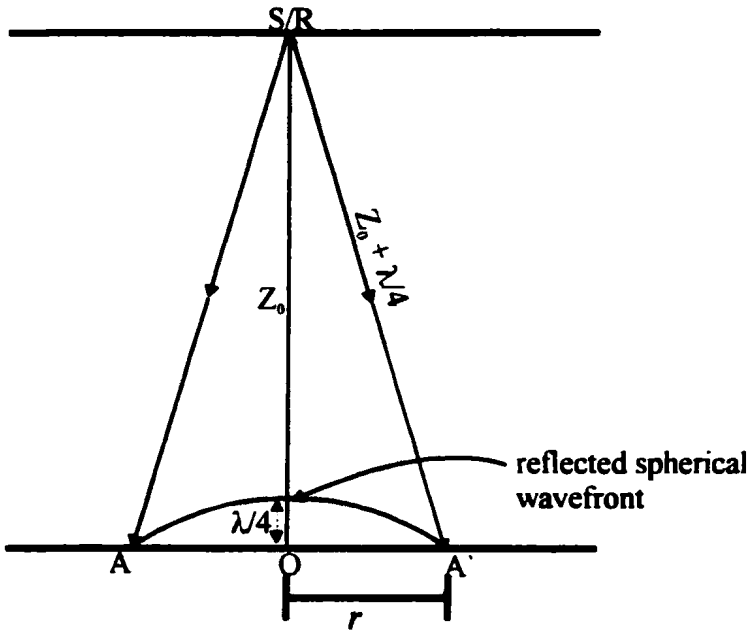

Figure 2.4-1: Definition geometry for the first Fresnel zone. The assumptions made in this diagram are that the reflector depth $Z_0 >> \lambda$, so that the spherical wavefront intercepted by the reflector between points A and A` is essentially plane (adapted from Yilmaz, 1987).

The second wavefront (raypath length $Z_0 + \frac{1}{4}\lambda$) describes a circular area around the normal ray within which any two separate features closer than its radius cannot be resolved. Thus, the reflector is illuminated in units of first Fresnel zone radii, and regions smaller than this do not produce full amplitude reflections, but diffractions. Higher order Fresnel zones also exist, but since they contribute little energy to the reflection amplitudes, they are normally ignored.

From the geometry in Figure 2.4-1, we can calculate the radius of the first Fresnel zone (r). We assume that $Z_0 >> \lambda$, so that the wavefronts can be considered essentially plane.

$$
\begin{aligned}
r^2 &= \left(Z_0 + \lambda/4\right)^2 - Z_0^2 \\
&= Z_0^2 + Z_0\lambda/2 + \lambda^2/16 - Z_0^2 \\
&= Z_0\lambda/2 + \lambda^2/16 \\
\therefore r &= \sqrt{\left(Z_0\lambda/2 + \lambda^2/16\right)} \\
&\approx \sqrt{\left(Z_0\lambda/2\right)}
\end{aligned}
\qquad (6)
$$

Since $\lambda << Z_0$, we can drop the second term under the square root.

Mineral deposits are generally of a small areal extent with complicated geometries. The complicated geometry and limited areal extent result in mineral deposits producing subtle and complex seismic responses in field data, dominated by diffractions and out-of-

plane events in 2D surveys. The detection and imaging of a target with reflection seismic is controlled by the dominant wavelength of the signal, its size compared with the radius of the first Fresnel zone, the reflection coefficient at the host rock and the target interface, and its geometry and attitude. It can be deduced from eqs. (5 and 6) that mineral deposits should at be least 25 m thick and 173 m wide in order to be imaged at 600 m with high resolution ($f \approx 60$ Hz) surface reflection seismic surveys. However, smaller targets can may be detected above the noise level. It will become apparent from the discussion in Chapter 3 that mineral deposits with sizes of this order of magnitude are common.

2.5 Seismic Data Processing

The objective of conventional reflection seismic data processing is to enhance primary reflections and attenuate direct, refracted, multiple, and diffracted seismic events. Direct and refracted seismic events are used to determine a near-surface velocity model from which static time corrections are calculated before common mid-point (CMP) stacking, after which they are removed from the data by muting. Multiple reflections are removed from the data with predictive deconvolution and the residuals thereof are attenuated with CMP stacking. Diffraction events are generated by reflector terminations, kinks on the reflector surface, and reflectors of finite length which are smaller than the radius of the first Fresnel zone. Diffractions should be preserved when working with small reflection seismic targets where specular reflections are absent, a rather common mining exploration problem.

Moreover, a complete reconstruction of the shape of the target from seismic data requires the presence of the full wavefield.

To appreciate the utility of diffractions and the information contained in them, it is necessary to examine their travel time equations. The travel time equations for reflection and diffraction events near a point diffractor are derived in Sheriff and Geldart (1995) and are reproduced here for illustration purposes. The truncated binomial expansion of the two-way reflection travel time in a CMP gather, t_{CMP}, gives (Sheriff and Geldart, 1995):

$$t_{CMP} = \left(\frac{2h}{v}\right)\left[1+\left(\frac{x}{2vh}\right)^2\right]^{\frac{1}{2}} = t_0\left[1+\left(\frac{x}{vt_0}\right)^2\right]^{\frac{1}{2}}$$

$$= t_0\left[1+\frac{1}{2}\left(\frac{x}{vt_0}\right)^2-\frac{1}{8}\left(\frac{x}{vt_0}\right)^4+\frac{1}{16}\left(\frac{x}{vt_0}\right)^6-\ldots\right] \qquad (7)$$

$$\approx t_0+\frac{x^2}{4vh} \approx t_0+\Delta t_{NMO}$$

where h is the depth of the reflector, v is the root-mean-square velocity, x is the source to receiver offset, t_0 is the two-way zero-offset time, and Δt_{NMO} is the normal moveout. The small spread approximation (the assumption that $h >> x$) allows the truncation of eq. (7) to the second term of the binomial expansion. This approximation is not violated in CMP spread designs which are guided by the rule-of-thumb that the spread length should be equal to the reflector depth (Knapp and Steeples, 1986).

For a diffraction, the truncated binomial expansion of the two-way travel time in a

common shot gather, t_D, for a shot point above the diffracting point is (Sheriff and Geldart, 1995):

$$t_D = \frac{2h}{v} + \frac{x^2}{2vh} = t_0 + 2\Delta t_{NMO} \tag{8}$$

The travel time expression for a diffraction changes accordingly as the source moves away from the point above the diffracting point, for which eq. (8) becomes (Sheriff and Geldart, 1995):

$$t_{Dx} = t_0 + 2\Delta t_{NMO} + \frac{a(a-x)}{vh} \tag{9}$$

where a is the horizontal offset of the source from the diffracting point.

In the CMP gather, the diffraction travel time becomes (Sheriff and Geldart, 1995):

$$\begin{aligned} t_{DCMP} &= \frac{1}{v}\left\{\left[h^2 + (x/2 + b)^2\right]^{\frac{1}{2}} + \left[h^2 + (x/2 - b)^2\right]^{\frac{1}{2}}\right\} \\ &= \frac{1}{v}\left\{\left[1 + \left(\frac{x_2 + b}{h}\right)^2\right]^{\frac{1}{2}} + \left[1 + \left(\frac{x_2 - b}{h}\right)^2\right]^{\frac{1}{2}}\right\} \\ &= \frac{1}{v}\left\{\left[1 + \frac{1}{2}\left(\frac{x_2 + b}{h}\right)^2 - \frac{1}{8}\left(\frac{x_2 + b}{h}\right)^4\right] + \left[1 + \frac{1}{2}\left(\frac{x_2 - b}{h}\right)^2 - \frac{1}{8}\left(\frac{x_2 - b}{h}\right)^4\right]\right\} \\ &\approx t_0 + \frac{x^2}{4hv} + \frac{b^2}{hv} \approx t_0 + \Delta t_{NMO} + \frac{b^2}{hv} \end{aligned} \tag{10}$$

where b is the horizontal offset from the source and receiver mid-point to the diffractor.

From eq. (10), it is apparent that the diffraction hyperbola has a normal moveout which exceeds that of a reflection event in a CMP gather (eq. (7)) by the term b^2/hv. NMO correction will cause under-correction of the diffractions since they propagate with the background velocity. Moreover, the normal moveout is more complicated when the source is not vertically above the diffractor (eq. (9)). Hence, in conventional seismic data processing, CMP stacking will attenuate the diffraction events because they have a different normal moveout from the reflections, except at their apices, where b tends to 0.

The CMP-stacking technique has two significant drawbacks: (i) it is not accurate at long source to receiver offsets where the small spread approximation breaks down, and (ii) it causes reflector smearing and therefore inaccurate imaging in the vicinity of structures with steep dips and lateral velocity variations. Steep dips and hence lateral velocity variations are a seismic manifestation of structural disruption of a stratigraphic column which juxtaposes high and low velocity formations. Such a situation commonly arises because of diapirism in marine sediments in which domes of rock salt are intruded into the overlying strata. An equivalent scenario arises from the inclusion of a high density ore lens within low density crystalline rocks. Since massive sulphide ore bodies are normally mantled by a pyritic alteration zone in which the mineral content increases from the edges to the core, there usually exist a strong density and velocity gradient around the ore lens. This is a seismically equivalent situation to the one described above, and the velocity variation arises from the increasing pyrite content towards the deposit core. In the presence of geological complexity of the type described here, it is desirable to use seismic imaging

techniques which are not affected by the above-mentioned problems. One such technique is the aplanatic pre-stack depth migration of Liner and Lines (1994).

Migration is a process that restores dipping reflections to their correct subsurface locations and removes diffractions by collapsing their energy to the apices, thereby making the stack geometrically correct for interpretation. It is normally implemented after CMP stacking in order to realise its objective of focusing the seismic events as indicated above. However, if lateral velocity variations should be present in the data, it is desirable to image them with migration prestack, in order to avoid the problems associated with CMP stacking.

The physical basis for the aplanatic prestack depth migration technique is elaborated in Liner and Lines (1994). The aplanatic prestack depth migration algorithm operates on the elliptic travel time trajectories described by the reflection and diffraction events between the source and the receiver locations, and discriminates against direct and refracted seismic events on the basis of their linear moveout. The algorithm requires an input of shot domain data with geometry and elevation statics correction, and an interval velocity model. It is attractive to use in seismic data where wavefield separation may be a problem.

2.6 Summary and Conclusions

Mineral deposits are potential targets for reflection seismic methods because of their high acoustic impedances, which implies that they may cause strong P-wave anomalies if hosted by crystalline rocks. Hence, the inability to detect or image them with reflection

seismic must reside with physical attributes which contribute to a weak signal other than the acoustic impedance. However, mineral deposits are typically small compared with the wavelengths used in seismic surveys, have complex geometries, and are sometimes mantled by alteration haloes. As a result, they do not produce strong and unambiguous seismic expressions, despite the high acoustic impedances, but rather subtle and complex diffractions in seismic records.

The effect of density on plane wave reflection coefficients is strong near normal incidence (0°-20°). The amplitudes of the reflection coefficients at intermediate to wide angles of incidence are controlled by the Poisson's ratio. P-wave reflection coefficients decrease in amplitude and take on a single value at 62°, regardless of the density contrast. Amplitude analysis shows that low grade mineral deposits would be undetectable if their seismic velocities are similar to those of the host rocks, such as those of pyrrhotite-rich deposits hosted by crystalline rocks. For a wholly density-driven acoustic impedance, P-wave reflection coefficients also decrease in the normal incidence region but the curves intersect at 57° and separate beyond. Since the effect of density on the reflection coefficients is strong only in the normal incidence region, high grade deposits do not show a strong seismic response at wider angles of incidence, except if they also have a high Poisson's ratio. Clearly, a density-driven acoustic impedance anomaly responds differently to increasing angles of incidence than a velocity-driven one.

The reflected SV-wave has stronger reflection coefficients than those of the P-wave at wide angles of incidence (30°-75°), but with a reversed phase. Clearly, long source to

receiver offsets cannot record strong P-wave reflection amplitudes, but are good to record converted-mode SV-waves if the impedance is largely density-driven.

CHAPTER 3

3.0 PROPERTIES OF MINERAL DEPOSITS

3.1 Introduction

Reflection seismic methods, as shown in §2.4, do not suffer greatly from a loss of resolution with increasing depth and are therefore a potential tool for detecting and imaging mineral deposits at depths ≥600 m. This chapter describes the physical properties of mineral deposits, which are divided into metallic, industrial, and mineral fuels (Lamey, 1967). This thesis deals with surface reflection seismic methods used to explore for metallic mineral deposits. The discussion includes other materials which are not mined for metals but are related to metallic mineral deposits and possess properties detected with reflection seismic methods.

Metallic ore minerals possess higher molecular weights than silicate minerals, and are therefore of higher density than the latter (Stanton, 1972). Massive sulphide ore minerals (except sphalerite) possess metallic bonding and are electrically conductive, while many oxide ore minerals are magnetic (Stanton, 1972). These physical attributes distinguish mineral deposits from silicate rocks by their electrical conductivity, density, and magnetic susceptibility. Based on these physical properties, conventional geophysical methods can detect and image mineral deposits at depths ≤600 m, beyond which the S/N ratio and resolution decline to low levels.

3.2 Volcanogenic Massive Sulphide deposits (VMS and SEDEX)

Volcanogenic massive sulphide deposits occur in submarine volcanic rocks of all ages and different tectonic settings (Guilbert and Parker Jr., 1986; Franklin, 1993; Ohmoto, 1996; Eastoe et al., 1996). VMS and SEDEX mineral deposits initially comprise a massive sulphide mound underlain by a disseminated and stringer zone (Ohmoto, 1996).[5] However, they are often subsequently deformed into more complicated geometries than the simple facies model portrayed here. Typical VMS deposits are 20 m thick with 300 m radii, with funnel-shaped disseminated and stringer zones 100 m wide, extending to depths of 100 m below the deposit (Ohmoto, 1996).

Volcanogenic massive sulphide deposits are divided into Cu-Zn and Zn-Pb-Cu, based on modal composition (Franklin, 1993). Cu-Zn deposits occur in mafic volcanic rocks where they are concordant and underlain by disseminated zones. They comprise ≥60% massive sulphide and have low aspect ratios (length to thickness) of 3:1 to 10:1 (Franklin, 1993). The top of a Cu-Zn deposit forms a sharp contact with the host rock but the base is transitional into the disseminated and stringer zone. This morphological disposition makes Cu-Zn deposits good reflection seismic targets if they are undeformed and of a sufficient lateral extent (Figure 3.2-1).

Zn-Pb-Cu mineral deposits are related to bimodal volcanism which is typical of back-arc basins. They are tabular and laterally extensive with high aspect ratios of >20, e.g.

---

[5] SEDEX is an acronym for Sedimentary Exhalative

the Sullivan deposit (BC) is ~50 m thick and ~1500 m long (Goodfellow et al., 1993). The deposits are massive and comprise alternating layers of ore and silicate minerals, wherein the stratigraphy varies laterally from a proximal ore to a distal sedimentary facies. The contact between the ore facies and the host rock is abrupt and should give rise to a strong acoustic impedance contrast. The sedimentary facies comprises ore minerals and gangue with a low sulphide content and forms a lateral halo around the ore facies with gradational contacts. Such a halo is detrimental to the reflection seismic technique because it reduces the acoustic impedance contrast of the deposit proper.

Cross-sections of typical metallic mineral deposits are presented in this chapter, together with normal incidence synthetic seismograms for each geological scenario. The synthetic seismograms show the seismic expression expected in field data recorded in

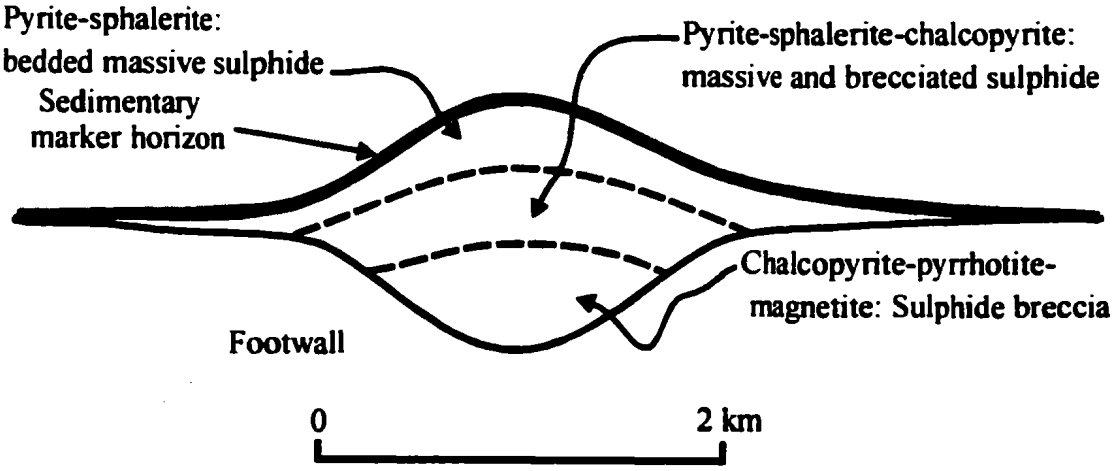

Figure 3.2-1: Morphology and mineral zoning found in Cu-Zn VMS deposits. The vertical scale is exaggerated for clarity. (Modified from Franklin, 1993).

similar geological conditions. However, the synthetic seismograms represent a strictly 2D case, whereas field data usually contain events from out of the plane of the seismic line.

The synthetic seismograms were created with the 2D FD algorithm of Kelly et. al. (1996), and designed using a Gaussian source wavelet with a dominant frequency of 60 Hz, digitized at a ½ ms sample interval and a trace spacing of 5 m. The seismiograms were produced by propagating an essentially plane wave (produced by closely-spaced sources) downward from the surface, so that the seismic response is approximately representative of a stacked seismic section. The design criteria were intended to be consistent with acquisition parameters used for high resolution seismic surveys. The seismograms were migrated using the post-stack F-K time migration method. All the synthetic seismograms presented in this chapter were created in the manner described here.

3.2.1 Tally Pond Deposit

The Tally Pond Volcanic Belt (NF) comprises structurally juxtaposed rock sequences (MacInnis and MacKenzie, 1988; Mackenzie and Squires, 1988; Squires et al., 1990) (Figure 3.2-2). The top rock unit comprises submarine mafic and felsic volcanic rocks, pyroclastic rocks, and graphitic sediments. It is intruded by gabbro, porphyry dykes, and sills. The base of this rock unit coincides with an NW-SE trending thrust fault dipping 45° SW (Duck Pond Thrust). The second rock unit occurs below this fault and consists of felsic and mafic volcanic rocks with mafic dyke intrusions. The felsic volcanic rocks host massive sulphide

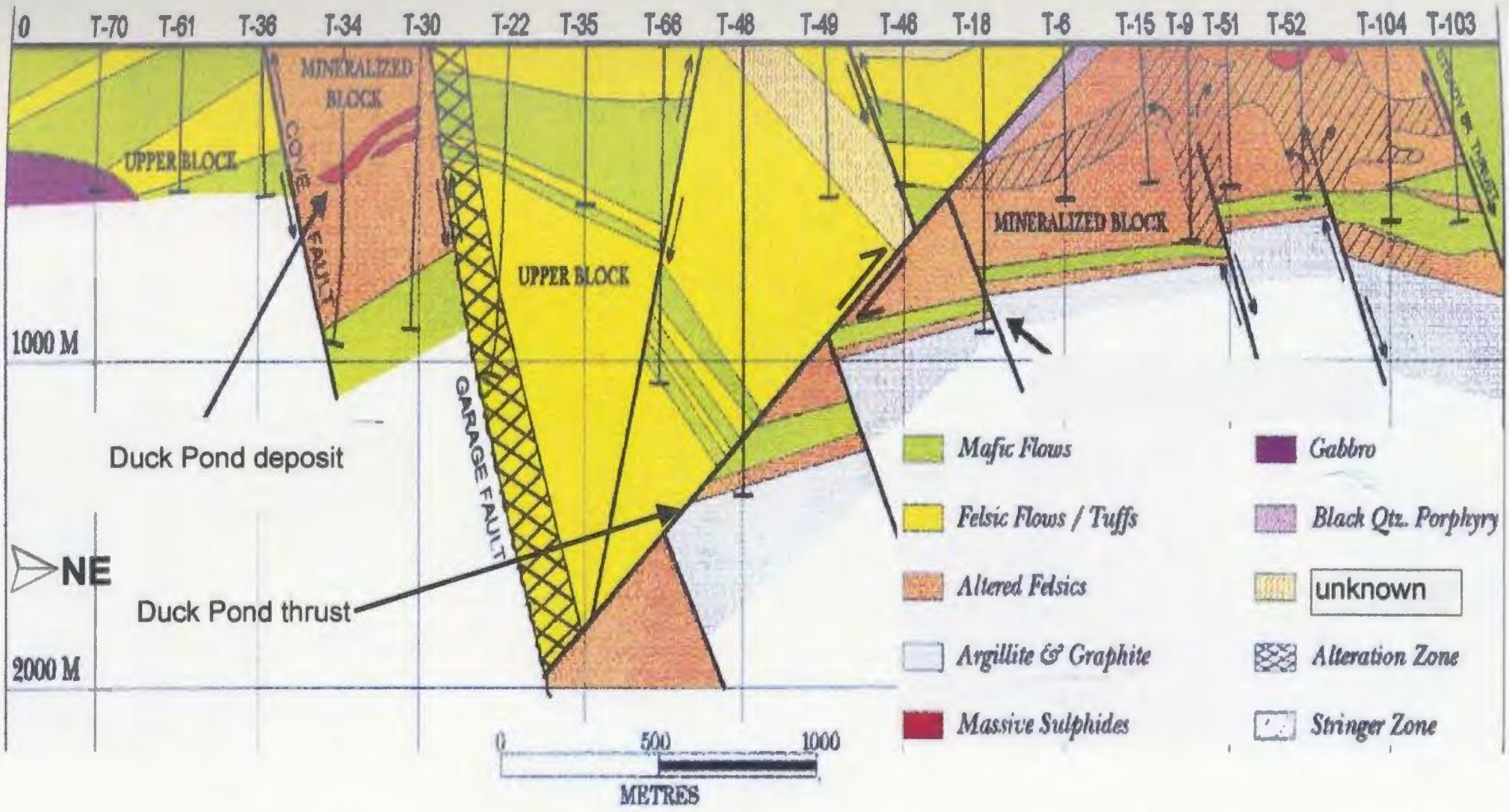

Figure 3.2-2: NE-SW longitudinal section through the Tally Pond Volcanic Belt. The section crosses through the Duck Pond deposit and coincides with the reflection seismic line discussed in Chapter 6. Exploration drill holes used to constrain the interpretation of the seismic data are indicated in the section. (Modified from Noranda Inc., 1993).

deposits. The third rock sequence underlies the second structurally and comprises graphitic and argillaceous sediments (Squires et al., 1990).

The Duck Pond deposit is hosted by the second rock sequence referred to above (Mackenzie and Squires, 1988; Squires et al., 1990). A longitudinal section through the Duck Pond deposit and the corresponding normal incidence synthetic seismogram are shown Figures 3.2-3 and 3.2-4. The Duck Pond deposit is a 500 x 500 x 18 m lens-shaped body lying at 250-450 m, and dipping 35°-40° SW. Two thirds of the Duck Pond deposit consists of a pyrite zone varying from massive near the deposit to stringer and disseminated ~100 m away (Squires et al., 1990). The Duck Pond deposit is underlain by small bodies called the 'Sleeper zones'. A second deposit occurs ~300 m below and offset by faulting some 200-400 m to the east from the Duck Pond deposit. At a depth of 750 m, this second deposit lies within the first Fresnel zone and might be detected by the 2D seismic line recorded over the upper deposit.

Figure 3.2-4 shows a normal incidence synthetic seismogram for the longitudinal section through the Duck Pond deposit produced from the simplified velocity-density model shown in Figure 3.2-3(B) before migration (A), and (B), after migration. In Figure 3.2-4(A), the seismic response caused by the deposit consists of diffraction events produced by the bends and terminations of the discrete segments on the surface of the deposit. The massive pyrite zone above the main Zn-Pb-Cu deposit is similarly mapped by diffraction events. The 'Sleeper Zones' also produces a diffraction response from the edges because it is only 150 m long, while the radius of the first Fresnel zone at this depth is 159 m (for the stipulated

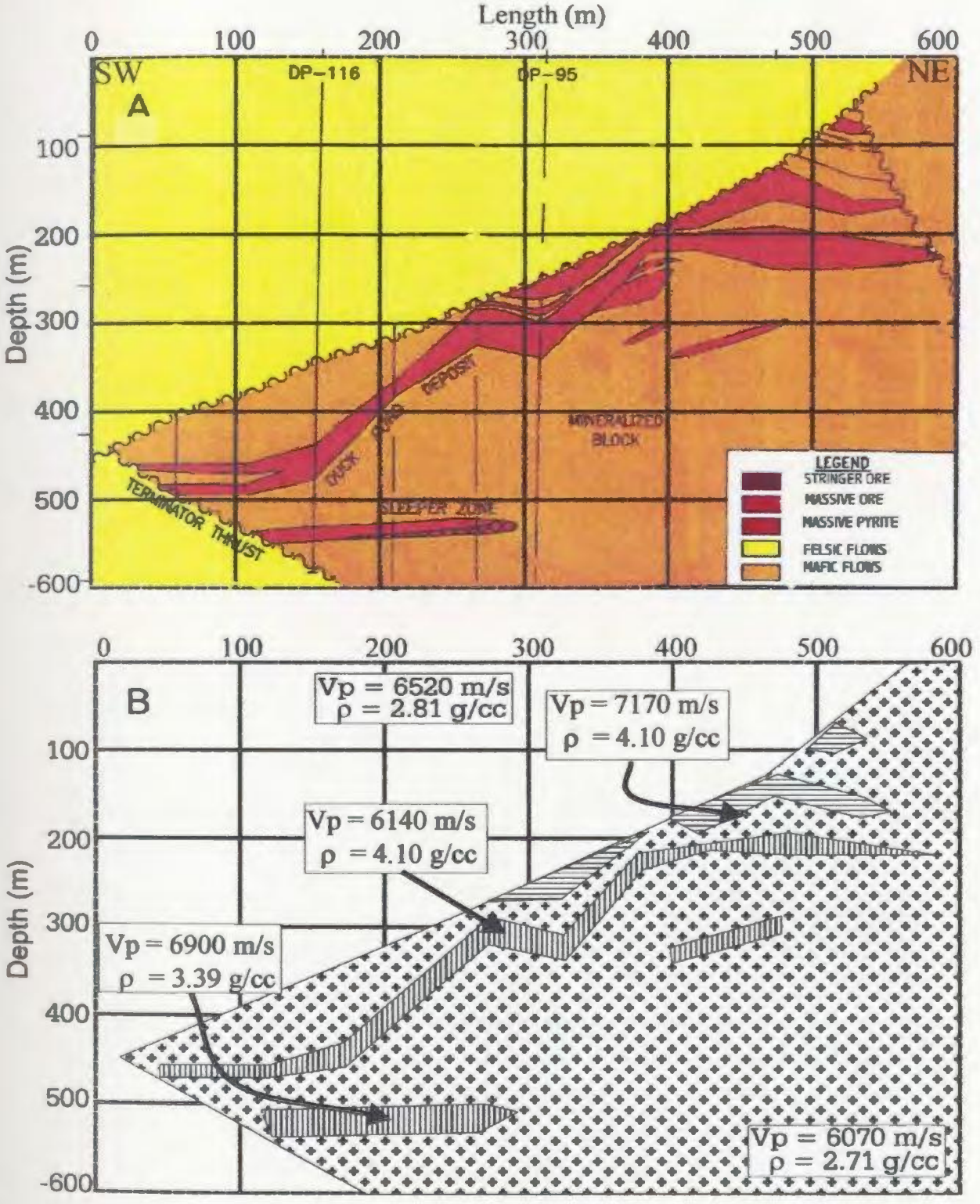

Figure 3.2-3: A simplified longitudinal section through the Duck Pond deposit (A). The velocity-density model derived from this section is shown in (B). Note that the top of the deposit lies in a fault plane. The seismic response caused by the fault is likely to complicate that caused by the deposit in field data. (Modified from Noranda Inc., 1993).

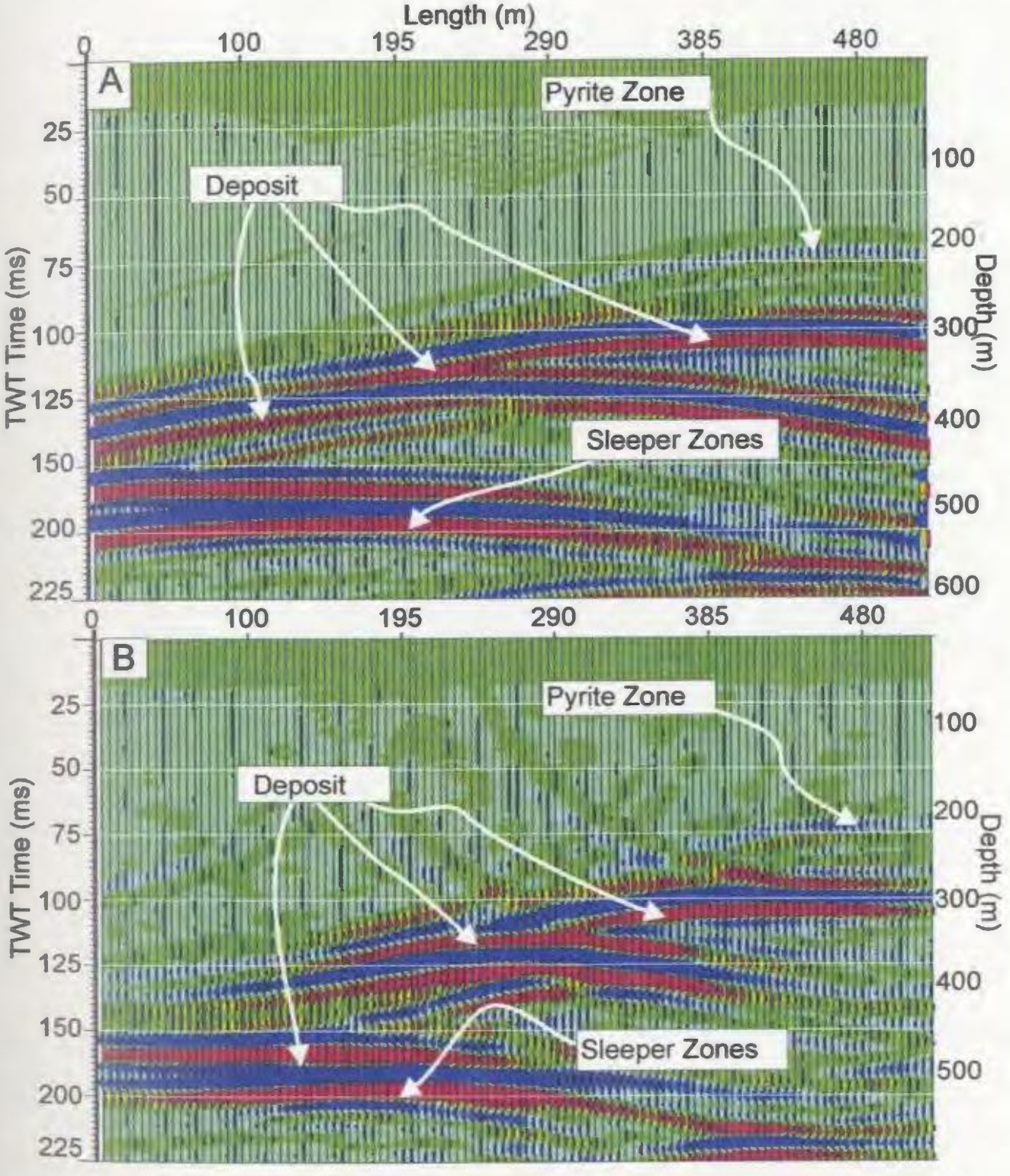

Figure 3.2-4: Un-migrated (A) and migrated (B) synthetic seismogram for the longitudinal section of the Duck Pond deposit shown in Figure 3.2-3. Note that only segments of the deposit are imaged in the migrated section. It is difficult to reconstruct the complete shape of the deposit from this seismic response alone.

model parameters). In Figure 3.2-4(B), the diffractions have been partially collapsed by migration to coincide with the bends and the discrete segments on the deposit.

Although the diffractions in Figure 3.2-4(A) are collapsed in the migrated profile (Figure 3.2-4(B)), it is difficult to reconstruct the complete form of the deposit from this seismic response because only the kinks and the discrete segments are represented. This situation is commonly encountered in 2D field data recorded over small and irregularly-shaped targets. Surface reflection seismic methods are effective only as a detection tool in this case, and cannot fully image the target. While the synthetic profile suggests that the deposit causes a strong response, the numerical simulation does not account for the seismic energy lost out of the plane of the section due to the variation of dip for the discrete segments of the deposit, which is commonly encountered in the case of field data. The 2D simulation is hence a very optimistic guide to the expected seismic response for this deposit.

The fault plane indicated in the cross-section (Figure 3.2-3(A)) is represented only by the contact between the mafic and felsic volcanic rocks in the velocity-density model. It is not visible in the synthetic profile because the acoustic impedance contrast at this interface gives rise to only a small reflection coefficient of 0.05. However, the actual fault plane contains breccia and graphitic sediments (Squires et al., 1990) and is expected to produce a stronger reflection.

Figure 3.2-5 shows a cross-section through the Komsomolskoye Cu-Zn deposit (Ural Mountains) (A), and the velocity-density model derived from it, (B). The deposit is lens-shaped, 200 m wide and 100 m thick, and lies horizontal at a depth of 200 m. This horizontal

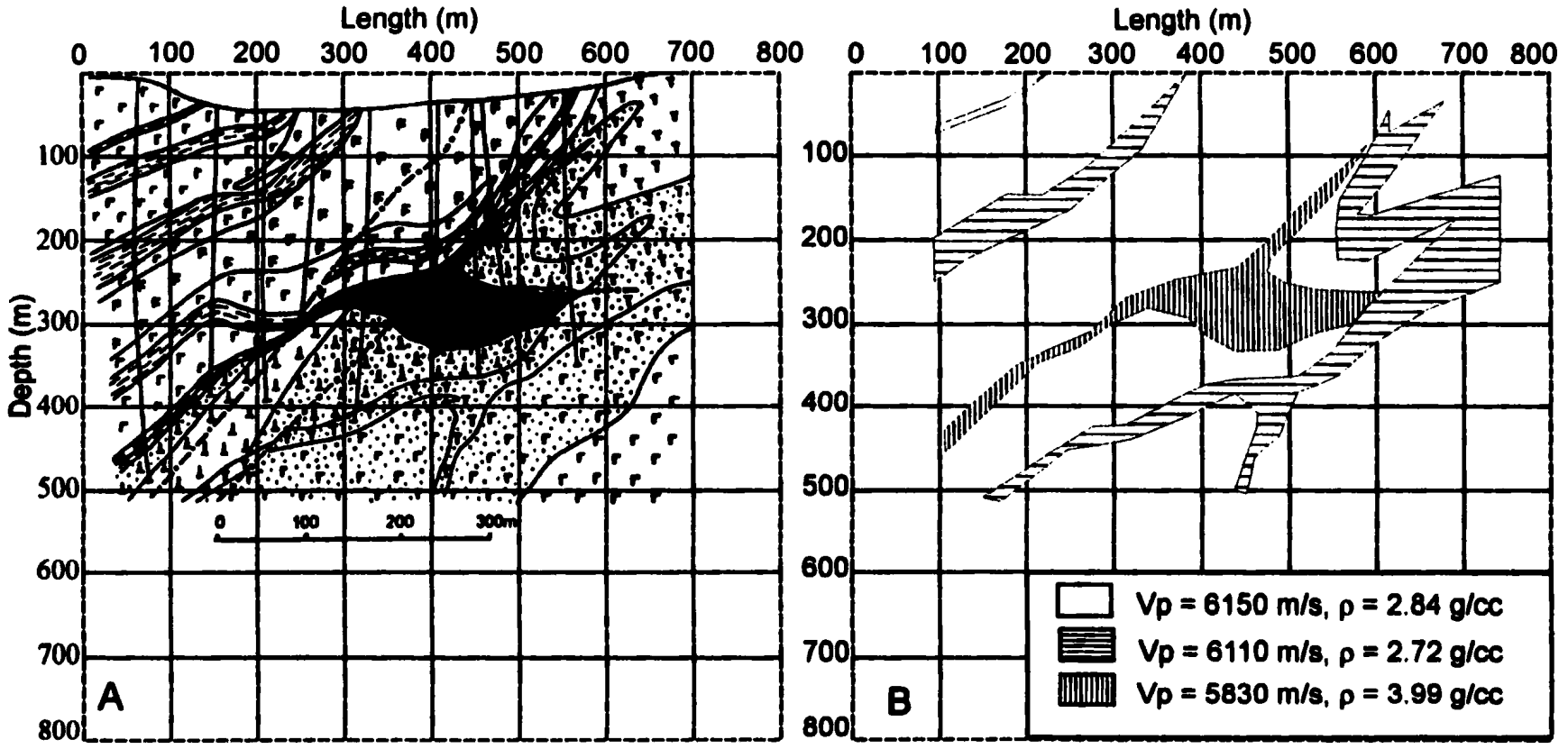

Figure 3.2-5: Cross-section through the Komsmolskoye Cu-Zn deposit (Ural Mountains) (A). (B) is the velocity-density model used to create the normal incidence synthetic seismogram shown in Figure 3.2-6. The surface topography is ignored in the numerical model. (Geological cross-section modified from Prokin and Buslaev, 1998).

attitude makes it a good reflection seismic target since no dip effects complicate the seismic response. It is hosted by basalts in fault contact with felsic and intermediate rocks containing disseminated pyrite, which increases the acoustic impedance of the host rock, thereby leading to a reduction in the seismic anomaly produced by the deposit.

The synthetic profile for the Komsomolskoye deposit before (A), and after (B), migration, is shown Figure 3.2-6. The acoustic impedance at the interfaces between lithologies of the host rock is low compared with that at the deposit and host rock interface. These interfaces therefore produce weak diffractions in Figure 3.2-6(A). The deposit shows diffractions caused by both the top and the bottom in the profile since it is thick (~100 m) compared with the dominant wavelength (~102 m). The migrated profile (Figure 3.2-6(B)) shows collapsed diffractions which, if considered together, closely delineate the deposit. This image, however, has no closure on both sides (partly because of the short profile length) and would be difficult to recognize as that being produced by the deposit in the absence of the cross-section. Identification of the seismic response would be especially difficult in 2D field data because of the presence of out-of-plane events (the sides are within the radius of the first Fresnel zone) and the typically low S/N ratio.[6] Nevertheless, the diffractions are localized such that the position of the deposit can be inferred from the data.

Figure 3.2-7 is a cross-section through the Podolskoye Cu-Zn deposit (Ural

---

[6]Because of the shape of the deposit, energy is lost even from within the Fresnel zone by being directed at wide angles from the source.

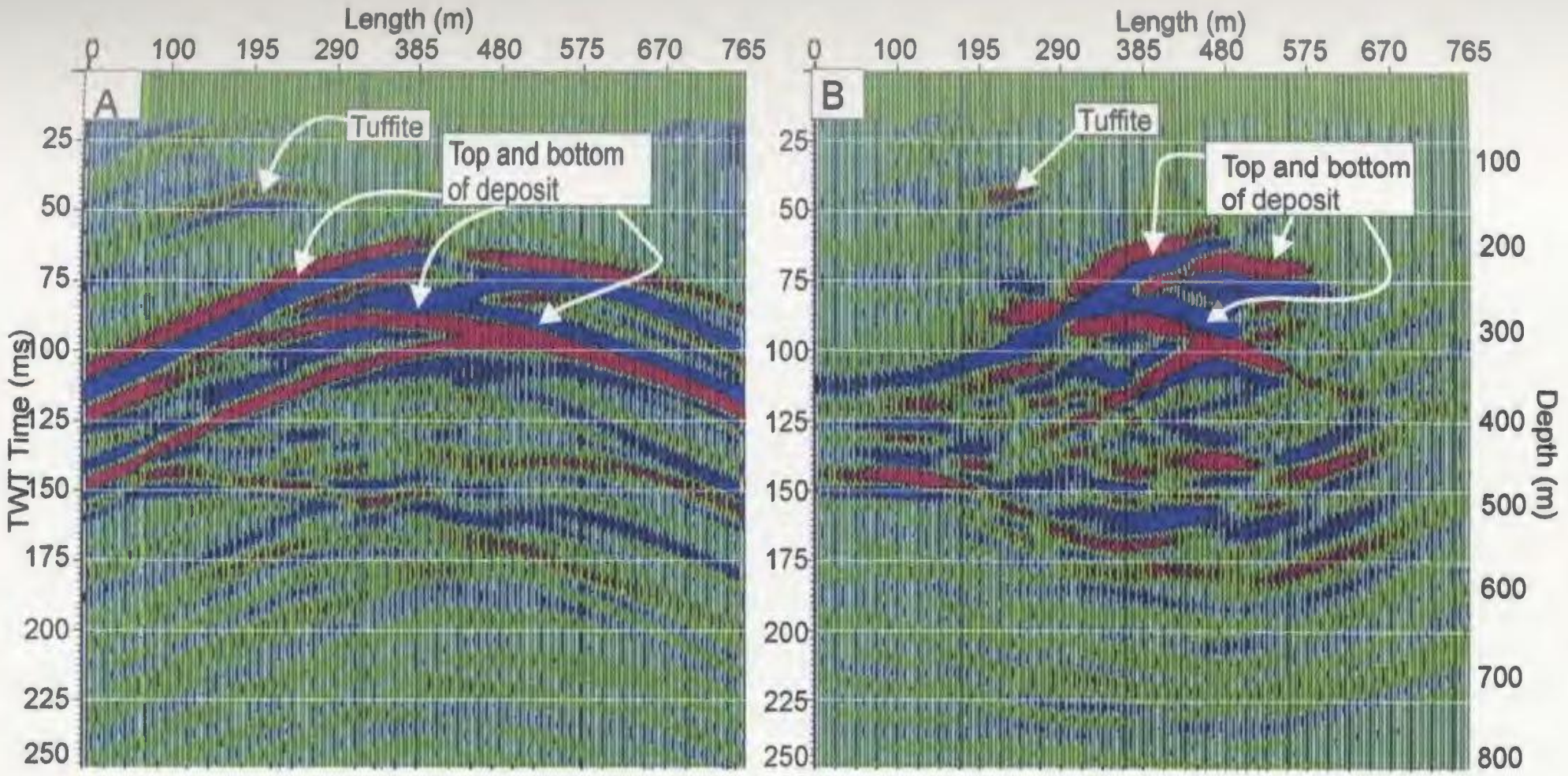

Figure 3.2-6: Synthetic profiles for the Komsmolskoye Cu-Zn deposit (Ural Mountains), (A) before, and (B) after migration. Note that both the top and bottom of the deposit are imaged in (A) and (B), and yet it is difficult to reconstruct the shape of the deposit from the seismic response because it is discontinuous after migration.

Mountains) and a simplified velocity-density model constructed from it. This deposit is hosted by sericite-quartz rocks overlain by felsic volcanic rocks. The top of the Podolskoye deposit is horizontal and conformable with the stratigraphy, but the base is irregular with protrusions into the host rock. The deposit occurs at 160-200 m depth and is ~50 m thick but it has high relief on its lower surface. It consists of a lateral distribution of massive and disseminated sulphides. For the purposes of modelling, the individual deposits are combined and represented with an average density of 4.00 g/cm^3, and the disseminated zone is ignored. The velocity-density model is further simplified by grouping the sediments together into a single unit underlain by felsic volcanic rock to facilitate event identification and reduce interference in the synthetic profiles.

Figure 3.2-8 is a synthetic profile for the Podolskoye deposit before (A), and (B), after migration. The top unit is mapped by an amplitude peak at 50 ms TWT, and the top of the deposit is also mapped by an amplitude peak at 75 ms TWT. The amplitude trough at 125 ms TWT does not correspond to any identifiable event in the cross-section and may be a ghost reflection caused by the top of the model. The bottom of the model is not mapped because of its rugged relief. The migrated section (B), shows portions of the top of the deposit, but again the bottom is not clear.

Figure 3.2-9(A) is a cross-section through the Sibaiskoye Cu-Zn deposit (Ural Mountains), and a simplified velocity-density model constructed from it (B). The Sibaiskoye deposit is hosted by basalt breccia in fault contact with intermediate to felsic rocks. It consists of several small deposits comprising massive Cu-Zn zones in combination with

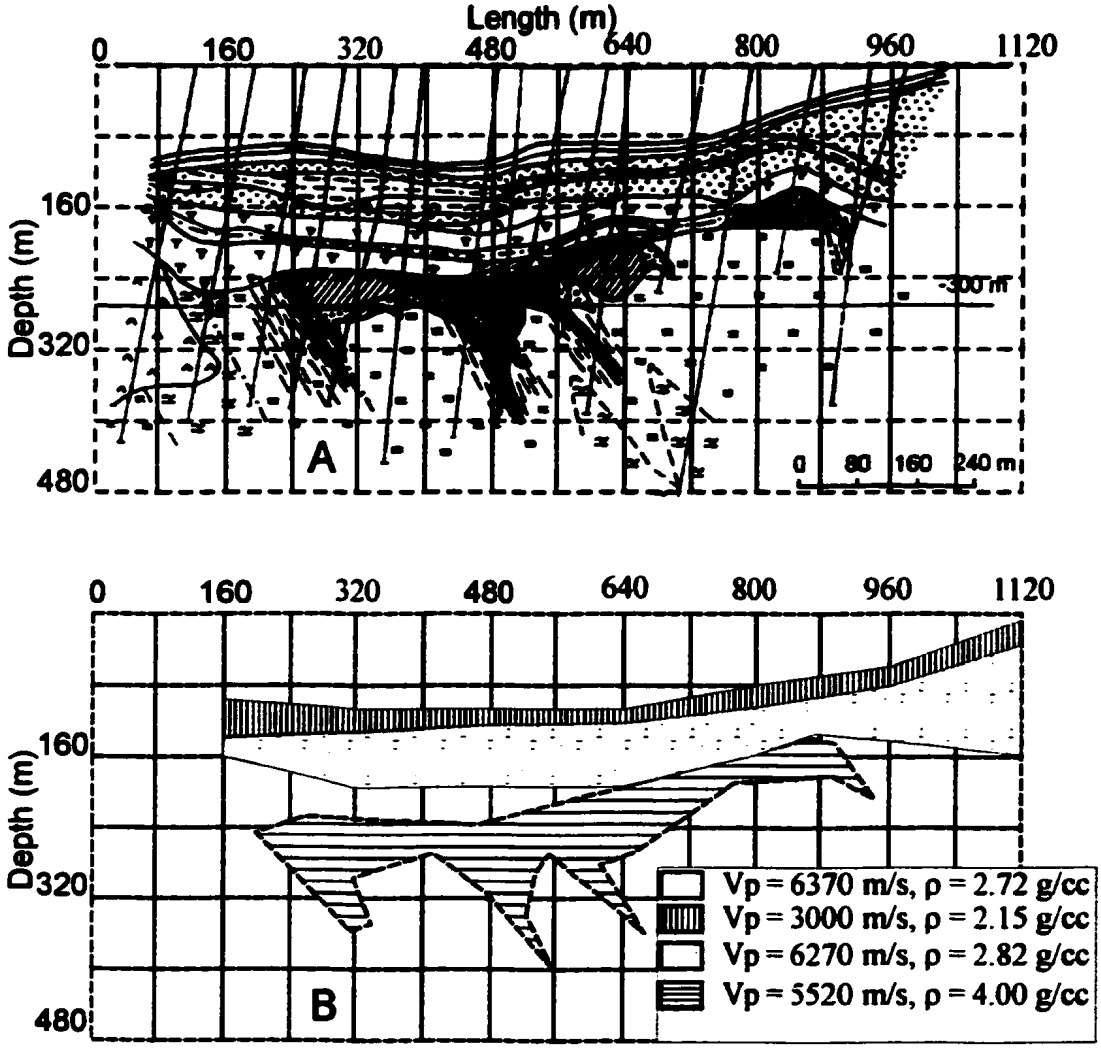

Figure 3.2-7: Cross-section through the Podolskoye Cu-Zn deposit (Ural Mountains) (A). (B) is a simplified velocity-density model for the cross-section. (Geological cross-section from Prokin and Buslaev, 1998).

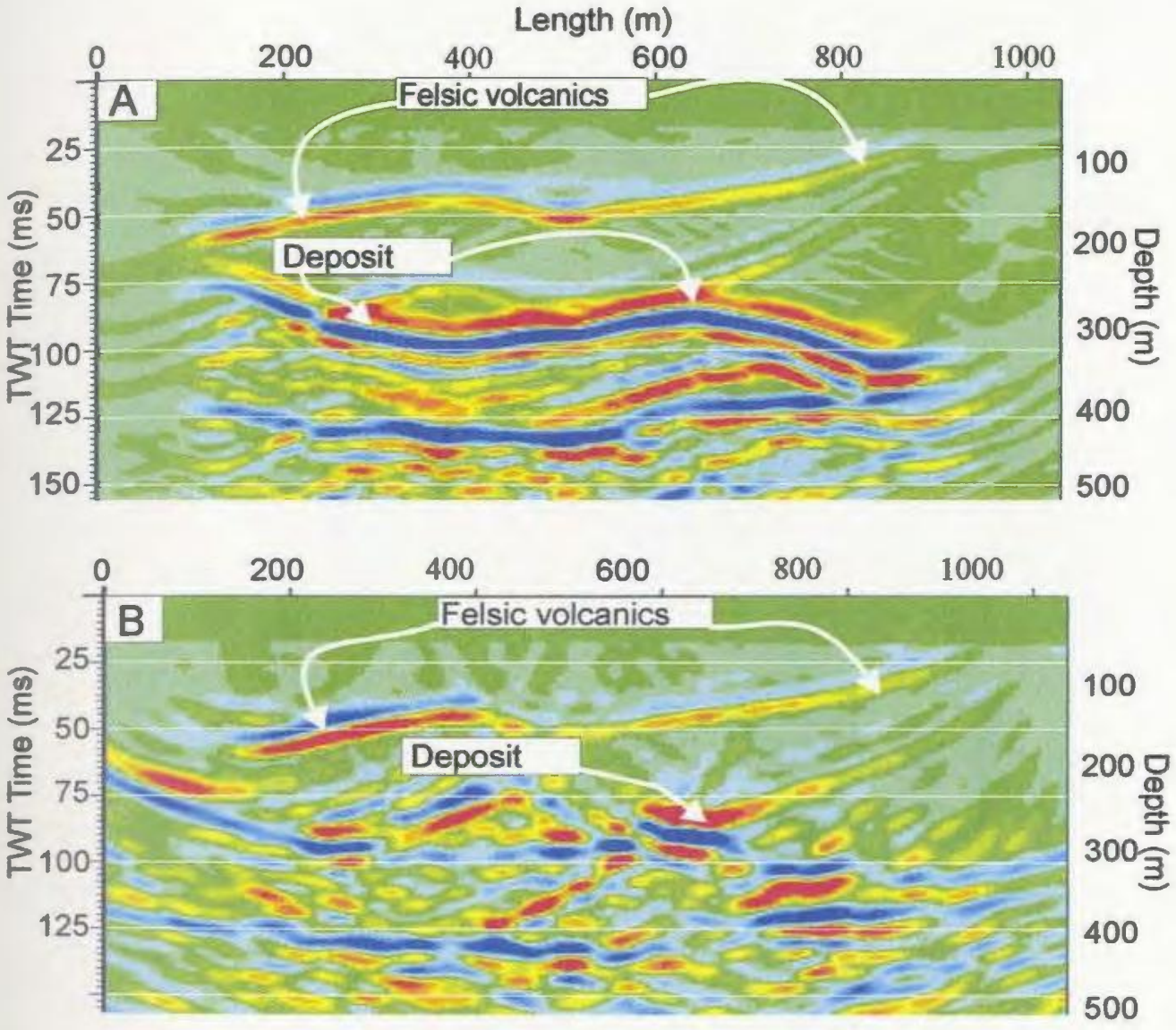

Figure 3.2-8: Synthetic profiles for the Podolskoye deposit (Ural Mountains) before (A) and after, (B) migration. The bottom of the deposit is weakly imaged in this profile because of the relief.

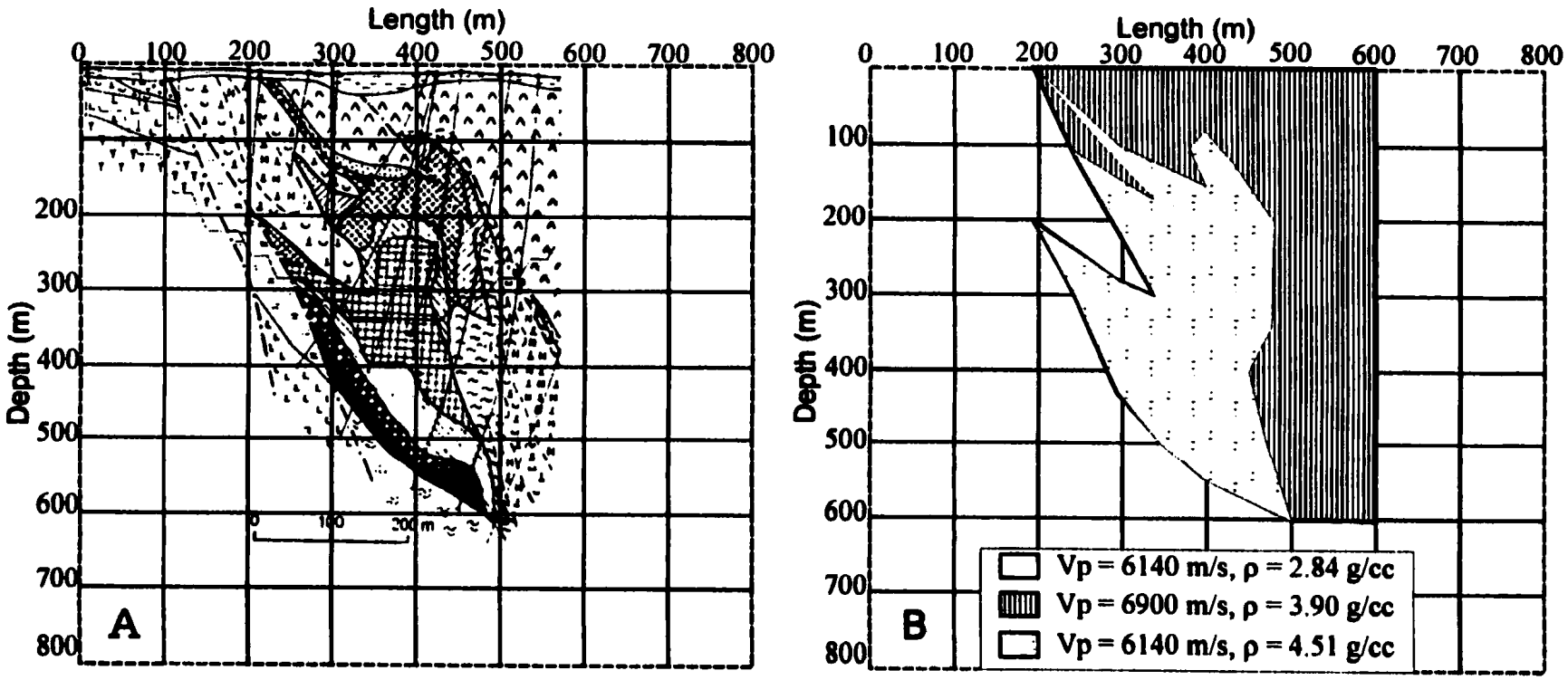

Figure 3.2-9: Cross-section through the Sibaiskoye Cu-Zn deposit (Ural Mountains) (A), and (B) is a simplified velocity-density model constructed from the cross-section in (A). (Cross-section modified from Prokin and Buslaev, 1998).

pyrrhotite, pyrite, and magnetite at different depths, and is roughly tabular in shape and steeply-dipping. It is ~300 m thick and occurs at a depth of 100-600 m. Apart from the structural disruption, the deposit retains the characteristics of an undeformed Cu-Zn VMS deposit, as shown in Figure 3.2-1. However, since the individual mineral deposits are thin, they are grouped together in the velocity-density model.

Figure 3.2-10 shows a synthetic profile for the Sibaiskoye deposit before (A) and (B), after migration. Even though the deposit is large compared with the dominant wavelength of ~100 m, the seismic response caused by the deposit consists mostly of diffractions produced at the vertices of the steeply dipping segments of the deposit. Using the model velocities and comparison with the cross-section, the seismic events caused by the deposit are identified in the synthetic profile. The migrated profile shows the top and bottom of the deposit accurately, but like the previous models, the exact shape of the deposit cannot be reconstructed completely from the 2D seismic response.

Figure 3.2-11 shows a cross-section through the Flin-Flon Zn-Pb-Cu deposit (MN) (A), and a simplified velocity-density model constructed from it (B). This mineral deposit is hosted in granite gneisses and thins progressively with increasing depth, with few bends and flat segments that can be mapped with surface reflection seismic methods.

Figure 3.2-12 shows a synthetic profile for the Flin-Flon deposit. Both the un-migrated (A) and migrated (B) profiles show diffractions at 40 ms and 80 ms TWT caused by the deposit where there are bends and flat segments. The asymmetry of the diffractions show that the deposit is steeply-dipping to the right. It would be difficult to reconstruct its

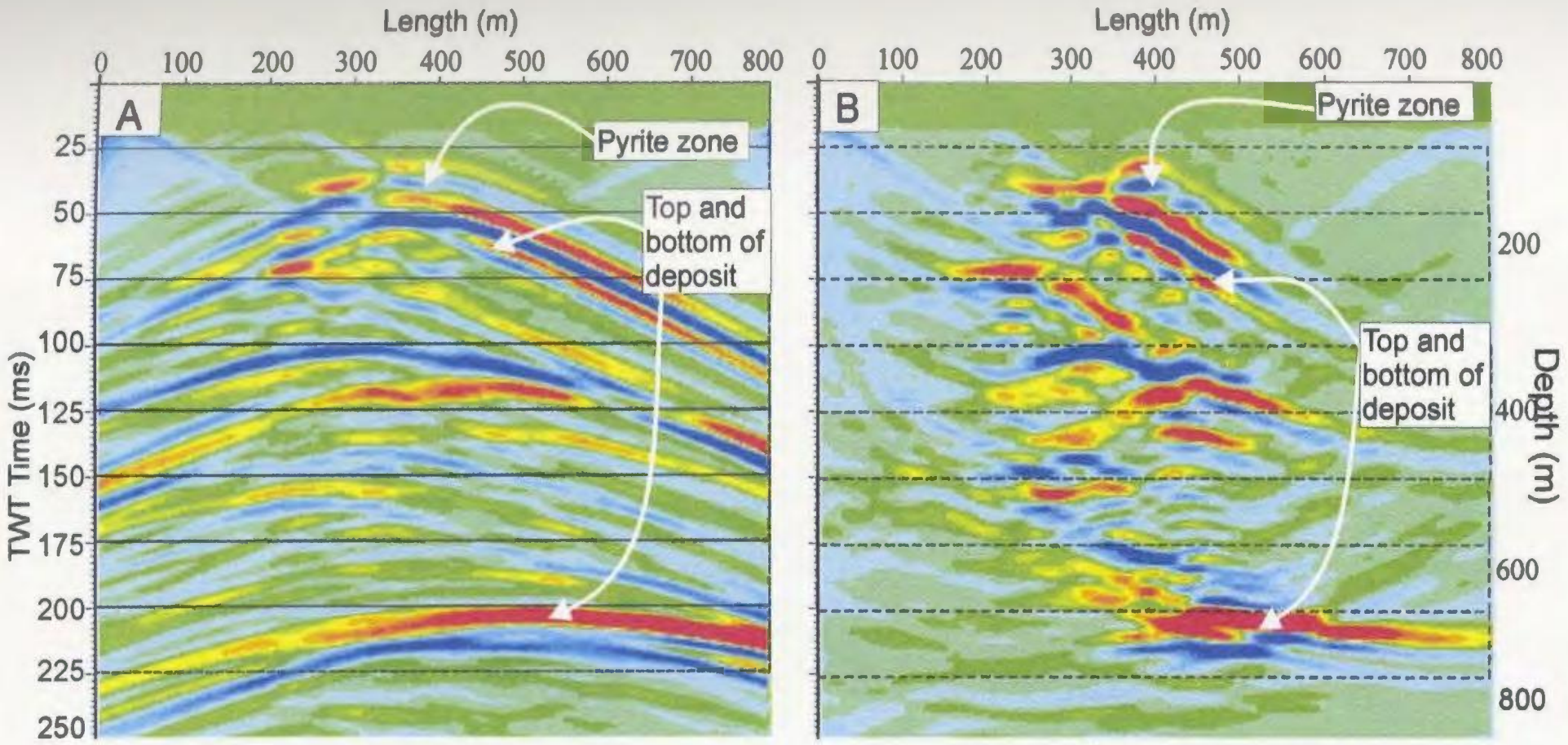

Figure 3.2-10: (A) Un-migrated and (B) migrated synthetic profiles for the Sibaiskoye deposit (Ural Mountains). The top and bottom of the deposit are clearly resolved because it is large compared with the seismic wavelength.

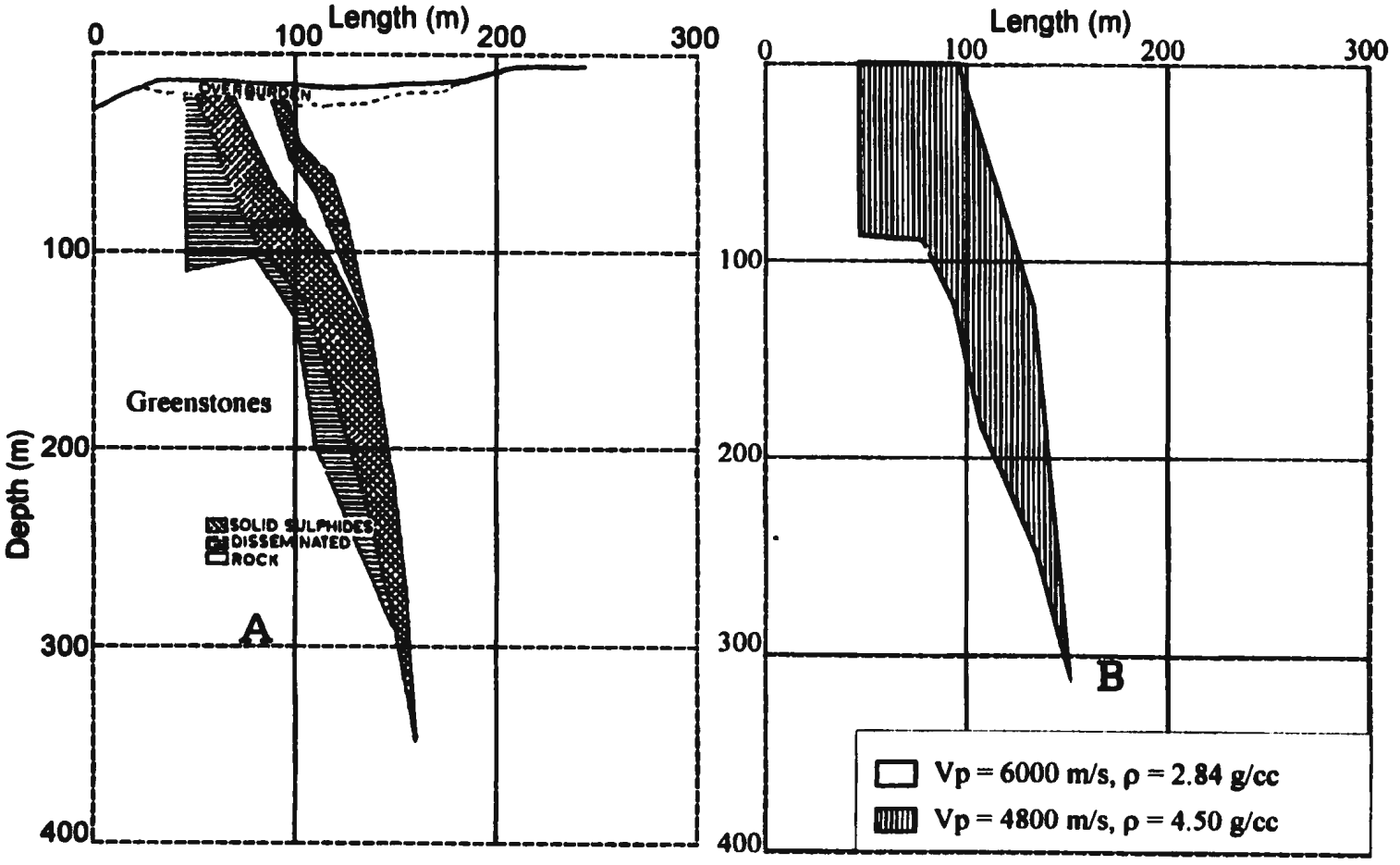

Figure 3.2-11: Cross-section through the Flin-Flon Zn-Pb-Cu deposit (MN) (A), and (B) is the velocity-density model constructed from it. (Modified from Smith, 1967).

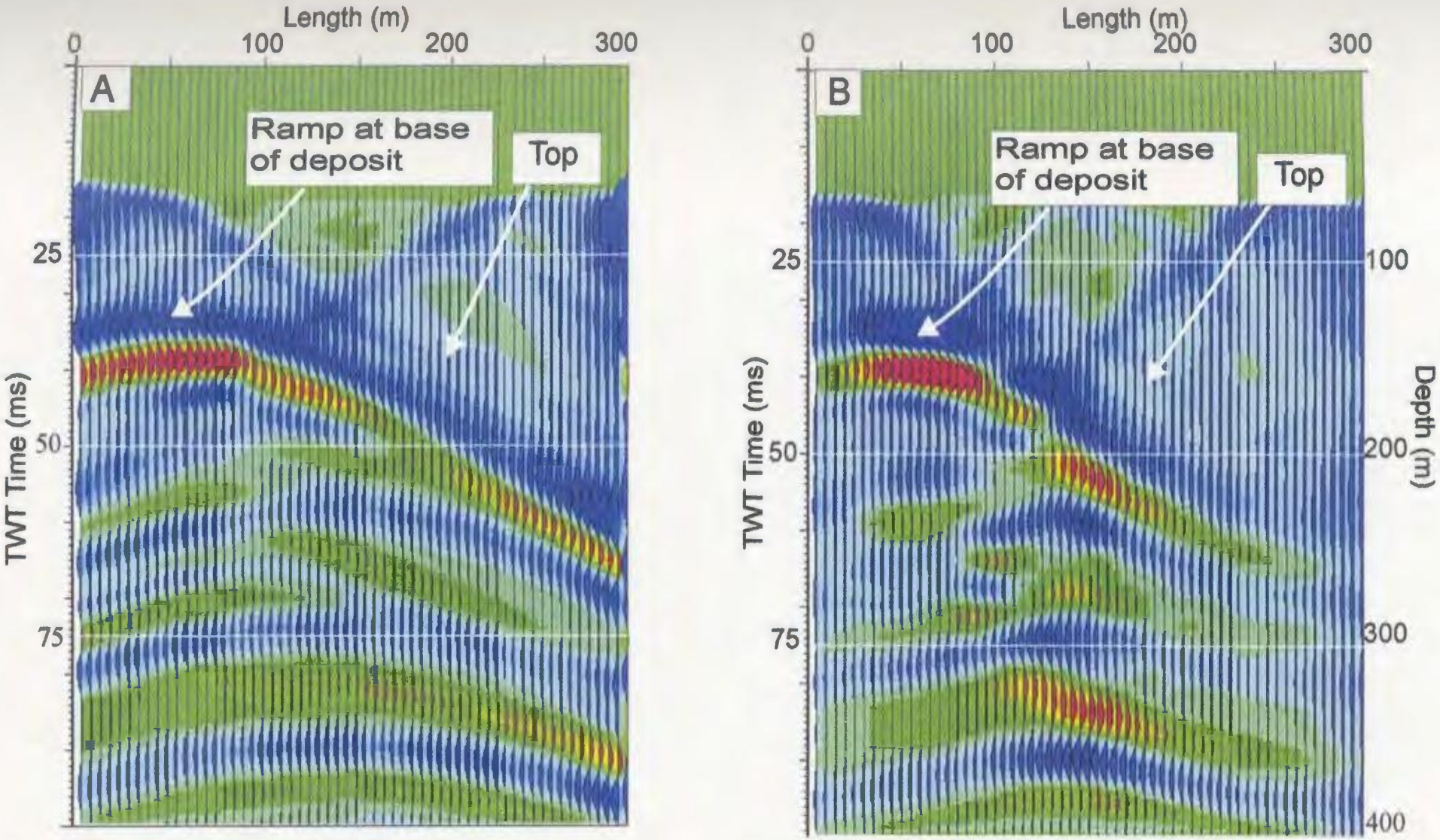

Figure 3.2-12: Synthetic profiles for the Flin-Flon Zn-Pb-Cu deposit (MN) (A) before migration, and (B) after migration. The diffraction pattern clearly shows that the deposit is steeply dipping to the right.

shape from these 2D profiles without the geological cross-section, especially after migration. In this case, a very long profile would required to position shot and receiver normal to the body.

3.3 Ni-Cu deposits

Voisey's Bay (NF) and the Sudbury Igneous Complex (ON), contain large quantities of magmatic Ni-Cu deposits. The geology of the Sudbury Igneous Complex (SIC) is described in Lightfoot et al. (1997). Ni-Cu deposits within the SIC are hosted by (i) basic rock inclusions within norite and gneiss breccias, (ii) structures within a norite-gneiss complex, and (iii) dykes of quartz diorite. Where the norites are felsic they contain magnetite, which increases the acoustic impedance of the host rock and thereby diminishes the impedance contrast against the deposits. The mineral deposits also occur within fractures and embayments at the contact between the footwall and hangingwall rocks. Sudbury-type mineral deposits span a wide range of sizes, e.g. the Copper Cliff deposit was initially 300 m long by 300 m thick, while that at Levack was 150 m long and 75 m thick (Harvey, 1997). The mineral deposits in the Sudbury mining camp are generally dipping toward the centre of the SIC structure.

Figure 3.3-1(A) is a cross-section through the original Frood-Stobie deposit in the Sudbury mining camp (ON). Figure 3.3-1(B) shows the velocity-density model used for the simulation of this cross-section. The deposit is hosted in greenstones and overlain by gabbro.

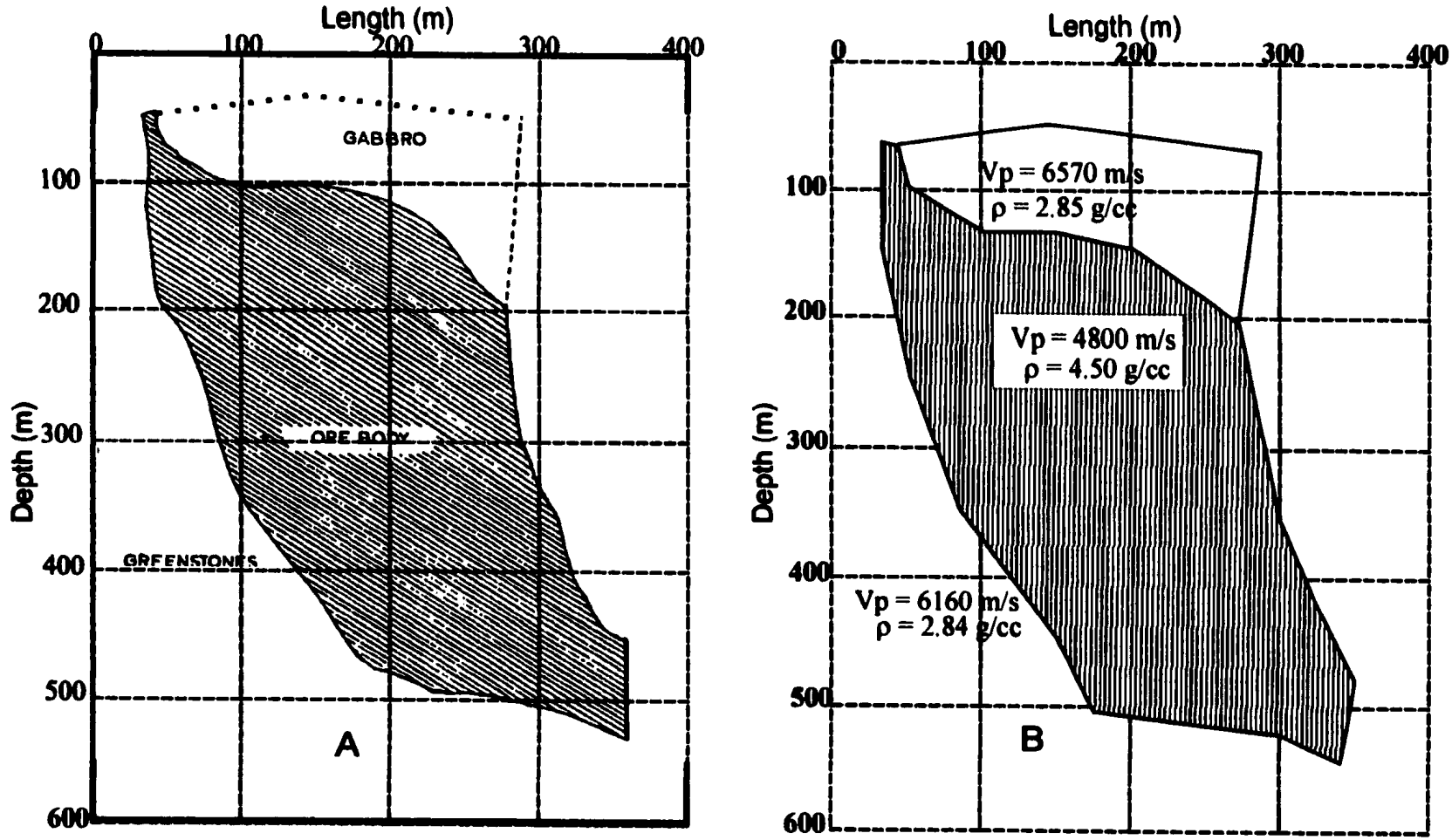

Figure 3.3-1: Cross-section through the Frood-Stobie (ON) mineral deposit (A), and (B) velocity-density model used to create the normal incidence synthetic profile in Figure 3.3-2. (Modified from Smith, 1967).

The Frood-Stobie Ni-Cu deposit is tabular and dipping at 55°. It is ~200 m wide at the top and extends from the surface to ~500 m depth. The top and bottom of the deposit are shallow dipping and hence the only locations expected to produce a seismic response, the sides being too steep to be illuminated with surface equipment, unless a very long profile is recorded.

A synthetic profile for the Frood-Stobie deposit is shown in Figure 3.3-2 before (A) and after (B) migration. It shows the seismic response caused by the top of the deposit for the individual dip segments with discrete diffractions at ~30 ms TWT. The bottom of the deposit is mapped similarly with diffractions produced by the individual dip segments. Apart from these diffractions, there is no closure on the sides of the deposit, and hence its reconstruction from these seismic responses would be incomplete and would allow only a rough estimation of its shape.

Figure 3.3-3(A) is a cross-section through the Levack Ni-Cu deposit in the Sudbury mining camp, and (B) is the velocity-density model used for its simulation. The Levack deposit extends from the surface to 350 m and dips 45°. The deposit varies in thickness from 20 m at the top to ~60 m at a depth of 300 m.

Figure 3.3-4 shows a synthetic profile for the Levack deposit. The dipping base of the norite body is mapped by a diffraction. The less steep segments in the deposit show clearly on the migrated section at 158 and 300 m. The flat area along the base of the deposit is also mapped by a strong amplitude peak at 400 m. Even though these events can be matched with the cross-section, the seismic response does not provide a complete image of

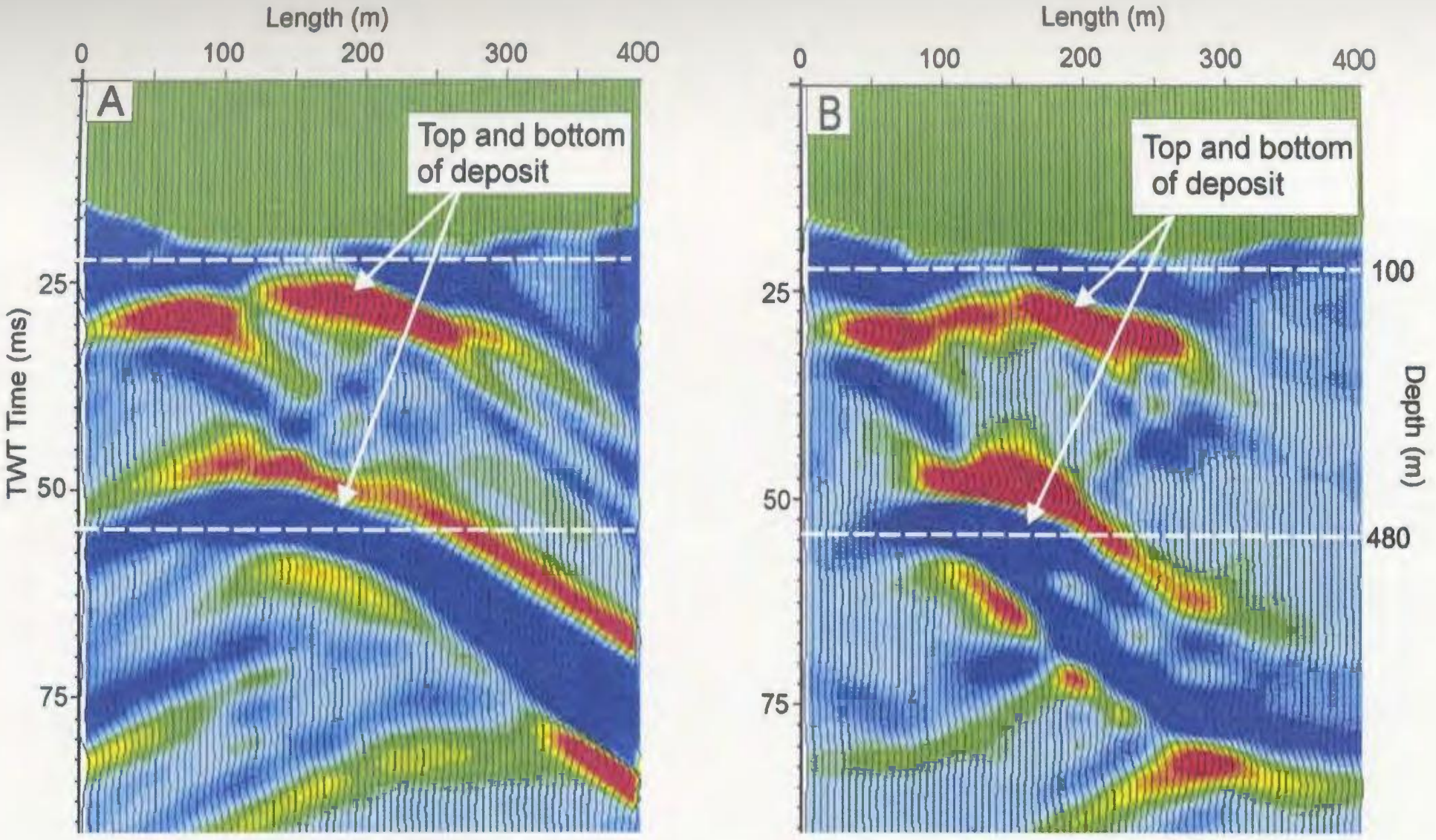

Figure 3.3-2: Synthetic profiles for the Frood-Stobie deposit shown in Figure 3.3-1 (A) before migration and (B) after migration. The event caused by the top of the gabbro unit was muted because it coincided with the sources.

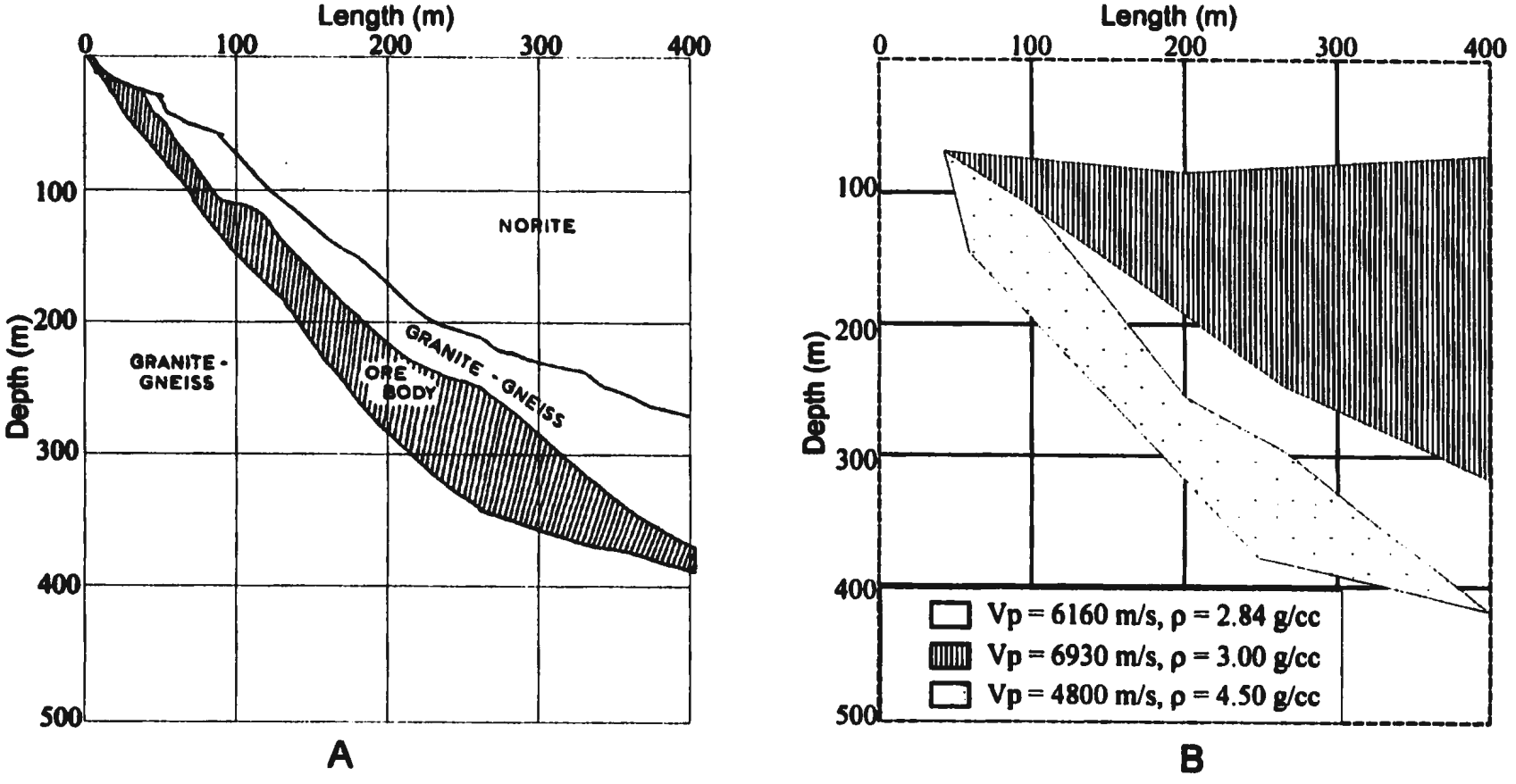

Figure 3.3-3: Cross-sections of the Levack Ni-Cu deposit (A), and (B) is the velocity-density model constructed from the section. (Cross-section modified from Smith, 1967).

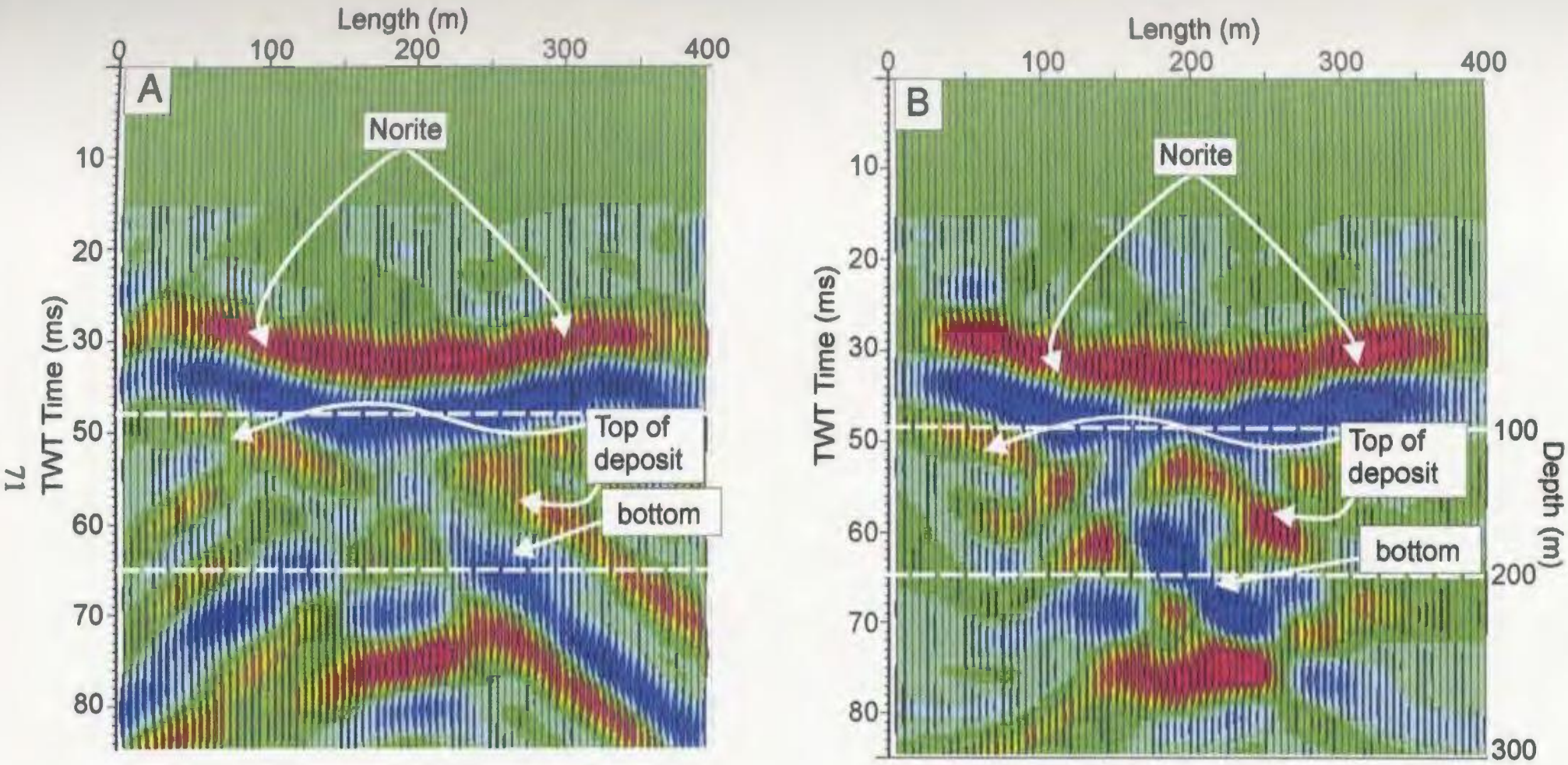

Figure 3.3-4: Synthetic profiles for the Levack deposit shown in Figure 3.3-3(B) before (A), and after (B) FK time migration. The response caused by the deposit is clearly visible in both profiles.

the deposit since the diffractions represent only the kinks on the surface of the deposit. Besides the sub-horizontal event at the base of the deposit, the events are weak because of the low acoustic impedance contrast between the deposit and the host rock and would be hard to pick in field data with ambient noise.

The geology of the Voisey's Bay (NF) Ni-Cu-Co deposits is described in Naldrett et al. (1996). The Voisey's Bay deposits contain large massive sulphide bodies occurring from the surface to a depth of ~900 m. The deposits are hosted by a troctolite sheet intruded into quartz-biotite gneisses. Mineralization at Voisey's Bay consists of pyrrhotite, pentlandite, chalcopyrite, and accessory cobalt and magnetite, localized in three zones: (i) the Western Extension Zone, (ii) the Ovoid Zone, and (iii) the Eastern Deeps Zone. The troctolite sheet is ~30 m thick and exposed in the Western Extension Zone. It is mineralized with disseminated and massive sulphide lenses and has sharp, chilled contacts with the host rock. The base of the troctolite intrusion is barren and contains gneiss breccia. In the Ovoid zone the troctolite intrusion contains a massive sulphide deposit overlying disseminated sulphides. In the Eastern Deeps Zone, the troctolite sheet is intruded by monzonite dykes.

Figure 3.3-5(A) shows a cross-section through the Ovoid deposit at Voisey's Bay (NF), and a simplified velocity-density model constructed from it (B). The massive sulphide zone is the shape of an inverted triangle, occurs from the surface to ~80 m, and ~250 m across at the surface. Figure 3.3-5(B) and (C) are un-migrated and migrated synthetic profiles for the deposit in (A). The un-migrated profile shows a clear diffraction response caused by the base of the ore zone.

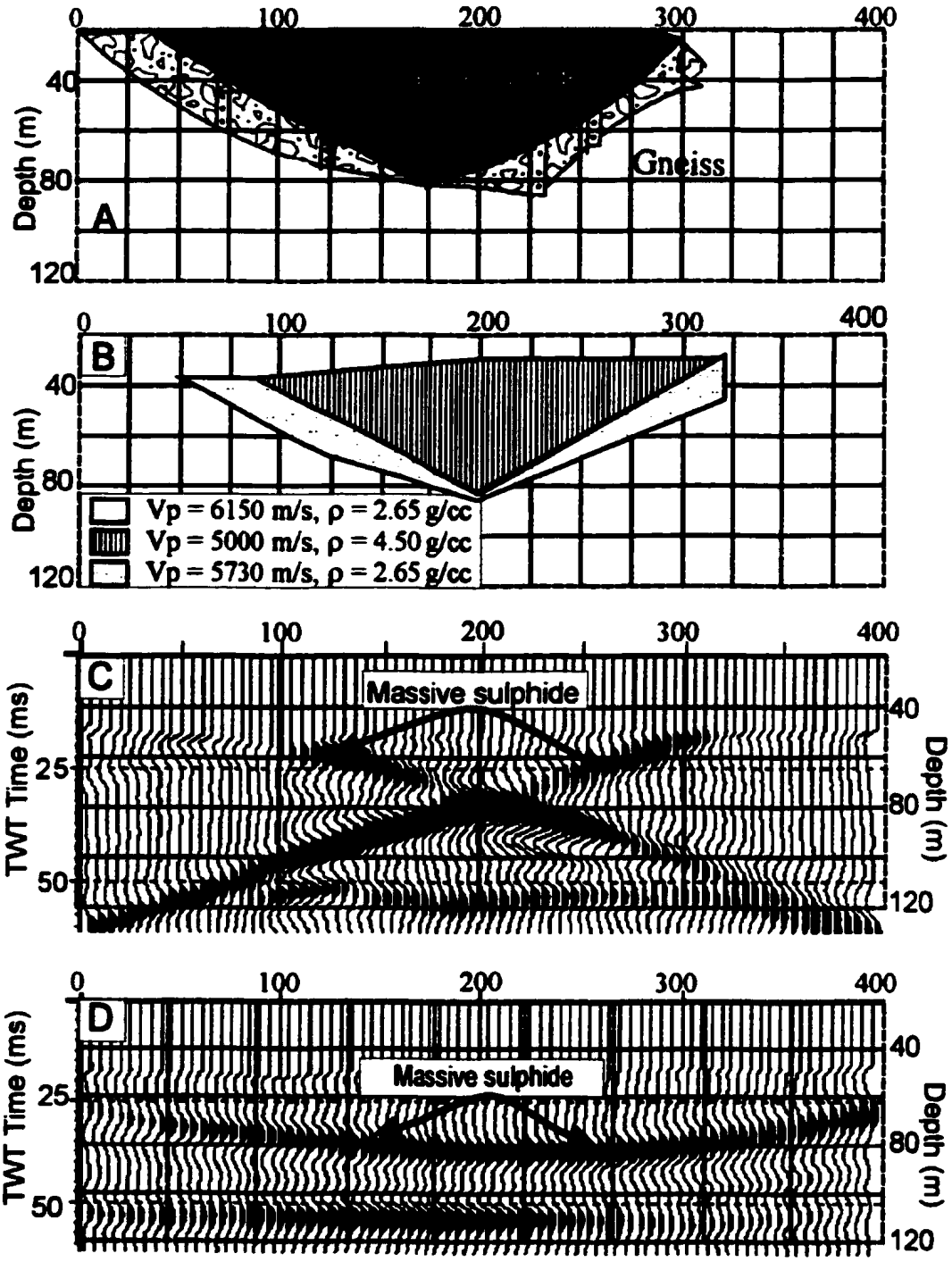

Figure 3.3-5: Cross-section through the Ovoid Ni-Cu-Co deposit at Voisey's Bay (NF) (A). (B) is a velocity-density model of the deposit, and (C, D) are synthetic profiles before and after migration respectively. (Geological section modified from Naldrett et al., 1996).

3.4 Chromite deposits

Chromite is mined from rocks of layered mafic igneous complexes, where it occurs in either of two forms: stratiform and podiform (pod-shaped). Stratiform chromite deposits occur in stratiform complexes, and those in alpine type complexes are podiform. The distinguishing features of these deposits are relevant to the present discussion because both the acoustic impedance and the geometry of a mineral deposit are important attributes in reflection seismic imaging.

Stratiform chromite deposits comprise laterally extensive cumulate crystal layers alternating with peridotite and dunite, the whole sequence being hosted by pyroxene gabbro. The chromite-peridotite pseudo-stratigraphy contains bedded platinum-bearing minerals in the Bushveld (S. Africa) and the Great Dyke (Zimbabwe) igneous complexes. Stratiform deposits are normally undeformed and attain widths of 1.5-6 m (Stanton, 1972). Podiform deposits comprise lenses of disseminated to massive mineralization with sharp margins against the host rock. Although most of the deposits are concordant with the fabric of the host rock, the boundaries are poorly-defined for the more massive podiform deposits. There are occurrences of chromite deposits where the deposit is wholly discordant to the fabric of acoustic impedances compared with peridotite.

Figure 3.4-2(A) and (B) shows a synthetic profile for the chromite ore pods shown in Figure 3.4-1(A) before and after migration respectively. Both the migrated and un-migrated synthetic profiles show clearly the seismic responses caused by the top and bottom of the sack-form masses. These seismic responses are entirely diffractions because the

individual masses are small compared with the dominant wavelength. The migrated profile clearly shows the limits of the deposit, but since there is no closure on the sides, it would be difficult to recognise this seismic response as that caused by an object of the indicated geometry in field data with a low S/N ratio.

3.5 Summary and Conclusions

Volcanogenic massive sulphide deposits comprise the low aspect ratio VMS and the laterally extensive high aspect ratio SEDEX varieties. VMS deposits have small lateral extents and hence seismically complex geometries. They are lens to tabular-shaped with length to thickness ratios ≤ 10, tens to hundreds of metres wide, and up to 100 m thick. Ni-Cu deposits are similarly lens to tabular-shaped and low aspect ratio, with sizes of up to 300 x 300 m. Due to their small sizes and irregular geometries, these mineral deposits produce predominantly diffraction responses in seismic records. I show five examples of VMS and two of Ni-Cu deposits together with the corresponding synthetic seismograms.

Chromite deposits occur in two varieties: stratiform deposits occur in stratiform mafic igneous complexes and comprise 1.5-6 m thick cumulate crystal layers. Podiform deposits comprise disseminated to massive lenses with sharp margins against the host rock, and sometimes the deposit is discordant to the host rock. Podiform deposits may also comprise discrete sack-form masses (Figure 3.4-1).

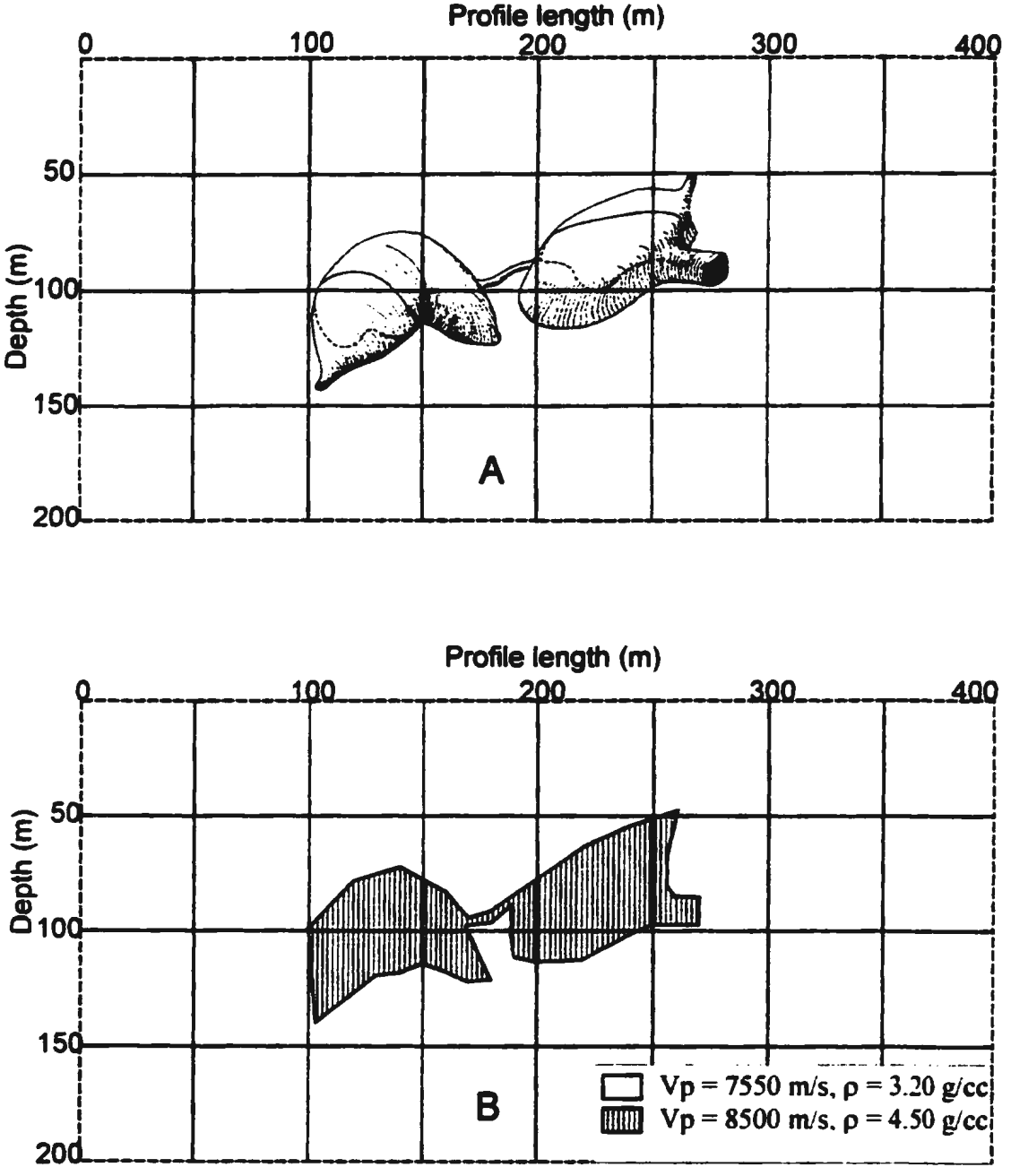

Figure 3.4-1: Sack-form chromite deposits hosted in dunites and harzburgites (A). Sack -form masses can be up to 1 km in length (Stanton, 1972). (B) is the velocity-density model used to create the normal incidence seismogram in Figure 3.4-2. (Cross-section modified from LeBlanc, 1987).

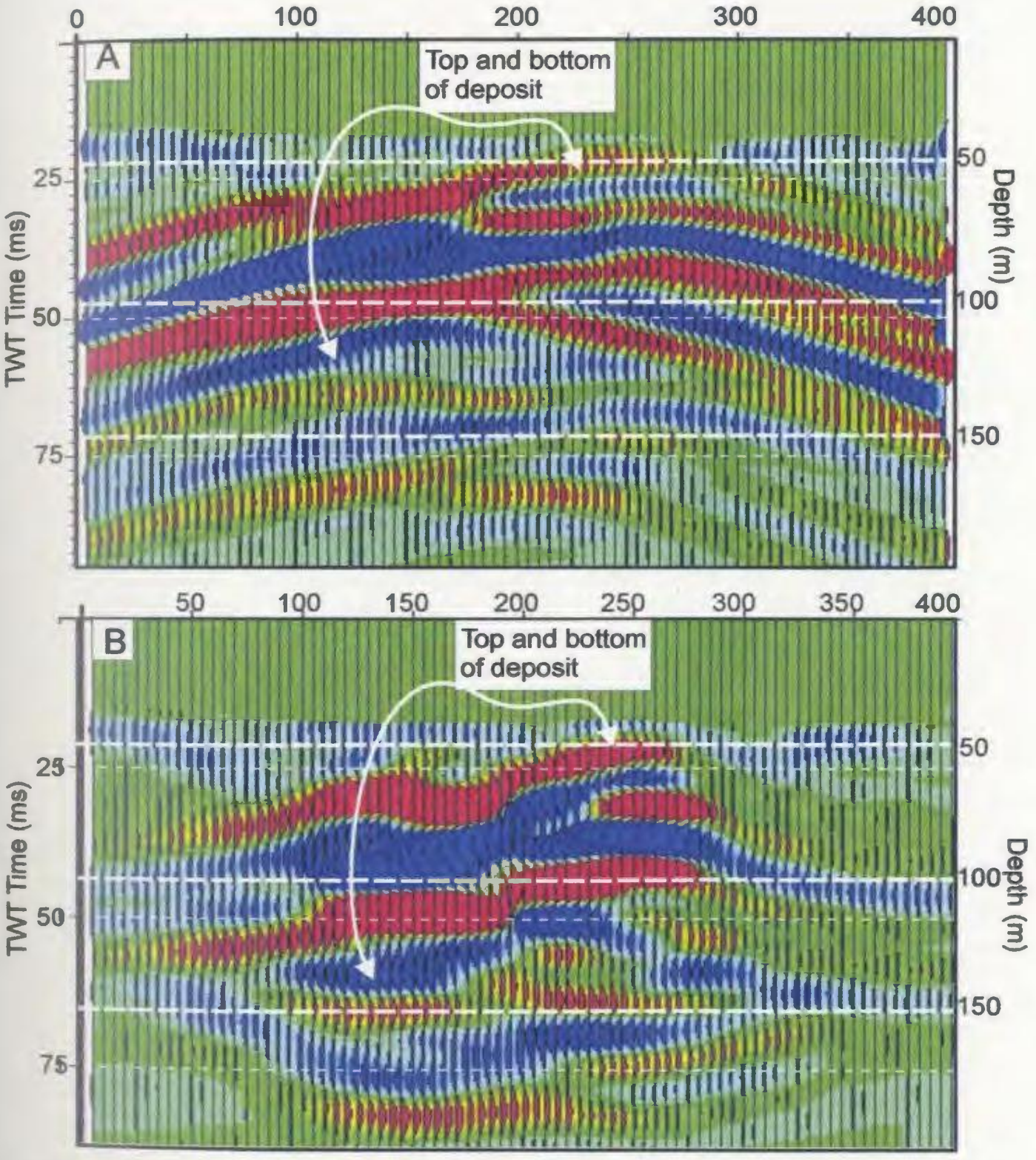

Figure 3.4-2: Normal incidence synthetic profiles for the deposits shown in Figure 3.4-1 before (A) and after (B) migration. Note that even though the seismic response is strong, it gives no indication of the shape of the deposits. This poses a problem in 2D field data since the seismic response cannot be distinguished from that caused by any other object.

Synthetic seismograms show strong diffraction seismic responses for the simulated deposits before migration, and still strong, but discontinuous responses after migration. Migration contracts the diffractions to their points of origin at the nodes in the model, thereby causing the seismic response to be discontinuous, as illustrated in Figures 3.2-6(B) and 3.2-7(B). Although the amplitude response is stronger after migration, it is the continuity of the diffraction response that helps to detect a small body target in field data. For this reason, it would be easier to detect the diffraction responses in field data before migration. The synthetic seismograms are strictly 2D, and hence give clear diffraction responses for situations where field data would be complicated by out-of-plane events, e.g. for the Komsomolskoye deposit (Figures 3.2-5 and 3.2-6).

It is apparent from the examples that common metallic mineral deposits attain sufficient sizes and acoustic impedances to be detected with reflection seismic in field data. However, since it is known that this is not generally the case, I conclude that other physical attributes are responsible for attenuating the seismic responses. These other physical attributes are investigated in Chapters 4 and 5.

CHAPTER 4

4.0 ANALOGUE MODELLING

4.1 Introduction

Synthetic seismic models and reflection coefficient analysis show that mineral deposits hosted by crystalline rocks must give rise to strong seismic anomalies (Chapters 2 & 3). However, mineral deposits hosted by these rocks generally show only subtle seismic anomalies in field data, and an explanation for the weak seismic responses is required. It is apparent from the discussion in Chapters 2 and 3 that other physical attributes of mineral deposits besides density and the Poisson's ratio must account for the subtle and complicated seismic responses observed in field data. One of these 'other' physical attributes is the geometry of a mineral deposit, whose effect on the seismic response is controlled partly by size, dip, aspect ratio, and surface relief.

The aim of the model experiments described in this chapter is to determine the effect that the geometry imposes on the seismic expression of mineral deposits using physical seismic models (also called analogue models). The modelling involves acquisition of offset 3D prestack data in a water tank, which are processed using conventional CMP-based and prestack depth migration methods. 2D seismic profiles are extracted from the 3D seismic data and subjected to a processing sequence similar to that applied to 2D field data recorded at Tally Pond (NF). The design of the models and the processing of the model seismic data are described in the following sections.

The basic assumption in seismic modelling is that the propagation of seismic waves

is identical in the scale model and the actual feature (White, 1965; Ivakin, 1966; Ebrom and McDonald, 1994). Physical modelling allows an unique examination of the seismic response of a complicated feature under controlled conditions, such that the components of a complex seismic response can be observed separately by varying the degree of model complexity (O'Brien and Symes, 1971). The ability to break a complicated seismic response into simpler components certainly allows better insight into the understanding of a complex seismic problem. Furthermore, the seismic response of a complicated physical model is not inhibited by a limited understanding of the problem since no simplifying assumptions are implicit in the initial formulation (Ebrom and McDonald, 1994). Seismic modelling is also used for evaluating data acquisition and processing parameters prior to field work because grid designs can be adjusted inexpensively on a model. It also allows recording of offset 3D shot records effectively at a low cost.

Physical models are scaled such that the seismic resolution is preserved.[7] For the fundamental quantities, length (λ) and time (τ), model ratios are chosen arbitrarily for the convenience of laboratory handling. Derived quantities such as velocity and frequency are scaled in accordance with their dimensional expressions and are hence not arbitrary, e.g. the scale factor for velocity is λ/τ. Once length and temporal similarity are satisfied, data acquisition parameters are calculated using the actual model dimensions, according to the Nyquist sampling criteria, to prevent aliasing. Physical seismic modelling involves the use

[7] Scale modelling for geological structures is discussed in Hubbert (1937).

of materials with properties which scale as closely as possible to the actual case. After model materials and ratios are determined, the model must be coupled to the signal source and receiver. An efficient coupling medium is water, whereby a conventional marine seismic survey is simulated. However, using water reduces the experiment to the acoustic case since shear waves do not propagate in fluids. Although this reduces the amount of information in the experiment, the results provide sufficient information on the model for the present purpose. Similar water tank seismic experiments have been performed by Hilterman (1970) and French (1973) to investigate different seismic imaging problems.

4.2 Model design and equipment

Three physical models representing different degrees of geometric complexity expected in mineral deposits are investigated. They include an egg-shaped model with a smooth surface, a cylinder-shaped model with a rugged surface relief and a complicated structure, and a disk-shaped model with moderate surface relief. These models are scaled such that the dimensions used for processing of the seismic data are consistent with the sizes of the actual features (Table 4.2-1).[8]

The models were carved from cured resin using high speed abrasion tools and a

---

[8] The length and time scale factors are chosen such that the actual dimensions of the seismic data are consistent with those commonly used in high resolution surveys.

Table 4.2-1: Model dimensions, model to original length and time ratios, and scale factors for the model tank experiments.

Quantity & geometry		Symbol	Model	Original	Ratio	Scale Factor
length	Egg	λ	0.120 m	300.0 m	0.0004	2500
	Cylinder		0.105 m	262.5 m	0.0004	2500
	Disk		0.084 m	210.0 m	0.0004	2500
sample rate	all	τ	0.20 μs	0.50 ms	0.0004	2500
frequency	all	ϕ	300 kHz	120 Hz	2500	0.0004
velocity	water	η	1500 m/s	1500 m/s	1	1
	model		2540 m/s	2540 m/s	1	1

computer-controlled lathe for more precise measurements (e.g. for the egg-shaped model, §4.2.1). Although the resin-water interface does not generate the same reflection coefficients expected from common crystalline rock - mineral deposit interfaces, the response is similar, and this system is suitable for its investigation. The resin was cured in cores 2.5 cm wide, which were cut into pieces of various lengths and weighed. The volume of each piece was determined by submerging it in water and recording the displaced volume in a graduated

glass container. The P-wave transit time through the cores was measured using the pulse transmission method described in Birch (1960a) and Harvey (1997), but no pressure jacket was used because the resin is not porous. In this method, a pressure pulse is passed through the sample and its transit time measured on a CRO display. The observations for density and P-wave transit time are plotted in Figure 4.2-1. The density and P-wave velocity of the resin were estimated from the slopes of the graphs and calculated more accurately using linear regression. They are, respectively, 1.20 ± 0.01 g/cm^3 and 2.55 ± 0.04 mm/μs (2550 ± 40 m/s).

Figure 4.2-2 shows the model data acquisition flow chart, which comprises the source and receiver, signal source, amplifier, and the recording unit. The source and receiver are lead zirconate titanate (PZT) P-wave piezo-electric transducers with a resonant frequency of 300 kHz. The source transducer was driven by an impulsive source wavelet with a bandwidth of 80-500 kHz (i.e. 2.3 octaves). The transducers were mounted on electronic motors programmed to move vertically and horizontally independent of one another, to allow the recording of normal incidence and offset 3D shot gathers. The models were submerged in the centre of the water tank and tied down to prevent shaking due to the turbulence caused by the movement of the transducers.

Data acquisition proceeded by moving the receiver one group interval at a time, while the source was fired at the same location until the receiver line was completed. This procedure was repeated for each receiver line, after which the source was moved to a new location on the shot line and the sequence repeated. In this way, shot gathers were recorded whereby each trace was stacked four times vertically to increase the S/N ratio. The data were

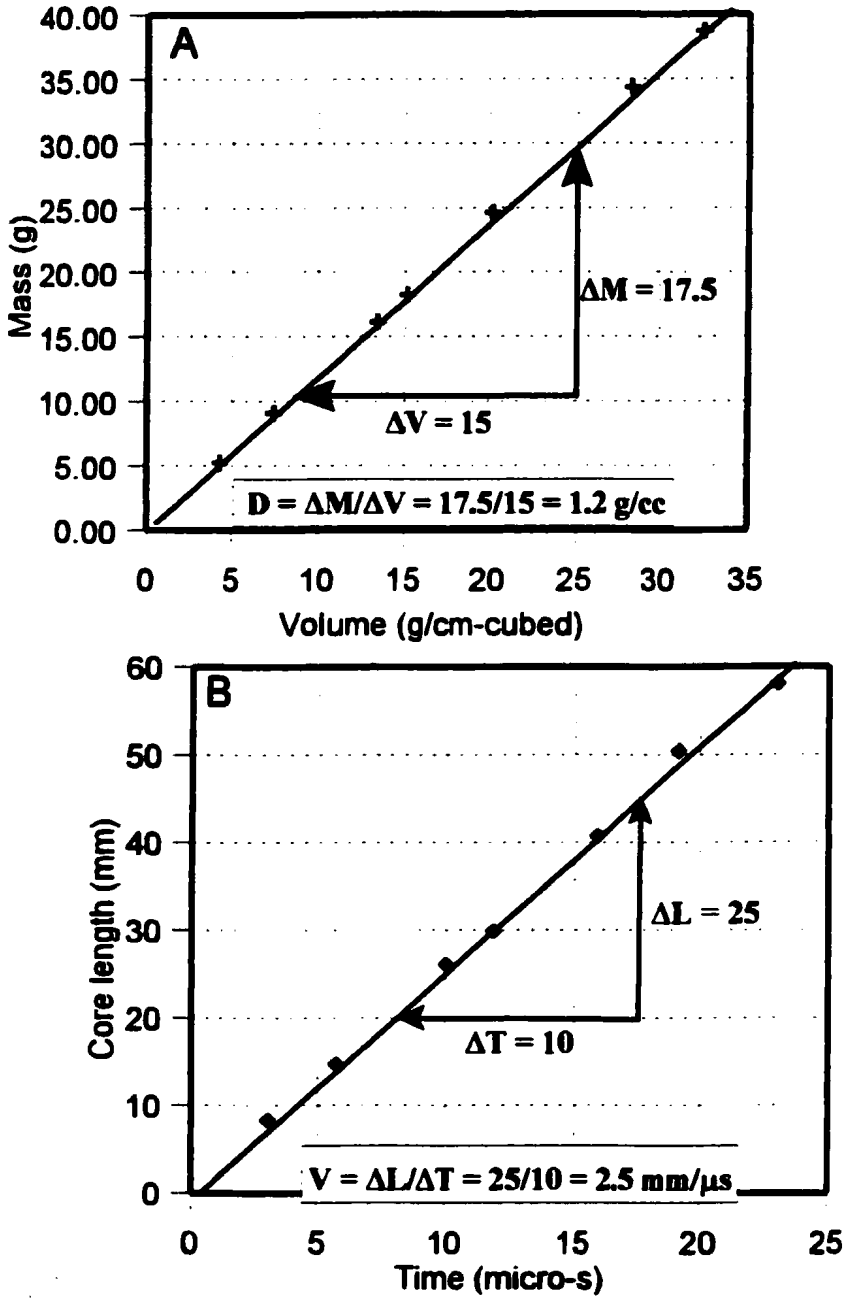

Figure 4.2-1: Experimental observations for the determination of the density and P-wave velocity of the epoxy resin, (A) density, and (B), P-wave velocity. The average values for these quantities are calculated from the slopes of the graphs and are therein indicated.

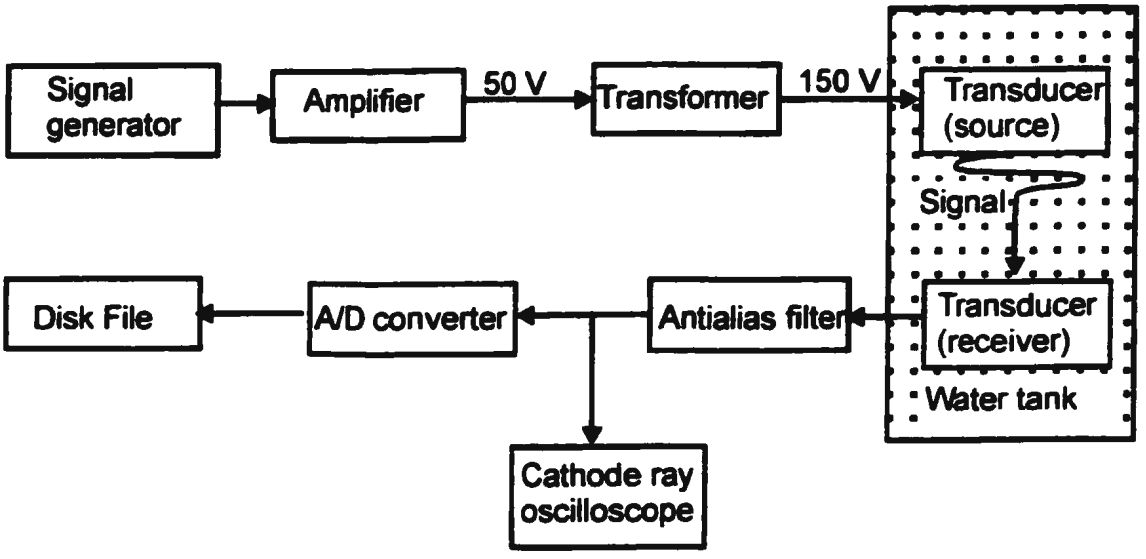

Figure 4.2-2: Flow chart showing the setup for the physical model data acquisition. The antialias filter was used only for the disk-shaped model.

sampled temporally and spatially according to the Nyquist sampling criteria using non-scaled model dimensions. A normal incidence profile was recorded on a flat model with a milled surface at the beginning and the end of every experiment to monitor the spectral consistency of the source. The data were recorded in binary format and later converted to the industry standard SEG-Y format.

4.2.1 Egg-shaped model

The egg-shaped model is used to investigate the effect of a strongly curved surface on the seismic response. It is 120.0 mm long and 65.0 mm wide, and has a smooth surface. Using a scale factor of 2500 (Table 4.2-1), this model represents a mineral deposit 300 m long and 162.5 m wide (Figures 4.2.1-1 and 4.2.1-2). Ni-Cu deposits of a similar size occur in the Sudbury mining district, e.g. Frood-Stobie (ON) (Figure 3.3-1). The egg-shaped model was placed in the radii for a scaled background velocity of 1500 m/s and a scaled dominant frequency of 120 Hz (see eq. (6)).[9] The seismic response caused by this model consists of diffractions parallel to both the short and long axes because of the continuous surface curvature. For an ellipsoidal shape, the mass of the simulated deposit, m, is given by;

$$m = V\rho = \tfrac{4}{3}\pi abc\rho \qquad (13)$$

where V is the volume, ρ is the density, a and c are the semi-minor axes, and b is the semi-major axis of the ellipsoid. Based on densities of the typical mineral deposits shown in Figures 2.2-1 and 2.2-2, the egg-shaped model represents either a 16 Mt Zn-Pb-Cu deposit (ρ_{av} = 3900 kg/m^3) or a 19 Mt Ni-Cu deposit (ρ_{av} = 4480 kg/m^3). Such mineral deposits are small at the depths of interest in seismic exploration for mineral deposits ($\geq$600 m).

---

[9] The first Fresnel zone is discussed in Chapter 2. It defines the minimum size of a target that can produce specular reflections. Smaller targets produce only diffractions.

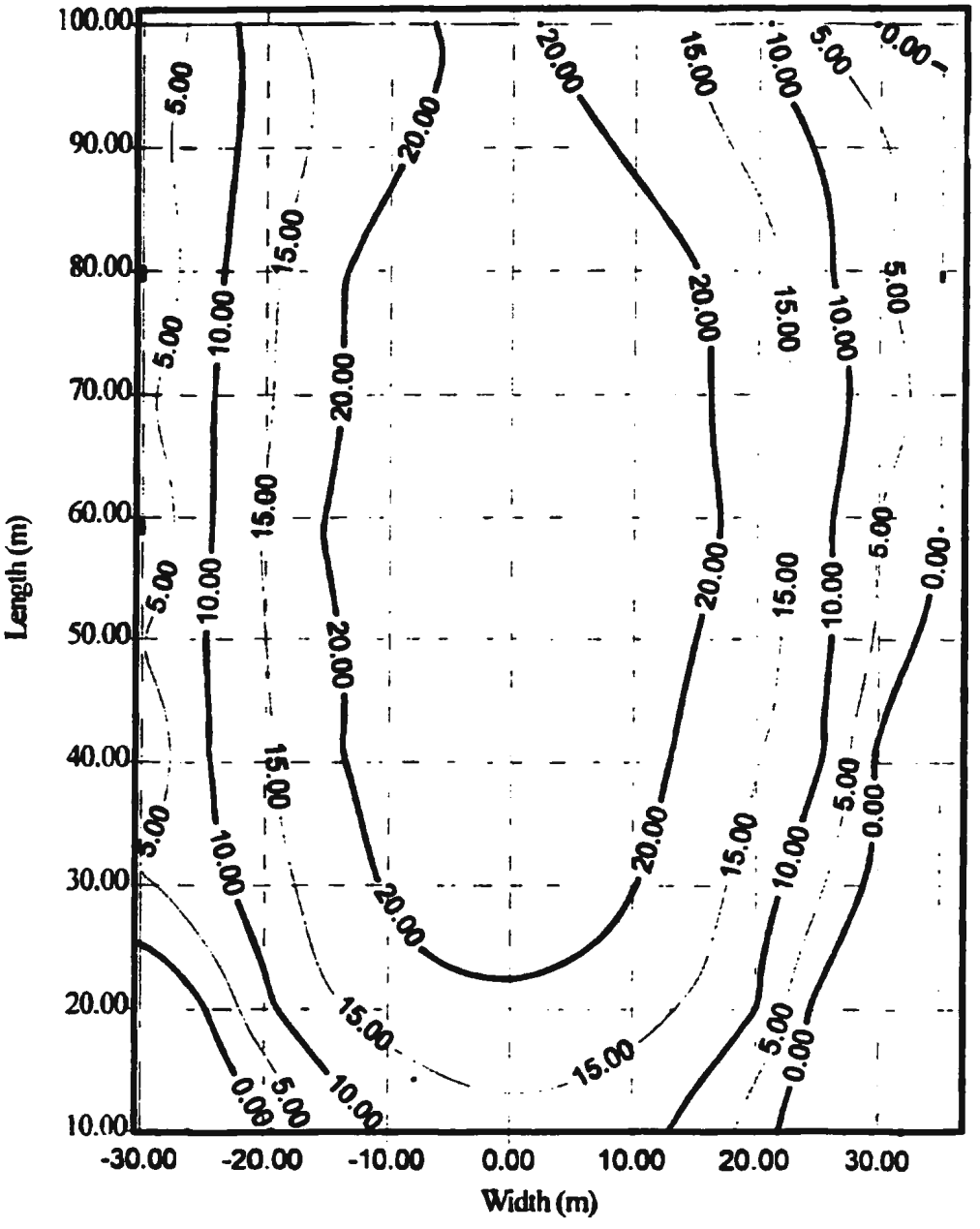

Figure 4.2.1-1: Contour map of the upper half of the egg-shaped physical model. The lower half is not shown since the model is almost symmetrical. The scale factor is 2500, and the contour interval is 5 m..

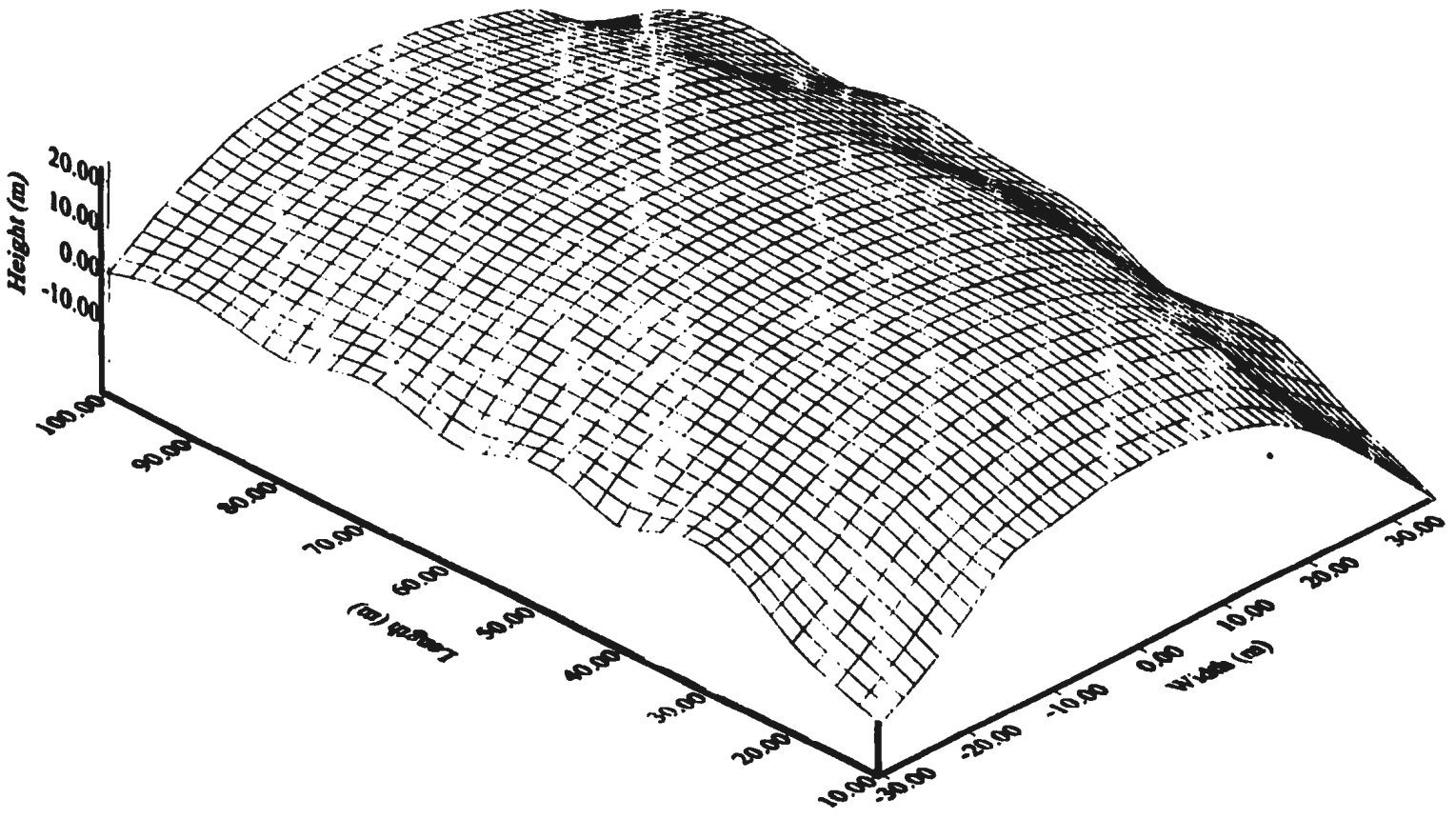

Figure 4.2.1-2: Isometric projection of the upper half of the egg-shaped physical model. The scale factor is 2500.

The convex surface of the model is problematic to detect or image with reflection seismic because it causes seismic energy to be deflected at wide angles from the source (Adam et al., 1998). The extent of this scattering is controlled by the ellipsoidal flattening of the lens which ranges from 0 for a spherical body to 1 for a flat lens. Eaton (1999) has shown from modelling that small spherical bodies produce no back-scattered energy in the normal incidence aperture, suggesting that small spherical mineral deposits may not be detected with conventional surface reflection seismic profiling. The egg-shaped model has an ellipsoidal flattening of ½, and is expected to produce back-scattered energy of detectable strength in the acquisition aperture possible with the available laboratory equipment.

The second effect of the curved surface is that seismic waves are refracted toward the normal at the model/water interface, and they are also focused by the curvature of the surface of the model. The combined effect of refraction and the convex surface focuses the waves to converge inside the model at a distance governed by (Sheriff and Geldart, 1995);

$$\frac{1}{d_1} + \frac{1}{d_2} = \frac{2}{r} \tag{14}$$

where d_1 is the distance of the source from the model, d_2 is the distance of the focal point from the surface of the model, and r is the radius of the model. Since the model has a circular cross-section of a small radius (32.50 mm), seismic events caused by this focusing mechanism should be visible in the stack sections. The longitudinal section through the egg-

shaped model has a low curvature and cannot generate strong seismic events by the optical phenomenon described above. Buried focus seismic events are commonly produced by synclines (concave lenses) whereby they occur above the depth of the structure causing them.

4.2.1.1 Data Acquisition

The data acquisition grid for the egg-shaped model is shown in Figure 4.2.1-3(A). Figure 4.2.1-3(B) is a 2D seismic line extracted from the 3D data. The data were acquired in a rectangular grid composed of parallel receiver lines 900 m long and 18.75 m apart.[10] The receiver lines were positioned such that they extend one target length (300 m) on either side of the target, and each line recorded 180 receivers at 5 m intervals. Seven shot lines normal to the receiver lines and 42.86 m apart with an 18.75 m interval were recorded. The shot points were positioned such that the grid covered the target evenly over its entire length. The data were recorded in two templates with four receiver lines per shot to achieve a fold of 56. The total record length is 1,500 ms scaled TWT, and the data are sampled temporally at a scaled interval of ½ ms.

The acquisition geometry shown in Figure 4.2.1-3(A) achieved a maximum source

---

[10]Scaled dimensions are used henceforth for all discussions of the seismic data. The scale factors for length and time are both 2500, as shown in Table 4.2-1.

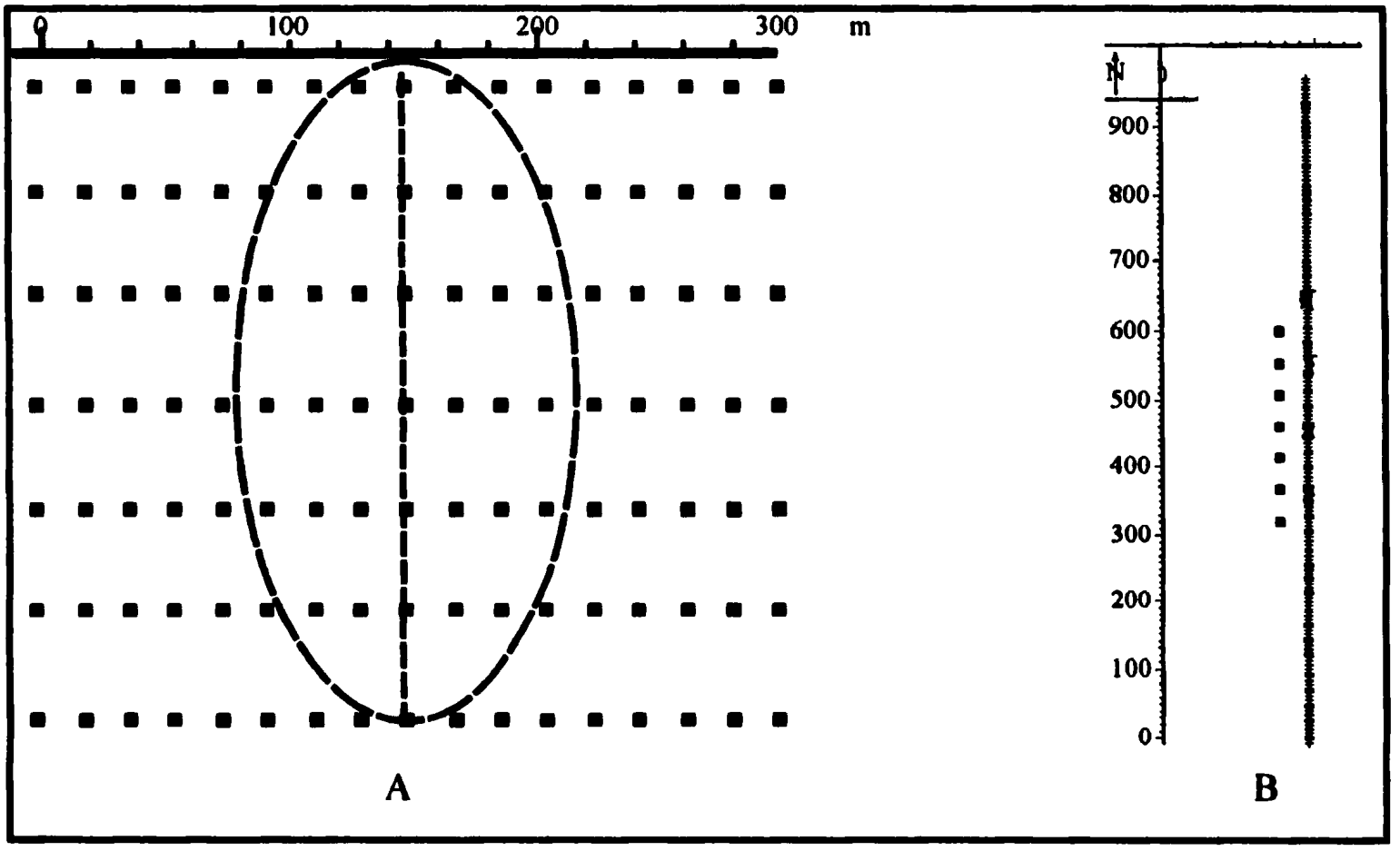

Figure 4.2.1-3: Data acquisition grid used for the egg-shaped model. Only the shot locations are shown (squares) and an outline of the model is overlain (dotted ellipse) (A). (B) is a 2D line extracted from the 3D grid at the location shown with the dotted line. Note that the source and receiver lines do not coincide in the 2D line.

to receiver offset of 650 m (i.e. a source to receiver aperture of ~39°), with a distribution of source-receiver azimuths biassed slightly parallel to the receiver lines as shown in the rose diagram in Figure 4.2.1-4(A). The bias in the source-receiver azimuth distribution is, however, not severe on the stacking results. The fold is low at the centre of the grid because the source and the receiver cannot be closer together than 10 mm, the diameter of the transducers. Data acquisition was sustained for six days at a rate of 860 traces/hour. Overall, 85,680 traces were recorded over the egg-shaped model with a good S/N ratio and a bandwidth of 2.3 octaves (Figure 4.2.1-4(B)).

4.2.1.2 Data Processing

The data were processed using the CMP-based sequence detailed in Table 4.2.1-1 to prepare them for interpretation using in-line stacks and time slices. Time slices enable identification of subtle structural trends and the construction of time structure maps directly from the seismic data. This is a critical asset of 3D data in areas where the structure is little known. Time slices are, however, limited in mapping detailed structure on the surface of a small target which truncates horizontal time planes rapidly. CMP-based processing was used so that problems in optimally detecting or imaging the model could be identified. Pre-processing involved examination of the signal quality and to edit bad traces, after which

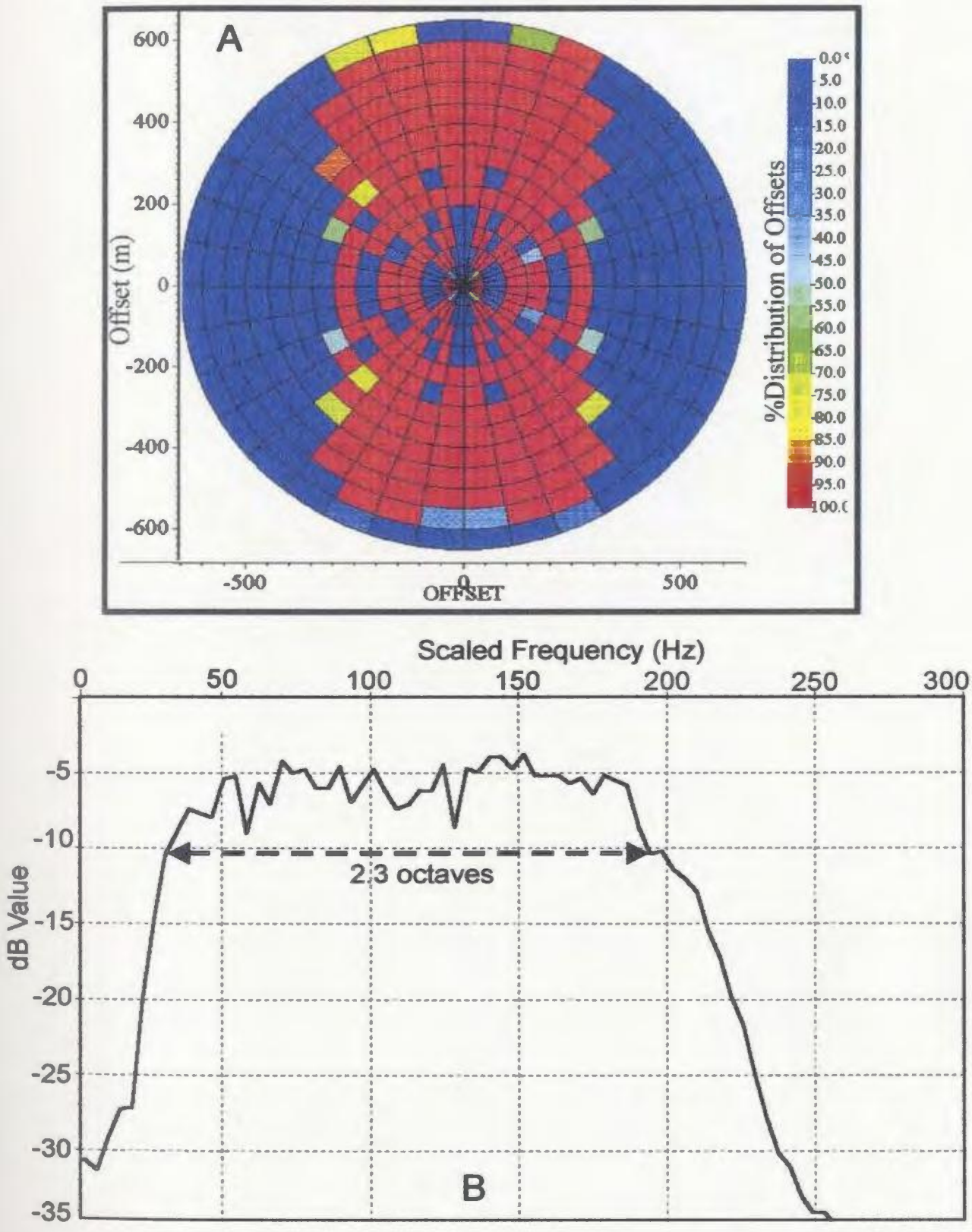

Figure 4.2.1-4: (A) Rose diagram showing the azimuthal distribution of source-receiver offsets. (B) Amplitude spectrum of the data for the egg-shaped model after spiking deconvolution.

Table 4.2.1-1: Data processing parameters

trace edit	trace kills, add trace headers
geometry	CMP binning (2.3 x 18.75 m, for the egg-shaped model)
gain	spherical divergence correction (1500 m/s for 0-1500 ms), exponential power gain (2.00), exponential time power gain (1.00)
filtering	spiking deconvolution (60 ms, 1000 ms time gate), front-end muting
velocity analysis	semblance
stack	CMP stacking, 20% stretch mute
mute	surgical mute to remove top and bottom of tank reflections
migration	2 pass 2D F-K time migration post-stack (first pass; sort data by in-line, second pass; sort data by cross-line)
display	in-line stacks and time slices

geometry was attached to the trace headers. The data were corrected for amplitude decay using a constant velocity spherical divergence function, an exponential gain function, and focused temporally with spiking deconvolution which also reduced the source-generated

ringiness. Velocity analysis was performed for 2D and 3D stacking velocity functions on semblance and common-offset stacks. The 2D velocity function was used for a two pass 2D migration to effect a full 3D migration. All migration was performed with the F-K technique, and only time migration was used.

4.2.1.3 Results and Observations

Figure 4.2.1-5(A) shows an in-line stack of the data before migration in which the top of the egg-shaped model is mapped by an amplitude trough at 1060 ms scaled TWT and the bottom by an amplitude peak at 1180 ms scaled TWT. The scaled two-way time difference between the top and bottom of the model is 120 ms, showing that the P-wave velocity of the model is 2500 m/s. This value confirms the P-wave velocity of 2550 m/s determined using the pulse transmission method (§4.2). The migrated stack (Figure 4.2.1-5(B)) shows an improved S/N ratio and focused diffractions caused by the top and bottom of the model. The diffractions are collapsed to the edge of the target, which is ~300 m long (scaled). This level of success with migration is possible because the data have a good S/N ratio, and the model has a simple geometry.

Coherent seismic events are visible in the stack between the events caused by the top and bottom of the model in Figure 4.2.1-5. The first of these events is an amplitude trough at 1090 ms scaled TWT. Substitution of d_1 and r into eq. (14) shows that the focal point is ~43 m (scaled) below the surface of the model. The focused event recurs at 1125 ms scaled

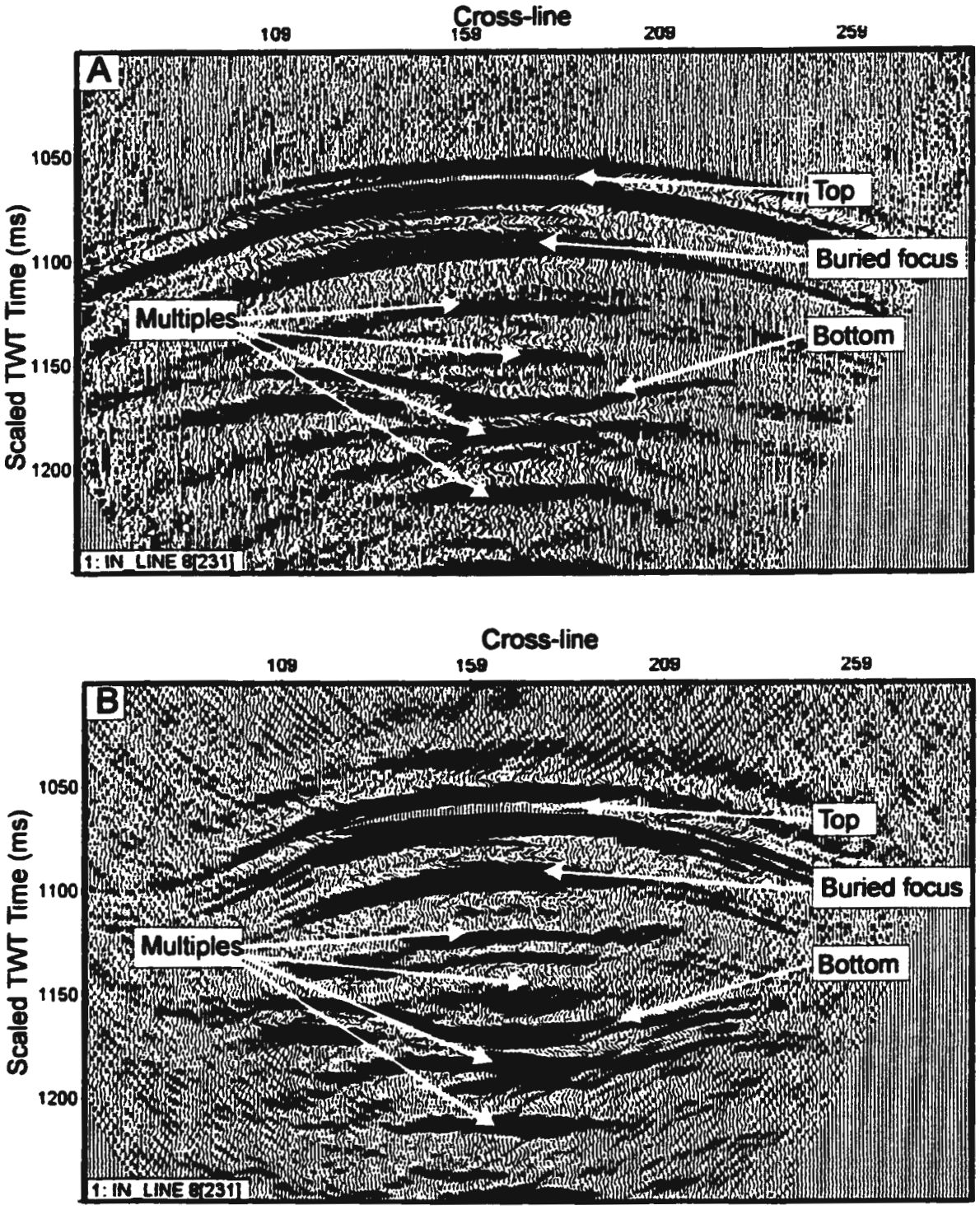

Figure 4.2.1-5: In-line stacks through the egg-shaped model before (A), and after (B) 3D post-stack migration. Notice the strong event below the model surface. This event and its multiples can complicate the seismic response of small targets.

TWT as a multiple reflection caused by the top of the model. The amplitudes of the focused event and its multiple are stronger in the migrated than the un-migrated stack. These events cause ambiguity in the interpretation of the stacks, and would cause even more difficulty in field data where the S/N ratio is lower.

Figure 4.2.1-6(A-D) shows time slices through the 3D data before migration. It is difficult to distinguish between primary and multiple reflection events in the time slices, but it is the overall diffraction response pattern which is of interest. The alternating peak and trough amplitude patterns in Figure 4.2.1-6(A-D) define elliptical time contours around the model. These time contours are plotted for the consecutive time slices to construct the time structure map shown in Figure 4.2.1-6(E). Clearly, the time slices show that the target is accurately mapped by the diffraction pattern.

Time slices for the migrated stack (Figure 4.2.1-7) show an improved S/N ratio compared with those shown in Figure 4.2.1-6 and the events are focused moderately well by 3D migration. The diffraction amplitude patterns on the migrated time slices show elliptical time contours arranged around the model as in the un-migrated stack, but more closely focused. These elliptical diffraction patterns do not indicate the shape of the causative body (which is also elliptical in this case) since diffractions are produced at discreet points on the model. The centre of the closed elliptical diffraction pattern coincides with the location of the model. It is apparent from these figures that time slices are an effective way of identifying the seismic response caused by small targets in 3D seismic data.

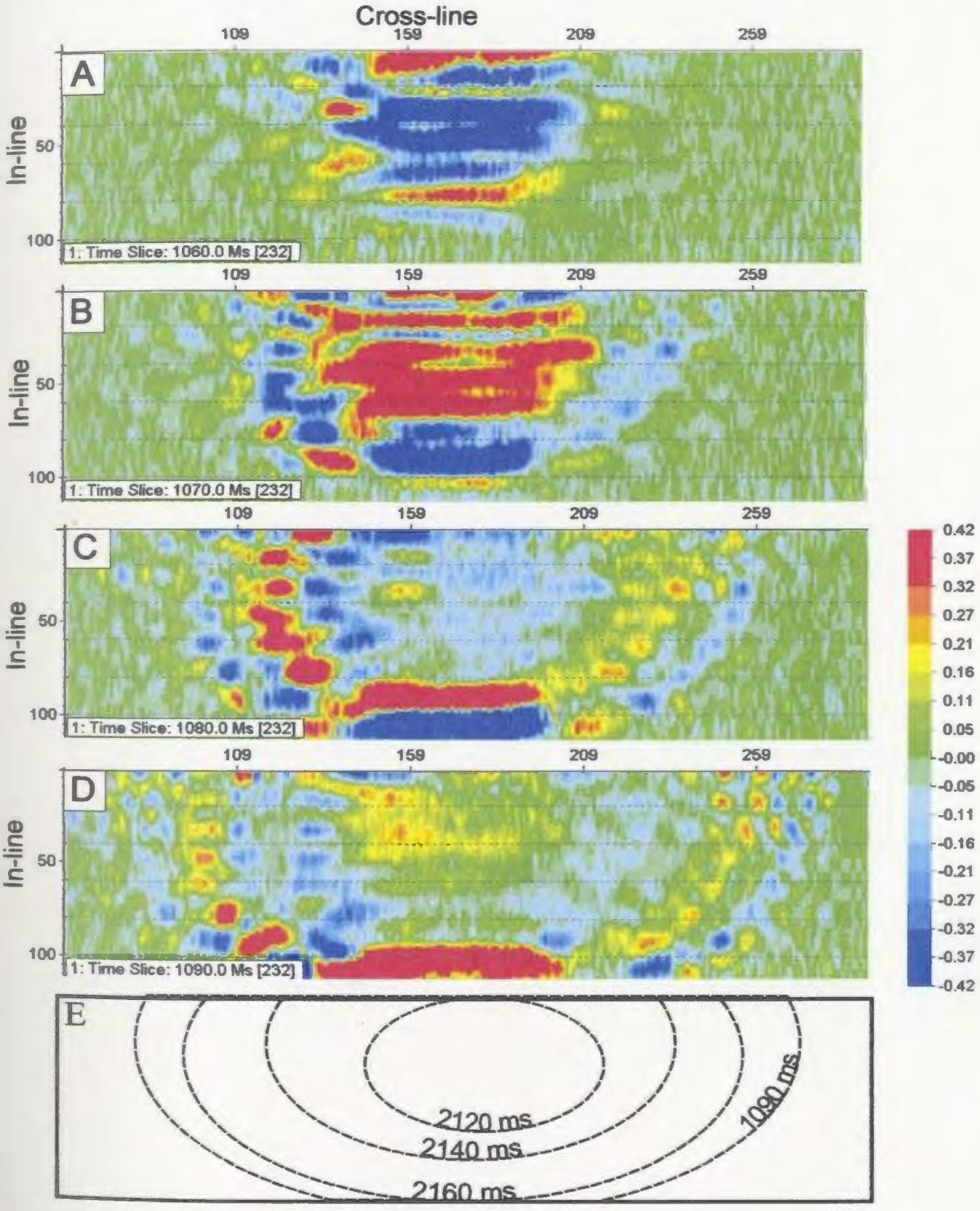

Figure 4.2.1-6: Un-migrated time slices through the egg-shaped physical model. E is a time structure map constructed from the time slices.

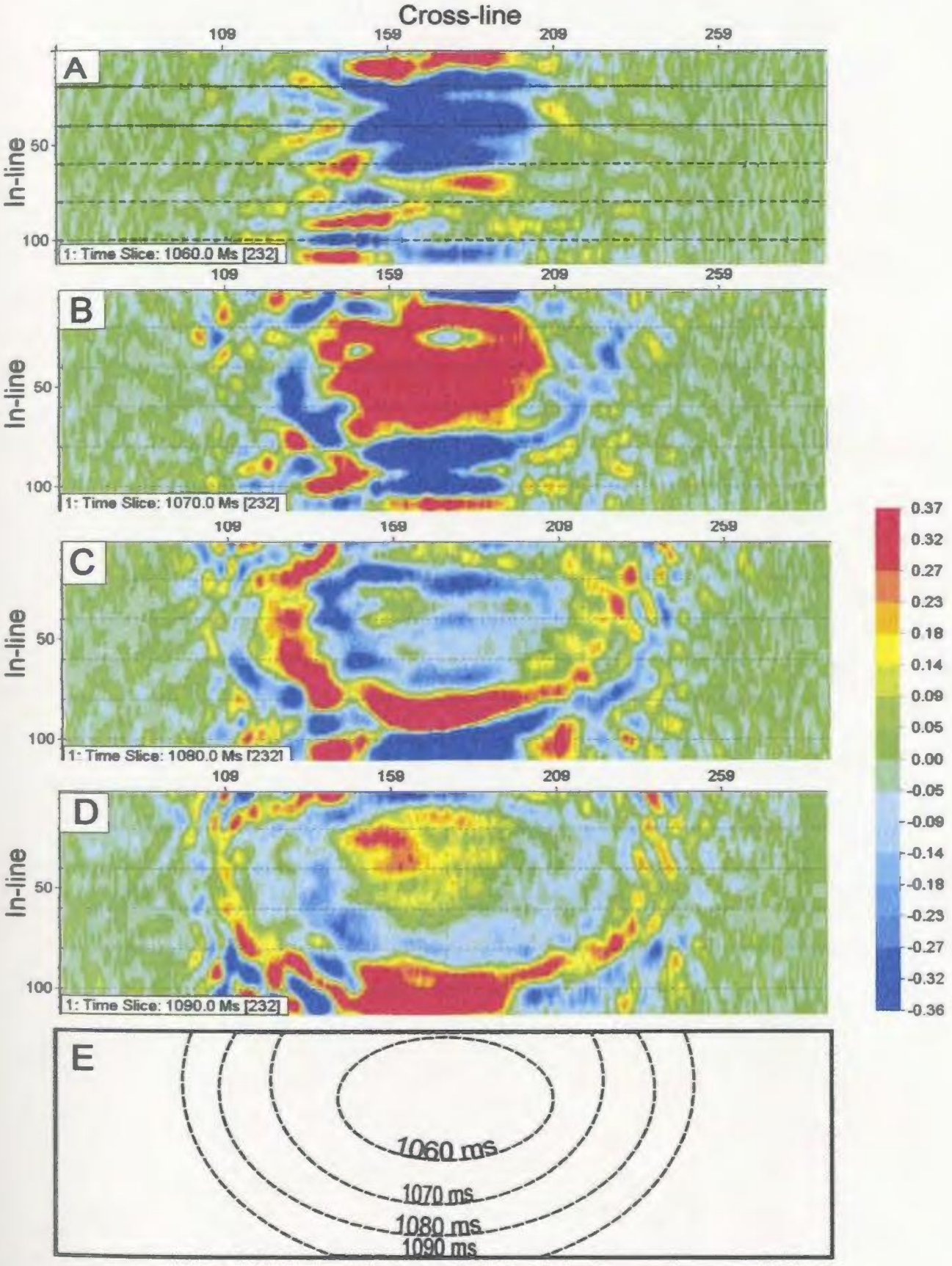

Figure 4.2.1-7: Time slices of the migrated data for the egg-shaped model. The time structure map (E) shows that the diffractions are focused successfully by 3D migration.

4.2.1.4 Discussion and Conclusions

The egg-shaped model is accurately imaged at a scaled depth of 795 m. This success occurred because: (i) the data have a good S/N ratio, and (ii) the model exceeds the radius of the first Fresnel zone, and has a simple geometry with a smooth surface. Time slices of the un-migrated and migrated data show elliptical diffraction patterns centred on the model. These time slices suggest that for field data, it may be easier to identify the seismic response of small and complex targets on time slices by their closed, circular diffraction patterns. Although the diffraction patterns are focused by migration to coincide with the location of the object, the latter may perform poorly in field data because of ambient noise, and hence may not enhance the detection or imaging significantly.

The smooth, convex surface of the egg-shaped model produces buried focus events which lead to ambiguity in the interpretation of the data. Clearly, this shows that even mineral deposits of a simple geometry such as undeformed Cu-Zn deposits can produce complex seismic responses if they have sharp contacts with the host rock. Internal multiple reflections are more likely in these deposits because of their very large acoustic impedance contrasts against the host rocks.

4.2.2 Cylinder-shaped model

The cylinder-shaped model is used to investigate the effect that a rugged surface relief on a strongly curved surface has on the seismic response. The rugged relief is expected to produce a complicated seismic response because the kinks on the surface of the model act as discrete sources of diffractions whose interference make it difficult to identify the seismic response of the target. The objective of introducing complexity on the model surface is to determine if it can be detected, or even imaged, with reflection seismic and to draw conclusions as to whether the seismic signature caused by similar targets can be identified in field data.

The cylinder-shaped model is 105 mm long with a variable width of 20 to 40 mm. For a scale factor of 2500 (see Table 4.2.1-1), it represents a geometrically complex deposit 262.5 m long and 50-100 m wide, with a surface relief of 5-40 m and a rugged surface with depressions of the same order of magnitude as the dominant wavelength (~18 m). Highly deformed deposits of this type are important in seismic exploration because they represent difficult cases for detection and/or imaging. The model is nearly three times as long as it is wide, and hence represents mineral deposits with an aspect ratio of 3:1. Mineral deposits of similar aspect ratio such as Ni-Cu and VMS deposits occur in crystalline environments, as shown in Chapter 3. The model scales to a deposit of 6-8 Mt with a density of 3900-4880 kg/m^3. While mineral deposits this size are considered small at depths $\geq$600 m, it is important to establish a minimum target size at which the reflection seismic method is no longer useful for the detection or imaging of small and complicated targets. Despite the

strong surface curvature, the model is not expected to generate strong buried focus events because of the chaotic nature of the surface relief.

Figure 4.2.2-1 shows contour maps of the top and bottom of the model and Figure 4.2.2-2 shows isometric projections of these surfaces intended to give a clear picture of the ruggedness of the model. The relief on the top of the model differs from that on the bottom (Figure 4.2.2-2), and as such represents a strong test for the capability of the reflection seismic method to detect or image small and complicated targets. It can be seen in Figures 4.2.2-1 and 4.2.2-2 that the relief is rugged everywhere on the surface of the model, except for the area marked X in Figure 4.2.2-1, where it is smooth on both sides. This area is used as a reference to identify events in the seismic sections. The area marked L in Figure 4.2.2-1 is smooth on the bottom but rough on the top of the model.

4.2.2.1 Data Acquisition

Figure 4.2.2-3(A) shows the data acquisition grid for the cylinder-shaped model, and Figure 4.2.2-3(B) shows the geometry of a 2D seismic line extracted from the 3D data. The 2D seismic data were processed using CMP-based and aplanatic prestack depth migration techniques. Data were recorded over the cylinder-shaped model in two experiments; in the first experiment the model was horizontal with its long axis parallel to the receiver lines, while in the second experiment it was dipping at 35° and oriented with its long axis parallel to the receiver lines.

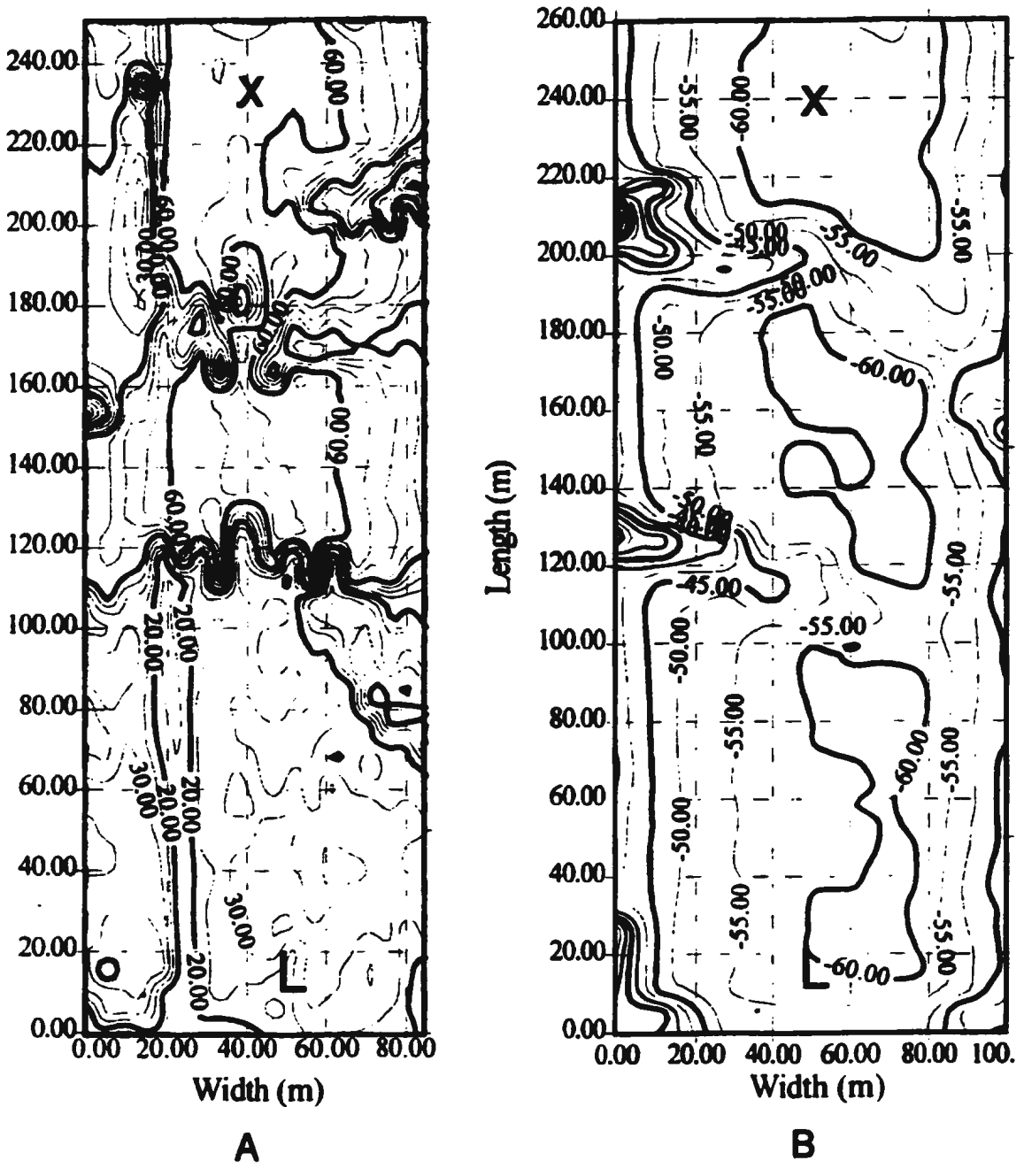

Figure 4.2.2-1: Contour maps of the cylinder-shaped model drawn with reference to a horizontal plane through the middle. (A) shows the upper half and, (B), the lower half. The scale factor is 2500.

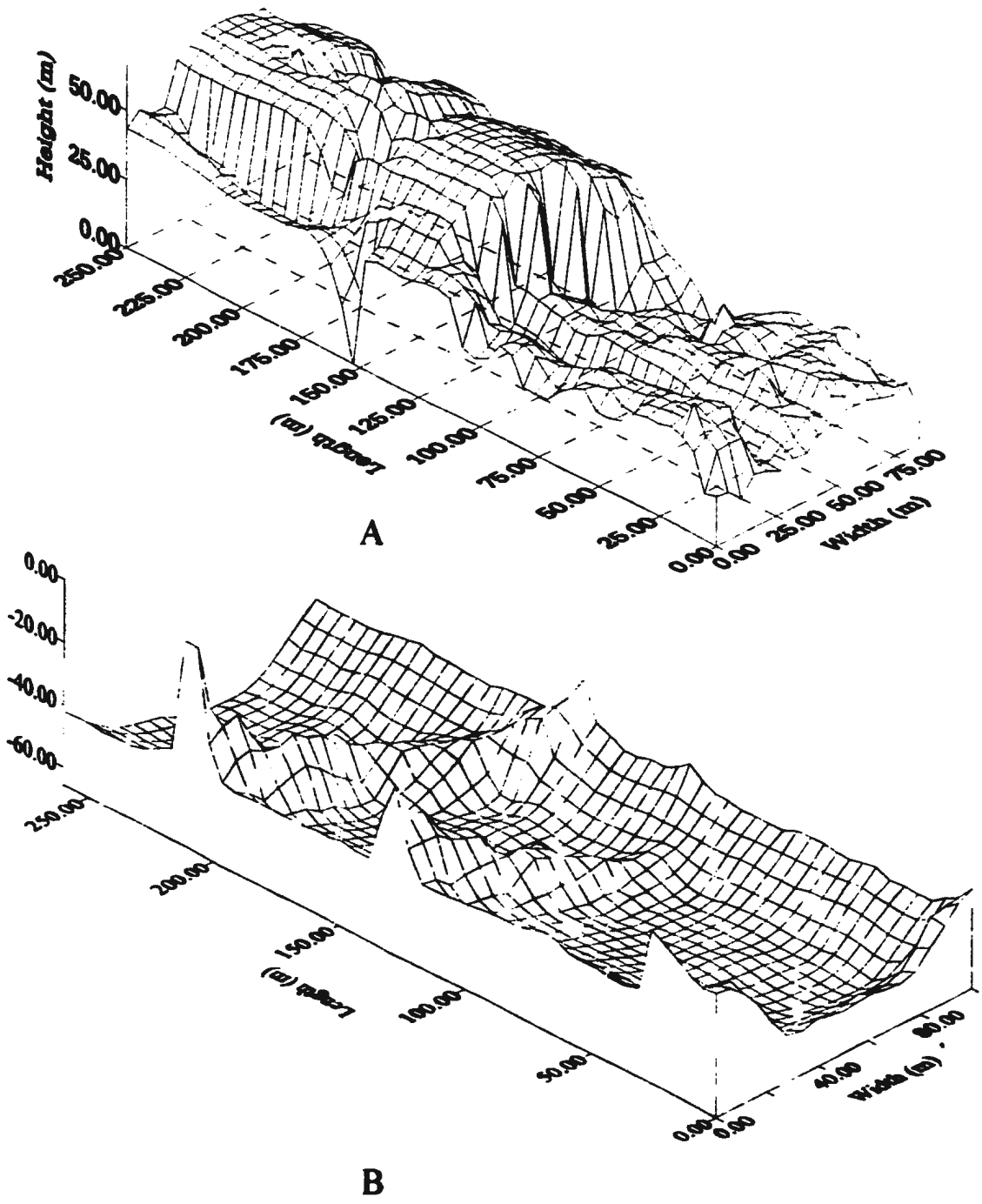

Figure 4.2.2-2: Isometric projections of the upper surface (A), and the lower surface (B), of the cylinder-shaped model. The lower surface, (B), is plotted as seen from above the model, i.e. a negative impression. The scale factor is 2500.

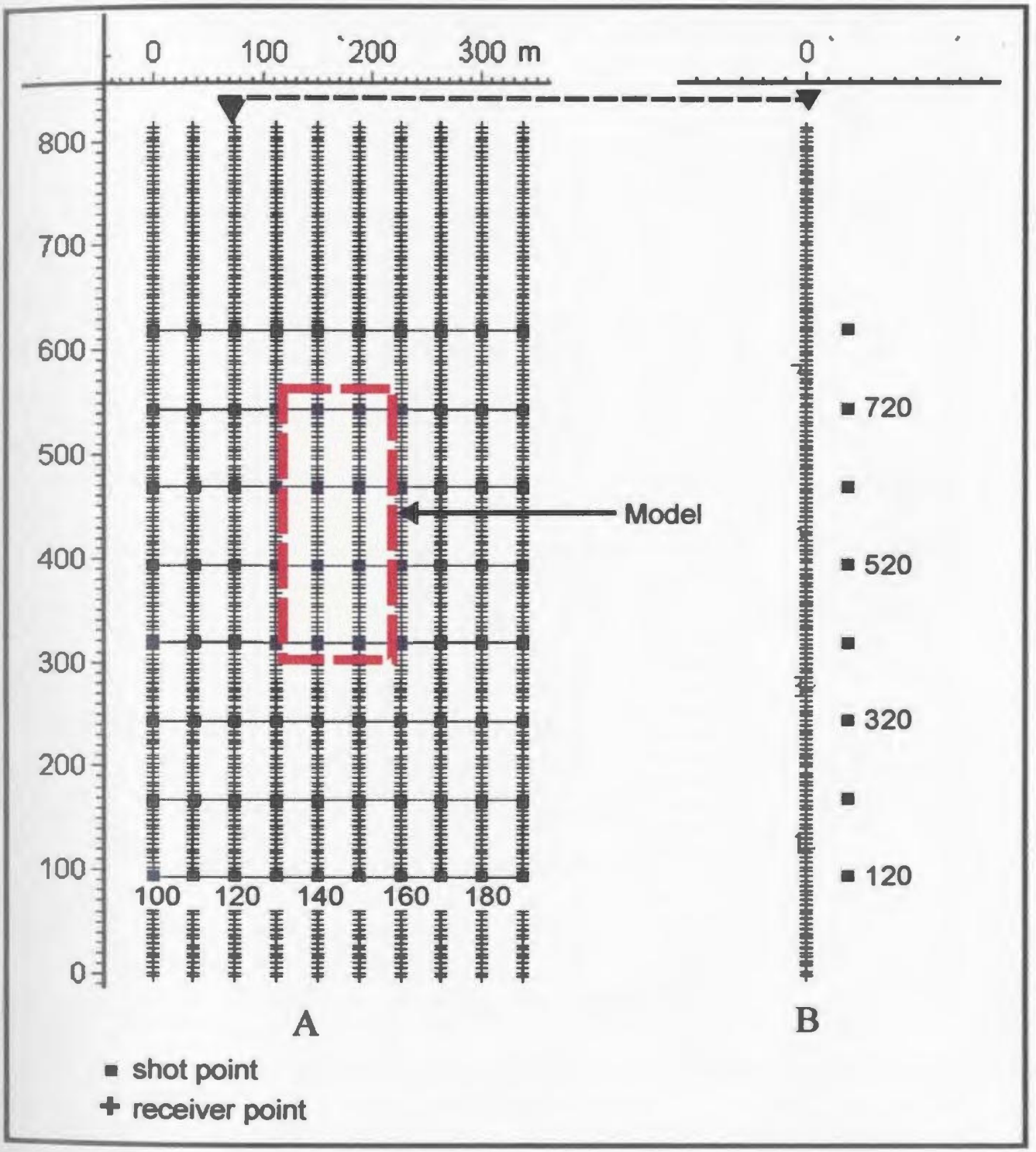

Figure 4.2.2-3: Data acquisition grid for the cylinder-shaped model (A), and (B) is a 2D seismic line extracted from the 3D data acquisition grid. An outline of the model is overlain on the acquisition plan to help in the interpretation of seismic sections.

The data were recorded on a rectangular grid consisting of 10 parallel receiver lines 814 m long and 37.5 m apart. Each receiver line consisted of 180 receivers at 4.55 m intervals. Eight shot lines perpendicular to the receiver lines, and 74.5 m apart, were recorded with a shot point interval of 74.5 m (Figure 4.2.2-3). The data were recorded in two templates of five shots recording five receiver lines each, overlapped by half the shot point interval. This procedure culminated with a final shot point interval of 37.5 m. The data acquisition geometry shown in Figure 4.2.2-3 recorded a maximum source to receiver offset of 804 m (i.e. a source to receiver aperture of ~47°), with an even distribution of source to receiver azimuths and a fold of 90. The acquisition grid was shifted down-dip when recording over the dipping model in the second experiment in order to record the displaced diffraction response.

A total of 144,000 traces with a scaled sample interval of ½ ms was recorded to a total of 1,500 ms scaled TWT in the experiments described above. The first session recorded 72,000 traces with the top of the model at a scaled depth of 742 m. The second session also recorded 72,000 traces but with the top of the model at a scaled depth of 660 m and dipping at 35° in the in-line direction. At a scaled depth of 742 m, the model measures 3.2 by 1.2 first Fresnel zone radii. Nevertheless, it should produce a seismic response composed of diffractions along the long axis because of the ruggedness of the relief on its surface. The amplitude spectra for the data recorded in each of these experiments are shown in Figure 4.2.2-4. The S/N ratio shown by these amplitude spectra is low to moderate, and mimics that consistent with field data more faithfully. The low dominant frequency and reduced

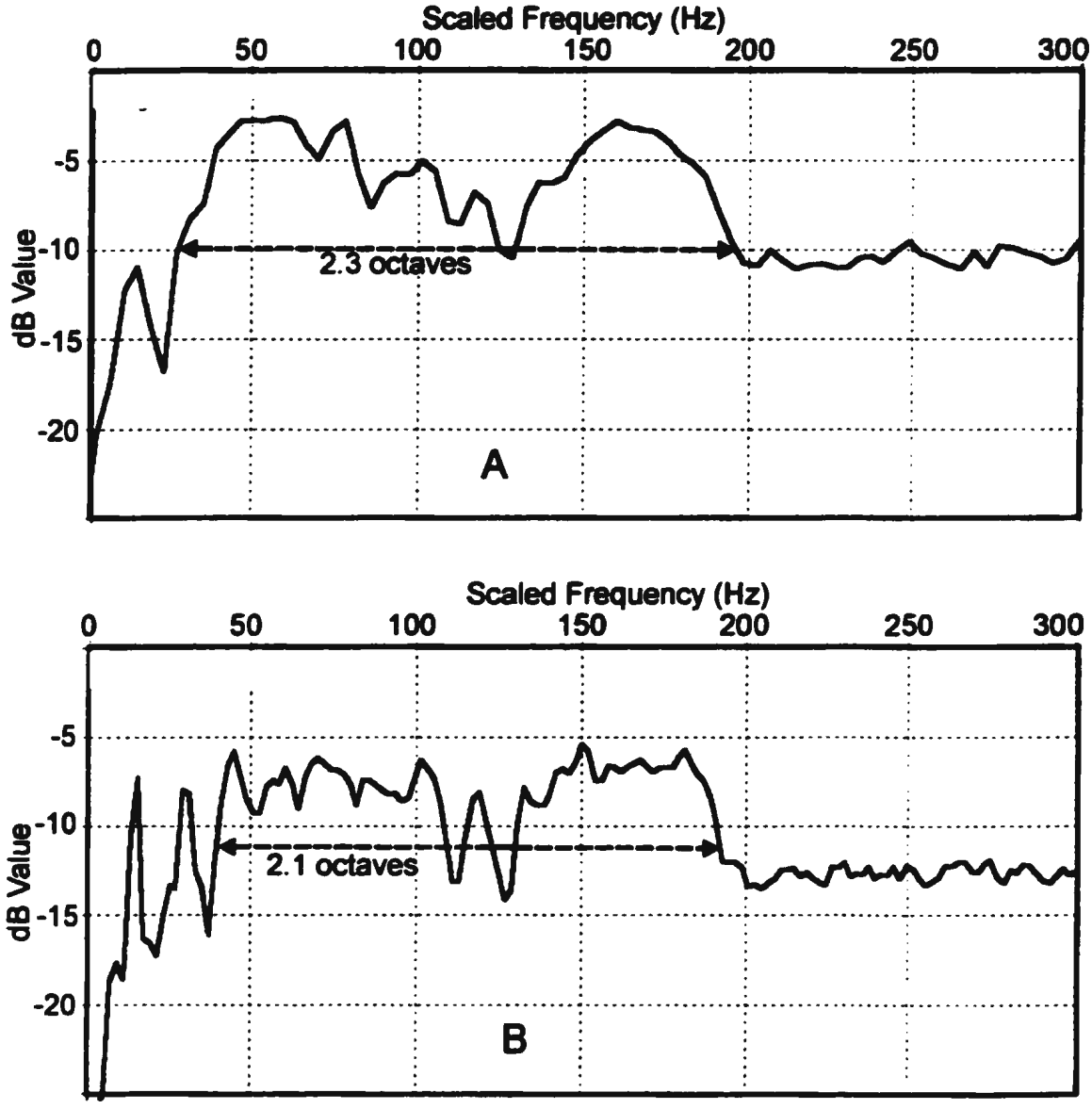

Figure 4.2.2-4: Amplitude spectra of the data for the horizontal cylinder-shaped model after deconvolution (A), and (B) the dipping cylinder-shaped model. The spectrum is strongly attenuated at 100-125 Hz because of the breakdown of the source transducer.

bandwidth are a result of mechanical deterioration of the source transducer.

4.2.2.2 Results and observations: *(i) Horizontal model*

Figure 4.2.2-5(A) shows an in-line stack of the data before migration in which a sub-horizontal event caused by the smooth area on the model (X in Figures 4.2.2-1(A) and 4.2.2-1(B)) is visible on the right hand side. The top of the model is mapped by an amplitude trough at 990 ms and the bottom by an amplitude peak at 1120 ms scaled TWT. The travel time difference between these two events shows that the model is 39.2 mm (98 m) thick. To the left of the sub-horizontal events the stack consists of coherent diffractions produced by the leading edge of the model and the structure on the top and lower surfaces. The maxima of the shallowest diffraction corresponds to the location of the leading edge of the model (L in Figure 4.2.2-1(A) and 4.2.2-1(B)), which cannot be identified with certainty in this stack because of event interference.

Figure 4.2.2-5(B) shows a post-stack 3D time migrated stack in which the sub-horizontal seismic events discussed above are visible on the right hand side. To the left of these events, the stack consists of partially contracted diffractions that are difficult to ascribe to identifiable features on the model. 3D migration did not fully collapse the diffractions in these data. However, this notwithstanding, the seismic response caused by the model is recognizable above the ambient noise. Besides the sub-horizontal seismic events on the right side of the stack, the other features of the model cannot be identified from the seismic events

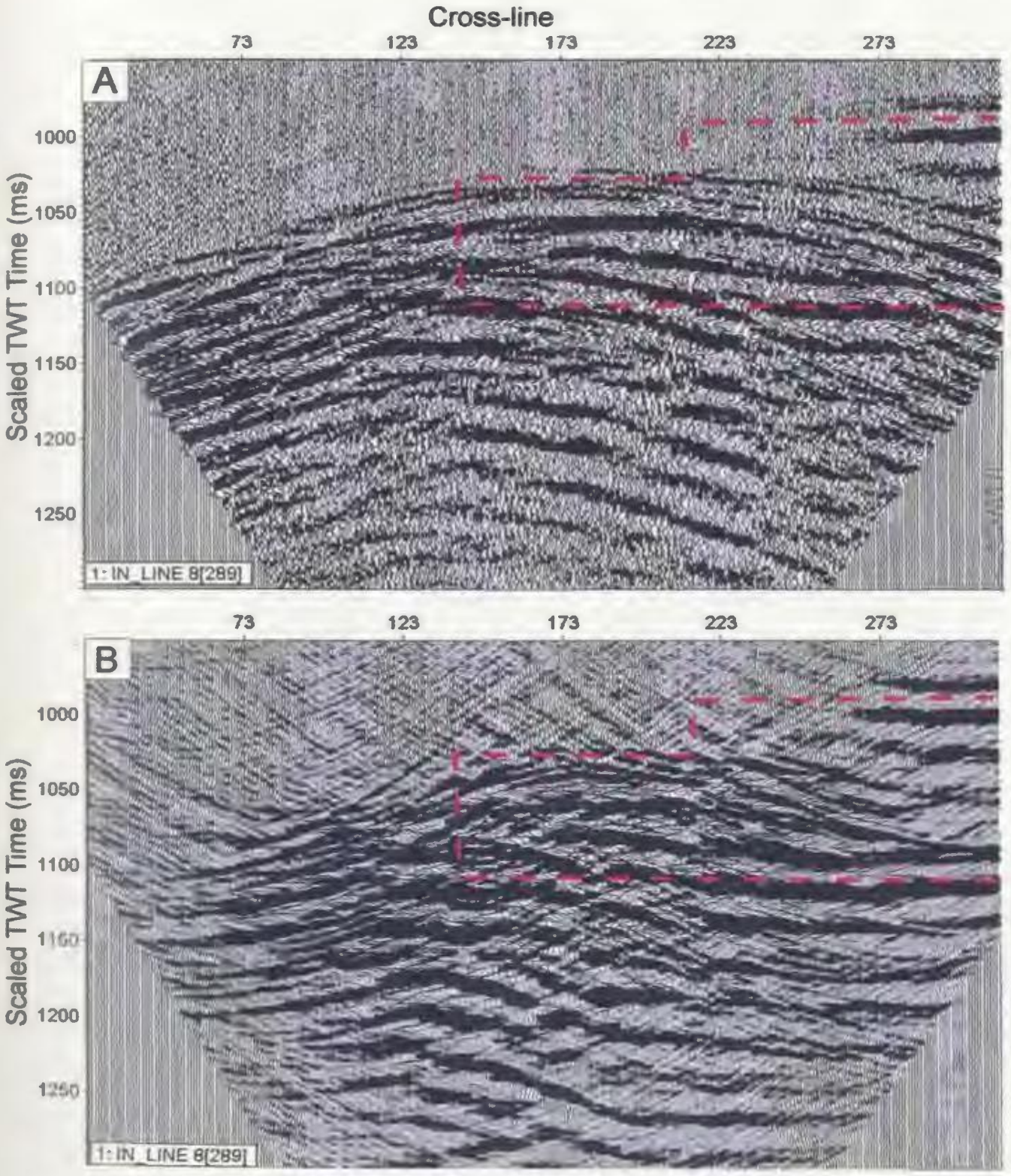

Figure 4.2.2-5: In-line stacks through the cylinder-shaped model before (A) and after (B) post-stack 3D F-K time migration. Note that the right side of the model is clearly mapped, but the migration has failed in the left hand side. An outline of the model is overlain to help in event identification.

with certainty in these in-line stacks.

Figure 4.2.2-6(A-D) shows time slices constructed from the data before migration. Figure 4.2.2-6(A) shows a moderate amplitude trough on the bottom right of the time slice at 990 ms scaled TWT. This amplitude anomaly corresponds to the smooth area on the surface of the model (X in Figure 4.2.2-1). In Figure 4.2.2-6(B), the diffraction pattern consists of a low amplitude trough which outlines a discontinuous, circular diffraction pattern around the entire model. The diffraction patterns in Figure 4.2.2-6(C) and (D) resemble that caused by a small elongated body. They consist of strong, concentric, alternating peak and trough amplitude anomalies, which, though not continuous, clearly show the location of the model. As such, they should enable easier identification of drill targets for similar small and complicated targets in time slices of un-migrated data.

The 3D migrated time slices corresponding to the ones described above are shown in Figure 4.2.2-7(A-D). The sub-horizontal seismic event on the right side of Figure 4.2.2-6 is mapped by an amplitude trough at 990 ms scaled TWT. The seismic response caused by the rest of the model shows in Figure 4.2.2-7(B) through (D) as a focused, high amplitude cluster of peaks and troughs with a poorly-defined trend. Besides the trough amplitude anomaly in Figure 4.2.2-7(A), which maps the smooth area on the surface of the model, the diffraction patterns in the deeper migrated time slices bear a poor resemblance to the elongated shape of the model. The seismic events in this figure cannot be ascribed to identifiable features on the model with confidence, even though it is clear that the diffractions have been focused well by migration. It is apparent that, had the migration fully

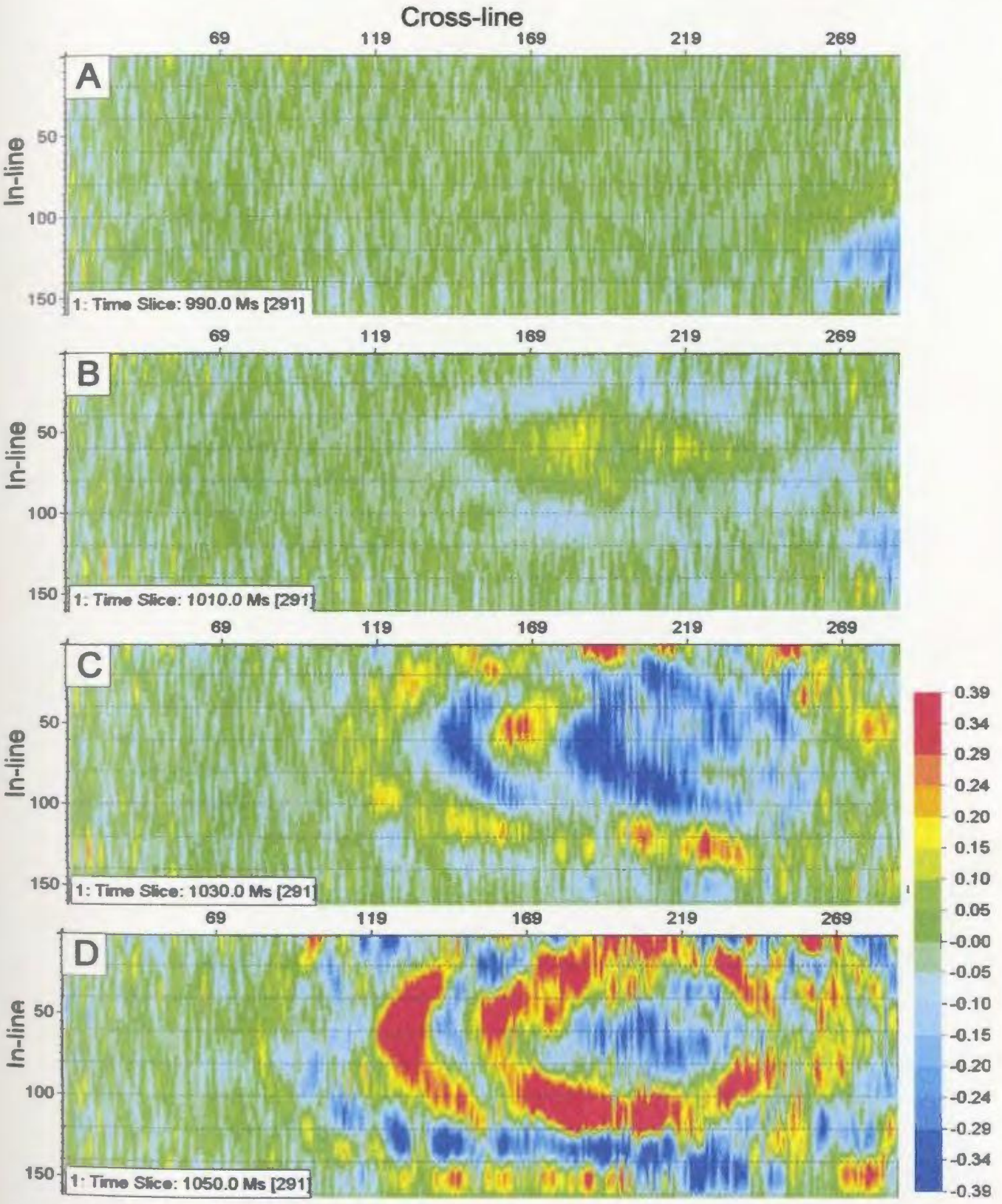

Figure 4.2.2-6: Time slices through the cylinder-shaped model before migration. Note that the diffraction patterns in C and D clearly outline the target, in contrast to the in-line stack shown in Figure 4.2.2-5.

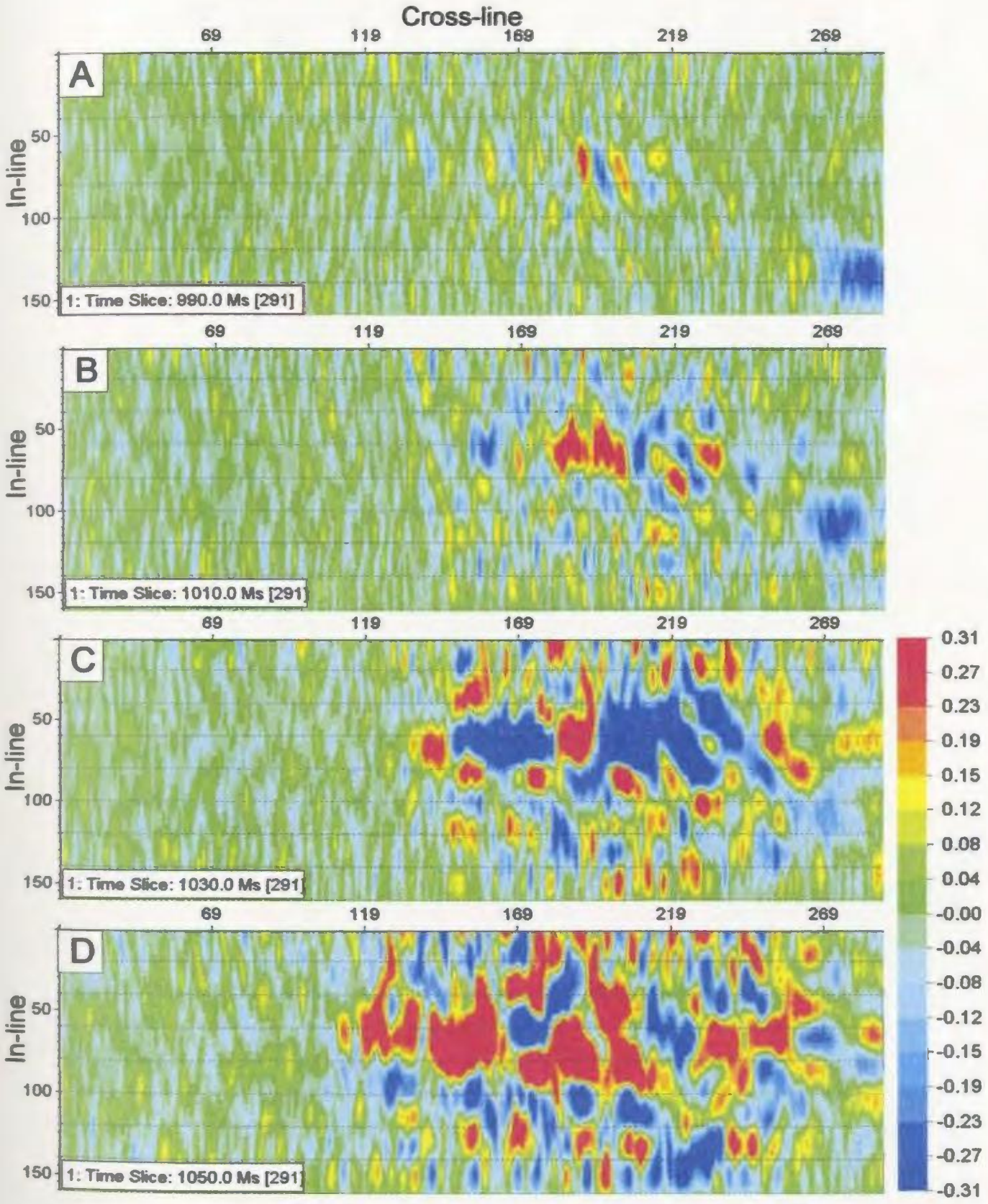

Figure 4.2.2-7: Times slices through the cylinder-shaped model after migration. Note that while the diffraction pattern is more localized, it is more discontinuous than it was before migration, and hence more difficult to recognize.

collapsed the diffractions to their discreet points of origin, the resulting image would be even more discontinuous. Nevertheless, the migrated time slices in Figure 4.2.2-7(B) through (D) outline the location of the model precisely. This would certainly enable the target to be detected in field data but no accurate inference can be made regarding its shape.

4.2.2.2 Results and observations: *(ii) Dipping model*

Figure 4.2.2-8 shows an in-line stack for the dipping cylinder-shaped model before (A), and after (B), 3D migration. The S/N ratio in these stacks is higher than that for the horizontal model because the scaled depth was less (660 m). The un-migrated stack (Figure 4.2.2-8(A)) shows coherent diffractions with higher amplitudes on the down-dip side of the model. The maxima of the shallow diffractions coincide with the location of the leading edge of the model. The seismic response caused by the deeper part of the model is difficult to identify with certainty because the diffraction tails merge with the dipping reflections. In the migrated stack (Figure 4.2.2-8(B)), the down-dip end of the model is not clearly mapped because of migration noise. The rough part of the model is also poorly mapped, and is represented by poorly coherent events. An outline of the model is superimposed on the stacks to facilitate interpretation.

Figure 4.2.2-9(A-D) shows time slices constructed through the 3D data before migration. Figure 4.2.2-9(A) shows a circular amplitude peak caused by the top of the model at 900 ms scaled TWT. The diffraction pattern in Figure 4.2.2-9(B) is also quite distinct and

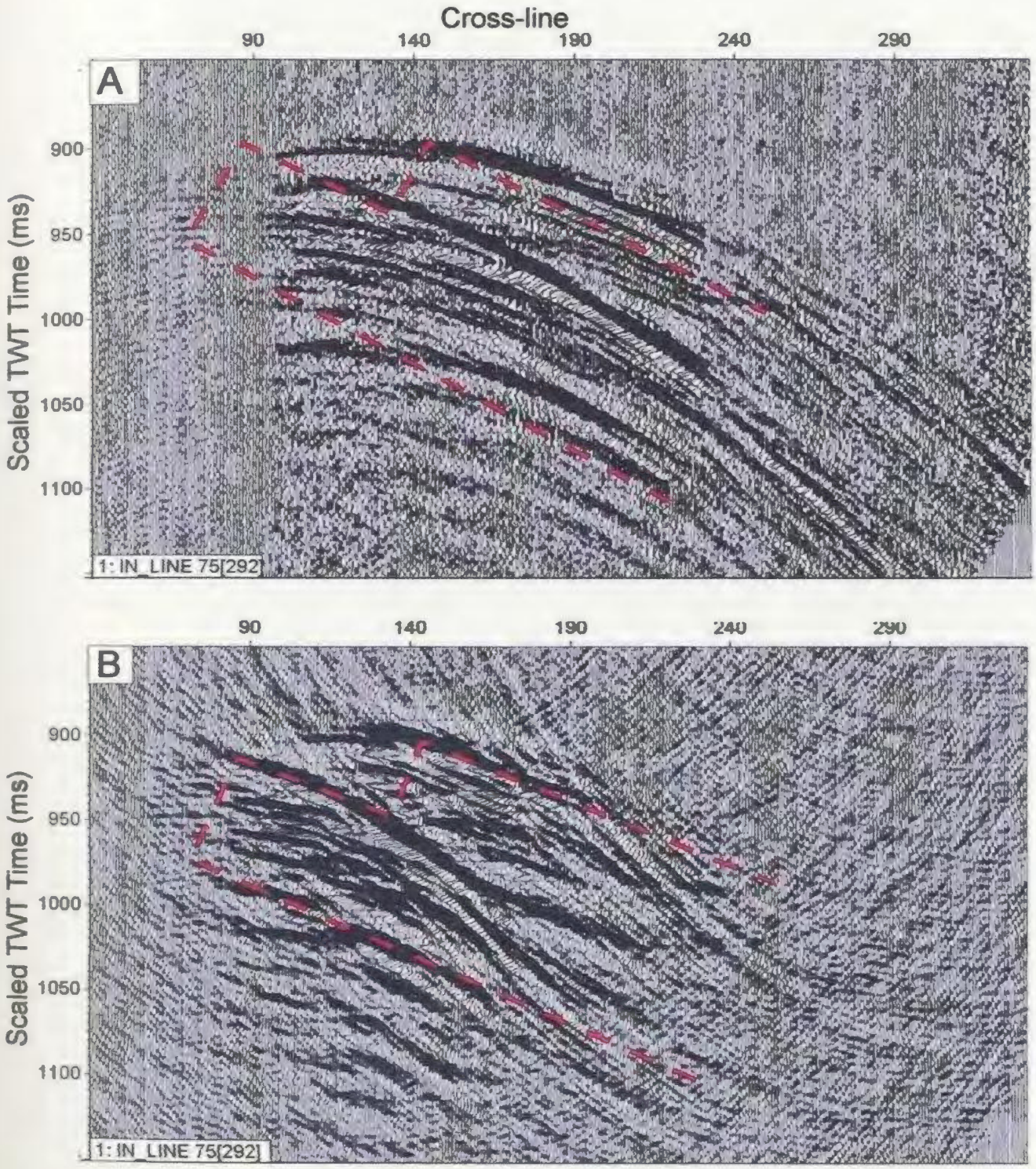

Figure 4.2.2-8: In-line stacks through the cylinder-shaped model dipping at 35° before (A) and after (B) post-stack 3D F-K time migration. A simplified cross-section of the model is overlain to facilitate interpretation.

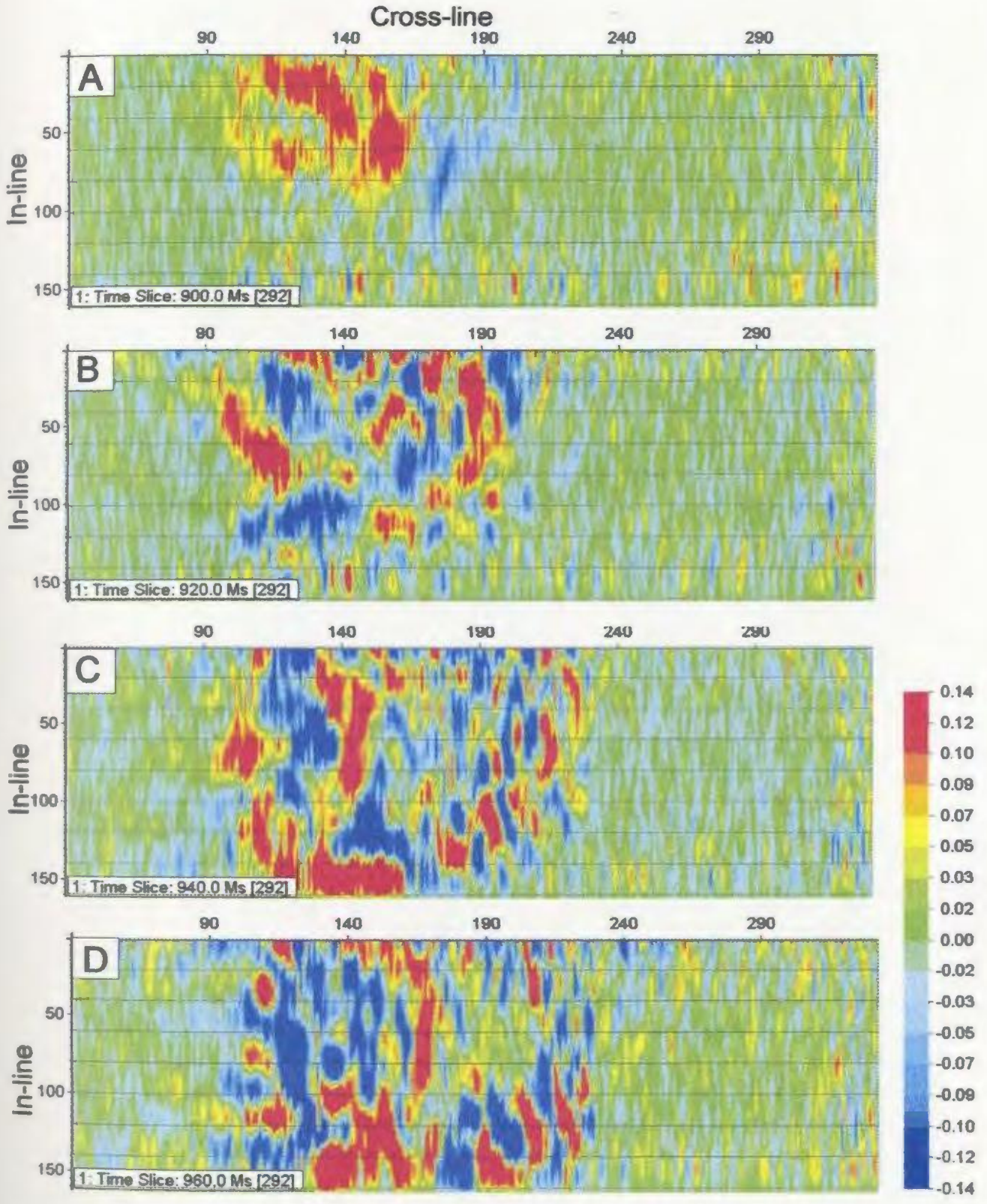

Figure 4.2.2-9: Time slices through the cylinder-shaped model dipping 35° before 3D F-K time migration. Note that the diffraction pattern is roughly circular but discontinuous because of the rugged surface relief.

composed of circular amplitude anomalies, but it is more discontinuous. Figure 4.2.2-9(C) and (D) show more complicated diffraction patterns which also clearly define the location of the model.

The migrated time slices corresponding to the ones discussed in Figure 4.2.2-9 are shown in Figure 4.2.2-10 (A-D). The time slice at 900 ms TWT (Figure 4.2.2-10(A)) shows a focused amplitude peak which maps the top of the model. In Figure 4.2.2-10(B-D), the diffraction pattern consists of alternating peaks and troughs with only a weakly-defined trend. Overall, the migrated time slices show the location of the model precisely, but do not show the detailed features on the surface of the model. The results for this model show that the ability to image the model has been reduced drastically by the dip, since it is imaged better when horizontal and at greater depth.

4.2.2.3 Discussion and Conclusions

The results for the first experiment show that the model is mapped moderately well when horizontal, despite the limited resolution of the data. The quality of the stack is drastically reduced by the effects of the rugged surface relief. Even though the time slices show that the target can be located precisely, the diffraction patterns are discontinuous and would be difficult to detect in field data with a low S/N ratio.

The second experiment shows that the dip has a strong impact on the seismic response caused by small seismic targets. Despite the higher S/N ratio compared with data

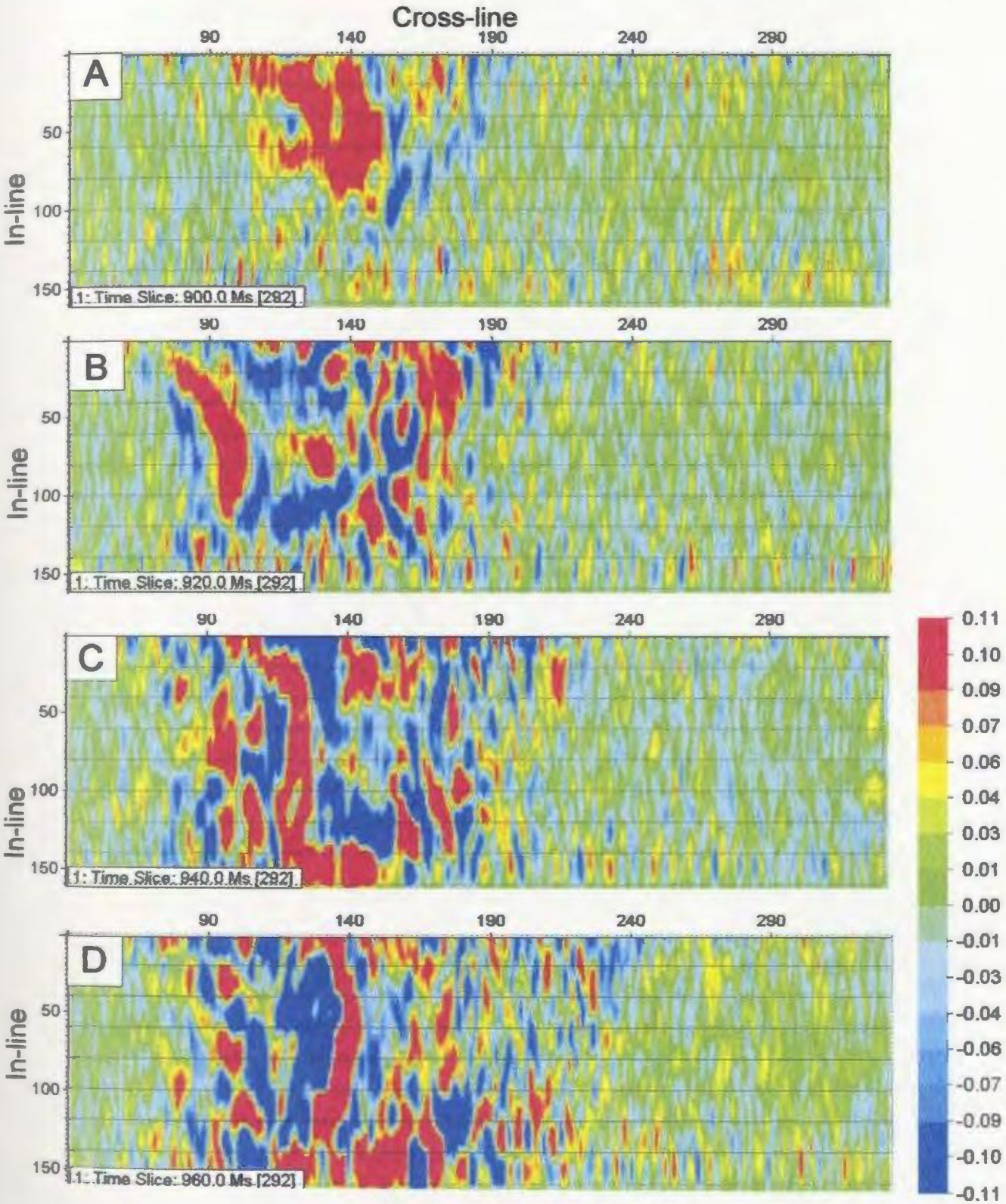

Figure 4.2.2-10: Time slices through the cylinder-shaped model dipping 35° after 3D migration. The diffraction pattern is more complicated than that for the horizontal model, but it nevertheless shows the location of the model clearly.

for the horizontal cylinder-shaped model, the diffraction response is complicated at a moderate dip of 35°. Nonetheless, the time slices show that the seismic response caused by the model can be identified with confidence. Overall, it is clear from these experiments that seismic targets with a geometrical complexity similar to that of the cylinder-shaped model can be detected with reflection seismic if they are horizontal, and can be detected even if they are dipping.

4.2.3 Disk-shaped model

This model is intermediate between the egg and cylinder-shaped models in size and geometric complexity. The latter models represent end-members of the geometrical diversity envisaged for natural mineral deposits. Data for the egg-shaped model show that a target with a smooth, convex surface can be imaged accurately, but its curved surface produces buried focus events that complicate the seismic response. Data for the cylinder-shaped model show that excessive geometric complexity leads to intractable event interference and hence poor imaging. The disk-shaped model is 84 mm long, 64 mm wide, and 16 mm thick with a depression in the middle as shown by the contour maps in Figure 4.2.3-1, and a smooth finish with relief of ~2 mm. It is used to determine the extent to which surface relief affects the seismic response of targets similar in size to the radius of the first Fresnel zone. This model simulates a flattened mineral deposit 210 m long, 160 m across, and 40 m thick, for a scale factor of 2500. Although it represents small deposits at depths ≥600 m, the emphasis here is placed on the effects of geometry on the seismic response.

4.2.3.1 Data Acquisition and Processing

3D data were acquired over the disk-shaped model in a grid comprising normal shot and receiver lines (Figure 4.2.3-2). The shot and receiver line spacing, as well as the shot and receiver intervals within each line, were the same as those described for the acquisition of data for the cylinder-shaped model (Figure 4.2.2-3). Data acquisition for this model used

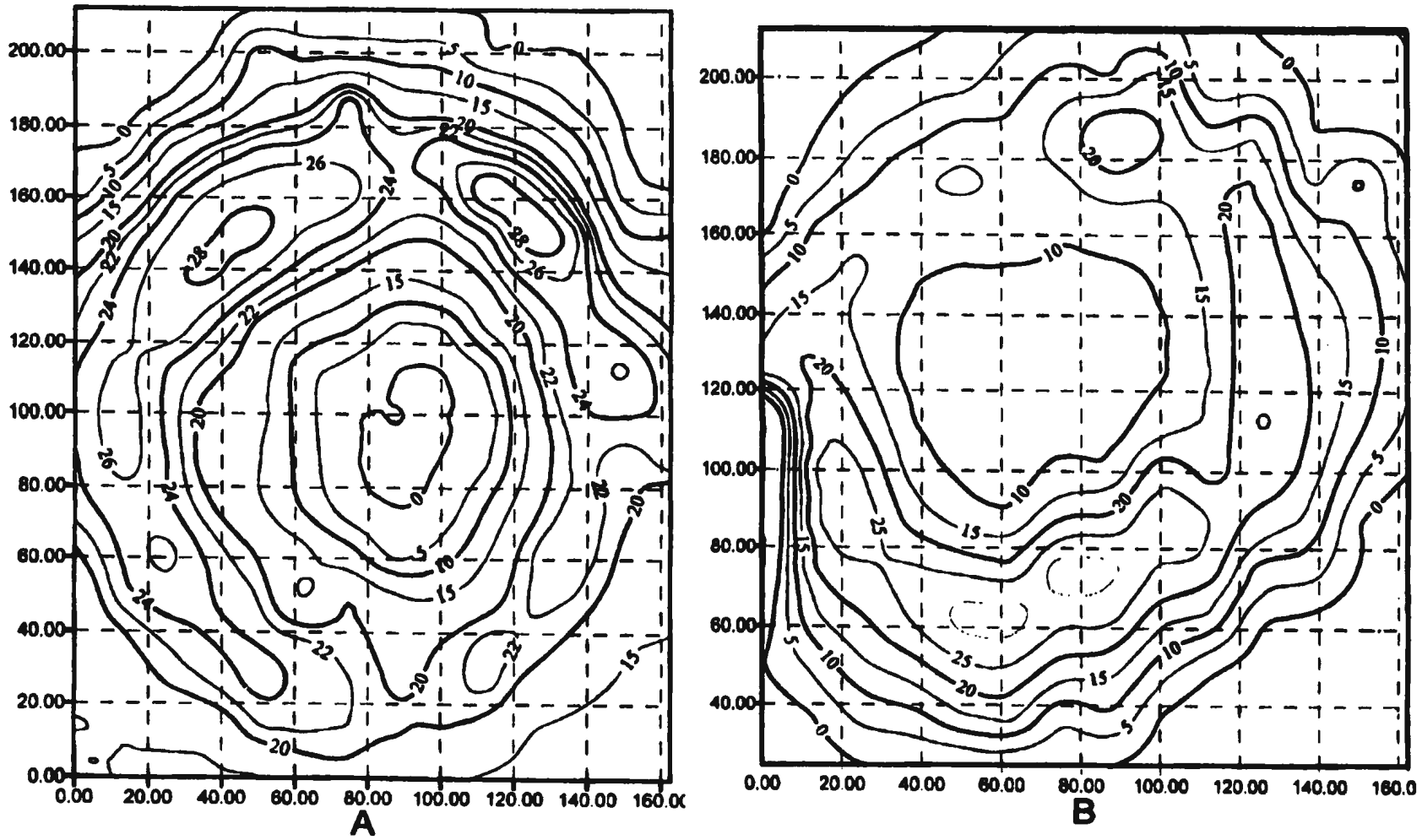

Figure 4.2.3-1: Contour maps of the upper (A) and lower (B) surfaces of the disk-shaped model. The contours are in metres (scaled) and drawn with reference to a horizontal plane through the middle of the model. The scale factor is 2500.

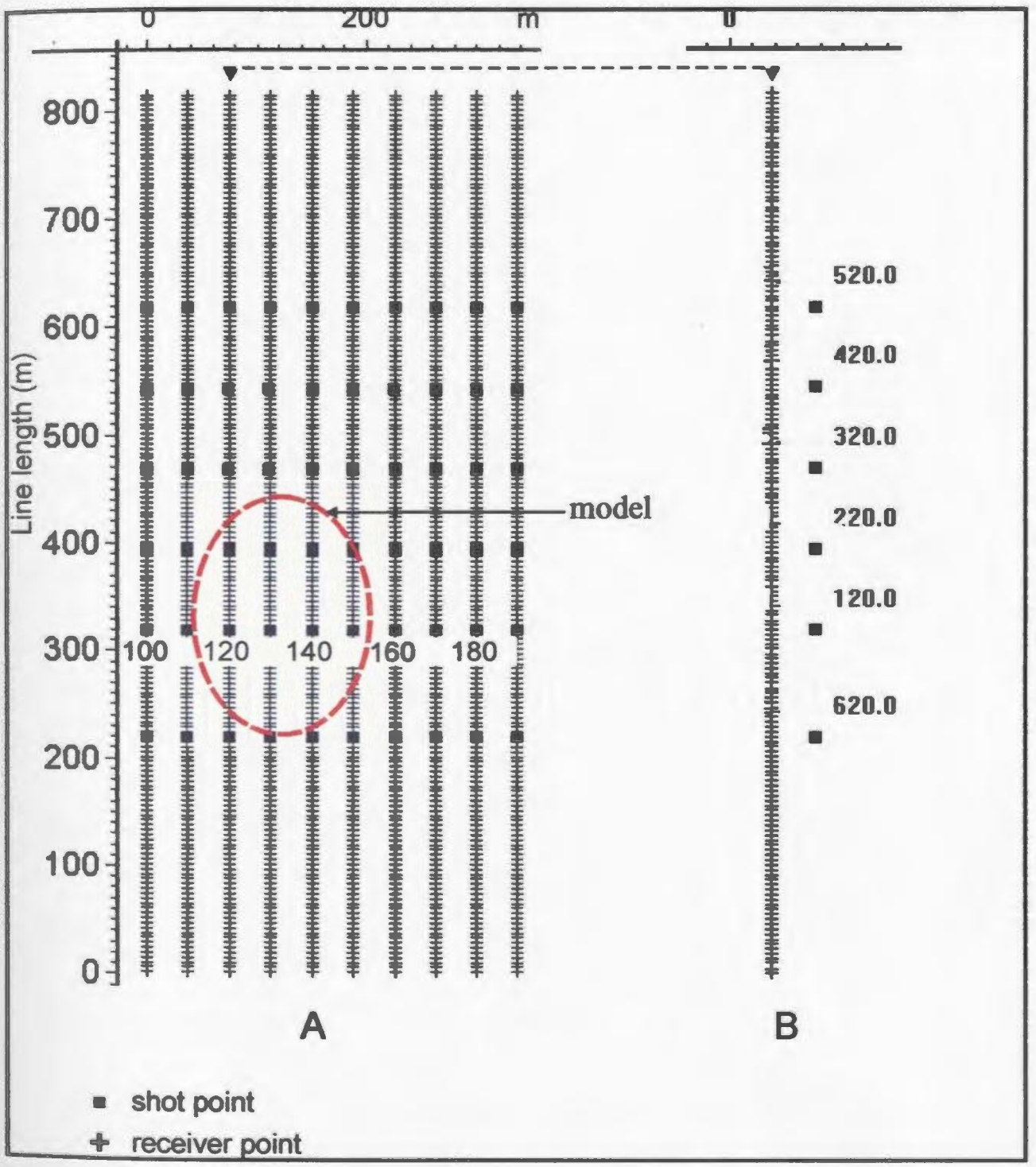

Figure 4.2.3-2: Data acquisition grid for the disk-shaped model (A). An outline of the model is overlain to help in interpretation. The model is dipping to the left and towards the top of the paper. (B) is a 2D line extracted from the 3D data volume.

two templates with five shots each per line. Six shot lines with 9,000 traces each were adequate to cover the model. Hence, 54,000 traces were recorded to a total scaled TWT of 1,500 ms, sampled at ½ ms (scaled). The acquisition geometry for these data attained a source to receiver offset of 686 m and a subsurface fold of 75. Figure 4.2.3-3 shows the amplitude spectrum of the data, which have a low S/N ratio.

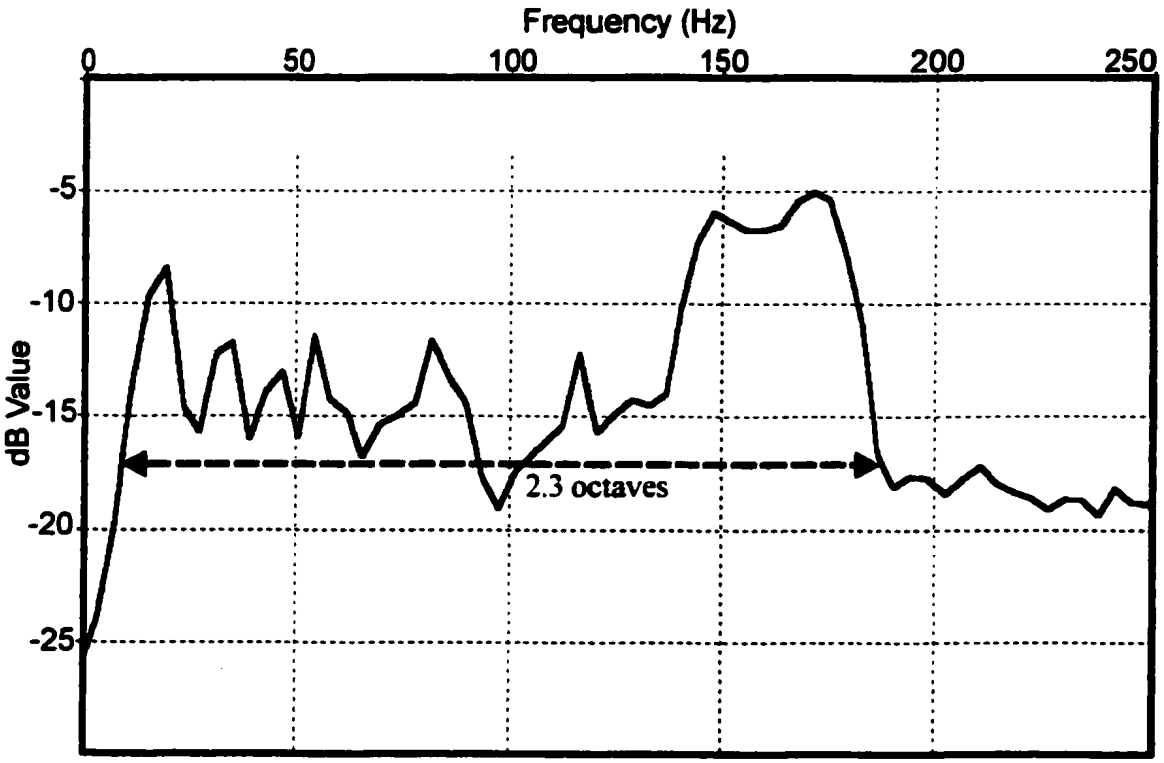

Figure 4.2.3-3: Amplitude spectrum of the data recorded on the disk-shaped model after deconvolution. Note that the amplitude is low below 125 Hz, so that the resolution is poor despite the two octave bandwidth.

The disk-shaped model was positioned dipping parallel to the receiver lines in the water tank at a scaled depth of 686 m, so that the far offsets were recorded at incidence angles of ~45°. At this depth, the model is 2.6 first Fresnel zone radii across. While the model exceeds the radius of the first Fresnel zone, it has surface relief of one wavelength (λ ~18 m).

Data processing followed the CMP-based sequence described in Table 4.2.1-1. A pie slice frequency domain dip filter was used to attenuate coherent source-generated noise on the data. Using this filter was a compromise because it enhances the lateral coherence of data by Rieber mixing. This effect smoothens structure on the seismic events, and impacts strongly on the interpretation. This problem can be avoided by using the aplanatic prestack depth migration method which discriminates against events with a linear moveout and does not require dip filtering. A 2D profile was extracted from the 3D seismic data and processed with CMP-based techniques and also with prestack depth migration.

4.2.3.2 Results and observations

Figure 4.2.3-4(A) shows an in-line stack of the data before migration. The stack contains dipping diffractions which map the top of the model with an amplitude trough at 920 ms TWT. The bottom of the model is mapped by an amplitude peak at 960 ms TWT. Both the seismic responses caused by the top and bottom of the model show no relief, despite the relief apparent in Figure 4.2.3-1. While this seismic response has been enhanced

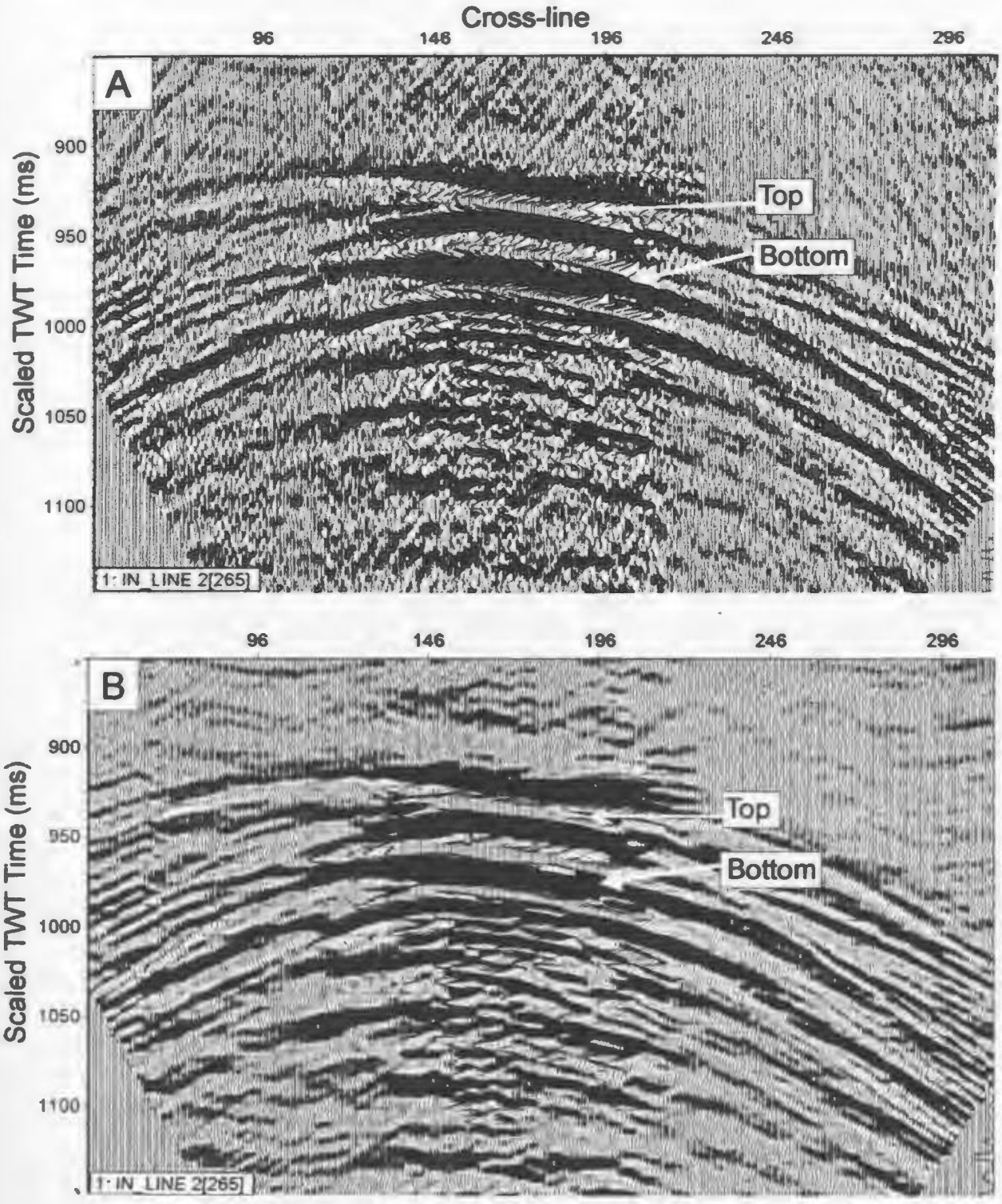

Figure 4.2.3-4: In-line stack through the data for the disk-shaped model before migration (A), and after migration (B). Although the S/N ratio is improved in the migrated stack, the structure is not visible on the model because of its size with respect to the width of the first Fresnel Zone.

by lateral trace mixing caused by the frequency domain dip filter, it is more likely to be due to the limited areal extent of the model.

Figure 4.2.3-4(B) is the 3D time migration of the stack shown in Figure 4.2.3-4(A). The S/N ratio in this stack is improved compared with that in the un-migrated stack. The top of the model is mapped by an amplitude trough at 920 ms TWT, dipping gently to the right. The bottom of the model is mapped by an amplitude peak at 960 ms TWT, and also dips gently to the right. Overall, even though the lateral limits and the relief of the model are not visible in the vertical stacks at this depth, the location and thickness of the model have been mapped.

Figure 4.2.3-5 shows time slices of the data before migration. The time slices (A-D) show a circular diffraction pattern defined by alternating amplitude peaks and troughs arranged partially around the model.

Figure 4.2.3-6 (A-D) shows time slices of the 3D data after migration. The diffraction pattern is focussed by 3D migration to a small area at the top of the model at 920 ms scaled TWT, with a poorly-defined trend. While the diffraction pattern shows the location of the target more precisely, it would be difficult to recognize above ambient noise because of the lack of a distinct pattern. This latter fact is important in terms of target detection in field data where the S/N ratio is low. Analysis of the seismic data for the disk-shaped model shows that the structure on its surface cannot be resolved.

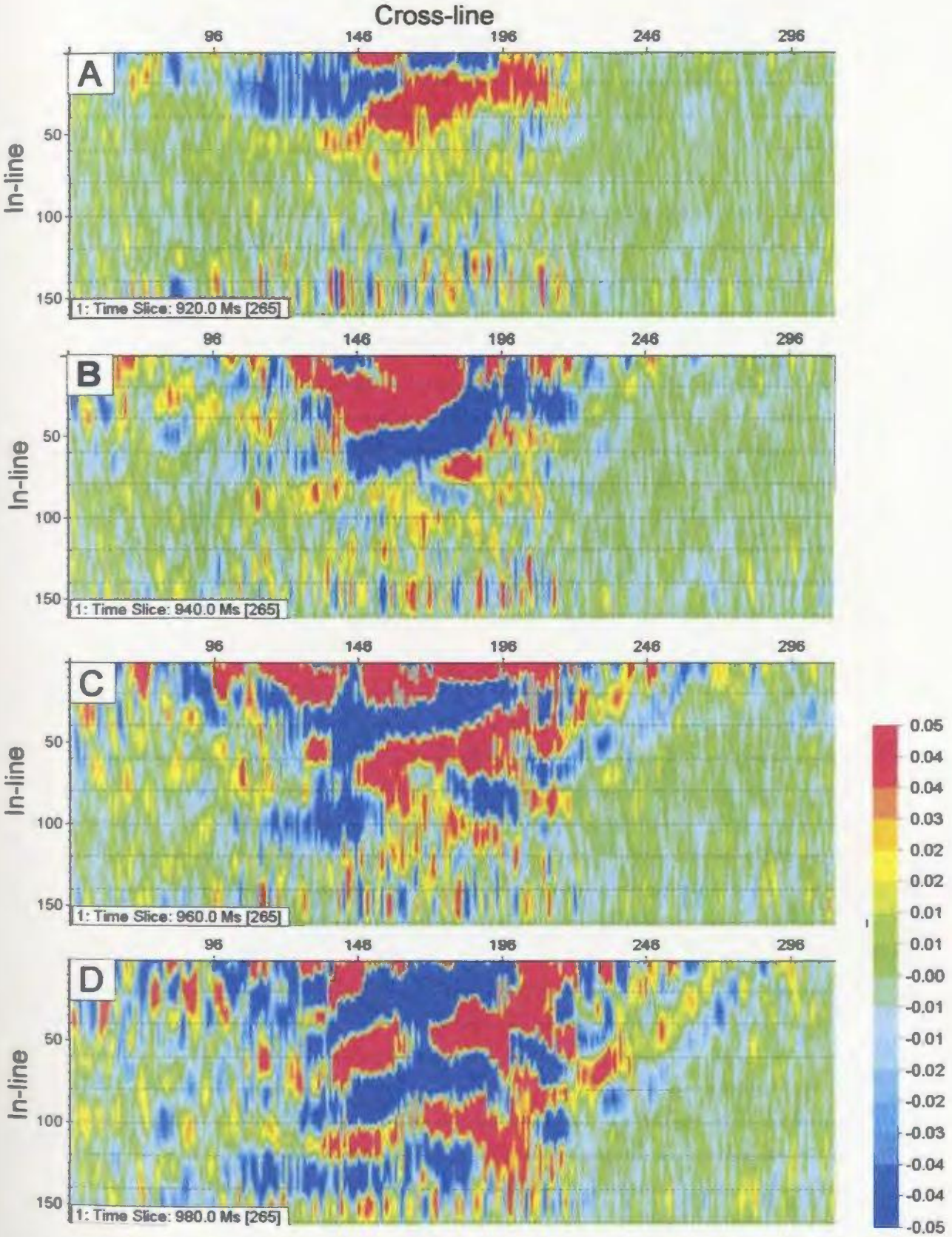

Figure 4.2.3-5: Time slices through the data for the disk-shaped model before 3D migration.

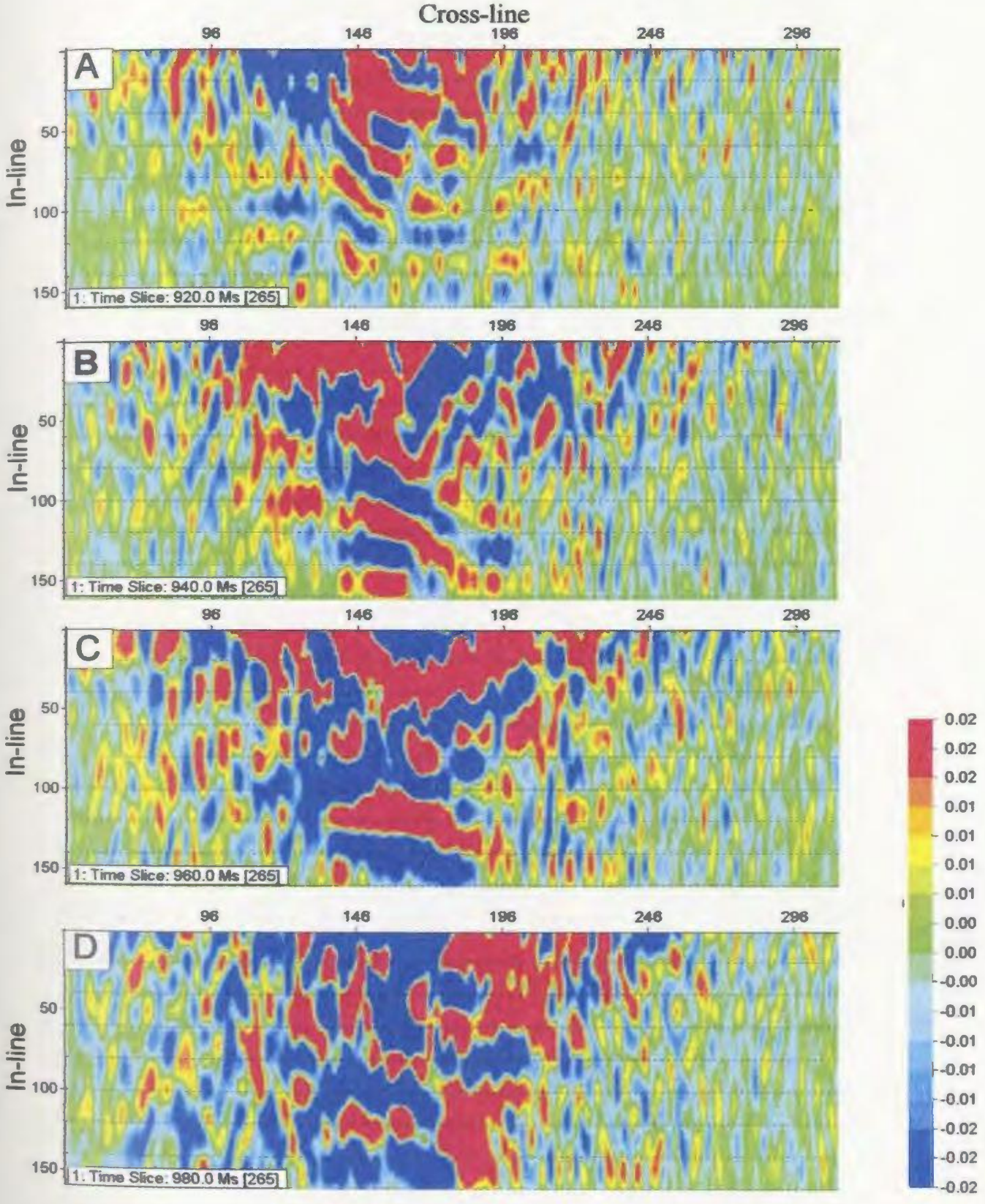

Figure 4.2.3-6: Time slices through the data for the disk-shaped model after 3D migration. The individual slices are discussed in the text.

4.2.4 Two-Dimensional Profiles

Although 3D seismic data achieve better resolution and are well-suited to map small and complex targets, conventional exploration uses mainly 2D surveys. The preference for 2D surveys is based partly on economics, but also on the available technology since 3D data acquisition and processing are more elaborate. In order to compare the observations made on the model 3D data with the 2D field data, 2D seismic profiles were extracted from the 3D volumes and subjected to CMP-based and prestack depth migration processing. This exercise allows a direct comparison of the 3D or 2D seismic response for the same model.

4.2.4.1 Data Processing

The geometry of the 2D seismic lines is shown in the acquisition plans in Figures 4.2.1-3, 4.2.2-3, and 4.2.3-2. Since the data were initially acquired for 3D processing, the subsurface fold is low (7-10). However, this is not a major problem because the data have a fair S/N ratio, as shown by the amplitude spectra (Figures 4.2.1-4, 4.2.2-4, and 4.2.3-3), and the CMP stacks are of acceptable quality.

Processing of the 2D data followed the CMP-based sequence described in Table 4.2.1-1. Front-end and surgical muting were applied, followed by NMO correction and CMP stacking, and the data were subsequently migrated post-stack using the F-K technique. After spiking deconvolution and bandpass filtering, the data were also input to the aplanatic prestack depth migration program, with a constant velocity model of 1500 m/s defined with

a 2.5 m x 2.5 m grid. The velocity model extends horizontally for the length of the stack and vertically for 1125 m. A constant velocity model was used because trials have shown that good accuracy can be attained due to the simple velocity distribution.

4.2.4.2 Results and observations

Figure 4.2.4-1(A) shows the post-stack time-migrated section in which the top and bottom of the egg-shaped model are mapped by a trough and peak amplitude events respectively at 1065 ms and 1175 ms scaled TWT. The buried focus event discussed in §4.2.1.3 is mapped by an amplitude trough at 35 ms scaled TWT behind the primary event, which tallies with the value predicted from eq. (14). The 2D profile is imaged well by the post-stack time migration.

Figure 4.2.4-1(B) shows the aplanatic prestack depth migration of the 2D profile for the egg-shaped model. Although the ambient noise is high, the signal caused by the model stands out clearly, and both the top and the bottom show the correct curvatures which are discordant to the noise pattern. The top of the model is mapped by a trough at 800 m and the bottom by a peak at 900 m, showing that the model has a scaled thickness of 100 m at the position of the seismic line. The buried focus event is mapped by a trough 43 m (scaled) below the surface of the model. The prestack depth migration produced an accurate image of the egg-shaped model, though not much better than the time migration since the model has a simple geometry.

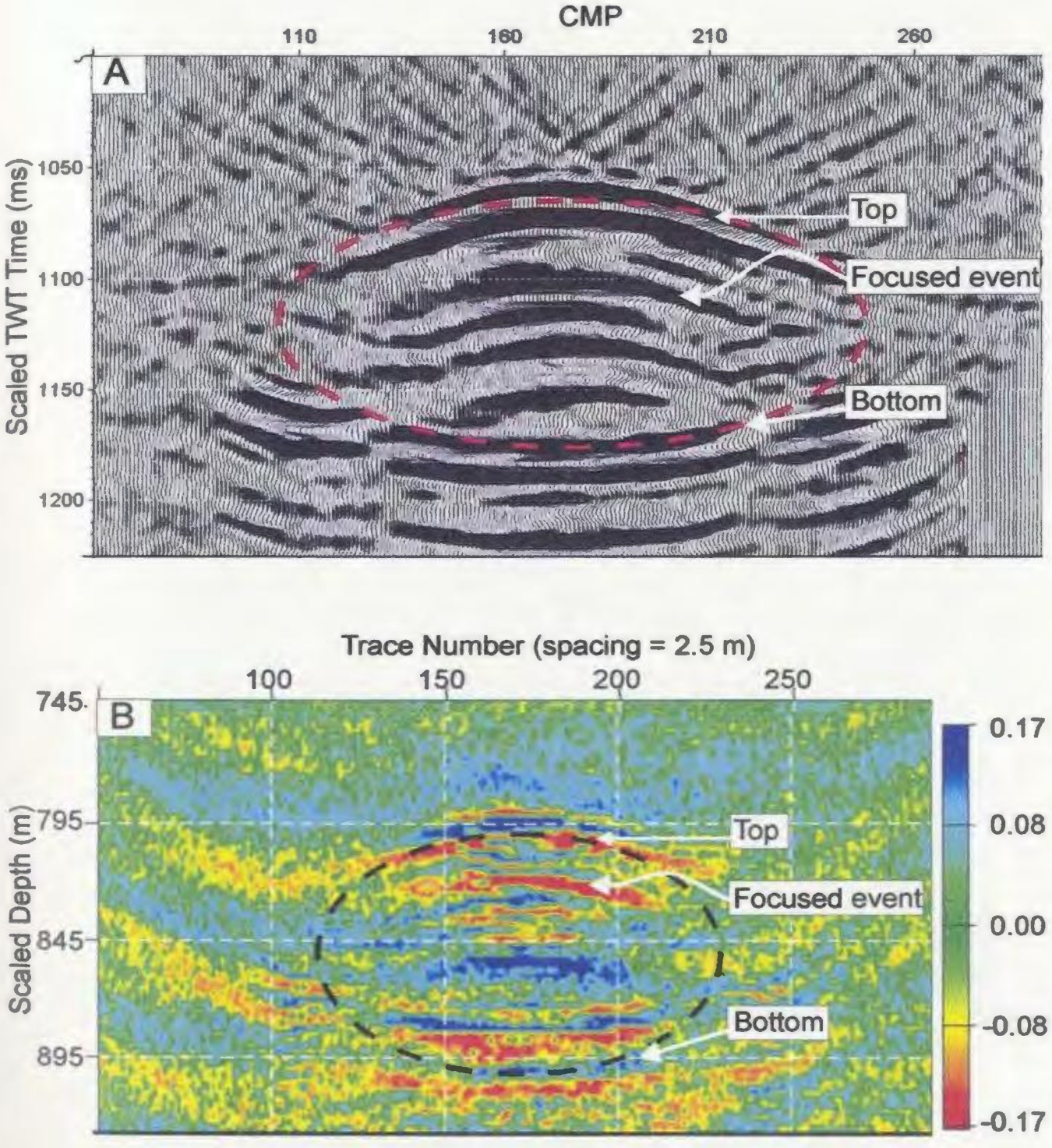

Figure 4.2.4-1: Post-stack time migration (A), and (B), pre-stack depth migration of the 2D profile for the egg-shaped model. Depth migration parameters were $\Delta z = \Delta x = 2.5$ m, and $v = 1500$ m/s. An outline of the model is overlain to facilitate interpretation.

Figure 4.2.4-2 shows the post-stack migrated stacks for the cylinder-shaped model when horizontal and dipping. In Figure 4.2.4-2(A), the stack shows the flat area on the model shown in Figure 4.2.2-1 at 990 ms scaled TWT. To the left of this event, the migrated stack consists of poorly coherent events which represent the top of the model with a trough at 1040 ms scaled TWT. The events on the left side of the stacks are partially collapsed diffractions which obscure the location of the edge of the model. The bottom of the model is mapped by a strong amplitude peak at 1100 ms scaled TWT.

Figure 4.2.4-2(B) is the migrated stack for the dipping cylinder-shaped model. The stack shows the top of model near the leading edge with an amplitude trough at 920 ms TWT. The top of the model to the right of the stack is indicated by partially collapsed diffraction events. These diffractions are only partially collapsed by post-stack time migration, and hence it is difficult to identify the features of the model with certainty.

Figure 4.2.4-3 shows the aplanatic prestack depth sections for the horizontal and dipping cylinder-shaped model. Figure 4.2.4-3(A) is the aplanatic prestack depth migration for the horizontal model and shows the top and bottom of the model mapped by an amplitude trough and peak respectively at scaled depths of 740 m and 820 m. Despite the prevalence of migration noise, seismic signal can be identified by its discordance to the ambient noise pattern. For this model, prestack depth migration has performed slightly better than post-stack migration in imaging the target.

Figure 4.2.4-3(B) is the prestack depth migration for the dipping cylinder-shaped model. The top of the model is mapped by a trough at 660 m. The lower portion of the

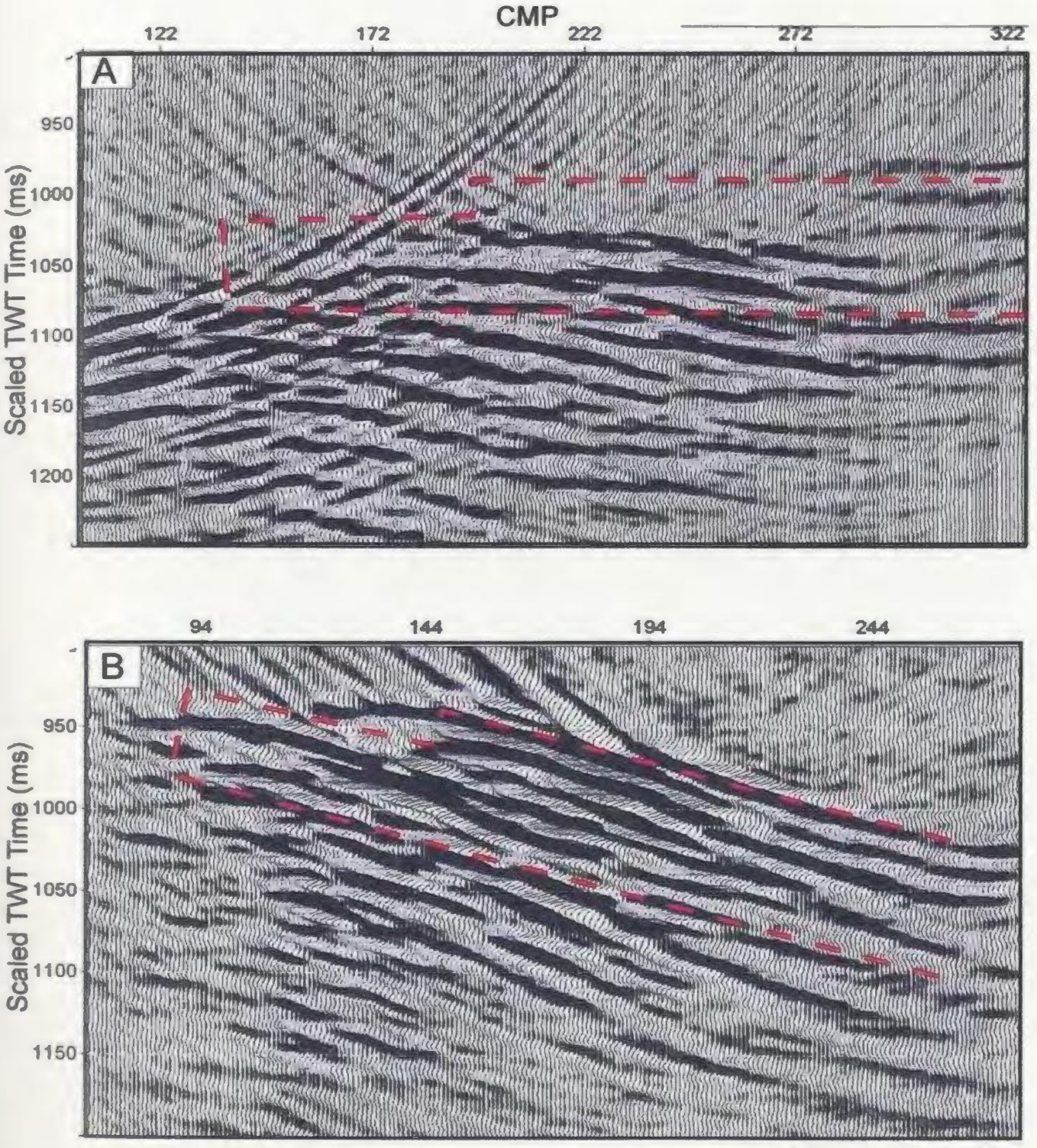

Figure 4.2.4-2: 2D stacks extracted from the 3D seismic data volume for the cylinder-shaped model. (A) post-stack migrated stack for the horizontal model, and (B) post stack migrated for the dipping model. An outline of the model is overlain to facilitate interpretation.

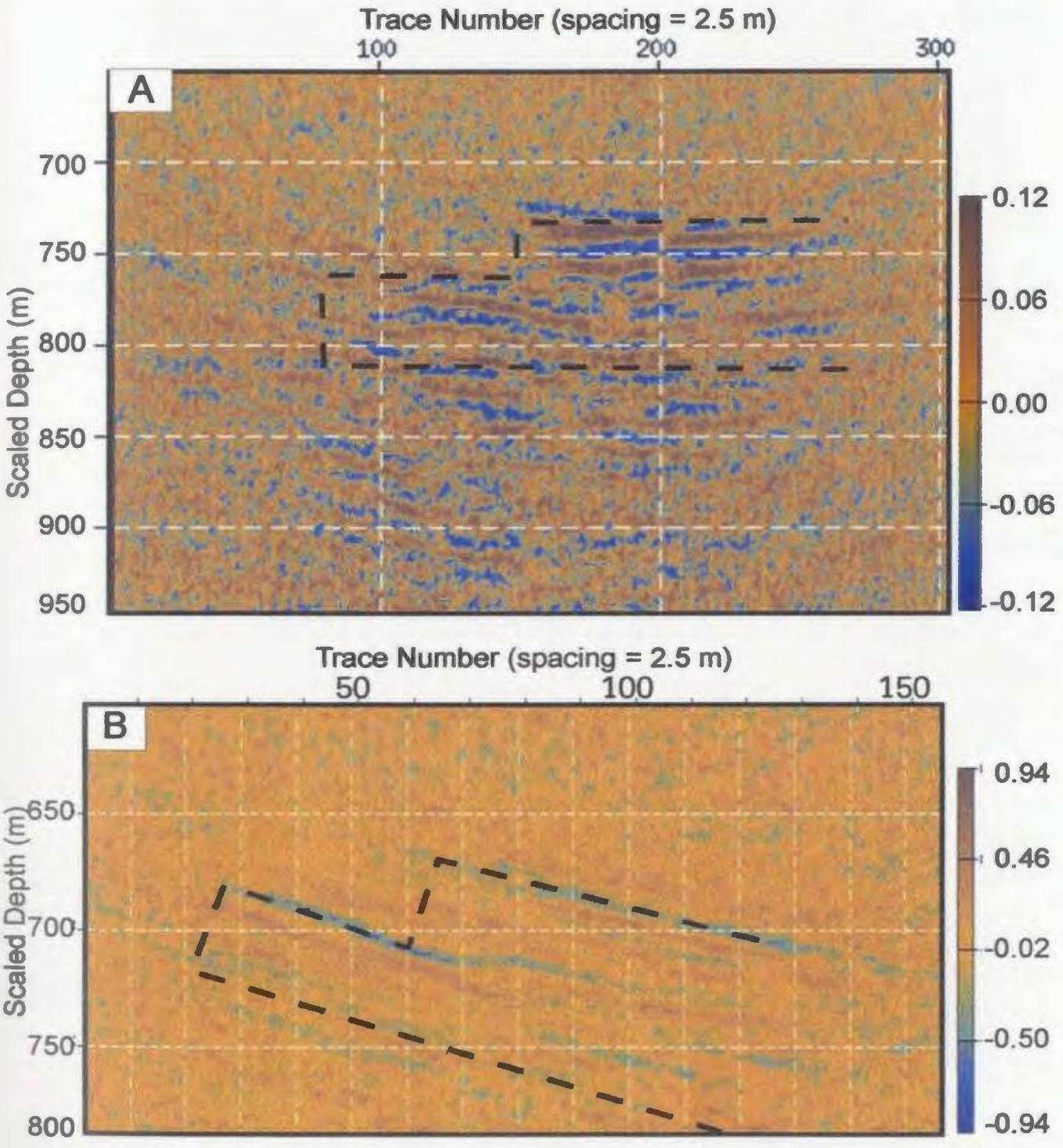

Figure 4.2.4-3: Aplanatic prestack depth sections of the 2D profiles extracted from the 3D data for the horizontal (A), and dipping (B) cylinder-shaped model. Migration parameters: $\Delta x = \Delta z = 2.5$ m, constant scaled velocity = 1500 m/s. The input data are shot gathers with geometry, gain, and deconvolution applied, but no muting or dip filter. An outline of the model is overlain to aid interpretation.

model is only weakly detected. It is clear from this figure that the prestack depth section has performed slightly better than the post-stack migration.

Figure 4.2.4-4(A) shows a post-stack time migrated stack for the disk-shaped model. The migrated stack shows the top of the model mapped by an amplitude trough at 975 ms and the base by an amplitude peak at 1060 ms scaled TWT. The stack clearly shows the location of the model and that it is dipping gently to the right. There is no indication that the surface of the model has significant structure, because the model is small compared with the radius of the first Fresnel zone.

Figure 4.2.4-4(B) is the aplanatic prestack depth migration for the disk-shaped model. The ambient noise is high, but the seismic response of the model is clearly identifiable. The top of the model is mapped by an amplitude trough at a scaled depth of 688 m and dipping to the right. The base of the model is mapped by an amplitude peak at a scaled depth of 741 m and also dipping to the right. Similar to the post-stack time migrated stack, the seismic events caused by the top and bottom of the model show no surface structure, confirming that the smoothness results from the limited resolution of the data. The input data to the aplanatic prestack depth migration program are not affected by the F-K filter. The results in this figure show that for a small seismic target, prestack depth migration may achieve better imaging compared with post-stack migration.

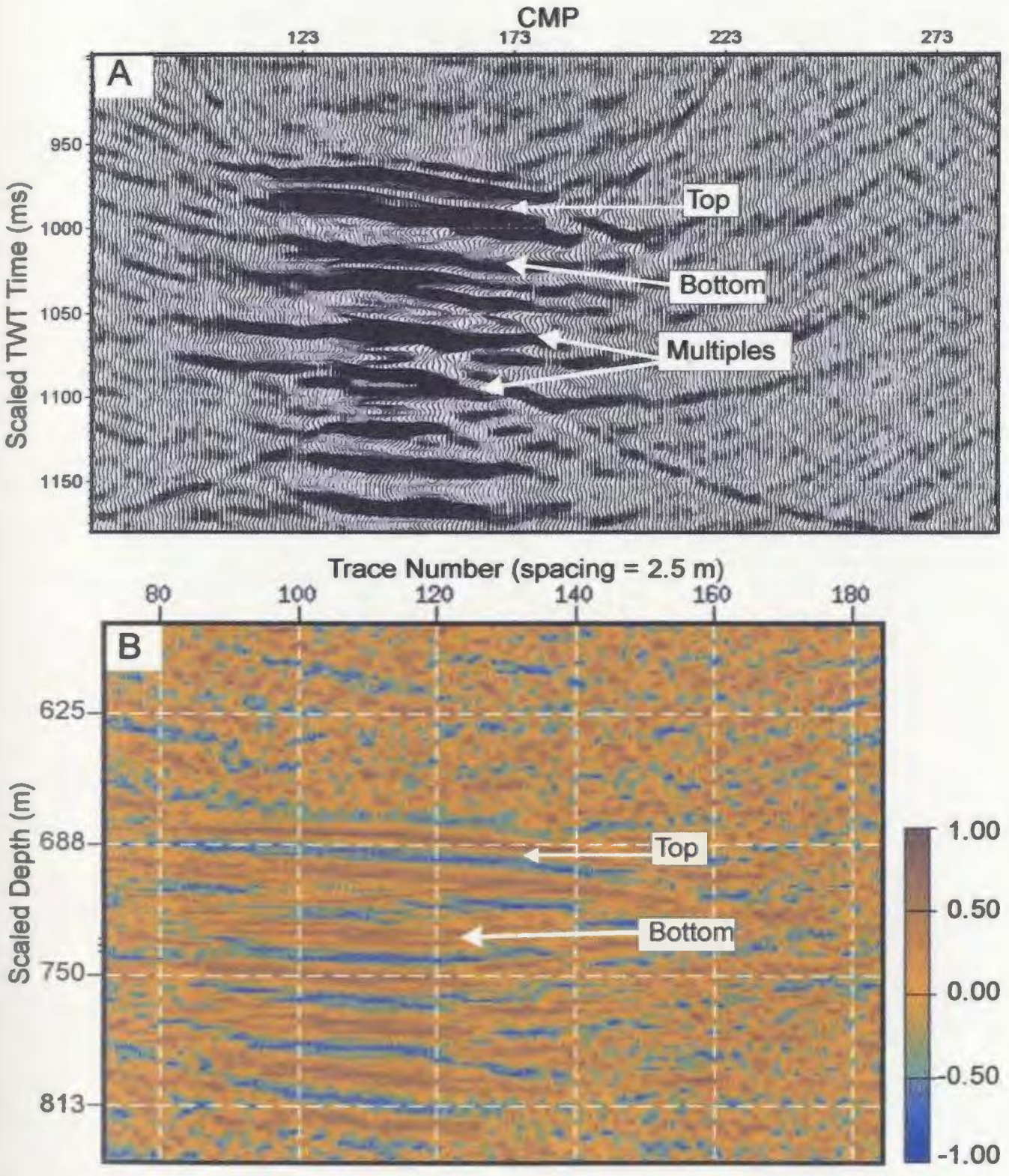

Figure 4.2.4-4: In-line 2D stack for the disk-shaped model after post-stack migration (A), and after aplanatic prestack depth migration (B). Prestack depth migration imaged the data better because it was not affected by the source-generated coherent noise.

4.2.4.3 Discussion and Conclusions

The results presented in the previous section show that 2D post-stack time migration cannot adequately image small and complicated seismic targets. This fact is demonstrated by comparison of the performance of the latter on the egg-shaped model and the dipping cylinder-shaped model. The egg-shaped model is imaged successfully by both the prestack depth migration and post-stack migration (Figure 4.2.4-1). This success was achieved because the model is large compared with the radius of the first Fresnel zone, has a smooth surface, and a simple geometry. However, post-stack time migration was less successful in imaging the dipping cylinder-shaped model, even though the S/N ratio here is better than that for the horizontal model (Figure 4.2.4-3).

The results for the 2D seismic profiles show further that the aplanatic prestack depth migration technique is effective and robust to image small and complicated seismic targets when conventional CMP processing fails. It is less prone to processing artifacts because it requires little preprocessing. A limitation of this method is, as other imaging techniques, the bandwidth and signal quality.

4.3 Interpretation

The analogue models presented in the previous section cover a wide range of geometric complexity and sizes considered plausible for mineral deposits; from a smooth lens to very complicated shapes. These models have produced seismic data of variable complexity, which provide insight into the range of possibilities of the effects imposed by the geometry on the seismic response of mineral deposits. The significant observations made on the seismic responses of these analogue models and their implications for mineral exploration are presented in this section.

For the egg-shaped model, the 3D seismic response consists of closed and continuous, circular diffraction patterns in time slices, which map out the target accurately. Such circular diffraction patterns should enable easy recognition of similar targets in field data. Due to its smooth, curved surface, and simple geometry, the egg-shaped model was imaged successfully with 2D and 3D data, and the S/N ratio was enhanced significantly by the post-stack 3D migration. It is clear from the foregoing that 3D data are valuable in mineral exploration for (i) their enhanced spatial resolution, (ii) to provide time slices needed to identify the seismic response of small and complicated targets, and (iii) to construct time structure maps. The latter are a critical asset of 3D seismic data in frontier areas where the structure is little known.

In-line stacks of the seismic data for the egg-shaped model show seismic events caused by the focusing effect of its convex surface. These optical focus events cause multiple reflections within the model which obscure the event caused by the bottom of the

model. Recognition of these optical focus events is important, particularly in the exploration for Cu-Zn deposits which are smooth, convex lenses with sharp contacts against the host rock. Such mineral deposits, as shown in Chapter 3, possess a high acoustic impedance and would cause strong multiple reflections of the optical foci that would lead to ambiguity in the interpretation of the seismic response, since field data also contain ambient noise.

For the cylinder-shaped model, the quality of the stack is strongly affected by the rugged surface relief. Even though the time slices show that the target can be located precisely, the diffraction patterns are discontinuous and would be difficult to detect in field data with a low S/N ratio. Moreover, the dip of the model has a strong impact on the seismic response caused by small seismic targets. The diffraction response for the dipping model is complicated and 3D post-stack migration could not image the model adequately. Nonetheless, the time slices show that the seismic response caused by the model can be detected with confidence. It is clear from the results that even seismic targets of great geometrical complexity similar to that of the cylinder-shaped model can be imaged with reflection seismic if they are horizontal, and can at least be detected if they are dipping.

The disk-shaped model represents the limiting case for imaging small and complex targets. Even though the contour maps in Figure 4.2.3-1 show that model has significant relief, the in-line stacks and the prestack depth migration show no relief on the surface of the model. However, the location of the model is clearly outlined by the diffraction patterns in the time slices. This shows further that small seismic targets can be easily detected by their circular diffraction patterns in times slices.

The results from the 2D seismic profiles show that the aplanatic prestack depth migration technique is more effective in imaging small and complicated seismic targets when conventional CMP techniques fail. One reason for its success with these data is that the data are dominated by linear but coherent noise which is difficult to remove with conventional filtering. The aplanatic prestack migration discriminates against these events by imaging only the diffraction and/or reflections with elliptical travel time trajectories between the source and the receiver. Aplanatic prestack depth migration imaged the egg-shaped model successfully in 2D. However, if the ambient noise was lower, the diffractions would collapse to a point. This is undesirable because if the signal consists entirely of diffractions, which is common in mineral exploration, then all evidence of the target would be lost from the data. As indicated in §2.4, migration aims to collapse the diffractions to a point, but this does not necessarily improve the detection or imaging of small targets because it makes the seismic response discontinuous and hard to detect above the ambient noise.

CHAPTER 5

5.0 NUMERICAL MODELLING

5.1 Introduction

The physical models discussed in Chapter 4 are restricted to the acoustic case because of logistical limitations. However, elastic wave modelling is required to examine the seismic response of mineral deposits hosted by crystalline rocks because the large seismic impedance contrast at the deposit/host rock interface gives rise to converted-mode SV-waves. Converted-mode SV-waves are considered noise on P-wave CMP stacks, but SV-wave reflections can potentially be used to produce an SV-wave CMP stack if they are sufficiently strong.

Although refracted converted-mode SV-waves are reported in the literature (e.g. Peron and Calvert, 1998), there is no account of the behaviour of the reflected or diffracted SV-waves produced at crystalline rock/mineral deposit interfaces. It is not even clear if SV-wave reflections or diffractions are commonly observed at deposit/host rock interfaces, and if so, what their role is with respect to the detection or imaging of mineral deposits. The significance of this matter is captured in the fact that mineral deposits possess high seismic impedances compared with crystalline rocks. Interfaces of such mineral deposits with crystalline rocks should produce converted-mode SV-waves in seismic records at medium to wide angles of incidence. It is therefore important to examine the nature of these SV-wave seismic responses in order to develop strategies to suppress or enhance them in the CMP stack.

The amplitude variation of reflected waves produced by an incident P-wave with increasing angle of incidence is examined for plane interfaces in Chapter 2 using Zoeppritz equations. The present treatment involves incident P and S-waves, non-planar interfaces, and diffraction seismic responses. The objective of the numerical modelling described herein is to investigate the amplitude variation of diffraction seismic responses with the location of the source for small and complicated seismic targets. The numerical models are restricted to the 2D case because of limited computing resources. Observations made on these numerical models are intended to enable an appreciation and understanding of the typical diffraction seismic response of mineral deposits on seismic records. This is important since mineral deposits are typically of a small areal extent and complicated geometry, and thus produce predominantly diffraction seismic responses.

5.2 Numerical Models

The Duck Pond deposit (Fig. 3.2-3) is modelled using the 2D FD program of Kelly et al. (1976). The results of the numerical modelling are intended to enable a better understanding and recognition of the seismic response of deposits of similar geometry and physical properties in the 2D field data described in Chapter 6. The numerical models are designed to simulate conventional high resolution reflection seismic surveys using a Gaussian wavelet with a dominant frequency of 60 Hz, digitized at ½ ms. A grid spacing of 5 m is used for all the models, which are designed with absorbing boundaries to attenuate multiple reflections

caused by the sides and bottom of the model.

A longitudinal section of the Duck Pond deposit and a velocity-density constructed for it are shown in Figure 3.2-3. In this chapter, synthetic seismograms are used to model deposit for different depth (434, 897, and 1375 m). For a host rock seismic velocity of 5790 m/s, the dominant wavelength is 97 m and the radii of the first Fresnel zone are 145 m and 261 m for the deposit at 434 m and 1375 m respectively. For the Duck Pond deposit, this shows that its seismic response will consist fully of diffractions since none of its individual segments with a different dip exceed the radius of the first Fresnel zones indicated above.

5.3 Results and observations

Figure 5.3-1(A) shows an acoustic model with the source displaced 5 m down-dip from the top edge of the Duck Pond deposit. In this figure, the amplitudes of the diffraction responses are stronger on the up-dip side of the deposit, but on the down-dip side of the individual segment causing them.[11] The top of the deposit is mapped by an amplitude trough at small angles of incidence which undergoes a phase rotation by π radians at an incidence angle of 54° up-dip of the deposit (offset = 548 m). This amplitude trough retains the same phase at all offsets on the down-dip side of the deposit. The phase rotation is likely to cause

---

[11]The individual segments of the deposit dip in different directions from the average dip of the whole deposit.

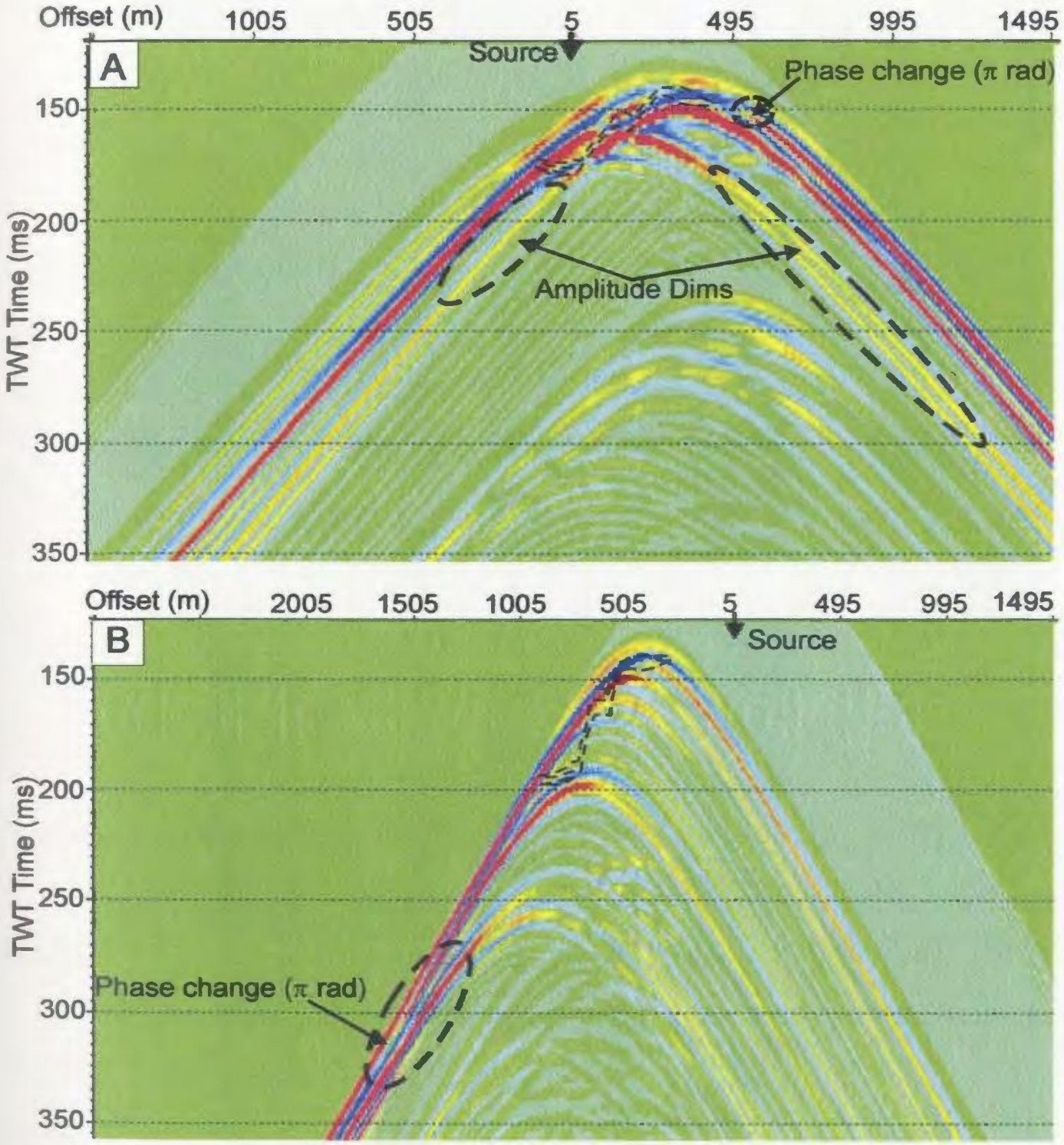

Figure 5.3-1: Shot records simulated using an acoustic FD algorithm for the Duck Pond deposit with the source displaced to the left (A) and to the right (B). (A) amplitudes are strong in the near offsets on both sides of the source. (B) Amplitudes are strong in the near -offsets and down-dip but are absent from the up-dip side. A outline of the deposit is overlain to facilitate interpretation.

destructive interference during CMP stacking and weaken the seismic response of the deposit. The incidence angles at which the phase reversals occur are different for each segment of the deposit with a different dip, so that in practice it is not possible to limit the offset to any given value to obtain a good CMP stack. The amplitude peak produced by the bottom of the deposit becomes weak at ~10 m offset on the down-dip side of the deposit, remains so up to 500 m, and becomes bright again. A similar amplitude behaviour occurs on the up-dip side of the deposit between offsets of 500 m and 1200 m.

Figure 5.3-1(B) shows an acoustic FD model with the source displaced 5 m up-dip of the top of the deposit. In this figure, the diffraction amplitude trough produced by the top of the deposit retains the same phase out to ~1000 m where it is lost in the direct wave (note that the direct wave has been muted). The amplitude peak produced by the bottom of the model reverses phase at 1500 m on the down-dip side of the deposit. The amplitude behaviour indicated in these figures shows that when the source is in the down-dip side of a small dipping target, the diffraction amplitudes will be displaced up-dip. When the source is displaced up-dip of the target, the diffraction amplitudes will be displaced to the down-dip side. The incidence angles at which the phase changes occur are dependant on the position of the source with respect to the target, and the dip of the deposit segment causing them, so that it is not possible to make a generalization regarding their relationship to offset.

Figure 5.3-2 shows another acoustic model of the Duck Pond deposit where the source is displaced a large distance down-dip. In this figure, the diffraction amplitude trough and peak caused by the top and bottom of the deposit are displaced up-dip of the deposit.

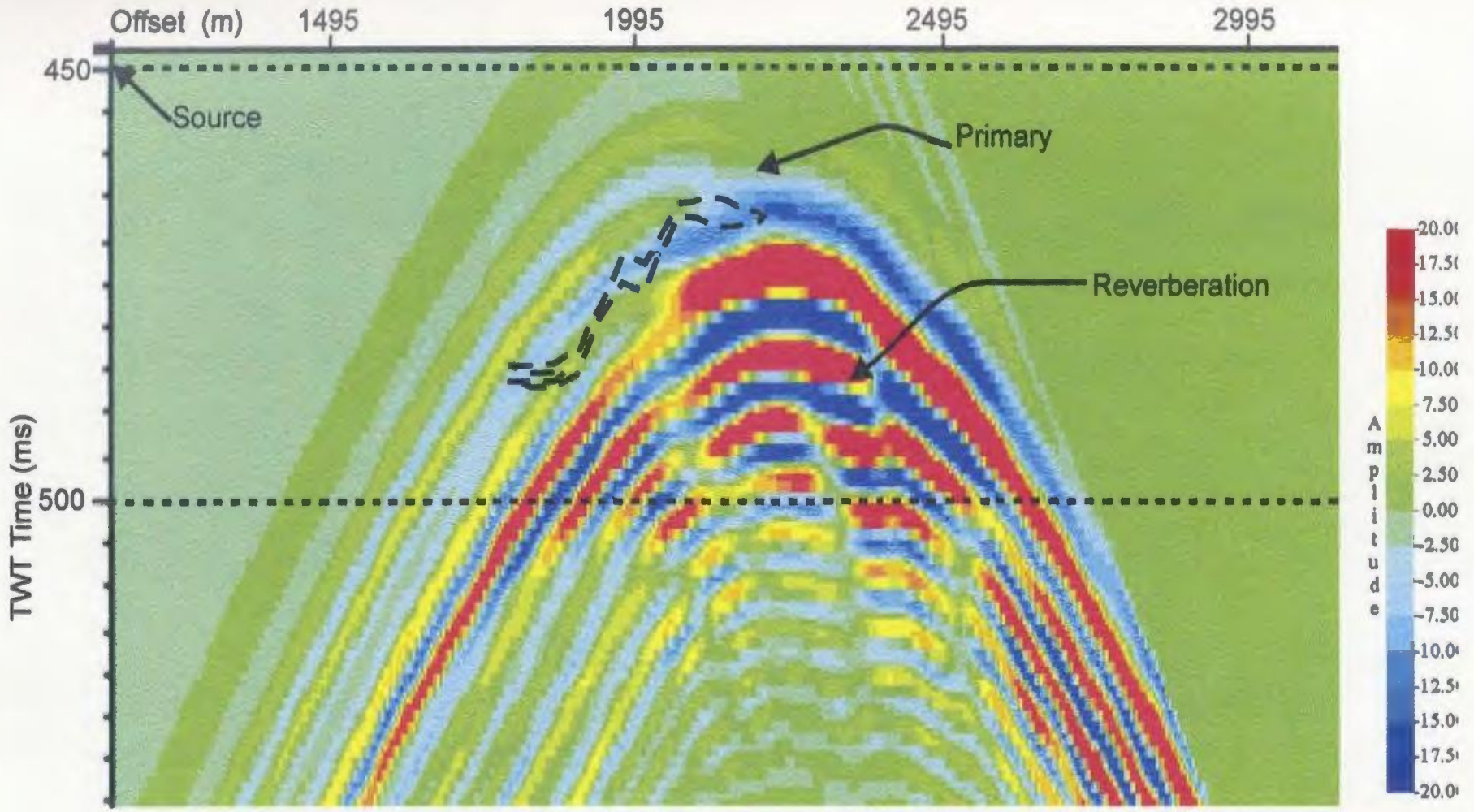

Figure 5.3-2: Shot record simulated using an acoustic FD algorithm with the source displaced 2000 m down-dip of a target dipping to the left. Diffraction amplitudes are strong at the apex of the diffraction and also along the up-dip side of the body. An outline of the model is shown to aid in the interpretation.

The diffraction response caused by the down-dip edge of the deposit is displaced down-dip. An interesting feature of this figure is the strong reverberations of the same strength as the primary. The presence of multiple reflections can cause ambiguity in the interpretation of field data which always contains ambient noise and have a low S/N ratio.

Figure 5.3-3 shows an elastic model for the Duck Pond deposit with the source located directly above its top. The P-wave diffraction response caused by the leading edge of the deposit is mapped by an amplitude trough at 310 ms TWT, with higher amplitude on the down-dip side of the leading segment but up-dip of the whole deposit. This amplitude trough persists to 750 m offset down-dip, but it is visible out to an offset of 995 m up-dip. The bottom of the deposit is mapped by peak in which the amplitude is displaced down-dip, since this segment of the deposit is dipping in the same direction.

The converted-mode SV-wave diffraction response occurs at 384 ms TWT. This travel time includes the down-going P-wave with 155 ms and the up-going converted-mode SV-wave diffraction with 229 ms. These SV-wave diffractions are weak within an aperture of 16° (250 m offset) either side of the source, since mode conversion is weak at narrow angles of incidence (see §2.3). Again, the amplitudes of these diffractions are higher up-dip, because the leading segment of the deposit is dipping in the opposite sense to the overall dip of the deposit. The amplitude trough caused by the top of the deposit becomes dim at an offset of 875 m up-dip of the deposit, but it retains the same strength at all offsets down-dip. Similar to the P-wave diffraction response, the bottom of the deposit is mapped by an amplitude peak which is wholly displaced down-dip. In this figure, the diffracted SV-wave

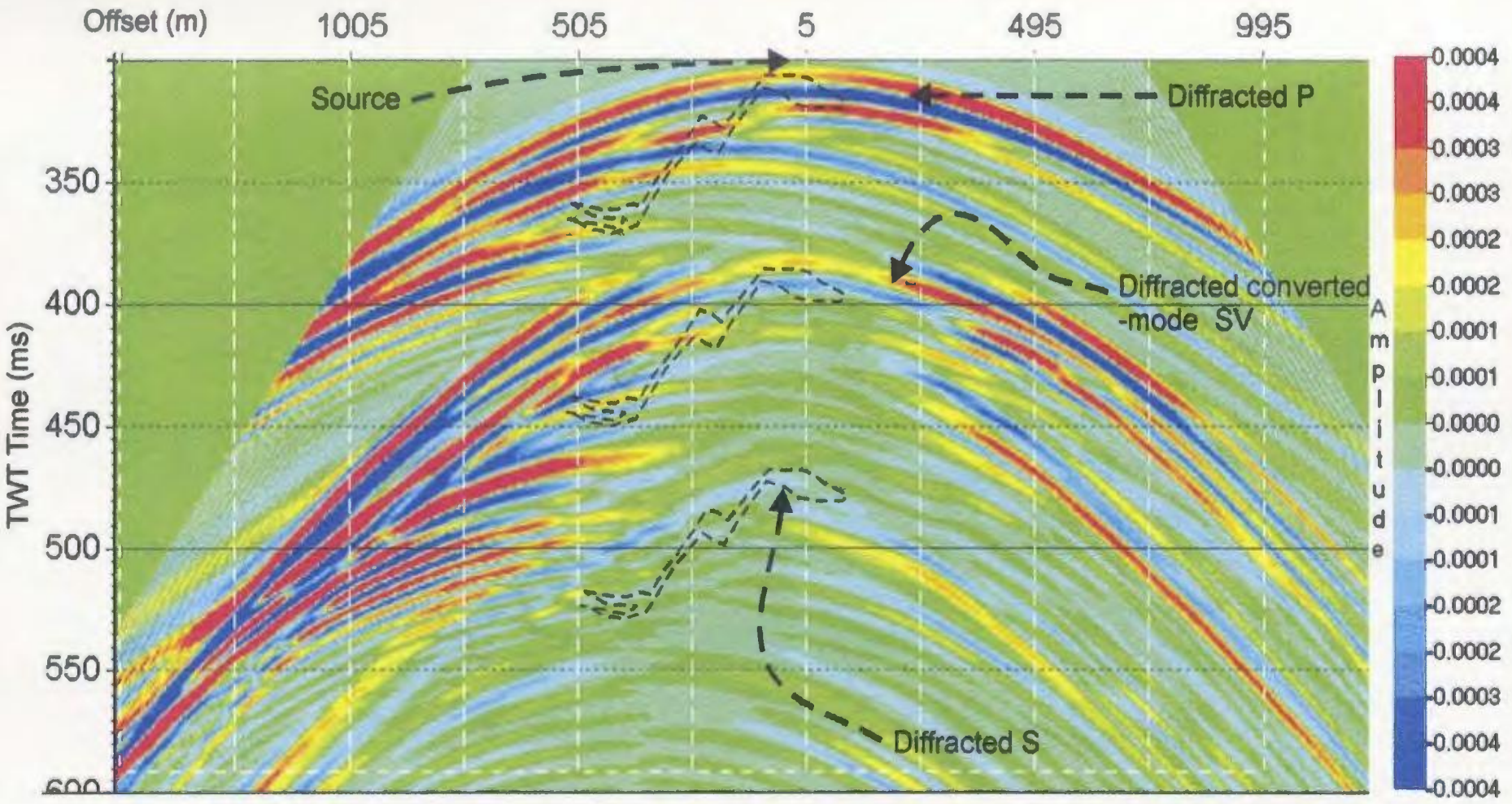

Figure 5.3-3: Shot record simulated using an elastic FD algorithm for a source above the Duck Pond deposit. Outlines of the deposit are shown to facilitate interpretation. Note that the diffracted converted-mode SV-wave occurs with similar amplitude to the P-wave, while the diffracted S-wave has a much lower amplitude. In all these, the diffraction amplitudes are stronger on the down-dip side of the deposit segments causing them.

events are of the same strength as the diffracted P-waves. This suggests that the SV-wave should be strong on P-wave seismic records and can cause destructive interference during stacking if not sufficiently suppressed since it has opposite polarity to the P-wave.

The diffraction response of the top of the deposit caused by the incident S-wave is a low amplitude trough at 458 ms TWT. This event is weak and discontinuous because of the relative scaling by the first two events, but also because the S-wave impedance contrast is weak for this deposit (see Chapter 2).

5.4 Discussion and Conclusions

The numerical models show that the diffraction pattern caused by a dipping target consist of amplitudes displaced in the down-dip direction (note that the first breaks were muted). The degree and direction of amplitude displacement is dependent on the location of the source with respect to the target. For a source above a dipping target, the diffraction amplitudes are displaced wholly down-dip. In all cases, the diffraction propagates with the background seismic velocity and is hence sub-parallel to the first breaks. The energy in the far offsets ($\geq$500 m) is coherent and strong for both P and SV-waves.

The situation is more complicated when the target occurs at a shallow depth, which results in the diffraction pattern from the target appearing close to the first breaks, such that it is impractical to remove the latter using conventional methods without also removing the signal. In addition, since the coherent signal occurs in the far offsets, wavelet stretching

caused by NMO correction is severe on the data. These stretched events must to be retained because they are the only available signal. Amplitude phase reversal with increasing angle of incidence is a problem for stacking because of destructive interference.

5.5 Interpretation

The numerical models show that a small, dipping target produces a predominantly diffraction seismic response with amplitudes displaced down-dip. For a complicated deposit composed of discrete segments with variable dip, the seismic response consists of diffractions with amplitudes displaced in the direction of dip of the individual segment. This phenomenon causes the overall seismic response to be weak because of the amplitude scattering and is partially responsible for the feeble seismic responses recorded on mineral deposits, despite their high seismic impedances. Furthermore, the situation is exacerbated in 2D data by the fact that some of the energy is directed out of the plane of the section. For this reason, 3D seismic surveys are critical for mapping small and complicated seismic targets encountered in mineral exploration.

The diffraction wavefields observed in the numerical models show amplitude phase reversals which occur at various angles of incidence. The amplitudes are displaced either up-dip or down-dip of the deposit, depending on the location of the source. These amplitude polarity reversals occur at different angles of incidence for different source locations and are therefore not diagnostic. The implication of the polarity reversals is that the events will be

attenuated by destructive interference during CMP stacking. Their presence suggests that offset-limited CMP stacking could be used to achieve better imaging of small seismic targets. However, this approach fails because the offset for the phase reversal is different for each CMP location due to the variation in the geometry of the deposit. In addition to polarity reversals, the acoustic numerical models show reverberating seismic events caused by internal multiple reflections within the deposit. These events are of the same amplitude and phase as the primary events and would impact strongly on the imaging of the seismic target in field data.

The elastic numerical model for the Duck Pond deposit shows that the diffracted SV-wave is strong in the medium to wide angles of incidence. The diffracted S-wave image in Figure 5.3-3 is weak compared with the P and converted-mode SV-wave events, and is not likely to show above ambient noise in CMP stacks. This is not surprising considering the discussion in §2.2 and Figure 2.2-2 which show that the S-wave reflectivity of mineral deposits is relatively weak compared with that of the P-waves.

CHAPTER 6

6.0 FIELD DATA

6.1 Introduction

The Tally Pond Volcanic Belt (NF) and its mineral deposits are described in MacInnis and MacKenzie (1988), MacKenzie and Squires (1988), and Squires et al. (1990). The deposits hosted by these rocks are described in Chapter 3 and modelled in Chapter 5. In this chapter, data acquisition, processing, and interpretation of seismic data recorded in Tally Pond are described. The deposits are affected by faulting which juxtaposes mafic with felsic volcanic rocks. Exploration shows that potential mineral deposits may occur at depths >500 m, beyond the resolution of conventional potential field and electrical techniques. Also, the deposits occur near graphitic sediments which make electrical methods ineffective.

To test the potential of deep ground and the ability of reflection seismic methods to detect or image the deposits, a seismic profile was acquired in Tally Pond in 1998. It coincides with the section in Figure 3.2-2 and is located strategically across the Duck Pond deposit, lying at a depth of 250-500 m and dipping 35-40° SW, to provide control for the interpretation of data at greater depths. Industry processing of the seismic data shows poor imaging even in areas where mineralization occurs such as the Duck Pond deposit.

Processing and interpretation of these data was completed in order to investigate the factors that control the detection or imaging of mineral deposits with reflection seismic methods. An attempt is made to identify the optimal processing parameters since routine processing failed to detect or image the mineral deposits themselves.

6.2 Data Acquisition

The objective of the seismic survey is to detect or image the Duck Pond deposit and possibly new ones at depths of 0.25-3 km. This objective dictates that small source to receiver offsets (relative to the target depth) are recorded with a sufficiently long line loength to detect or image the shallow and deep targets simultaneously. Since the targets are small with complicated geometries, a high dominant frequency and broad bandwidth is necessary to increase the resolution of the data. This was accomplished with small explosive charges, and significant effort was directed at effective geophone coupling.

The acquisition geometry of the seismic line is shown in Figure 6.2-1, and the shot co-ordinates are included in Appendix B. The data were recorded with a 715-channel Geo-X Aram24 digital telemetry system, using 14 Hz Oyo Geospace geophone groups at 10 m intervals. The groups comprised nine equally-spaced (0.25 m) geophones in a 2 m linear array oriented parallel to the seismic line. The geophones were planted firmly in the ground and covered with snow to reduce wind noise. The geophone groups were laid out along the entire line (7085 m) prior to recording and were all live for each shot with 712 data and 3 auxiliary channels. Data acquisition proceeded by moving the source through the fixed geophone groups. This procedure differs from conventional CMP acquisition where both the source and receivers move forward along the line (roll-along). The long source to receiver offsets (7 km) allow the direct and refracted waves to penetrate deep into the ground, so that a good estimate of the seismic velocity can be made.

The signal source was 500-850 g dynoseis boosters placed at the base of soft ground

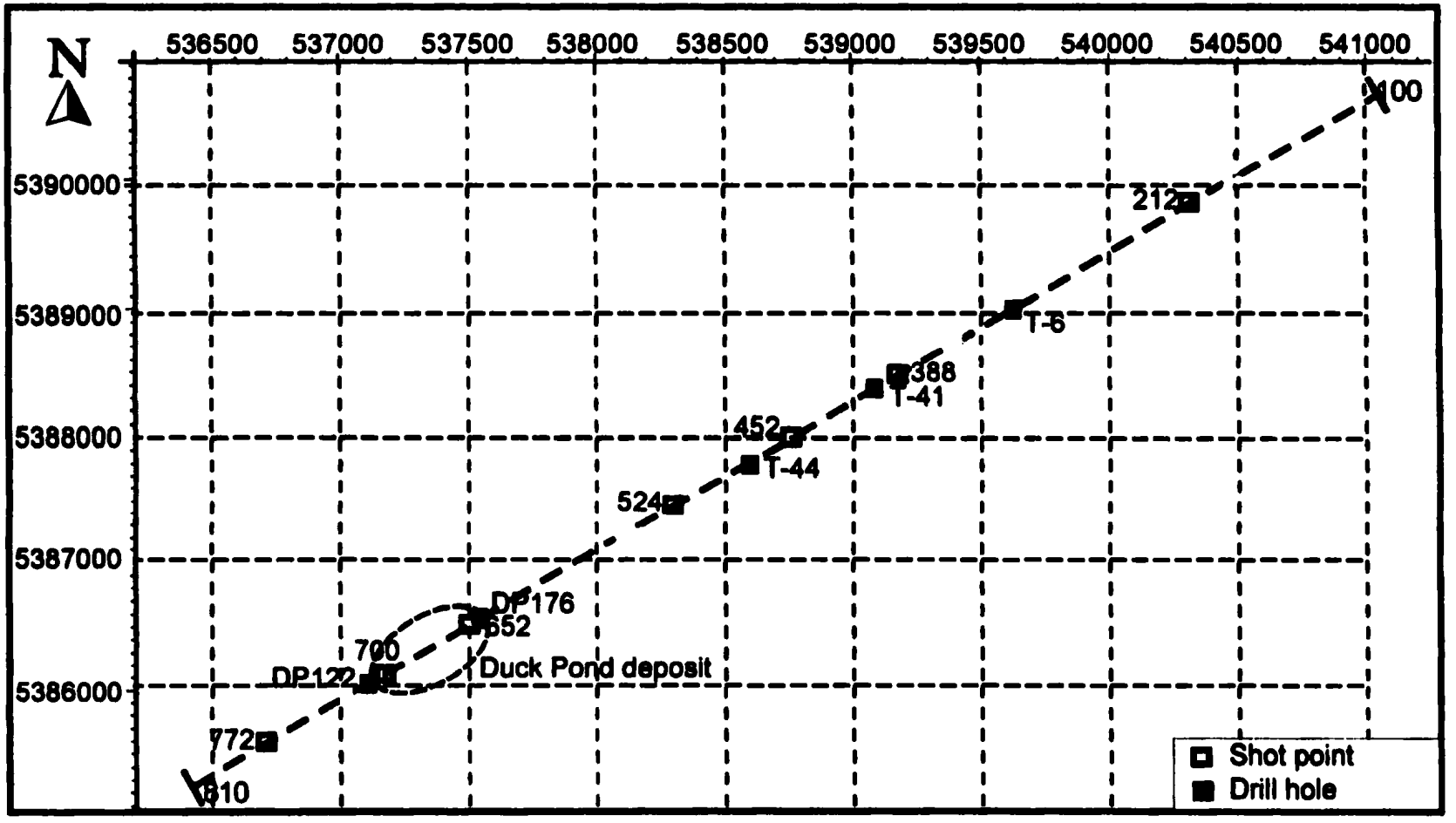

Figure 6.2-1: Survey plan of the seismic line. Drill holes DP122 and DP176 are on the limits of the Duck Pond deposit, and the Duck Pond fault outcrops near T-6. These drill holes provide control for the interpretation of the data. The co-ordinates are in metres, projection UTM and datum NAD27.

(2-6 m). A source interval of 20 m was used initially for stations 100-180 to build up the fold, increased to 40 m for the middle stations 184-728, and reduced again to 20 m for the end stations 730-810. The maximum fold achieved with the geometry described here is 234. Surface source arrays made from C-10 explosive cones were used at stations where buried explosive could not be used. Overall, 234 shots were recorded to 3,000 ms TWT with a 1 ms sample interval. The data show clear first breaks, but they are dominated by strong converted-mode SV-wave refractions, ground-roll, and an aliased air wave. Drill logs show that the ground consists of ~15 m of overburden above a high velocity basement. The base of this overburden produces converted-mode SV-wave refractions from the incident P-wave, which are difficult to remove from the signal because they have the same spectral content.

6.3 Data Processing

The longitudinal section in Figure 3.2-2 shows that seismic reflections might be produced by the surface of the Duck Pond thrust fault from the near surface to ~690 ms TWT (~2,000 m at 5,790 m/s). The mafic and felsic volcanic rocks above the Duck Pond fault are thin and altered, so that the acoustic impedance contrast between the units is small. Although the Duck Pond deposit is thin and dipping, it has a large acoustic impedance compared with the felsic volcanic rocks, and it should produce a strong seismic response. The interfaces between the mafic and felsic rocks should produce a significant seismic response, as indicated in §2.2. The interface between the graphitic sediments and the felsic

rocks is sub-horizontal and should be mapped by the seismic data. Due to the high velocity of the rocks, the first 1,500 ms TWT are adequate to image the data to ~3 km, hence only this time window is used in this discussion.

The processing objective for the seismic data is to enhance the S/N ratio to enable identification of the anomalies caused by the known rock interfaces, and to identify similar seismic anomalies elsewhere in the data. However, despite the expectations cited above, the shot gathers show only weak reflections and/or diffractions in the medium to far offsets. Figure 6.3-1 shows a typical shot gather from the data with clear direct and refracted waves, converted-mode SV, ground-roll, and air blast, but only a weak reflection or diffraction event. One reason for the absence of clear reflections in the near to medium offsets is that since the velocity is very high, seismic events arrive early and may be overridden by the direct and refracted waves. One possible way to enhance the reflections is to create a super CMP stack with bins incorporating several group intervals. Such a procedure causes reflector smearing, however, it enhances the lateral continuity of seismic events, making them easier to identify. The super CMP stack (Figure 6.4-2) maps the structure and most of the expected seismic events indicated earlier.

The data were processed using the conventional CMP-based (Table 6.3-1) and aplanatic prestack depth migration methods. For the CMP-based processing, the source-receiver offsets were restricted to ≤ 3 km. Data processing commenced with editing to remove bad traces and check for reversed polarity. CMP bins were defined at half the group interval (5 m) parallel to the line but 20 m across because of bends in the survey line.

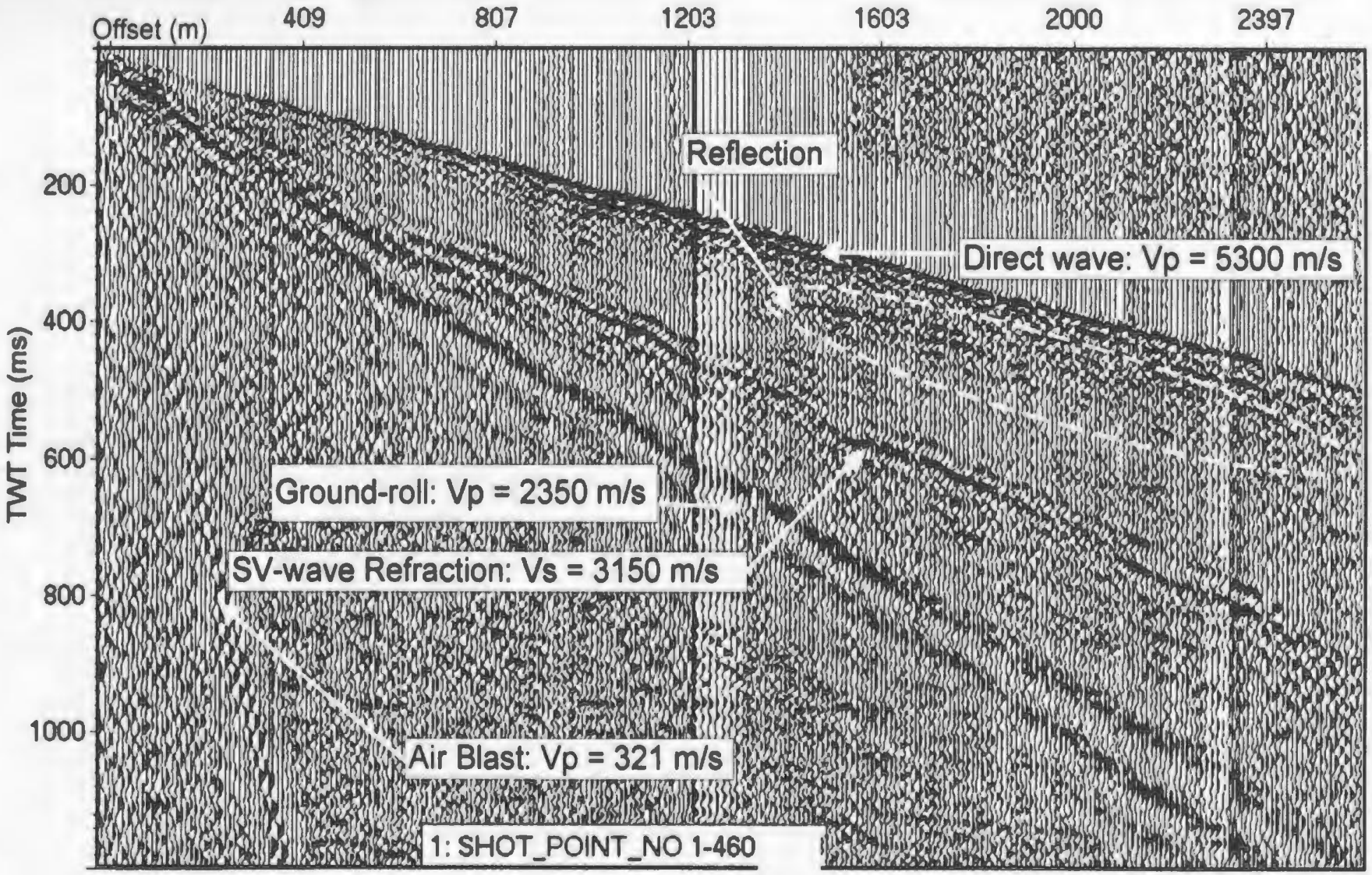

Figure 6.3-1: A typical raw shot gather from the seismic data. The record is dominated by ground-roll and SV-wave refractions. The latter have the same spectral content as the reflections and diffractions. The traces are sorted by offset, 200 ms AGC gain.

Automatic first break picking was performed with the Vista 2.50D™ program. Refraction statics analysis was performed using the plus-minus method (Hagedoorn, 1959) with the Vista 2.50D™ program and also the generalized reciprocal method (GRM) (Palmer, 1981) with the Hampson-Russell GLI3D™ program. Source and receiver statics calculated by both methods were applied alternately to the data. The data were corrected for geometric amplitude decay with an exponential gain function, an exponential time power function, and an amplitude mean function over a time gate of 0-1,000 ms. Spiking deconvolution with an operator length of 120 ms was used to improve the vertical resolution of the data. A Butterworth bandpass filter of 20/25-100/120 Hz was used after deconvolution. A narrow F-K pie slice dip filter was also used to remove the SV-wave refractions, air blast, and ground-roll from the data.

Velocity analysis was performed using semblance and common offset stacks centred on CMPs at a coarse interval of ½ km because, even though the structure is complicated, the rocks have similar seismic velocities. Different values of the NMO stretch mute were tested to determine the one appropriate to preserve the signal caused by an object to the SW of the Duck Pond deposit. It was determined from the common offset stacks (Figure 6.3-2) that a 50% NMO stretch mute gives the best results. It can be seen in Figure 6.3-2 that a stretch mute of 20% removes the entire signal caused by the dipping body. This situation arises in high velocity rocks because the seismic events arrive early and are restricted to the medium to far offsets if the target is dipping. Seismic events in both cases suffer more from NMO stretching, and are lost from the data if a conventional stretch mute of 20% is used.

Table 6.3-1: Summary of the data processing sequence and parameters.

Trace Edit	check for trace reversals, kill bad traces
Geometry	datum: 305 m.a.s.l, weathering and replacement velocity: 5,300 and 5,600 m/s, calculate bulk statics from up-hole times, CMP binning: first 40 x 20 m for the super CMP stack, 5 x 20 m for the regular CMP stack, calculate source-receiver offset and fold
Refraction statics	automatic first break picking, refraction statics analysis: (i) Plus-minus method (Hagedoorn, 1959) - Vista 2.50D™, (ii) GRM method (Palmer, 1981) - GLI3D™
Amplitude correction & Noise attenuation	exponential gain (1.85), exponential time power (0.45), amplitude mean (1.00, 0-1,000 ms), apply field statics, spiking deconvolution: time window 0-1,000 ms, operator length 120 ms, Butterworth bandpass filter: 20/25-100/120 Hz, F-K velocity dip filter
Velocity analysis	pick interval velocities on semblance and common offset panels at ½ km CMP intervals, design and test NMO stretch mutes: 20%, 50%, 75% and 95%
Residual statics, stack, and migration	NMO correction, front-end mute: 40 ms below first breaks for near offsets ($\leq$500 m), and 10 ms below first breaks thereafter, brute CMP stack, residual statics: stack power method (Ronen and Claerbout, 1985), final stack, F-K time migration

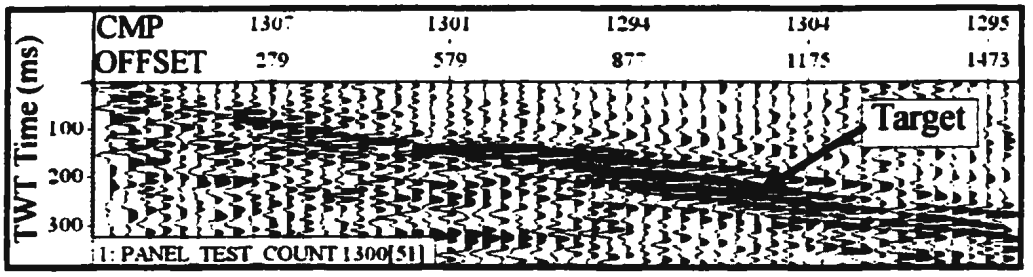

(A) No NMO

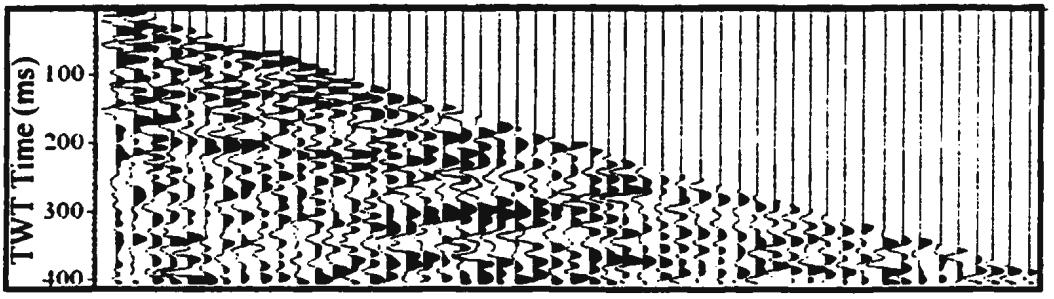

(B) NMO: 20% stretch mute

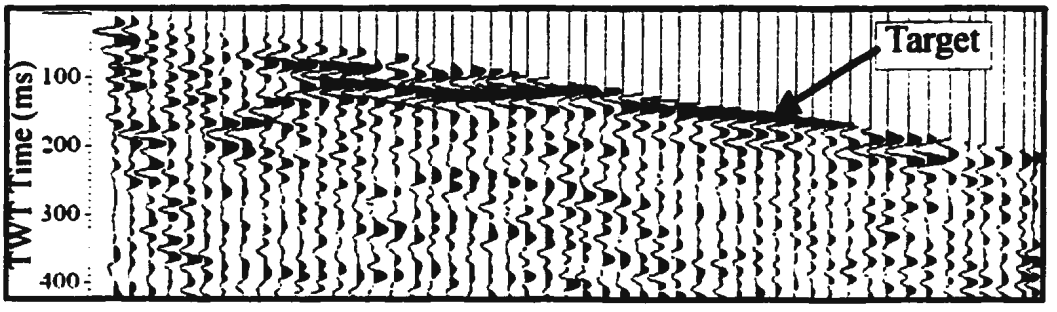

(C) NMO + 50% stretch mute

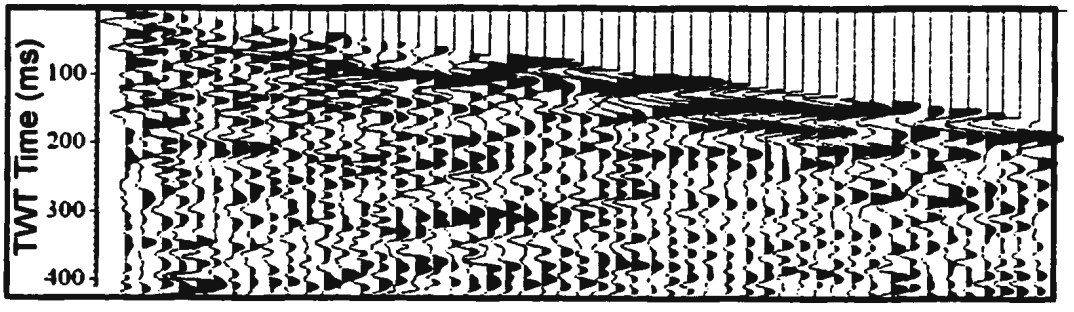

(D) NMO + 95% stretch mute

Figure 6.3-2: Common offset stack centred on CMP 1300. The events at 579-1473 m offsets are caused by a dipping body. (A) before NMO correction, (B) to (D) after NMO correction with the stretch mutes shown. Note that a 20% stretch mute removes all evidence of the target.

Subsequently, a front- end mute was applied to the data at 40 ms below the first breaks in the near offsets, but reduced to 10 ms below the first breaks in the middle and far offsets ($\geq$500 m).

Initial CMP stacking was used to produce a brute stack for the calculation of residual statics with the stack power method (Ronen and Claerbout, 1985). The best residual statics were obtained with a no model building option, and trials show that using a model-guided statics calculation leads to a poor stacking of the dipping object below station 700. The residual statics were applied before the final CMP stacking. The data were subsequently migrated with the F-K time migration method.

After geometry definition and preprocessing, the data were also processed with the aplanatic prestack depth migration method of Liner and Lines (1994). The velocity model (Figure 6.3-3) for this technique was created with the DepthWorks™ program using the migrated CMP stack constrained with the drill logs. It is defined for the true medium velocity with an 8 x 5 m grid to a depth of 3000 m, but it is poorly constrained at depths beyond 1500 m because of limited information. The aplanatic prestack depth migration method selectively images only the seismic events whose travel time equations describe elliptical trajectories between the source, reflector, and receiver locations. This obviates the need for muting and dip filtering of events with a linear moveout because they are minimized in the imaging process. Preferential imaging of events is desirable if the data contain noise with the same spectral content as the reflections and diffractions, as this can be difficult to with other processing strategies.

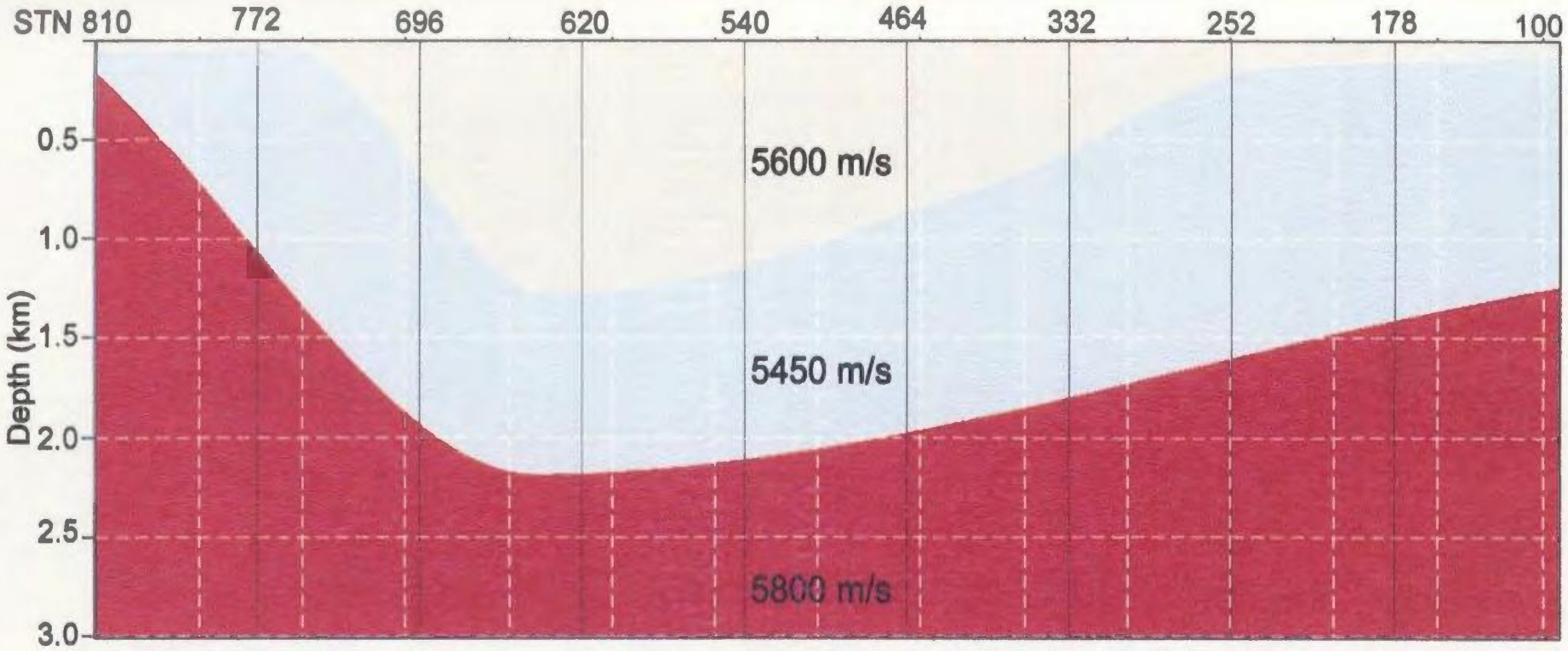

Figure 6.3-3: Velocity model for the aplanatic prestack depth migration. The model was constructed using the migrated CMP stack and constrained by the drill holes. It is defined for an 8 m vertical by 5 m horizontal grid.

6.4 Results and observations

Figure 6.4-1 is a migrated CMP stack with a 50% NMO stretch mute and maximum source to receiver offsets of 3,000 m. In this stack, the subsurface fold is low compared with that of the super CMP stack, and the seismic events are more discontinuous, especially in the near surface. However, the seismic response caused by an object located to the south of the Duck Pond deposit is clearly mapped at stations 700 to 772. This event consists of a trough over peak amplitude pattern dipping to the left and persistent over 500 m. The Duck deposit is mapped by a similar but weak seismic response at stations 652 to 696, which also extend over 500 m.

The surface of the Duck Pond fault is mapped in Figure 6.4-1 by discrete seismic events from near the surface at station 252 to a depth of ~1,450 m (500 ms TWT) at station 652. The mineralized volcanic rocks below this fault plane are seismically transparent but their interface with the graphitic argillaceous sediments is clearly mapped. Two other fault planes parallel to the Duck Pond fault are mapped below the graphitic argillaceous sediments. The shallower fault plane is mapped from the near surface at station 100 to a depth of ~2,316 m (800 ms TWT) at station 620. The second fault plane is mapped from 450 ms TWT at station 100 to 800 ms TWT at station 500 (~ 4 km). These faults bound rocks with a different pattern of reflectivity from those above and below, and contain rock units displaced by faults dipping to the right.

Figure 6.4-2 is the super CMP stack before migration and it also shows the seismic response caused by a body located at stations 700 to 772 and dipping to the left, composed

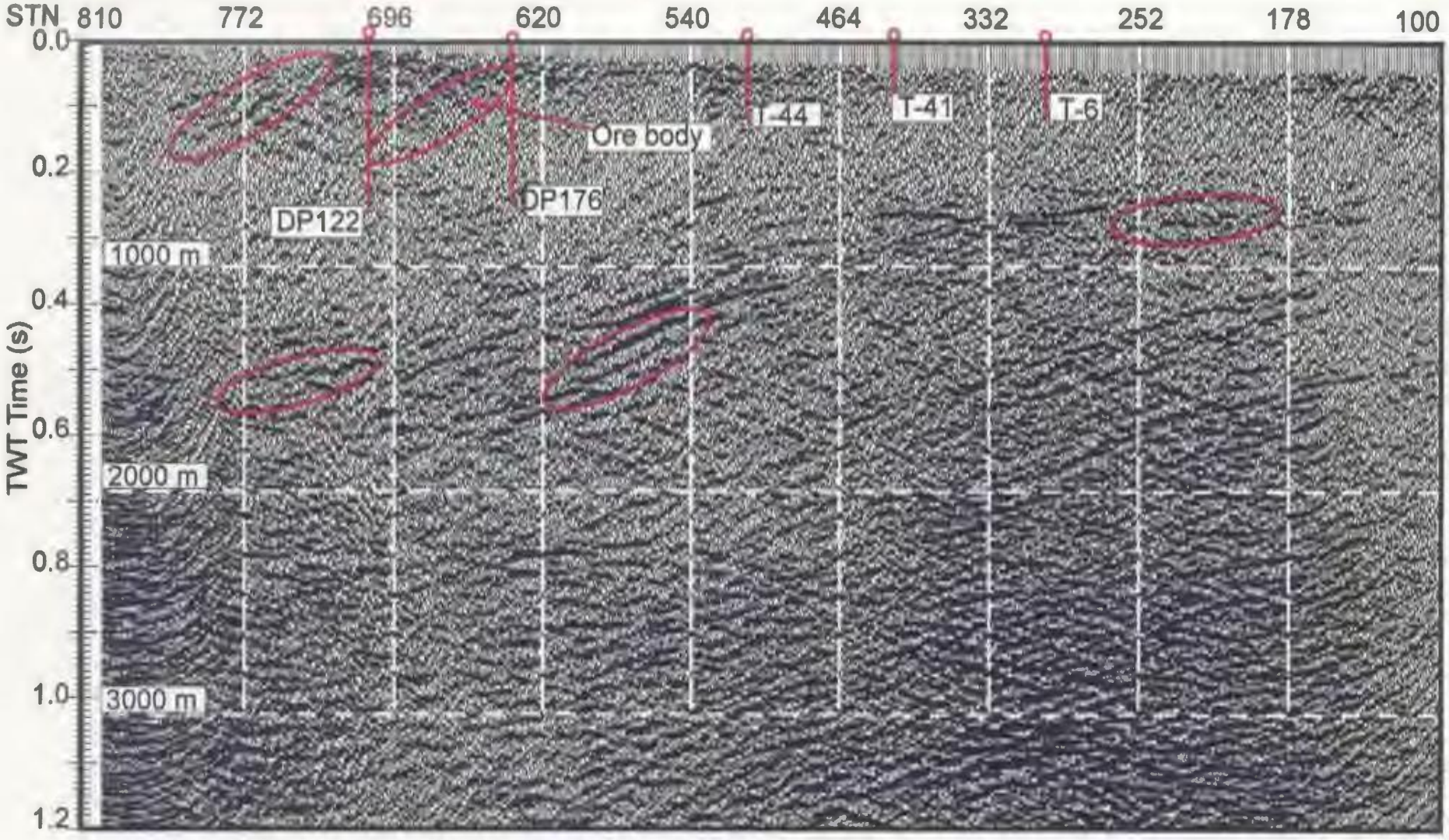

Figure 6.4-1: Migrated conventional CMP stack. Note the structure clearly imaged below stations 700 to 772.The Duck Pond deposit is very weakly discernible between drill holes DP122 and DP176. Trace spacing is 20 m, i.e every 4th trace is plotted. The events indicated with ellipses are possible exploration targets.

of an amplitude trough over peak pattern. This event persists over 13 traces (520 m). Other seismic events of a similar character and lateral extent are indicated with ellipses of the same size as that drawn around the latter. These events are distinctive in that they are discordant to the dominant structure and occur in the mineralised felsic volcanic rocks. They are thus possible targets for further exploration.

The Duck Pond fault is mapped at shallow depth near drill hole T-6 and down to 500 ms TWT (~1,450 m) at station 696. The mineralised felsic volcanic rocks underlying the Duck Pond fault are seismically transparent, but their contact with the graphitic argillaceous sediments is clearly mapped. The sub-horizontal seismic events mapped within the graphitic argillaceous sediments are likely to be caused by the mafic dykes present in Figure 3.2-2. A strong seismic event occurs at 800 ms TWT on the left of the super CMP stack and can be traced across the entire section. This event becomes shallow between stations 540 and 620 (~750 ms TWT) and dips downward henceforth to the right. The reflection patterns above it and below the Duck Pond fault consist of domains of seismic reflections displaced by faults dipping to the right. The rocks below it show poor reflectivity and hence are probably crystalline basement. The events discussed hitherto are traced in the migrated super CMP stack and are the basis of the interpretation presented in Figure 6.5-1.

Figure 6.4-3 shows the prestack depth section. It is dominated by migration noise possibly because of a poor choice of the migration velocity and also reduced ray path sampling near the edge of the section. Nevertheless, most of the seismic events identified in the CMP stacks are imaged clearly in the prestack depth section, with correct dips and

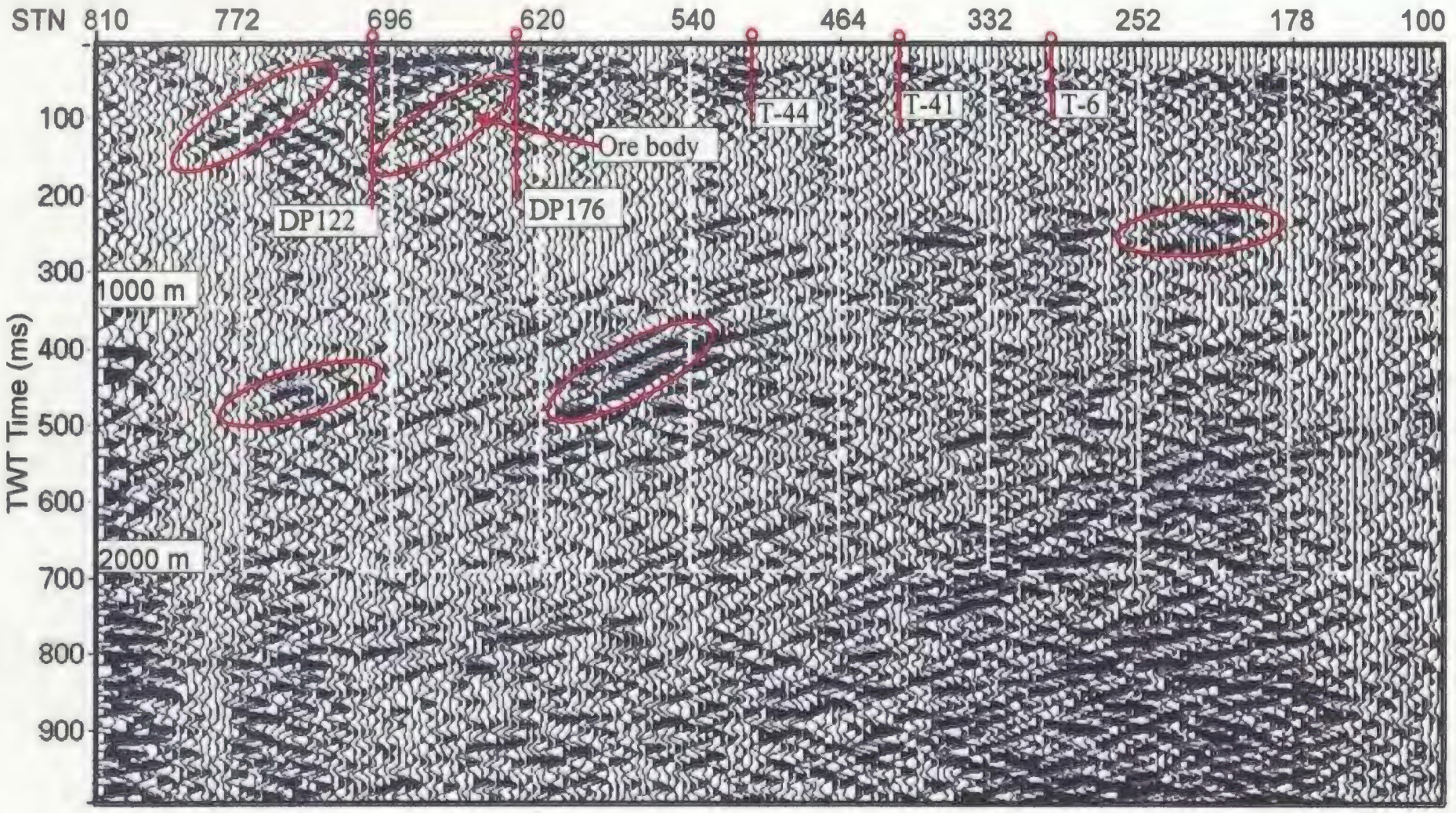

Figure 6.4-2: Super-CMP stack before migration. Note the dipping event clearly imaged below stations 700 to 772. The Duck Pond deposit is only barely detectable between drill holes DP122 and DP176, but the structure is imaged well. Trace spacing is 40 m. A depth grid is overlain to facilitate event identification and interpretation.

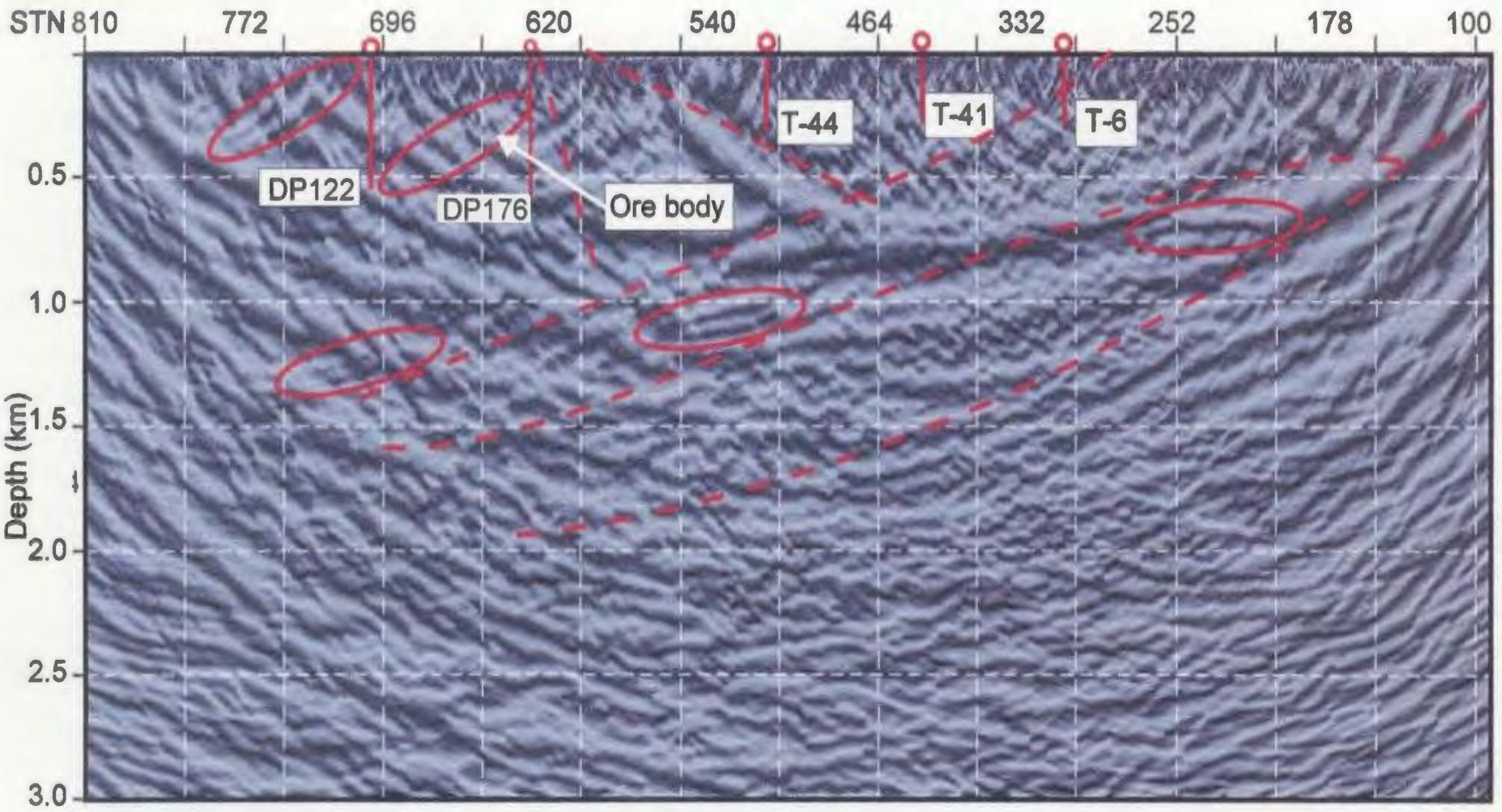

Figure 6.4-3: Aplanatic prestack depth section (grey scale) of the seismic data. The superimposed lines indicate structure which is also identified in the CMP stacks. The Duck Pond deposit is detected very weakly between stations 620 and 696. The areas indicated with ellipses are also identified in the CMP stacks and are hence potential exploration targets.

locations. The prestack depth section has imaged the near surface structures, but the deep structure is obscure because of limited geological control. The Duck Pond deposit is weakly detected below station 652 with a trough over peak amplitude pattern like that in the CMP stacks, and dipping to the left.

6.5 Interpretation

Figure 6.5-1 shows an interpretation of the migrated super CMP stack. The structure consists of thrust faults with a sole thrust at a depth of 2,316 m (800 ms TWT). The sole thrust is sub-horizontal between stations 540 and 810 (~3 km), and dips to the right of the section between stations 100 and 540 (~4 km). A thrust fault branches from the sole thrust at station 620 and propagates upward to outcrop near station 772. This thrust fault has carried a block of the felsic volcanic rocks to the surface from a depth of ~1,700 m.

The Duck Pond fault is terminated at 1,450 m below station 696 by the outcropping thrust fault. Within this framework, the Duck Pond fault appears to be a back-thrust which accommodates the differential strain created by the movement of the main thrust fault that terminates it. Similarly, the faults below and parallel to the Duck Pond fault are a brittle response to the differential strain caused by the movement of the main thrust. These back-thrusts bound rocks which are displaced by faults dipping to the right.

The structure below station 540 is similar to that south of the Duck Pond deposit, suggesting that these rocks are part of the volcanic rocks that host the Duck Pond deposits.

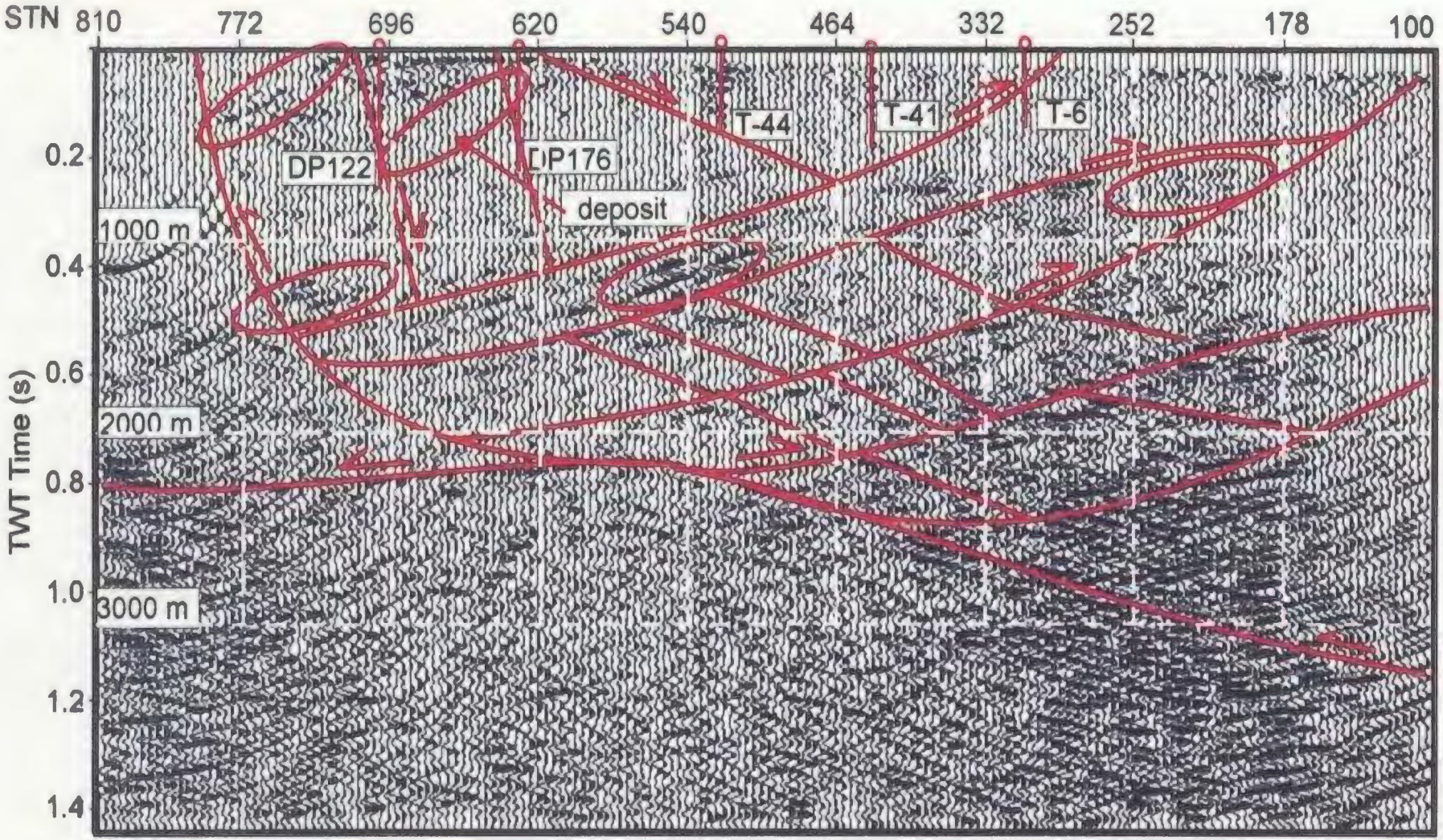

Figure 6.5-1: Migrated super CMP stack showing the structural interpretation of the Tally Pond seismic data based on the seismic events in this stack, the conventional CMP stack, and the prestack depth section. Note that the Duck Pond deposit is not visible below station 652, as in the un-migrated stack, but the structure is imaged well. A depth grid is overlain to aid the identification and interpretation of events.

Hence, there may be additional deposits at 1,500 m to 2,000 m below station 540. The argillaceous sediments below the mineralized felsic volcanic rocks are dominated by horizontal structures from stations 100 to 464. To the left of station 464, the structure comprises rock units separated by NE dipping faults.

6.6 Discussion and Conclusions

The seismic data were acquired with the objective to detect or image the deposits and structure at depths of 0.25 to 3 km in order to improve the geological model for further exploration. The results show that a modified data acquisition design and a CMP-based processing sequence successfully mapped the structure but did not detect the deposit directly with a strong, convincing seismic response. This is not surprising because the shot gathers above the deposit do not show any seismic event caused by it. The longitudinal section through the deposit (Figure 3.2-3) shows that it comprises segments with different dips, and none of these segments exceed the radius of the first Fresnel zone. For this deposit, only a limited amount of back-scattered energy resides in the plane of the seismic section or the first Fresnel zone, and hence 3D seismic data are required to obtain a better response. The analogue models (Chapter 4) show that 3D seismic data are suitable to detect and image small and complicated targets because it enables better resolution and provides time slices.

In data processing, it is critical to restrict NMO stretch muting to a liberal value of 50%. Conventional CMP stacking uses NMO stretch muting of 20%, which allows

minimum wavelet distortion in the CMP stack. Apart from lowering the frequency in the CMP stack, a stretched wavelet prevents a match from being made with sonic logs for acoustic impedance inversion. However, in mineral exploration, it is critical to detect or image the deposit, and acoustic impedance inversion is of less priority since density and sonic logs are generally not available.

CHAPTER 7

7.0 CONCLUSIONS

Direct detection and imaging of massive mineral deposits with reflection seismic methods requires an in-depth understanding of their density-driven acoustic impedance contrast and the effects of geometry on their seismic expression. This thesis was conceived to examine these issues through a theoretical analysis of the density-driven acoustic impedance contrast and both analogue and numerical seismic modelling. In this way, the appropriate seismic data acquisition and processing parameters for mineral exploration were identified. Knowledge of these parameters is needed to optimize the search and improve the chances of making new discoveries of mineral deposits with reflection seismic. In this chapter, I summarize the important contributions of this thesis towards the understanding of the issues enumerated above, draw the relevant conclusions, and make some recommendations pertinent to the exploration of mineral deposits with reflection seismic.

The velocity-density relation for massive mineral deposits shows that they possess high density-driven acoustic impedances compared with their host silicate rocks, which suggests that they should produce strong P-wave responses in seismic data. The effect of density on the reflection coefficients is strong at and near normal incidence (0-20°). In addition to density, the magnitude of the reflection coefficients is affected by the Poisson's ratio at intermediate to wide angles of incidence (20-60°). P-wave reflection coefficients for a wholly density-driven acoustic impedance contrast are strong near normal incidence even for mineral deposits with a low density contrast of 1.20. This strongly suggests that MVT

responses before migration, and strong but discontinuous responses after migration. Migration collapses the diffractions to their points of origin in the model, thereby causing the seismic response to be discontinuous. This does not enhance the detection or imaging of small seismic targets where the entire signal consists of diffractions but it rather makes the response hard to detect. For this reason, it is easier to detect the diffraction responses in field data before migration.

The analogue models show that the 3D seismic response of small targets consist of closed, circular diffraction patterns in time slices, which delineate the targets precisely. Such diffraction patterns allow easier identification of similar targets in field data. Hence, 3D data are valuable in mineral exploration not only for their enhanced spatial resolution, but to provide time slices needed to identify small and complicated targets, and also to construct time structure maps. Furthermore, it is shown with the cylinder-shaped model that the surface relief and attitude of a target has a profound impact on the seismic response.

For a target with discreet segments of variable dip, the diffraction amplitudes are displaced down-dip of each segment, such that some energy is directed out of the plane of the section in 2D data. For this reason, 3D seismic data are critical for mapping the small and complicated seismic targets likely to be encountered in mineral exploration. The field data successfully imaged the structure in Tally Pond but failed to detect the deposit directly with a strong, convincing seismic response. The longitudinal section through the Duck Pond deposit (Figure 3.2-3) shows that it comprises segments with different dips, and none of these segments exceed the radius of the first Fresnel zone.

wave imaging of massive mineral deposits.

I have used cross-sections of typical massive mineral deposits in Chapter 3 to show that VMS and Ni-Cu deposits are commonly of a small areal extent and have complicated geometries. They are generally lens-shaped and low aspect ratio, with dimensions less than the width of the first Fresnel zone at depths exceeding 600 m. Because of the limited areal extent and complicated geometries, these mineral deposits typically produce diffraction seismic responses in field data. 2D normal incidence synthetic seismograms for the cross-sections of the typical mineral deposits show continuous diffraction seismic responses before migration, and discontinuous seismic responses after migration.

Migration collapses the diffraction amplitudes to their points of origin at the apices of the diffraction hyperbolas, which is its intended purpose in less complicated geology where specular reflections dominate. This preferentially enhances the specular reflections, removes the diffractions, and repositions the reflections such that they are geometrically correct. However, this does not enhance the detection or imaging of small seismic targets where the seismic response consists entirely of weak diffractions, but it makes the seismic response more difficult to detect above the noise level. For this reason, I conclude that it is better to detect the diffraction seismic responses in field data before migration, and migration should be performed after the potential target has been isolated.

I have shown with the analogue models in Chapter 4 that the 3D seismic response of small targets consists of closed, circular diffraction patterns in time slices, which indicate the location of the target precisely. Such diffraction amplitude patterns should allow easier

isolation of similar targets in field data. Furthermore, I have also shown with the cylinder-shaped model that the surface relief and attitude of a seismic target have a profound impact on the seismic response. Despite its complicated geometry, the cylinder-shaped model was mapped with a strong and unambiguous seismic response in time slices. From the foregoing, I conclude that 3D data are critical for mineral exploration, not only for their enhanced spatial resolution, but also because they provide time slices needed to identify small and complicated targets, and allow the construction of time structure maps.

Stacked seismic sections for the egg-shaped analogue model show events caused by the focusing effect of its convex surface, and internal multiples which obscure the event caused by the bottom of the model. Recognition of these events is especially important in the exploration for Cu-Zn mineral deposits which are smooth, convex lenses with sharp contacts against the host rock. Such mineral deposits possess a high density-driven acoustic impedance contrast and can cause strong internal multiples of the lens-focused events that would lead to ambiguity in the interpretation of the seismic data.

I have used numerical models to demonstrate that small, dipping targets produce diffraction seismic responses with amplitudes displaced down-dip. The diffractions show phase reversals occurring at intermediate to wide angles of incidence (30-60°) for different source locations with respect to the target. The phase reversals imply that the events will be attenuated by destructive interference during CMP stacking, and suggest that offset-limited CMP stacking could be used to achieve better imaging of small seismic targets. However, this approach fails in practice because the offset for the phase reversal is different for each

shot location due to the variation in the geometry of the deposit.

For a 3D target with discrete segments of variable dip, the diffraction amplitudes are displaced in the down-dip direction of each individual segment (note in Figure 3.2-3(A) that some segments of the Duck Pond deposit dip to the NE, while the average dip of the entire deposit is 35-40° SW). This causes the overall seismic response to be weak because of the scattering in opposite directions and different planes, and may be partially responsible for the weak seismic responses commonly observed on mineral deposit targets, despite their high acoustic impedances. The situation is particularly bad in 2D data because some of the energy is directed out of the plane of the section. From this, it is again apparent that 3D seismic surveys are critical for mapping the typically small and complicated seismic targets encountered in mineral exploration, because in this case the seismic energy will be captured from all planes.

2D seismic data were acquired at Tally Pond (NF) with the objective to detect or image the mineral deposits and fault structures at depths of 0.25 to 3 km to improve the geological model for further exploration. The data successfully mapped the fault structures but detected the Duck Pond deposit with only a weak seismic response. This is not surprising because even the shot gathers located directly above the Duck Pond deposit do not show any seismic event caused by it. The longitudinal section through the Duck Pond deposit (Figure 3.2-3(A)) shows that it comprises segments with different and even opposing dips, and that none of these segments exceed the width of the first Fresnel zone. For this deposit, only a limited amount of back-scattered energy resides in the plane of the seismic section or within

the first Fresnel zone, and hence 3D seismic data are required to obtain a better response.

Overall, the issues discussed in the preceding sections show that in order to successfully detect or image massive mineral deposits with reflection seismic techniques, it is important to examine the physical properties of the target rocks before hand. This thesis has clearly demonstrated that it is only through such an approach that an informed estimate of the appropriate data acquisition and processing parameters can be made. Finally, I conclude that the thesis has successfully achieved its goal of identifying the typical seismic response of metallic mineral deposits and elucidating on the behaviour of such a seismic response.

REFERENCES

Adam, E., Mathews, L., and Milkereit, B.,1998. 3-D seismic data processing for mineral exploration. SEG Expanded Abstracts, Houston.

Adam, E., Milkereit, B., Arnold, G., and Pineault, R., 1996. Seismic response of the Bell Allard ore body, Matagami, Quebec. Noranda Mining and Exploration Inc., Report Nº MN 2.5.

Adam, E., Milkereit, B., Mareschal, M., Barnes, A.E., Hubert, C., and Salisbury, M., 1992. The application of reflection seismology to the investigation of the geometry of near-surface units and faults in the Blake River Group, Abitibi, Quebec. Canadian Journal of Earth Sciences, 29, 2038-2045

Balch. S.J., Crebs, T.J., King, A., and Verbiski, M., 1998. Geophysics of the Voisey's Bay Ni-Cu-Co Deposits. SEG Expanded Abstracts, Houston.

Birch, F., 1960a. The velocity of P-waves in rocks to 10 kilobars, part 1. Journal of Geophysical Research, 65, 4, 1083-1102.

Birch, F., 1960b. The velocity of P-waves in rocks to 10 kilobars, part 2. Journal of Geophysical Research, 66, 2199-2224.

Boerner, D.E., Spencer, C.P., Wright, J.A., Caroll, P., and Reed, L.E., 1990. Developing new methods at an old mine: High-resolution seismic and electromagnetic mapping at Buchans mine. Engineering and Mining Journal, 191, Nº 7, 25-29.

Brown, A.R., 1991. Interpretation of three-dimensional seismic data. Third edition,

American Association of Petroleum Geologists, Tulsa.

Christensen, N.I., 1982. Seismic Velocities, in Handbook of Physical Properties of Rocks, Volume II, edited by Robert S. Carmichael, CRC Press Inc., Boca Raton.

Cooksley, J.W., 1992. Seismics - general discussion of seismic methods, in Practical Geophysics II, compiled by Richard van Blaricom, Northwest Mining Association, Spokane, pp 275-306.

Dahle, A., Gjrystdal, H., Grammeltvedt, G., and Hansen, S.T., 1985. Application of seismic reflection methods for ore prospecting in crystalline rocks. First Break, 3, Nº 2, 9-16.

DepthWorks™ 5.1, Landmark© Graphics Corporation, 1993. Houston, U.S.A.

Diering, D.H., 2000. Mining at ultra depths in the 21st century. The Canadian Mining and Metallurgical Bulletin, 93, Nº 1036, 141-145.

Eastoe, C.J., and Gustin, M.M., 1996. Volcanogenic massive sulphide deposits and anoxia in the Phanerozoic oceans. Ore Geology Reviews, 10, 179-197.

Eaton, D.W., 1999. Weak elastic scattering from massive sulphide ore bodies. Geophysics, 64, Nº 1, 289-299.

Ebrom, D.A., and McDonald, J.A., 1994 (eds). Seismic Physical Modeling, *in* Seismic Physical Modeling, edited by Daniel A. Ebrom and John A. McDonald. Geophysics reprint series Nº 15, Series editor Franklyn K. Levin, Society of Exploration Geophysicists, Tulsa, pp. 1-3.

Fowler, C.M.R., 1990. The Solid Earth, an introduction to global geophysics. Cambridge University Press, Cambridge.

Franklin, J.M., 1993. Volcanic-associated Massive Sulphide Deposits, in Kirkham, R.V., Sinclair, W.D., Thorpe, R.I., and Duke, J.M., eds., Mineral Deposit Modelling: Geological Association of Canada, Special Paper 40, 315-334.

French, W.S., 1973. Two-dimensional and three-dimensional migration of model experiments reflection profiles, *in* Seismic Physical Modeling, edited by Daniel A. Ebrom and John A. McDonald. Geophysics reprint series Nº 15, Series editor Franklyn K. Levin, Society of Exploration Geophysicists, Tulsa, pp. 347-359.

GLI3D™, 1994. Hampson-Russell Software Services Ltd, Calgary, Canada.

Goodfellow, W.D., Lydon, J.W., and Turner, R.J.W., 1993. Geology and Genesis of Stratiform Sediment-hosted (SEDEX) Zinc-Lead-Silver Sulphide Deposits, in Kirkham, R.V., Sinclair, W.D., Thorpe, R.I., and Duke, J.M., eds., Mineral Deposit Modelling: Geological Association of Canada, Special Paper 40, 201-251.

Goulty, N.R., 1997. Lateral resolution of 2D seismic illustrated by a real data example. First Break, 15, Nº 3, 77-80.

Grant, F.S., and West, G.F., 1965. Interpretation Theory in Applied Geophysics. McGrah-Hill Book Co., New York.

Guilbert, J.M., and Parker Jr., C.F., 1986. The Geology of Ore Deposits. Second edition, W.H. Freeman and Company, New York.

Hagedoorn, J.G., 1959. The plus-minus method of interpreting seismic refraction sections. Geophysical Prospecting, Nº 7, 158-182.

Hallof, P.G., 1992. Grounded electrical methods in geophysical exploration, in Practical Geophysics II, edited by Richard van Blaricom, Northwest Mining Association, Spokane, pp 39-173.

Harvey, C.W., 1997. Shear wave velocities of sulphide-bearing assemblages as determined from high pressure laboratory experiments. M.Sc. thesis, Dalhousie University, Nova Scotia. Unpublished.

Hearst, R.B., 1998. Reflections on Kimberlite: a seismic adventure. SEG Expanded Abstracts.

Heiland, C.A., 1968. Geophysical Exploration, Hafner Publishing Co, New York.

Hilterman, F.J., 1970. Three Dimensional Seismic Modeling, *in* Seismic Physical Modeling, edited by Daniel A. Ebrom and John A. McDonald. Geophysics reprint series Nº 15, Series editor Franklyn K. Levin, Society of Exploration Geophysicists, Tulsa, pp. 284-301.

Hubbert, M.K., 1937. History of scale models as applied to the study of geologic structures. Bulletin of the Geological Society of America, 48, 1459-1520.

Ivakin, B.N., 1966. Methods of Seismic Modelling, *in* Seismic Physical Modeling, edited by Daniel A. Ebrom and John A. McDonald. Geophysics reprint series Nº 15, Series editor Franklyn K. Levin, Society of Exploration Geophysicists, Tulsa, pp. 15-20.

Kelly, K.R., Ward, R.W., Sven Treitel, and Alford, R.M., 1976. Synthetic seismograms, a

finite difference approach. Geophysics, 41, Nº 1, 2-27.

Knapp, R.W., and Steeples, D.W., 1986. High-resolution common-depth-point seismic reflection profiling: Instrumentation. Geophysics, 51, Nº 2, 276-282.

Koefoed, O., 1955. On the effect of Poisson's ratio of rock strata on the reflection coefficients of plane waves, Geophysical Prospecting, 3, 381-387.

Koefoed, O., 1962. Reflection and Translation coefficients for plane longitudinal incident waves. Geophysical Prospecting, 9, 305-340.

Lamey, C.A., 1966. Metallic and Industrial Mineral Deposits. McGraw-Hill. New York.

LeBlanc, M., 1987. Chromite in Ocean Arc Environments, in Evolution of Chromium Ore Fields, edited by Clive W. Stowe, Van Nostrand Reinhold Co., New York, pp 265-296.

Lightfoot, P.C., Keays, R.R., Morrison, G.G., Bite, A., and Farrell, K.P., 1997. Geologic and geochemical relationships between the contact sublayer, inclusions, and the main mass of the Sudbury Igneous Complex - a case study of the Whistle Mine Embayment. Economic Geology, 92, 647-673.

Liner, C.L., 1999. Elements of 3-D Seismology. PennWell Publishing, Tulsa. Oklahoma.

Liner, C.L., and Lines, L.R., 1994. Simple prestack migration of crosswell seismic data. Journal of Seismic Exploration, 3, 101-112.

Macnae, J., 1988. Deep Conductor Search - An analysis of survey design for EM and

Electrical methods applied to specific Noranda targets. Noranda Mining and Exploration Inc. Unpublished.

MacKenzie, A.C., and Squires, G.C., 1988. Geology and mineralisation of the Appalachian Duck Pond VMS deposit. Noranda Exploration Co. Ltd. Paper presented at the 94th Annual Northwest Mining Association Convention.

MacInnis, D., and MacKenzie, C.A., 1988. The Duck Pond Massive Sulphide Deposit - a case study, Newfoundland. Noranda Exploration Co. Ltd. Paper presented at the 1988 Prospectors and Developers Association of Canada Annual Convention, Toronto, ON.

Milkereit, B., Berrer, E.K., King, A.R., Watts, A.H., Roberts, B., Adam, E., Eaton, D.W., Wu, J., and Salisbury, M.H., 2000. Development of 3-D seismic exploration technology for deep nickle-copper deposits - A case history from the Sudbury basin, Canada. Geophysics, 65, Nº 6, 1890-1899.

Milkereit, B., Eaton, D., and Wu, J., Perron, G., Salisbury, M., Berrer, E.K., and Morrison, G., 1996a. Seismic Imaging of Massive Sulfide Deposits: Part II. Reflection Seismic Profiling. Economic Geology, 91, Nº 5, 829-834.

Milkereit, B., Eaton, D., and Berrer, E., 1996b. Towards 3D seismic exploration technology for the crystalline crust. Noranda Mining and Exploration Inc., Report Nº MN 2.6.

Milkereit, B., Adam, E., Barnes, A., Beaudry, C., Pineault, R., and Cinq-Mars, A., 1992. An application of reflection seismology to mineral exploration in the Matagami area, Abitibi Belt, Quebec. Current Research part C; Geological Survey of Canada, Paper 92-1C, 13-18.

Mutyorauta, J.J., 1987. High resolution seismic reflection, an exploration tool within an

underground environment - example from Zimbabwe. Journal of African Earth Sciences, 6 Nº 1, 109-115.

Naldrett, A.J., Keats, H., Sparkes, K., and Moore, R., 1996. Geology of the Voisey's Bay Ni-Cu-Co Deposit, Labrador, Canada. Exploration and Mining Geology, 5, Nº 2, 169-179.

Noranda Mining and Exploration Inc., 1993. Tally Pond Final Assessment report. Unpublished.

O'Bien, P.N.S., and Symes, M.P., 1971. Model Seismology, *in* Geophysics reprint series Nº 15, Society of Exploration Geophysicists, Tulsa, pp. 29-53.

Ohmoto, H., 1996. Volcanogenic massive sulphide deposits: The Kuroko perspective. Ore Geology Reviews, 10, 135-177.

Ostrander, W.J., 1984. Plane wave reflection coefficients for gas sands at non-normal angles of incidence. Geophysics, 49, Nº 10, 1637-1648.

Palmer, D., 1981. The generalized reciprocal method of seismic refraction interpretation, Geophysics, 46, 1508-1518.

Pemberton, R.H., 1989. Geophysical response of some Canadian Massive Sulphide Deposits, in Proceedings of Exploration '87, Geological Survey of Ontario, Special Volume 3, pp. 517-531.

Perron, G., and Calvert, A.J., 1998. Shallow, high resolution seismic imaging at the Ansil mining camp in the Abitibi greenstone belt. Geophysics, 63, 2, 379-391.

Pretorius, C.C., Jamison, A.A., and Irons, C., 1989. Seismic Exploration in the Witwatersrand Basin, R.S.A., in Proceedings of Exploration '87, Geological Survey of Ontario, Special Volume 3, pp. 241-253.

Pretorius, C.C., Trewick, W.F., Foure, A., and Irons, C., 2000. Application of 3D seismics to mine planning at Vaal Reefs gold mine, number 10 shaft, R.S.A. Geophysics, 65, Nº 6, 1862-1870.

Prokin, V.A., and Buslaev, F.P., 1998. Massive copper-zinc deposits in the Urals. Ore Geology Reviews, 14, 1-69.

Ronen, J., and Claerbout, F.J., 1985. Surface Consistent Residual Statics by Stack Power Maximization. Geophysics, 50, Nº 12, 2759-2767.

Salisbury, M.H., Milkereit, B., and Bleeker, W., 1996. Seismic Imaging of Massive Sulphide Deposits: Part 1. Rock Properties. Economic Geology, 91, Nº 5, 821-828.

Schmidt, G., 1959. Results of underground seismic reflection investigations in the siderite of the Seigerland. Geophysical Prospecting, 7, 287-290.

Sheriff, R.E., and Geldart, L.P., 1995. Exploration Seismology. Second Edition, Cambridge University Press, Melbourne.

Shuey, R.T., 1985. A simplification of the Zoeppritz equations. Geophysics, 50, 4, 609-614.

Singh, S., 1983. A study of shallow reflection seismics for placer tin reserve evaluation and mining. Geoexploration, 21, Nº 2, 105-135.

Smith, B.W., 1967. The World's Great Copper Mines. Hutchinson & Co. LTD, London.

Spencer, C., Thurlow, G., Wright, J., White, D., Caroll, P., Milkereit, B., and Reed, L., 1993. A vibroseis reflection seismic survey at the Buchans Mine in Central Newfoundland. Geophysics, 58, Nº 1, 154-166.

Stanton, R.L., 1972. Ore Petrology. McGraw-Hill, New York.

Squires, G.C., MacKenzie, A.C., and MacInnis, D., 1990. Geology and genesis of the Appalachian Duck Pond Deposit. Noranda Exploration Co. Ltd. Internal Report. Unpublished.

Stevens, K.M., 1998. On the detection of Ni-Cu ore hosting structures in the Sudbury Igneous Complex using the magnetotelluric method. SEG Expanded Abstracts, Houston.

Thayer, T.P., 1963. Geologic features of podiform chromite deposits, in Methods of the prospection for chromite, Proceedings of an OECD Seminar on modern scientific methods for chromite prospecting, Athens, 1963. Ed. Robert Woodtli, pp135-145.

Vista™ 2.50D, 1998, Seismic Image Software©, Calgary, Canada.

White, D., Boerner, D., Wu, J., Lucas, S., Berrer, E., Hannila, J., and Somerville, R., 2000. Mineral exploration in the Thompson nickel belt, Manitoba, Canada, using seismic and controlled-source EM methods. Geophysics, 65, 6, 1871-1881.

White, J.E., 1965. Seismic Waves: radiation, transmission, and attenuation. McGraw-Hill, New York.

Wright, C., Wright, J.A., and Hall, J., 1994. Seismic reflection techniques for base metal exploration in eastern Canada: examples from Buchans, Newfoundland. Journal of Applied Geophysics, 32, 105-116.

Yilmaz, Ö, 1987. Seismic Data Processing. Society of Exploration Geophysicists, Tulsa.

APPENDICES

A. Determinant expansion of Zoeppritz Equations using Cramer's Rule

The Zoeppritz relations comprise four equations with five unknowns. Since the amplitude of the incident wave is less important in reflection seismic methods, it was decided to normalize both the transmitted and reflected waves with its amplitude to allow easier solution of the resulting simultaneous equations. After normalizing with the amplitude of the incident wave to reduce the number of variables from five to four, the Zoeppritz equations were expressed as (Fowler, 1990);

$$\begin{bmatrix} \cos\theta_1 & -\sin\delta_1 & \cos\theta_2 & -\sin\delta_2 \\ \sin\theta_1 & \cos\delta_1 & -\sin\theta_2 & -\cos\delta_2 \\ Z_1\cos 2\delta_1 & -W_1\sin 2\delta_1 & -Z_2\cos 2\delta_2 & W_2\sin 2\delta_2 \\ \gamma_1 W_1\sin 2\theta_1 & W_1\cos 2\delta_1 & \gamma_2 W_2\sin 2\theta_2 & W_2\cos 2\delta_2 \end{bmatrix} \begin{bmatrix} A_1 \\ B_1 \\ A_2 \\ B_2 \end{bmatrix} = \begin{bmatrix} \cos\theta_1 \\ -\sin\theta_1 \\ -Z_1\cos 2\delta_1 \\ \gamma_1 W_1\sin 2\theta_1 \end{bmatrix} \quad \text{(A1)}$$

where the variables are the same as defined in eqs. (2 & 3). We can rewrite the equation above as $\boldsymbol{AX} = \boldsymbol{B}$, where $\boldsymbol{A}$ is the coefficient matrix, $\boldsymbol{X}$ is a column vector of the variables, and $\boldsymbol{B}$ the column vector of the constants. If det $\mathbf{A} \neq 0$, the solution to this equation is

$$X_i = \frac{\det iA}{\det A} \quad \text{(A2)}$$

where det ($i\boldsymbol{A}$) is obtained from matrix $\boldsymbol{A}$ by substitution in the i^{th} column of $\boldsymbol{A}$ with the column vector $\boldsymbol{B}$. The determinant of $\boldsymbol{A}$ can be simplified using the square matrix a_{ij}, where the subscripts ij refer to the column and row position of each element. Thus;

$$\det A = \begin{vmatrix} a_{11} & -a_{12} & a_{13} & -a_{14} \\ a_{21} & a_{22} & -a_{23} & -a_{24} \\ a_{31} & -a_{32} & -a_{33} & a_{34} \\ a_{41} & a_{42} & a_{43} & a_{44} \end{vmatrix}$$

$$= a_{11}\left\{a_{22}\begin{vmatrix} -a_{33} & a_{34} \\ a_{43} & a_{44} \end{vmatrix} + a_{32}\begin{vmatrix} -a_{23} & a_{24} \\ a_{43} & a_{44} \end{vmatrix} + a_{42}\begin{vmatrix} -a_{23} & a_{24} \\ -a_{33} & a_{34} \end{vmatrix}\right\}$$

$$- a_{21}\left\{-a_{12}\begin{vmatrix} -a_{33} & a_{34} \\ a_{43} & a_{34} \end{vmatrix} + a_{32}\begin{vmatrix} a_{13} & -a_{14} \\ a_{43} & a_{44} \end{vmatrix} + a_{42}\begin{vmatrix} a_{13} & -a_{14} \\ -a_{33} & a_{34} \end{vmatrix}\right\}$$

$$+ a_{31}\left\{-a_{12}\begin{vmatrix} -a_{23} & -a_{24} \\ a_{43} & a_{44} \end{vmatrix} - a_{22}\begin{vmatrix} a_{13} & -a_{14} \\ a_{43} & a_{44} \end{vmatrix} - a_{42}\begin{vmatrix} a_{13} & -a_{14} \\ -a_{23} & -a_{24} \end{vmatrix}\right\}$$

$$- a_{41}\left\{-a_{12}\begin{vmatrix} -a_{23} & -a_{24} \\ -a_{33} & a_{34} \end{vmatrix} - a_{22}\begin{vmatrix} a_{13} & -a_{14} \\ -a_{33} & a_{34} \end{vmatrix} + a_{32}\begin{vmatrix} a_{13} & -a_{14} \\ -a_{23} & a_{24} \end{vmatrix}\right\}$$

$$= a_{11}\left\{-a_{22}a_{33}a_{44} - a_{22}a_{34}a_{43} - a_{23}a_{32}a_{44} + a_{24}a_{32}a_{43} - a_{24}a_{33}a_{42} - a_{24}a_{33}a_{42}\right\}$$

$$- a_{21}\left\{a_{12}a_{33}a_{44} + a_{12}a_{34}a_{43} + a_{13}a_{32}a_{44} + a_{14}a_{32}a_{43} + a_{13}a_{34}a_{42} - a_{14}a_{33}a_{42}\right\}$$

$$+ a_{31}\left\{a_{12}a_{23}a_{44} - a_{12}a_{24}a_{43} - a_{13}a_{22}a_{44} - a_{14}a_{22}a_{43} - a_{14}a_{24}a_{42} - a_{14}a_{23}a_{42}\right\}$$

$$- a_{41}\left\{a_{12}a_{23}a_{34} + a_{12}a_{24}a_{33} - a_{13}a_{22}a_{34} + a_{14}a_{22}a_{33} + a_{13}a_{24}a_{32} + a_{14}a_{23}a_{32}\right\}$$

This determinant expansion allows the equation to be solved for specific geologic interfaces quickly and efficiently by substitution in a spreadsheet.

B. Seismic survey data

CLIENT : NORANDA MINING AND EXPLORATION
PROSPECT : Tally Pond, Newfoundland
LINE : TLP98-001
CONTRACTOR : GeoScott Exploration Consultants Ltd.
ORIGIN : U.T.M. ZONE 21
DATUM : NAD27
UNITS : METERS
SURVEYOR : Len Mandville GPS
SURVEY DATE : April 97

Station	Northing	Easting	Elev
100	5390656.843	541028.861	280.860
102	5390645.999	541019.802	280.846
104	5390631.059	541006.723	280.860
106	5390617.788	540990.947	280.576
108	5390601.469	540979.326	280.883
110	5390587.754	540967.230	281.010
112	5390574.811	540958.422	281.695
114	5390555.123	540944.085	280.425
116	5390539.153	540929.978	280.707
118	5390532.734	540907.899	281.209
120	5390519.206	540891.922	280.777
122	5390498.694	540886.397	280.206
124	5390484.727	540872.287	280.511
126	5390468.679	540859.378	280.512
128	5390453.393	540845.276	280.512
130	5390435.114	540837.806	280.508
132	5390420.217	540825.838	280.852
134	5390404.752	540812.557	281.172
136	5390388.021	540798.038	281.258
138	5390372.198	540785.399	281.458
140	5390357.308	540772.871	281.516
142	5390342.027	540759.760	281.564
144	5390327.283	540746.971	281.603
146	5390311.656	540733.962	281.662
148	5390296.354	540721.179	281.852
150	5390281.180	540708.352	281.580
152	5390265.406	540695.256	281.959
154	5390250.150	540682.277	282.400

156	5390235.137	540669.347	282.931
158	5390219.617	540656.830	282.978
160	5390204.552	540643.675	283.518
162	5390189.227	540630.623	283.612
164	5390173.973	540617.448	283.718
166	5390158.198	540603.841	283.860
168	5390141.738	540590.096	284.017
170	5390127.007	540578.394	284.189
172	5390111.840	540564.722	284.206
174	5390097.001	540551.683	284.178
176	5390085.927	540540.998	284.044
178	5390068.209	540526.284	284.631
180	5390050.674	540513.295	284.580
184	5390019.961	540487.847	284.621
188	5389989.783	540464.797	285.728
192	5389957.045	540434.326	286.931
196	5389927.590	540409.257	288.291
200	5389897.381	540385.435	288.971
204	5389866.336	540358.075	290.362
208	5389836.848	540332.915	291.777
212	5389807.169	540307.778	293.294
216	5389775.659	540280.359	295.246
220	5389744.304	540255.029	296.521
224	5389715.624	540230.069	294.921
228	5389693.739	540211.469	296.113
232	5389654.959	540178.254	297.373
236	5389626.084	540153.495	298.321
240	5389593.146	540125.148	299.112
244	5389563.103	540101.174	300.592
248	5389533.748	540075.100	301.719
252	5389502.690	540049.430	302.945
256	5389473.125	540023.094	304.171
260	5389442.272	539997.659	305.574
264	5389412.869	539972.687	306.248
268	5389381.124	539946.344	306.871
272	5389350.416	539921.328	307.248
276	5389320.205	539894.874	308.882
280	5389289.921	539869.755	309.441
284	5389259.920	539843.602	311.208
288	5389228.657	539818.209	313.776
292	5389197.279	539795.584	320.385

300	5389137.023	539742.275	318.464
304	5389108.902	539716.014	318.149
308	5389078.065	539690.274	317.906
312	5389047.335	539664.448	317.369
316	5389017.794	539638.236	317.474
320	5388987.748	539612.002	317.282
324	5388957.186	539586.402	316.645
328	5388929.717	539564.491	317.062
330	5388895.770	539535.956	318.054
334	5388865.727	539510.278	316.911
340	5388832.426	539485.589	317.789
344	5388804.359	539458.870	314.034
348	5388774.364	539432.930	313.431
352	5388744.154	539406.898	313.927
356	5388713.808	539380.907	313.093
360	5388683.603	539354.314	312.182
364	5388655.954	539330.523	310.927
368	5388622.390	539303.938	308.795
372	5388592.623	539277.688	308.724
376	5388562.001	539252.031	307.536
380	5388531.661	539226.523	306.655
384	5388501.223	539200.919	307.282
388	5388471.116	539174.585	307.728
392	5388440.847	539148.877	307.504
396	5388410.777	539122.073	309.796
400	5388380.129	539097.070	309.045
404	5388349.555	539071.595	308.546
408	5388319.864	539046.762	312.341
412	5388289.501	539019.701	309.269
416	5388258.912	538994.072	309.770
420	5388228.462	538969.257	310.275
424	5388197.853	538943.409	309.988
428	5388167.787	538918.141	309.151
432	5388136.971	538890.800	309.912
436	5388106.267	538865.448	308.156
440	5388075.923	538839.626	306.614
444	5388046.217	538813.517	306.154
448	5388015.377	538788.541	305.572
452	5387986.149	538761.816	308.235
456	5387953.960	538736.077	307.213
460	5387923.715	538710.914	306.594

464	5387893.968	538684.300	307.203
468	5387863.450	538659.012	306.938
472	5387833.306	538633.645	306.980
476	5387803.786	538606.854	307.649
480	5387773.539	538580.411	308.026
484	5387742.994	538554.952	308.089
488	5387712.436	538528.734	307.850
492	5387682.100	538503.017	307.346
496	5387651.251	538477.728	306.911
500	5387620.350	538452.534	306.095
504	5387589.854	538426.995	305.111
508	5387558.808	538402.362	304.655
512	5387528.347	538376.787	304.558
516	5387498.674	538350.035	305.017
520	5387468.008	538324.584	303.753
524	5387437.259	538299.085	303.494
528	5387407.198	538272.993	303.595
532	5387376.926	538246.963	303.499
536	5387346.801	538221.114	303.679
540	5387316.280	538195.229	303.348
544	5387285.993	538169.360	303.050
548	5387255.645	538143.697	303.045
552	5387225.562	538117.240	302.943
556	5387194.483	538092.039	303.336
560	5387165.058	538065.677	301.394
564	5387134.279	538040.202	300.767
568	5387103.764	538014.740	300.822
572	5387073.227	537989.271	300.803
576	5387042.687	537963.779	300.748
580	5387012.483	537937.468	301.413
584	5386981.841	537911.858	302.131
588	5386952.163	537886.618	302.926
592	5386921.249	537860.080	303.452
596	5386890.704	537834.412	303.755
600	5386860.920	537808.107	304.347
604	5386830.269	537782.670	304.397
608	5386799.726	537757.299	304.284
612	5386769.328	537731.413	304.025
616	5386738.409	537706.348	303.769
620	5386707.512	537679.490	303.845
624	5386677.211	537654.881	303.941

628	5386647.024	537628.800	304.420
632	5386616.752	537603.136	304.118
636	5386586.662	537576.963	304.312
640	5386556.330	537550.941	304.304
644	5386525.711	537524.928	304.565
648	5386495.459	537499.477	305.119
652	5386466.207	537472.410	305.689
656	5386435.243	537447.359	305.442
660	5386404.794	537421.715	305.473
664	5386374.321	537396.203	305.489
668	5386344.522	537369.971	305.261
672	5386314.308	537343.961	304.592
676	5386283.224	537319.245	303.654
680	5386254.266	537291.533	302.575
684	5386223.463	537266.439	302.451
688	5386193.554	537240.583	301.342
692	5386162.528	537214.978	301.113
696	5386132.178	537188.911	302.325
700	5386102.246	537162.920	302.336
704	5386071.282	537137.366	302.498
708	5386041.292	537111.498	303.137
712	5386010.817	537086.020	303.962
716	5385980.385	537059.774	304.535
720	5385950.019	537033.912	304.264
728	5385888.913	536982.921	304.162
730	5385872.774	536969.701	304.327
732	5385858.165	536956.893	304.597
734	5385842.569	536943.849	304.400
736	5385827.646	536930.929	304.123
738	5385812.095	536918.110	303.912
740	5385795.974	536904.353	303.875
742	5385781.779	536891.948	304.175
744	5385767.088	536879.564	304.091
746	5385751.791	536865.909	304.708
748	5385737.156	536853.847	305.117
750	5385721.263	536840.290	305.372
752	5385706.572	536828.215	305.792
754	5385690.615	536814.860	305.684
756	5385675.718	536802.546	305.949
758	5385660.145	536789.327	305.839
760	5385645.568	536776.459	305.922

762	5385630.007	536763.357	305.683
764	5385613.925	536750.316	305.961
766	5385598.600	536739.362	305.705
768	5385584.054	536725.948	305.253
770	5385568.463	536713.040	305.242
772	5385553.536	536700.131	305.462
774	5385538.083	536687.422	305.646
776	5385523.159	536674.411	305.806
778	5385507.760	536661.836	305.794
780	5385492.772	536648.844	306.219
782	5385477.271	536636.183	307.332
784	5385462.489	536622.725	306.984
786	5385447.506	536609.825	306.856
788	5385431.985	536596.928	307.155
790	5385416.281	536584.348	308.817
792	5385401.239	536571.619	308.851
796	5385371.605	536545.021	307.942
800	5385341.653	536522.152	308.874
802	5385326.185	536508.533	309.783
804	5385310.688	536494.375	311.329
806	5385294.813	536480.974	313.246
808	5385280.004	536467.429	314.669
810	5385265.172	536453.936	315.009
BCHN1111	5388691.229	539524.903	327.954
stjo CACS-ACP 920000	5280160.813	824827.985	164.781

Drill Hole co-ordinates (UTM projection, Datum NAD27).

Hole	Northing	Easting	Elevation (m)
TP-6	5388999.30	539615.20	311.40
TP-41	5388393.70	539097.50	304.10
TP-44	5387785.70	538578.90	299.50
DP-176	5386562.70	537545.10	295.90
DP-122	5386181.60	537222.60	290.80

C: Examples of the raw shot gathers from the analogue models.

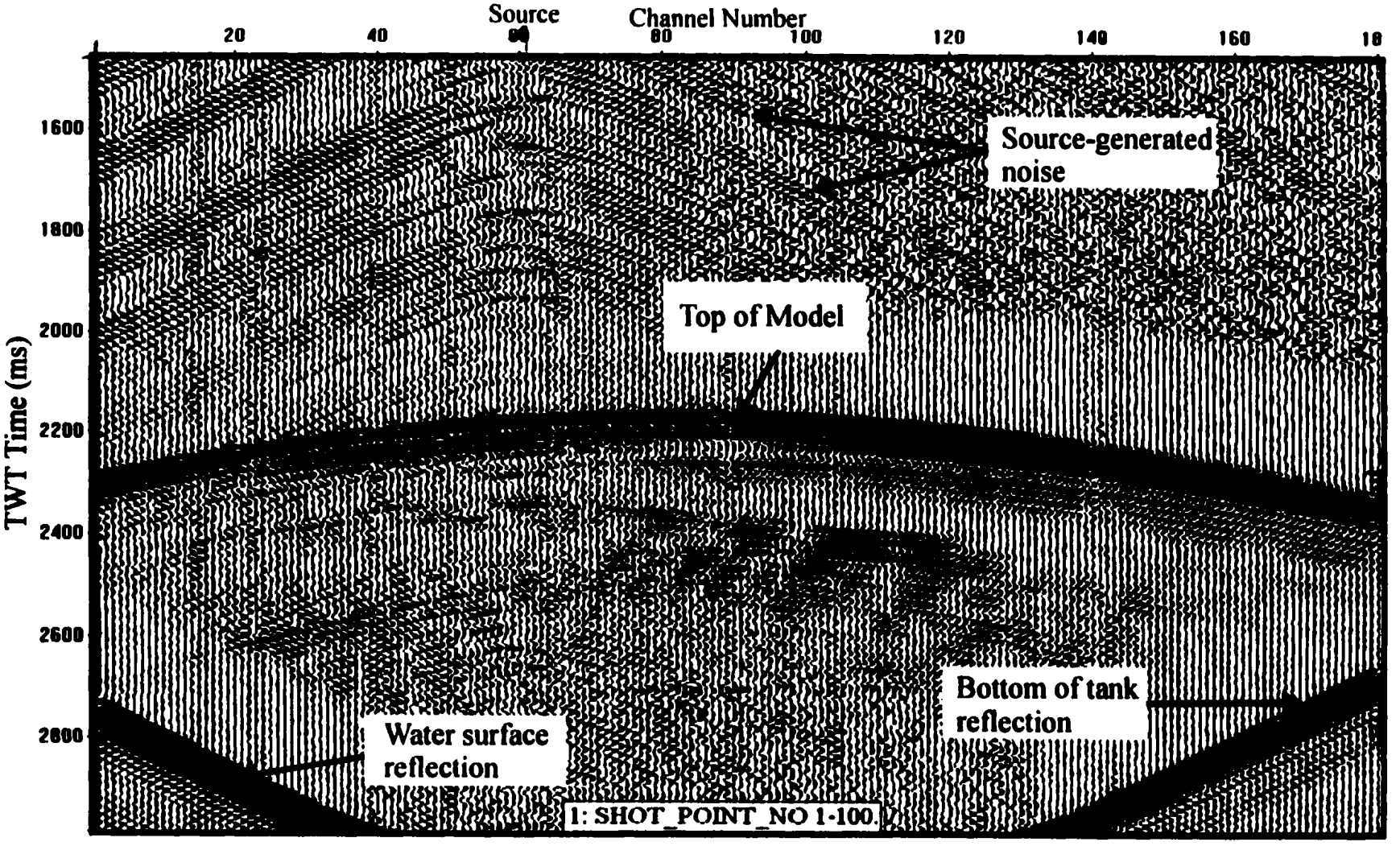

Figure C1: Shot gather from the 3D data recorded over the egg-shaped model. Note the strong coherent noise generated by the source. No processing applied. Trace spacing is 5 m (scaled).

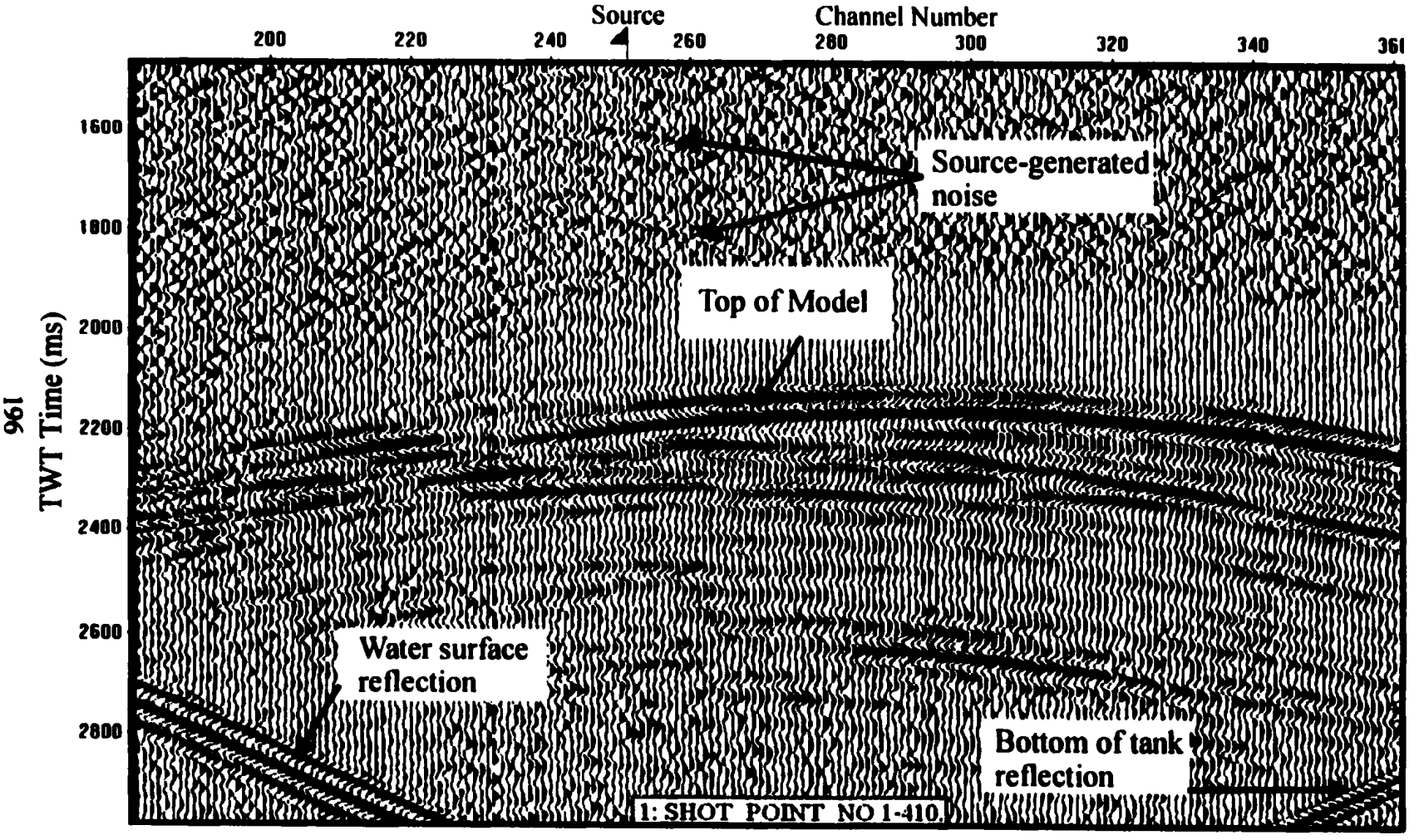

Figure C2: Shot gather from the 3D data recorded over the cylinder-shaped model. No processing. Trace interval is 4.55 m (scaled).

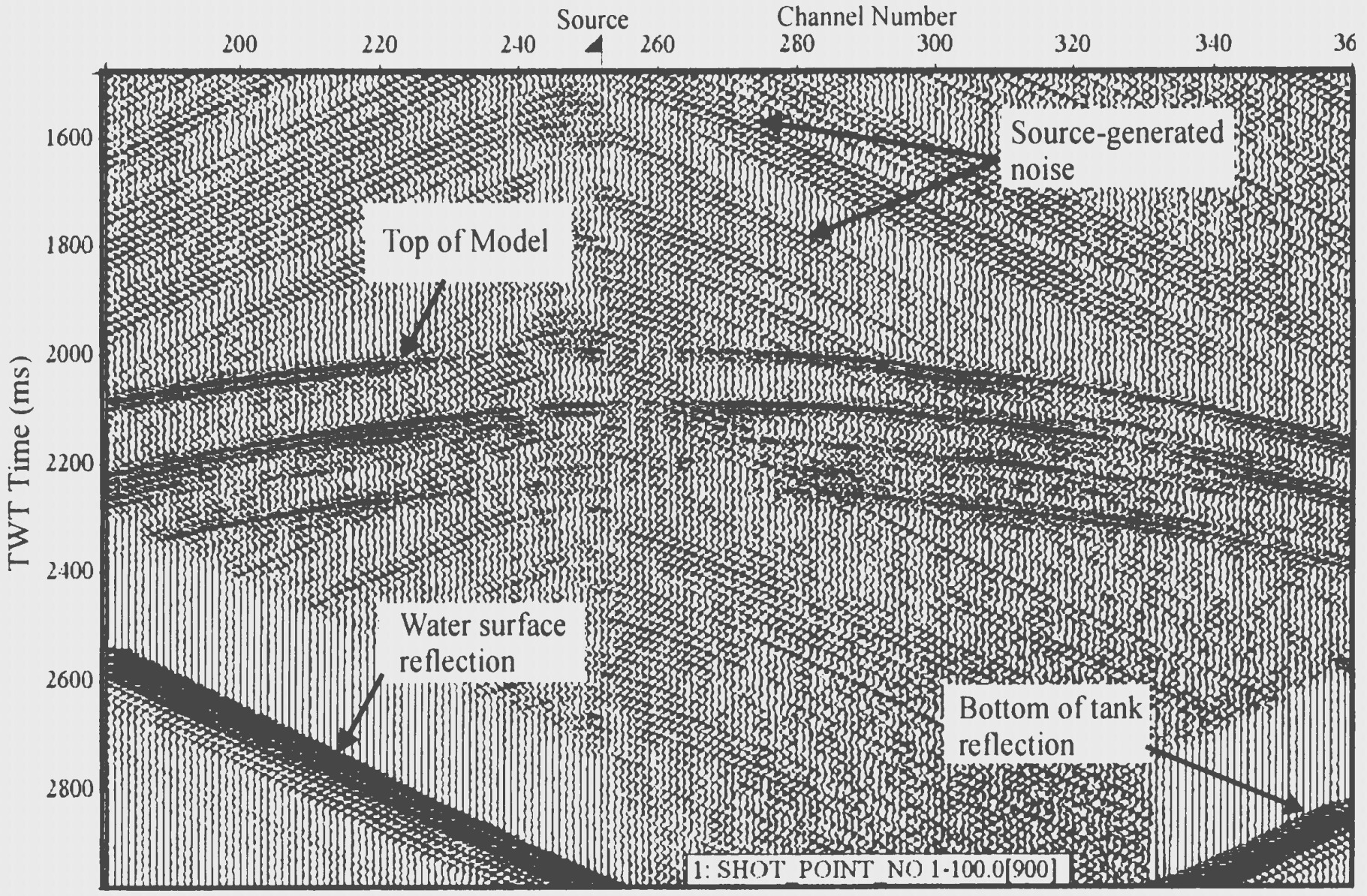

Figure C3: Shot gather from the 3D data recorded over the disk-shaped model. Note the strong coherent noise generated by the source. No processing applied. Trace interval is 4.55 m (scaled).